# SPATIALLY RESOLVED TERAHERTZ PROPAGATION

By

MATTHEW T. REITEN

Bachelor of Science, Physics
Bachelor of Science, Electrical Engineering
Bachelor of Science, Engineering Physics
University of North Dakota
Grand Forks, ND
1991

Master of Science, Applied Physics
Rice University
Houston, TX
1994

Submitted to the Faculty of the
Graduate College of the
Oklahoma State University
in partial fulfillment of
the requirements for
the Degree of
DOCTOR OF PHILOSOPHY
May, 2006

SPATIALLY RESOLVED TERAHERTZ PROPAGATION

Dissertation Approved:

R. Alan Cheville

Daniel Grischkowsky

Charles Bunting

James Wicksted

A. Gordon Emslie

Dean of the Graduate College

# ACKNOWLEDGEMENTS

Special thanks to everyone who put up with me throughout this process. Research is an inherently selfish pursuit, in both time and personal energy. Beth had the worst of it, but grad school was better than being deployed to Afghanistan. My friends and colleagues made it a worthwhile endeavor and reminded me to keep my eyes on the goal: Suchitra Ramani, Stacee Harmon, Mohammad Awad, and Steve Coleman. Singular thanks go to Suchi, who went through the process of writing, defending, and understanding at the same time, for rekindling my fading curiosity. A shared ordeal forges strong bonds among the remaining two.

The days of the mad scientist working alone (or even with a single hunchback) are gone. The work inscribed herein was due in part to the contributions of a large number of individuals who worked with me and have moved on to different pursuits. I'll surely forget one or two, but that is a reflection of my poor memory and not that person's valued assistance. Wendy Siemens helped produce the X-Y stage that finally died in the last moments of my data taking as well as the infamous box around my THz system. Steve Constein handled the control programs and data acquisition. Katy McClatchy assisted during the initial fiber coupling days. Jeff Daniels developed the rapid scanner software on his project. Christine Co fabricated and stretched fiber for the multiple illumination beams. Lesley Hess whipped up ceramic samples and busted ball bearings. Suzanne Kammer made bubbles in an up ended THz system.

I must thank my parents. My mother for her understanding in this process and my father for his support while not understanding why I felt compelled to spend so many productive years in school.

I also have to thank my advisor and friend, who lured me to Rice University years ago and once again pulled me into his Wiley Coyote styled schemes here in Oklahoma. Our relationship is an odd one, but continues the rather incestuous advisor/student precedent that makes for good story telling at conferences. Alan Cheville, someday they'll realize that we've fooled them. But until then, we'll have an interesting time.

# TABLE OF CONTENTS

# LIST OF TABLES

# LIST OF FIGURES

# LIST OF SYMBOLS AND ACRONYMS

| Symbol/Acronym | Meaning |
|---|---|
| $\alpha$ | Field loss coefficient |
| $A_n$ | Parameters for lens surface calculation |
| Ae | Effective area for an antenna (electrical size) |
| AR | Anti reflective |
| c | Speed of light in vacuum |
| C | Curvature for lens surface calculation |
| CW | Continuous wave (single frequency) |
| $d$ | Lateral beam displacement due to the GH shift |
| d | Distance along normal to the faces between prisms |
| D | Surface wave propagation distance due to the GH shift |
| $\Delta$ | Gap width between prism faces for FTIR |
| $D_{beam}$ | Beam diameter |
| DC | Direct Current |
| $\Delta\nu$ | Frequency spacing |
| dt | Time shift/time step in FDTD simulation |
| $\Delta t$ | Time spacing/change in time |
| $\Delta x$ | Horizontal spacing/change in position |
| dx | Length parameter for FDTD simulation |
| $\delta_y$ | Transverse shift |
| $\delta_z$ | Attenuation distance |
| $e$ | Euler's number |
| E ($E_T$/$E_O$) | Electric field (transmitted across FTIR barrier/Reference) |
| $f$ | Frequency |
| $\Phi$ | Vertex angle for prism/Total phase |
| FDTD | Finite Difference Time Domain |
| $f_L$ | Focal length |

| | |
|---|---|
| FRU | Field Replaceable Unit |
| FTIR | Frustrated Total Internal Reflection |
| FWHM | Full Width Half Maximum |
| $\gamma$ | Phase correction due to translation of input/exit prism/propagation angle out of lens with respect to optic axis |
| GH | Goos-Hanchen |
| H | Transfer function |
| h | Planck's constant |
| $i$ | Imaginary number $(-1)^{½}$ |
| k | Wave vector |
| $\lambda$ | Wavelength |
| $l$ | Dipole length |
| n | Index of refraction |
| N | Count of scans/data points |
| $\nu$ | Frequency |
| N.A. | Numeric Aperture |
| $n_{eff}$ | Effective index (complex) |
| $n_o$, $n_1$ | Index of refraction for indicated medium |
| $n_{real}$ | Real index of refraction |
| P | Polarization in the plane of incidence TM |
| PSNR | Peak signal-to-noise ratio |
| $\theta c$ | Critical angle |
| $\rho$ | Radius on lens |
| $r_{01}$, $r_{10}$ | Fresnel field reflection coefficient |
| R | Radius of curvature for Si lens |
| $R_A$ | Antenna resistance |
| $R_L$ | Loss resistance |
| $R_r$ | Radiation resistance |
| S | Polarization out of the plane of incidence (TE) |
| SOS | Silicon on sapphire |
| $t_{01}$, $t_{10}$ | Fresnel field transmission coefficient |
| $\tau_c$ | Complex transversal time |

|  |  |
|---|---|
| $\tau_\phi$ | Phase time for tunneling barrier |
| $\tau_L$ | Loss time for tunneling barrier |
| V | Potential |
| $\omega$ | Angular frequency |
| $w_e$ | Effective width (electrical width) |
| $W_i$ | Incident power from a plane wave |
| $w_o$ | Beam waist (radius) |
| $\Psi$ | Wave function/Optical path length for stationary phase analysis |
| z | Propagation distance |

# 1 Introduction

## 1.1 Terahertz Propagation

The research presented here investigates the spatial behavior of near single cycle freely propagating terahertz radiation with special emphasis on propagation through frustrated total internal reflection also known as an optical tunneling barrier. The terahertz pulses were generated through optoelectronic means by an experimental system based on established terahertz time domain spectroscopy techniques. By raster scanning the terahertz beam detector orthogonally to the optic axis with a fiber-coupled reduced aperture receiver, the electric field of the propagated beam was measured directly. This system was used to investigate a broad bandwidth pulse transiting an optical tunneling barrier comprised of a matched pair of high resistivity silicon prisms cut at an incident angle above critical angle. Spectral analysis and numeric modeling tested claims of superluminal (faster than the speed of light) propagation through an optical tunneling barrier and found the claims to be ill-founded.

## 1.2 Motivation

Every measurement system has advantages and limitations. For best performance and results, matching a set of experiments to a system's strengths can prove to be the greatest challenge. This may appear obvious; however too often because an experiment *can* measure a given phenomena, heroic efforts are made to measure the effects with a less than ideal system. Measurement of terahertz pulse propagation through an optical barrier is particularly well suited to the strengths of the experimental system.

Terahertz (**THz**) pulses generated and detected though optoelectronic means [1] provide an ideal broad bandwidth (greater than 1:1 ratio of bandwidth to center frequency), near single cycle, freely propagating, electromagnetic radiation. The phase of the radiation is directly measurable without the application of non-linear optical techniques as is required for optical frequencies. The wavelengths are mesoscopic, small enough to not require large anechoic chambers for scattering measurements as microwave radar experiments would, yet large enough to make target fabrication and manipulation relatively uncomplicated. No liquid helium bolometers are required to measure the beam intensity of the deep infrared radiation.

| Advantages | Challenges |
|---|---|
| Near single cycle pulses well delimited in time | Slowly varying amplitude approximations not rigorously applicable |
| Broad bandwidth pulse allows spectroscopic measurements | Highly absorptive atmospheric water vapor lines limit many field applications |
| Peak signal-to-noise of detection methods better than 10,000:1 in cases | Low power, on the order of nanowatt average power per pulse |
| Measurement of electric field phase and amplitude | Requires precise optical beam alignment* |
| High index-low absorption material (Si) available for optical components | Losses due to reflection at optical interfaces with high index materials |
| Insensitive to thermal background | |
| Mesoscopic wavelengths | Scalability of material properties |

**Table 1.1** Advantages and challenges inherent to photoconductive THz generation and applications. Issues arising from precise optical beam alignment is addressed in Chapter 4 by fiber coupling the THz receiver.

Table 1.1 lists a few of the advantages and challenges associated with THz experimental systems, with emphasis on opoelectronically generated THz pulses. The challenges presented do not impact the spatial profile measurements reported here with the exception of the precise optical beam alignment. However this list will serve as criteria to select appropriate applications of THz technology and techniques.

The near single cycle pulses are localized in time, allowing physical interpretation of scattering mechanisms from time of flight measurements. However the slowly varying amplitude approximation often used to make simplifications to treating propagation of optical pulses does not rigorously hold. The short pulse has a correspondingly large bandwidth, which when numerical Fourier transformations are applied can render spectroscopic information. This in turn can limit the applications outside of a controlled laboratory environment since the presence of atmospheric water vapor, which is highly absorptive in much of the THz region. The detection schemes employed, specifically lock-in phase sensitive detection and the typically high pulse repetition rate (~100 MHz), coupled with inherent time gating of the ultrashort optical pulse on the fast response detector can yield very high signal-to-noise ratios. The absolute power per pulse though is low, 10 nW or so average power in a typical system, limiting THz techniques to the linear response of weakly perturbative material interactions. The receiving antennas are phase sensitive, but the small (~5 μm) active areas within the lithographically produced structures require precise focusing and alignment of the optical beam to achieve peak performance. Small changes in positioning of the receiver can alter the absolute timing and decrease or even modify the spectral components of the detected THz waveform. The advantage of mesoscopic wavelengths in the submillimeter range is that the length scales involved are mechanically realizable while still allowing an economy of scale that can fit experiments on a single laboratory bench. The mesoscale wavelength can be applied to modeling radar scattering. The challenge for true modeling of a target's impulse response though is the scaling of the dielectric properties to properly represent a realistic object.[2]

## 1.3 What makes THz interesting

The terahertz regime spans the gap in the electromagnetic spectrum between microwaves and infrared light. Generation and detection of terahertz frequencies had been historically difficult and, with no obvious driving application, development of appropriate techniques received little attention by the optical or microwave communities until fairly recently.[3]

Although alternative methods to generate and detect terahertz frequencies have been developed, such as electro-optic detection or photomixing[4], the techniques described here will focus on photoconductive antennas gated by short optical pulses. This capability arose from the merging of two technologies, ultra-fast lasers and lithographically fabricated planar transmission line structures.

When a new measurement technique is developed, new discoveries are made. If one considers a few experimental advances in optics, such as the introduction of the telescope, microscope, x-ray photography, radar, or short pulse lasers, all instances of improved detection methods provided new abilities to probe new phenomena too numerous to list here.

THz time domain spectroscopy (**THz-TDS**) is a relatively new method, developed initially at Bell Labs and AT&T Labs in the late 1980's.[5] Since then, interest in the potential applications and enhancements to the technology has grown, such that commercials THz-TDS systems are becoming available and industrial applications are currently being explored.[6]

Spectroscopic applications performed with THz systems have identified states in gasses[7,8] and electronic characteristics of semiconductors[1] and exotic perovskite materials[9]. Likewise THz-TDS has been applied to imaging objects by various schemes such as raster scanning an object through the focus of the system in both reflection and transmission,[10]synthetic aperture reconstruction,[11] sub-wavelength back projection tomography,[12]time reversal Huygens-Fresnel integration,[13] or synthetic phased array imaging.[14]

The systems described here are primarily applied to examining the propagation of a short electromagnetic pulse with emphasis on the behavior through an optical tunneling barrier, which is the transmission of light through a region classically forbidden in a simple ray optics treatment. Previous observations of this phenomena had led investigators to incorrectly claim superluminal propagation through this optical barrier in part due to the temporal localization of THz pulses.[15] The methods used in this investigation blend spectroscopic and imaging techniques to describe the processes that occur when a short pulse interacts with an optical tunneling barrier.

## 1.4 **Outline of Dissertation**

Chapter Two covers the basics of a terahertz time domain spectroscopy (THz-TDS) system as a starting point for the experimental work presented here. Background concepts that will be applied in later chapters, such as extraction of material properties from measurements, are also addressed.

Chapter Three covers the basic one dimensional measurements of frustrated total internal reflection (**FTIR**)[16] performed on silicon wedges.[17] Linear dispersion theory is shown to predict the performance of the system without assuming a path for the beam to propagate. Additional experiments involving polarization response of the FTIR system and propagation across a dielectric slab at a range of incident angles is investigated.

Chapter Four details the fiber coupled THz receiver experiments that are applied to FTIR and lens coupled propagation. Basic measurements of beam profiles are shown to demonstrate the performance characteristics of the fiber coupled systems. The different dispersion compensation schemes are also evaluated.

Chapter Five extends the work developed to treat the one dimensional analysis to two dimensional pulse reshaping.[18] Direct measurements of the lateral Goos-Hanchen shift[19] and analysis of the complex tunneling time[20] are presented. Additional three dimensional measurements are presented as well as numerical treatments for visualization of the time evolution of a THz pulse through a FTIR barrier.

Chapter Six details measurements and analysis of the beam coupling from a silicon lens and the contribution of evanescent fields.[21]

Chapter Seven concludes this work with a brief summary, future directions for research, and the conjecture as to potential applications of the research presented. It briefly touches on applications and additional results enabled by the fiber coupled system.

# 2 THz Basics

## 2.1 Standard TDS system

THz-TDS serves as the basis for the experimental systems utilized in the work detailed in this document, so the description of a standard TDS system is presented as a starting point in this chapter. The main focus of the main body of this dissertation, however, is on the departures from standard applications and experimental configurations. Subsequently, those familiar with THz-TDS and associated analytic techniques are encouraged to move ahead to the following chapters.

A typical confocal THz-TDS system is shown in Figure 2.1. The basic principle of operation is to pass a near single cycle THz pulse through a given material or structure under test. The short pulse has a corresponding wide bandwidth. Applying a numerical Fourier transform, the material's spectral response can be extracted from a transfer function determined through comparison to a reference pulse. This provides information about frequency depended absorption, index, or chemical content of a given sample.[4]

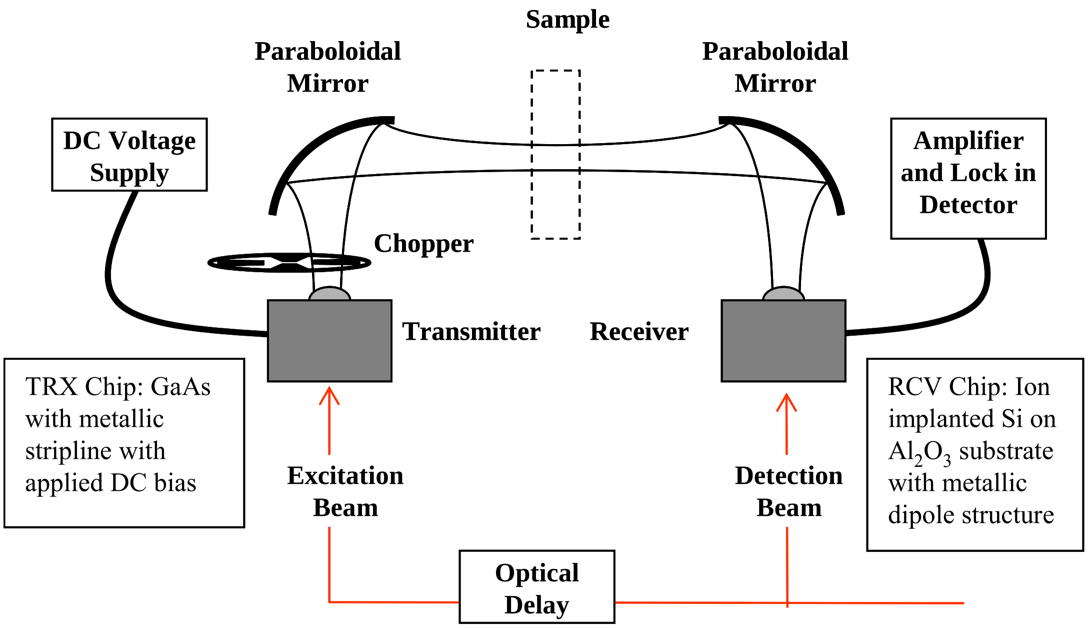

**Figure 2.1** Schematic of a THz-TDS system.

An optoelectronically generated THz pulse is created with a coplanar stripline structure on a GaAs substrate biased at 60-90 $V_{DC}$ using focused laser pulses to produce a localized electron-hole plasma in the semiconductor. The optically generated charge carriers in the applied field are accelerated and emit radiation in the THz frequency range, resulting in a near single-cycle pulse. The THz pulse is preferentially radiated into the high index GaAs substrate by a ratio of $n^3$:1 due to the effect of a small dipole located just below the surface of the semiconductor shown schematically in Figure 2.2.[22] A silicon lens in contact with the THz transmitter substrate directs the emitted radiation which is then collimated by a paraboloidal reflector with focal length $f_L$ = 119 mm.

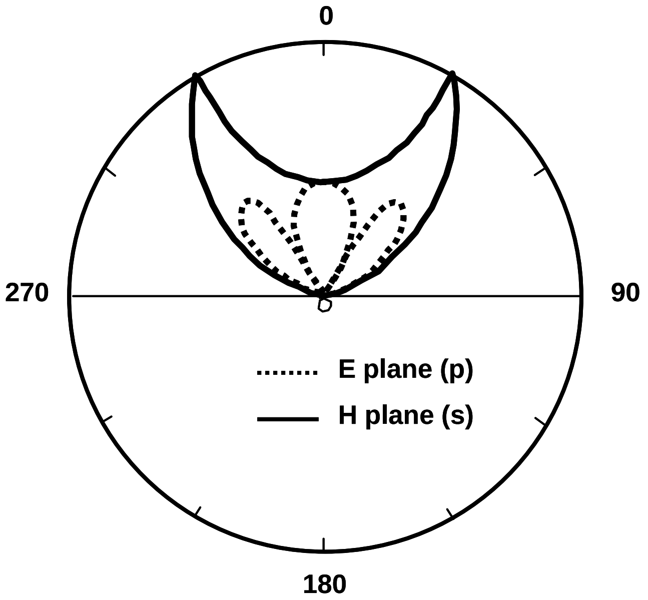

**Figure 2.2** E and H plane power intensity distributions for a small dipole near a dielectric interface after Lukosz. Here $n_1 = 4$.

A second paraboloidal reflector is placed at twice the focal length away from the transmitter side reflector. This yields a unity optical transfer function between the transmitter and receiver, maximizing signal and bandwidth,[23] if Gaussian beam behavior is assumed. The typical system has a propagation range of less than 1/2 meter utilizing collimating off-axis-paraboloidal mirrors. These same mirrors collect the majority of incident THz radiation and integrate over the entire face of the beam. The optical transfer function of the optics can limit the spectral response if not properly aligned. The receiver reflector redirects and refocuses the THz beam onto the lens of the receiver.

The receiver chip is typically comprised of oxygen implanted silicon on sapphire (SOS) substrate with a metalized dipole antenna. The silicon lens collects the focused THz beam onto the dipole area where optical laser pulses time gate the antenna. The incident THz field is only measured during the response time of the carriers in the SOS[24] after illumination.

By varying the time of arrival between the optical excitation beam on the transmitter and optical detection beam on the receiver by changing the path length of a given delay arm, the electric field of the THz pulse impinging on the dipole induces a current that can be measured. This current is proportional to the field and will represent the pulse shape if the relaxation time of the detector is sufficiently short. For the purposes of this work, a gating pulse of 100 fs or less is suitable to resolve a THz pulse on the order of picoseconds in duration.

## 2.2 Standard TDS components

The standard THz-TDS experiment is comprised of a standard set of components as outlined above (see Figure 2.1.) The detector and receiver modules, THz beam directing and focusing optics, optical beam directing and delay lines, supporting electronics for data collection, and the ultrafast laser oscillator. Any of these components may be modified as determined by the nature of a given experiment, but all are common to any TDS system.

*Laser Oscillator*

The optical laser system used a passively mode locked titanium doped sapphire (**Ti:Sapph**) laser system from Kapteyn Murnane Laboratories pumped by a diode pumped frequency doubled neodymium doped orthovanadate laser—a Verdi system from Coherent. The turn-key Verdi laser provides up to 5 W of 532 nm continuous wave optical pumping power for the Ti:Sapph, however the best behavior and long term stability was achieved at output powers of 4.5 to 4.85 W.

The Ti:Sapph can produce over 530 mW continuous power of sub 50 fs pulses at a repetition rate of 88 MHz determined by the cavity length. The spectrum of the short pulse is centered at 820 nm with a measured bandwidth of 40 nm FWHM determined with an Ocean Optics fiber coupled spectrometer. The Ti:Sapph is tunable due to the broad fluorescence spectrum available in the gain medium, though the near infrared with photon energies on the order of 1.5 eV are preferred. This is near the 1.43 eV band gap of GaAs. Higher photon excitation energies (~ 2 eV) contribute strongly to intra-band scattering of "hot carriers" into the L side valleys that experience a time dependent decrease in electron mobility.[25] This decreased mobility damps the ballistic transport and can decrease the THz generation efficiency by increasing the current rise time.

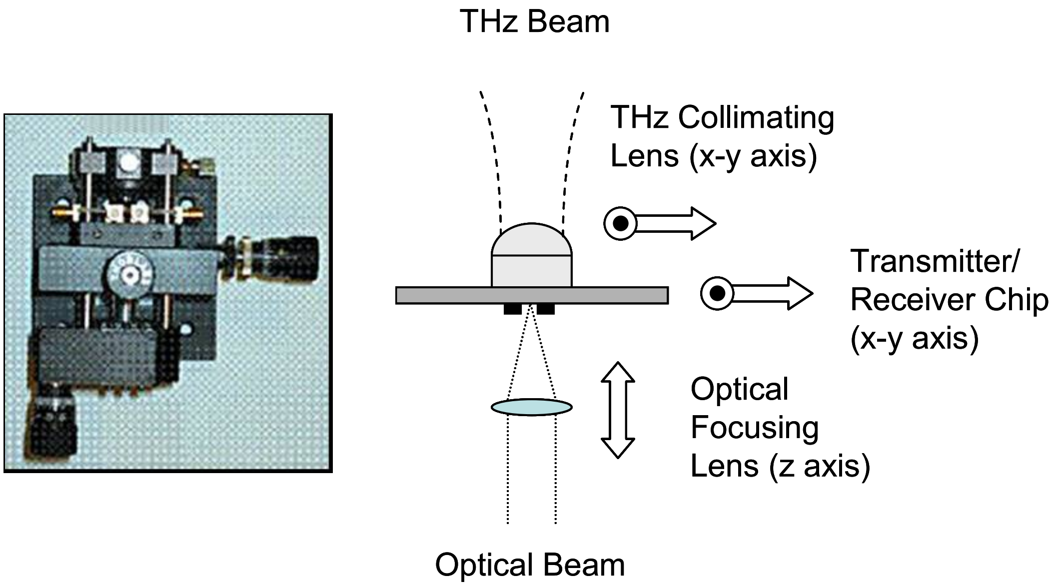

**Figure 2.3** A version of a FRU is pictured on the left. The basic concept is illustrated on the right.

*Transmitter/Receiver*

Each transmitter or receiver module (Field Replaceable Unit or **FRU**) consists of an optical lens to focus the femtosecond laser pulse onto the antenna structure on the chip. A translation stage provides a single degree of freedom (z axis) for the optical lens to adjust the distance to the substrate along the direction of beam propagation. Both the chip and the collimating silicon lens are mounted on 2 dimensional translation stages (x-y axes) and are independently adjustable. As shown in Figure 2.3, the optical beam acts as the fixed alignment point. The silicon lens may move independently of the chip or may be attached to the same stage as the chip. There are inherent benefits and drawbacks to either lens mounting system, but the operation remains conceptually the same.

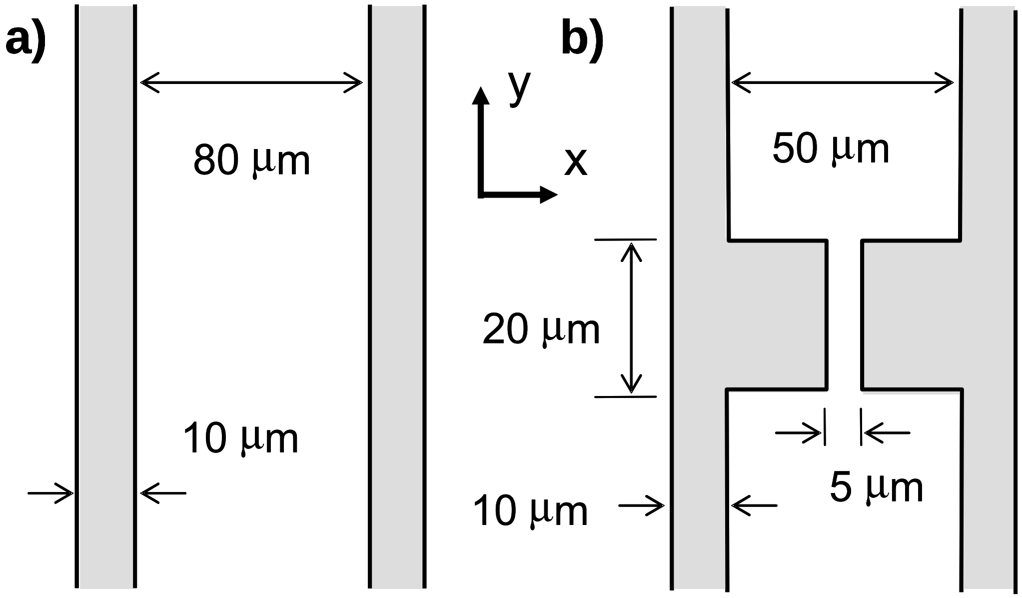

**Figure 2.4** a) Standard layout for transmission lines and b) dipole receiver. Shown for the receiver is the 10-50-10 configuration.

*Standard chip design*

The GaAs transmitters produce more frequencies than are typically detected. The limiting factors are the receiver carrier mobility and antenna structure.[26] The transmitter systems are simple parallel strip transmission lines fabricated on semi-insulating GaAs substrates. The coplanar striplines have a typical configuration of 10 μm wide metallic electrodes separated by 80 μm as shown in Figure 2.4 a). A DC bias voltage is applied across the lines in the range of 60 to 90 V. The bias voltage is determined by current behavior when illuminated by the optical pump beam (5 to 15 mW CW power) with 3 mA of DC current as measured by the voltage supplies taken as the upper limit for maximizing the lifetime of the transmitter chips. Higher voltages combined with higher optical power tends to yield diminishing increases in THz signal strength at an increased noise level and bring on shorting of the electrodes due to electro-migration of the surface deposited metal.

A variety of dipoles are used in the receivers for detection of THz pulses. The frequency response is determined by the dipole size.[2] A balance between bandwidth response (small dipole) and signal strength (large dipole) is found in the so-called 10-50-10 dipoles and is shown schematically in Figure 2.4 (b). For the work reported in this document, additional systems—5-10-5 and 10-30-10 dipoles—were used as required. The first number indicates in micrometers the width of the transmission line leading up to the dipole. The second number indicates the size of the metalized area that made up the physical dipole. Each dipole antenna had a 5 μm gap that would be illuminated by the gating pulse from the laser with a 20 μm wide structure between the transmission lines.

The SOS structures are far more robust with respect to the level of incident optical power, due in part to the absence of a bias voltage. However, with increased optical probe intensity there is a corresponding increase in noise and a roll off in the signal response leading again to diminishing signal gains.[26]

### *Silicon Collimating Lens*

The collimating silicon lens (5 mm radius of curvature) in contact with the emitter chip collects the THz radiation, which is emitted in an expanding spherical wave with intensity distribution as shown in Figure 2.2. The height of the lens is determined by the substrate thickness and the index of refraction of the substrate material. The typical height values are 6.45 mm for the SOS and 6.55 mm for GaAs substrates for collimation of the emitted radiation. Unless otherwise noted, these are the lenses for the transmitter and receiver systems.

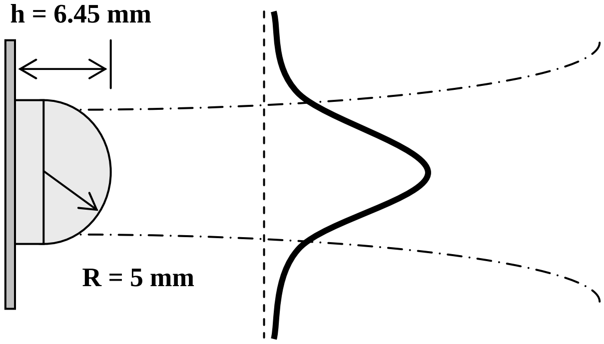

**Figure 2.5** Standard Gaussian propagation assumes Gaussian intensity profile across beam and planar phase at lens surface. Physical dimensions for collimating silicon lens.

The standard picture used for THz beam propagation is that used extensively in optics. A Gaussian intensity profile is assumed with constant phase across the aperture formed by the lens and the beam evolves according to standard diffraction theory. Figure 2.5 demonstrates the paraxial lens picture. This is a direct method of treating THz beams.[27] The trace represents the Gaussian profile assumed for the propagating broad bandwidth pulses with the expanding dash-dot line demonstrates the divergence of the $e^{-1}$ amplitude, which defines the beam radius as a function of distance from the lens.[28] However, some aspects of this treatment require more careful consideration. These will be addressed in the following chapter on beam profile measurement techniques. The measured current is proportional to the incident THz electric field on the dipole.

*Electronics*

The current is measured with a current amplifier (HMS Elektronik Model 564) typically operating at $10^{-7}$ A/V feeding into a lock-in detector (SRS Model SR830 DSP). The THz beam is modulated with an optical chopper near the transmitter lens. The chopper does not perfectly modulate the THz signal, however as long as the size of the blades is greater than the diameter of the THz beam, the resulting modulation will approximate a square wave. The internal reference of the lock-in detector taken from the chopper compares to the fundamental harmonic of the Fourier expanded square wave. By taking the difference frequency between the internal reference and the modulation, a DC signal is measured. This has the benefits of being above the 1/frequency noise when modulating the THz beam, but the difference frequency measurement provides a DC signal where high quality low pass filters become useful for further elimination of noise.

*Optical Delay Line*

A roof reflector mounted on a motion controlled delay line (Newport ) provides the delay between the pump and the probe beams to resolve the THz pulse. The step size determines the spectral resolution by the following relation[29]:

$$\Delta \nu = \frac{1}{N\Delta t} \qquad 2.1$$

$N$ is the number of data points taken in the time domain, $\Delta\nu$ is the spectral width, and is the time step per data point. The time step is determined by the spatial movement of the delay line between successive current measurements. As the speed of light is constant and the optical path introduced by the delay line must be doubled,

$$\Delta t = 2\Delta x / c \qquad 2.2$$

where $\Delta x$ is the delay line step distance and $c$ is the speed of light.

## 2.3 **Single cycle pulses**

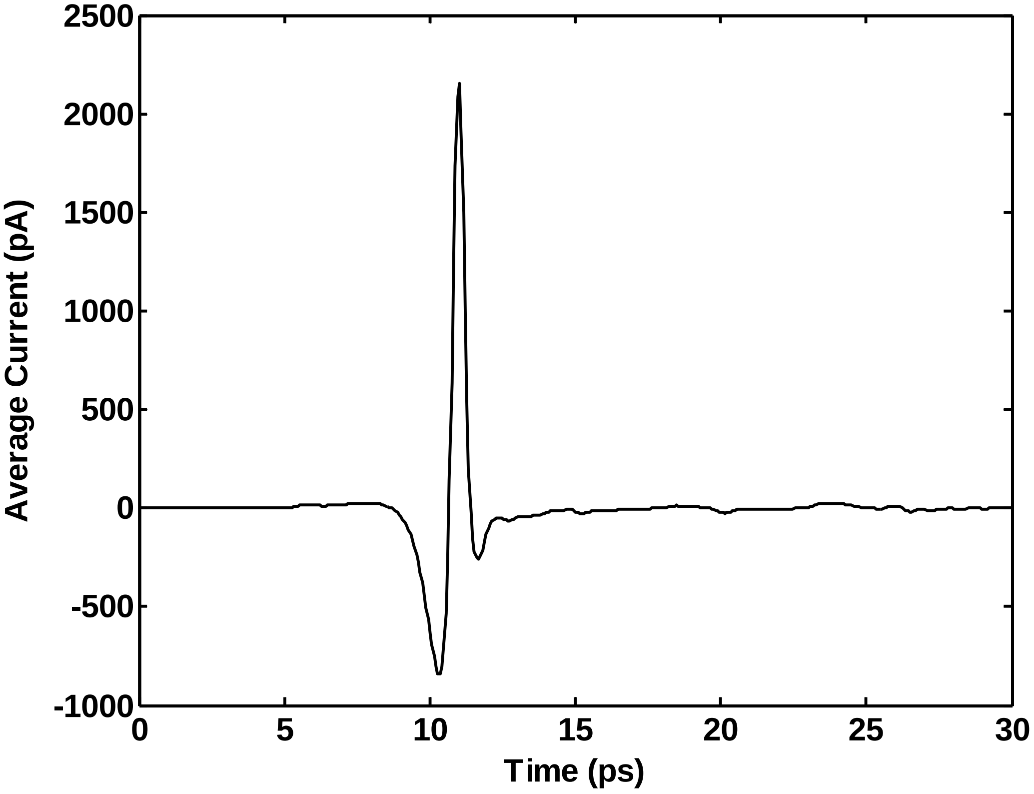

**Figure 2.6** Representative near single cycle THz pulse as measured in a typical TDS system. The non uniform base line from approximately 15 ps onward is due to traces of water vapor (~2.5% RH).

Figure 2.6 shows a typical pulse generated in a standard THz-TDS experiment. The spectral content of the pulse is readily calculated by applying an optimized numerical Fourier transform algorithm[29] to the measured current trace. Figure 2.7 presents the spectrum associated with the temporal pulse shape of Figure 2.6.

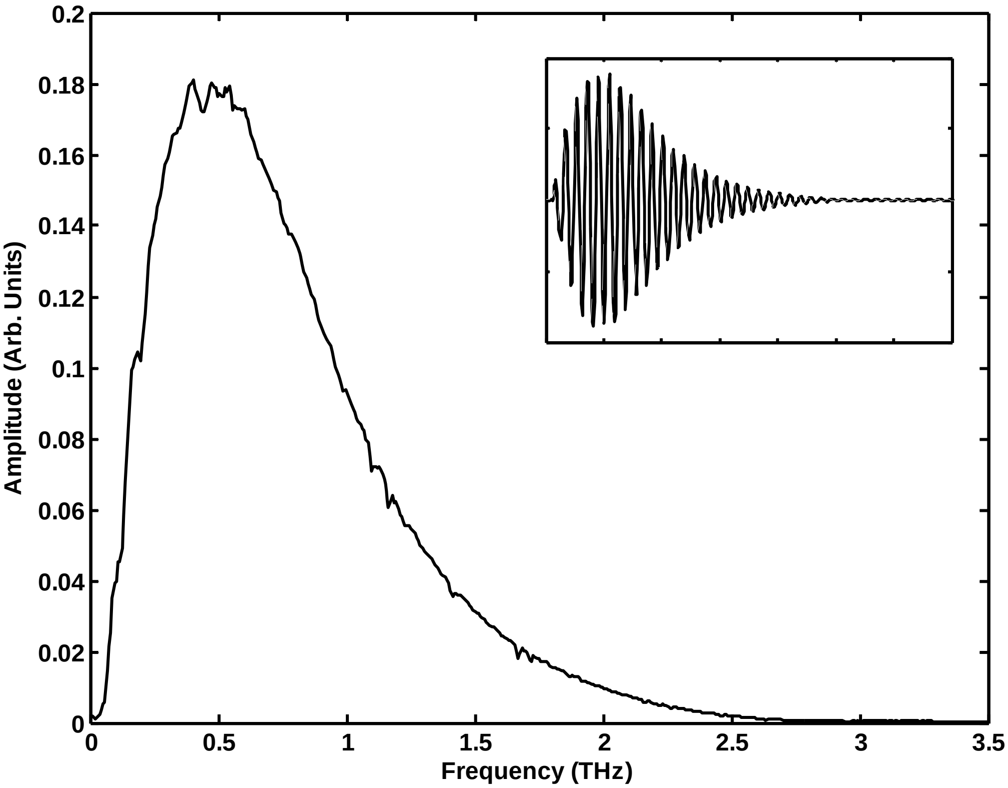

**Figure 2.7** The spectral magnitude of the temporal waveform in Figure 2.6 calculated by numerical Fourier transformation. The inset shows the real part of the complex spectra.

The spectral magnitude exhibits weak water vapor absorption lines[30] in a system where the relative humidity was at ~2.5%. The inset shows the real component of the complex spectrum.

## 2.4 **Transfer functions**

Most physical properties determined by TDS are performed by placing a sample in the THz beam—as illustrated by the dotted box in Figure 2.1. As an example of the analysis process, Figure 2.8 shows the THz pulse measured after passing through a mixture of powdered $Al_2O_3$ mixed with paraffin wax (5% wax by weight) that had been compressed into a disk (25.4 mm diameter and 7.7 mm thick). This unfired amalgam is called a green body ceramic and was chosen as an arbitrary demonstration sample.

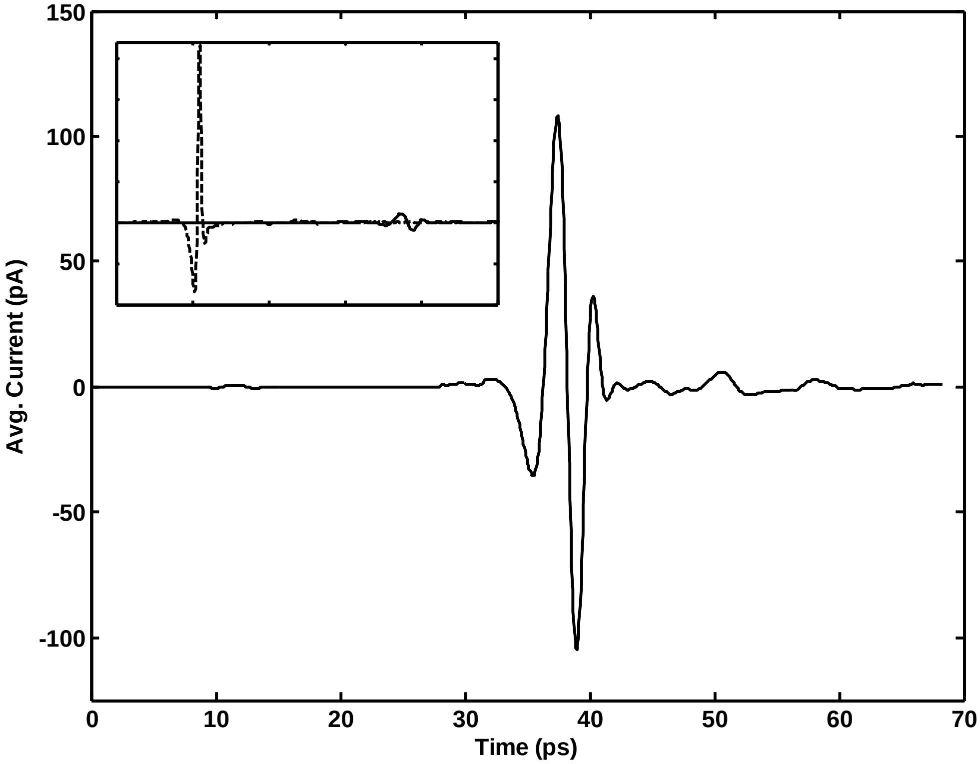

**Figure 2.8** Measured THz pulse after passing through unfired ceramic sample. The inset demonstrates the delay in time due to the increased index of the sample material. The leading pulse (dashes) is the reference and the attenuated trailing pulse (solid) is the sample.

To extract information on the material from the transmitted THz pulse, a comparison is made between the resultant pulse and a reference pulse taken with no sample. By simple observation of the differences in the time domain, a variety of qualitative conclusions can be deduced. The inset of Figure 2.8 shows the sample pulse arriving 26 ps after the reference pulse by comparing the separation between the peak current arrival times. The amplitude is reduced, indicating absorption or reflection, and the pulse is broadened, indicating dispersion or frequency dependent absorption.

The localization of the energy of the THz pulses allows tracing the propagation path and applying a physical optics treatment in the time domain.[31] The time delay experienced when passing through a sample can be estimated by measuring the separation between a reference pulse and sample pulse. By measuring the thickness of the sample, $\Delta z$ = 7.7 mm, it is a simple exercise to calculate a frequency independent approximation for the real component of the index of refraction.

$$n_{real} = \frac{\Delta t}{\Delta z} c + 1 \qquad 2.3$$

With the known sample thickness of $\Delta z$, the effective index is found to be $n_{real} = 2.01$. However, this technique will not yield accurate results in materials with dispersion or that are highly absorptive due the reshaping of the pulse. If the pulse is deformed sufficiently, identical features (centroids, maximum peak intensities, zero crossing point, etc.) are no longer reliable benchmarks.

If the system response is assumed to be linear, the interaction of the THz pulse and the sample can be treated as a convolution in the time domain.

$$s(t) = \int_0^t h(\tau) r(t-\tau) d\tau \qquad 2.4$$

*s(t)* is the resultant pulse in the time domain after interacting with the sample, *h(t)* is the time dependent behavior of the sample, and *r(t)* is the reference pulse. By applying Fourier analysis, the frequency dependent material behavior can be extracted in a more direct manner. The convolution becomes a simple multiplication operation in the frequency domain, converting Equation 2.4 into Equation 2.5.

$$S(\omega) = H(\omega)R(\omega) \qquad 2.5$$

Figure 2.9 shows the magnitude of the transform of the sample pulse. By taking the ratio of the complex spectra, the response of the sample (or transfer function due to the sample) is determined.

$$\frac{S(\omega)}{R(\omega)} = H(\omega) = e^{i(n_{eff}(\omega)-1)k_o\Delta z} \qquad 2.6$$

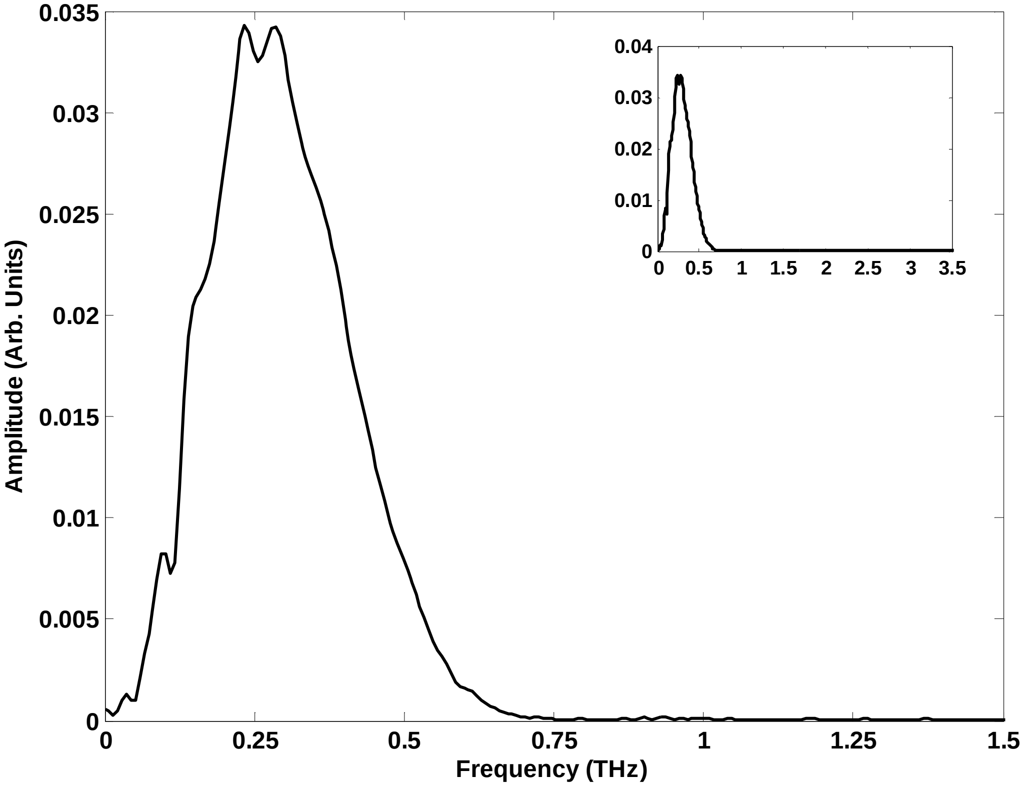

**Figure 2.9** Spectral magnitude of the THz pulse after transmitting through green body ceramic sample. The inset shows the spectral response over the same frequency range as the reference pulse spectrum in Figure 2.7 indicating no additional features are evident.

Once the transfer function *H(ω)* is determined in Equation 2.6 from the experimental results, plane wave behavior is assumed near the beam waist of the THz system. The transfer function is expressed as a complex exponential dependent upon the $n_{eff}(\omega)$. The phase argument assumes an effective index, $n_{eff}(\omega)$, to describe the phase accumulation and magnitude change of the pulse across the sample of thickness $\Delta z$ where $k_o$ is the free space wave vector magnitude. $n_{eff}$ is modified by -1 to account for the displaced free space that the reference pulse traversed through, accumulating phase, that was displaced by the sample.

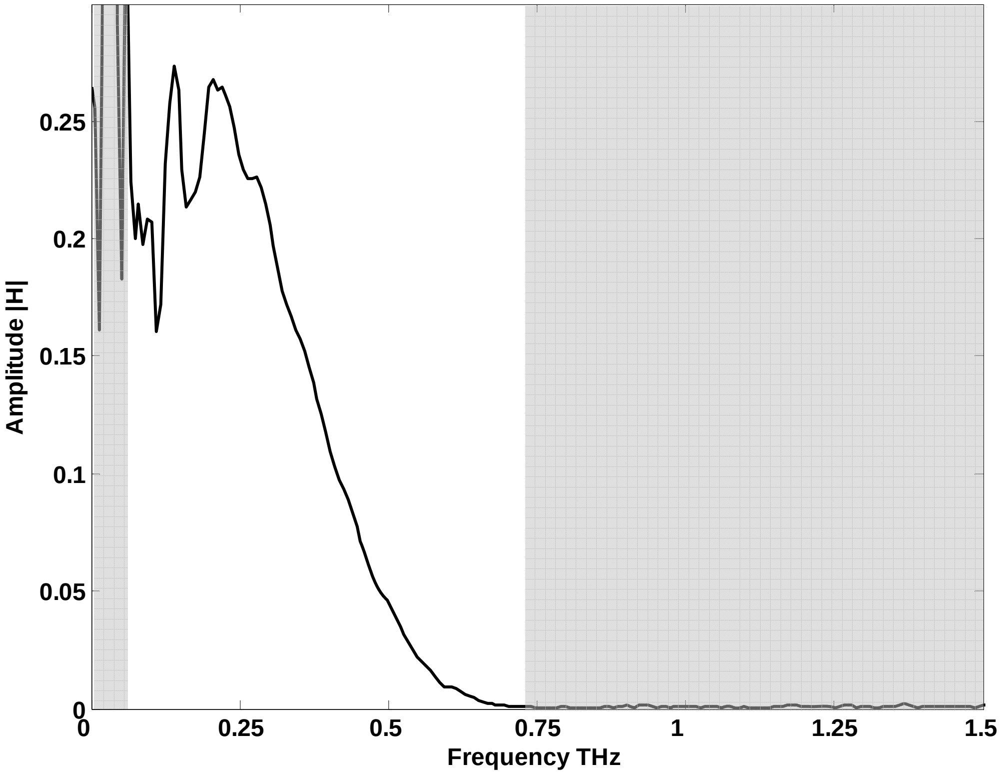

**Figure 2.10** |H(ω)| as a function of frequency. The shaded areas indicate regions where the signal strength drops below the noise limit for the experiment.

The frequency dependent amplitude coefficient is determined by taking the real component of the generated complex transfer function. Figure 2.10 shows $|H(\omega)|$ against frequency in THz. The measured response drops to nearly zero above 0.7 THz. This illustrates some of the limitations inherent to THz-TDS. Referring to Figure 2.7, the reference spectrum has extends out past 2.5 THz and also drops down to zero in the sub 0.1 THz region. No behavior can be inferred from the regions beyond the available reference frequencies, as noise resulting from a near zero denominator then dominates the resultant ratio.[32]

Determining $n_{eff}(\omega)$ from Equation 2.6 yield Equation 2.7:

$$n_{eff}(\omega) = \frac{\ell n[H(\omega)]}{ik_o \Delta z} + 1 \qquad 2.7$$

Where the effective index can be expressed as the complex sum of the real index, $n_{real}(\omega)$, and the field loss coefficient, $\alpha(\omega)$ as in Equation 2.8

$$n_{eff}(\omega) = n_{real}(\omega) + i\alpha(\omega)/k_o \qquad 2.8$$

Subsequently, $n_{real}(\omega)$ can be found from Equation 2.9.

$$n_{real}(\omega) = \mathrm{Im}\left\{\frac{-\ell n[H(\omega)]}{k_o \Delta z}\right\} + 1 \qquad 2.9$$

And $\alpha(\omega)$ can be found from Equation 2.10.

$$\alpha(\omega) = \mathrm{Re}\left\{\frac{-\ell n[H(\omega)]}{\Delta z}\right\} \qquad 2.10$$

Care must be taken in keeping track of the minus signs in the development of the representations for the propagation coefficients as non-physical behavior can be inferred by an improper definition of the direction of propagation along the z axis.

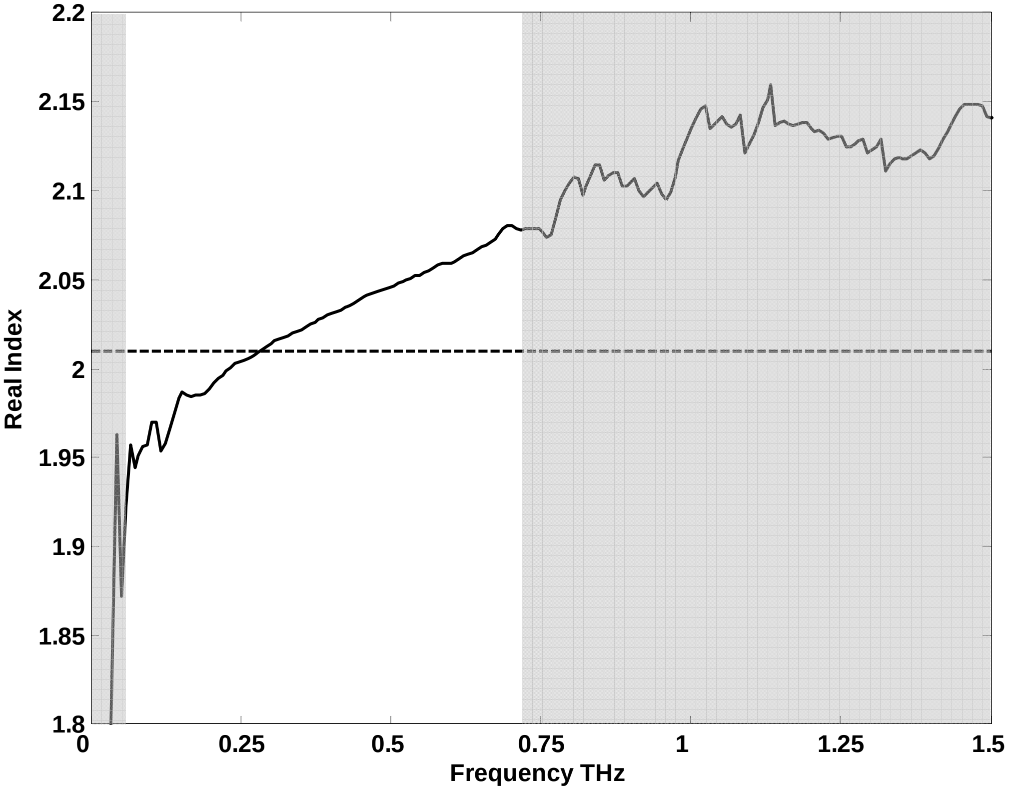

**Figure 2.11** Real index of green body ceramic sample. The shaded areas indicate regions where the signal strength drops below the noise limit for the experiment.

Figure 2.11 shows the real part of the effective index for the green body ceramic disk sample as calculated from the transfer function in Equation 2.9. The dashed line indicates the frequency independent results derived from the pulse delay from Equation 2.3. The time independent index does approximate the frequency dependent index, though there is a substantial variation in the values between 0.2 and 0.7 THz. This illustrates that though the reference spectrum has measurable strength out to 2.5 THz, the phase relationship between the sample and reference pulses will break down once the sample signal has been reduced to the noise level.[32]

Likewise the field loss coefficient $\alpha(\omega)$ can be determined from the complex transfer function $H(\omega)$ as shown in Equation 2.10.

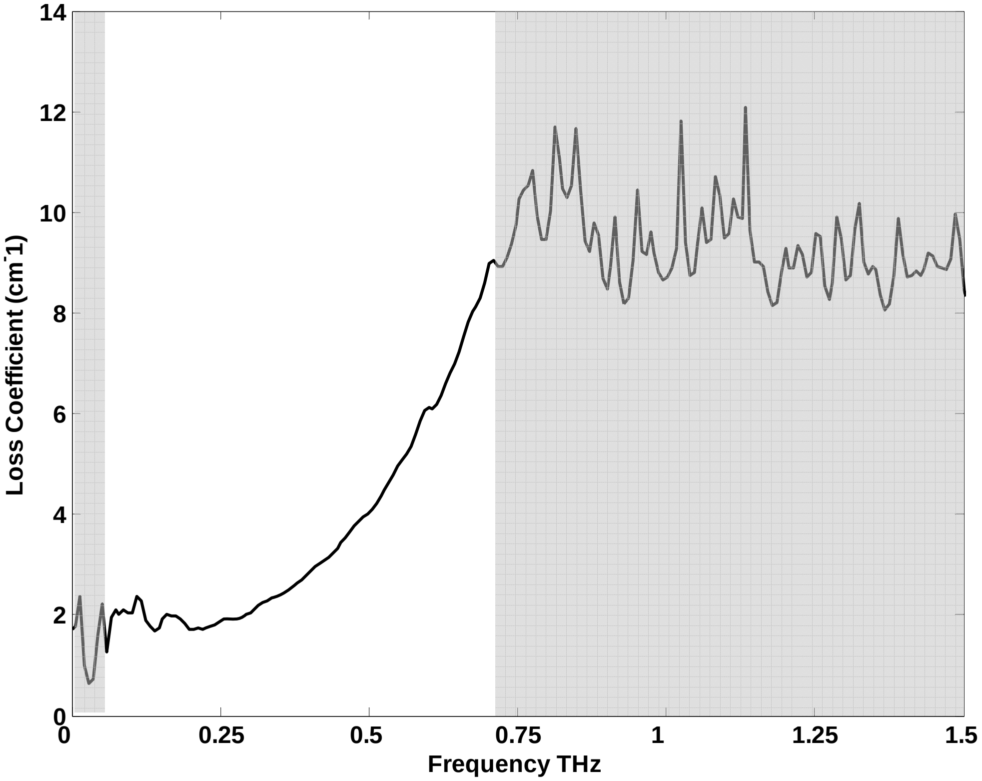

**Figure 2.12** Field loss coefficient $\alpha(\omega)$ over valid measurement range for green body ceramic material. The shaded areas indicate regions where the signal strength drops below the noise limit for the experiment.

Other analysis treatments can yield information about complex conductivity, dielectric constant, etc. as required.

# 3 FTIR—Part I

## 3.1 Background Motivation

Frustrated total internal reflection has been a source of controversy due in part to the analogy often drawn to quantum mechanical tunneling.[33] In 2000, Carey, Wynne, et. al. [15] proposed observation of superluminal propagation across a free space gap on a matched pair of Teflon prisms using time resolved THz pulses. Their publication included claims such as: *"Superluminal propagation is a result of the evanescent character of a wave. Since the evanescent component of a wave does not oscillate with distance, it does not accumulate any phase and therefore propagates through the evanescent region with zero delay."* [15] *"Theoretical analysis shows that in FTIR part of the incoming pulse travels backwards in time."* [15] *"In the evanescent case, the temporal advance across the gap is, in fact, much larger than apparent because the waves have to travel through more prism material as the gap is increased…"*[15] These claims were due to the assumption of a propagation direction to the evanescent field normal to the incident surface of the gap.

Scattering measurements that applied physical optics approaches to surface wave behavior observed different behavior between surface waves that coupled into the scattering target and those that only coupled into the surface wave.[34,35] Radiation couples into surface wave modes at the critical angle as the propagation direction is tangential to the given surface. Investigation of the behavior of THz pulses focused at planar surfaces are intended to uncover a lateral shift in the position of the beam, a manifestation of the Goos Hanchen (GH) effect.[19] These measurements may be applied to explaining previously observed phenomena, while simultaneously refuting erroneous assertions on superluminal pulse propagation.

The first step in making these measurements of the lateral shift is to address linear measurements of the effect of FTIR on THz pulse propagation.

## 3.2 **Theory**

The THz beam is considered to have a Gaussian spatial distribution, so a spread of k vectors describes the propagation of the phase front. Just as the temporal THz pulse can be treated as a summation of single frequency components, each single frequency component is bounded spatially and can be treated as a summation of plane waves, with a unique propagation direction.[36] The behavior of plane waves is well established and provides a tractable method dealing with complicated beams.

### 3.2.1 Quantum mechanics and optical tunneling

Parallels have been drawn between quantum mechanical tunneling and FTIR or "optical tunneling." This is in large part due to the one dimensional treatment of a wave function $\psi$ propagating through a location dependent potential as expressed in Equation 3.1.

$$\left(\frac{d^2\psi}{dz^2}\right)+\mathrm{X}(z)\psi(z)=0 \tag{3.1}$$

For the case of optical propagation, the index changes as a function of position and the function X(z) can be written as in Equation 3.2 where n(z) is the index of refraction and $\lambda_o$ is the free space wavelength.

$$\mathrm{X}(z) = \left( \frac{2\pi n(z)}{\lambda_o} \right)^2 \qquad 3.2$$

The corresponding one dimensional time-independent Schrödinger equation with X($z$) shown in Equation 3.3.

$$\mathrm{X}(z) = \left( \frac{2m\left[E - V(z)\right]}{\hbar^2} \right) \qquad 3.3$$

In this case, *m* is the mass of the particle, *E* is the energy, *V(z)* is the position dependent potential (i.e. a step function for a square well or barrier). As the equations are the same in form, the sets of solutions will display analogous behavior. To further extend the analogy, an incident beam striking the barrier at the critical angle corresponds to the case when E equals V(z).

Zhu, et. al.[37] and Steinberg and Chiao [38]point out that the transfer functions describing the result from quantum mechanical barrier penetration and FTIR are identical only under specific conditions of polarization and incidence angle. FTIR is a two dimensional effect that depends upon the field orientation as well. So the solutions for quantum tunneling and optical tunnel are mathematically identical only under the conditions of 45° incidence angle and S polarization (field is normal to the plane of incidence.)

To draw a true parallel between FTIR and a one dimensional tunneling barrier would require the field interaction to occur at normal incidence. However, at normal incidence an infinite index change would be required to obtain total internal reflection. The limitation in form does not detract from investigating the behavior of the evanescent field in the non-propagating (classically forbidden) region.

Overextending the similarities between FTIR and 1 dimensional quantum tunneling, for example assuming the evanescent field path is purely normal to the gap face, results in increasingly larger non-physical superluminal velocities. For example, applying the model supposed by Carey et. al.[15] to the measurement results presented in this chapter yields evanescent propagation of 5 times the speed of light in vacuum for 0.5 mm gap and 7 c for 1.0 mm. Increasing the gap increases the velocity in the gap (16 c for 2.0 mm gaps.)

## 3.3 Experiment

The measurements of optical tunneling using THz Time Domain Spectroscopy (THz-TDS) performed directly contradict earlier claims of noncausal propagation. In this experiment the time resolved electric fields of single cycle THz pulses transmitted through a pair of cylindrical wedges (prisms) are measured with femtosecond accuracy as a function of tunneling gap thickness. The corresponding phase and amplitude changes fit a frequency-domain linear dispersion theory incorporating absolute optical phase which describes propagation of a plane electromagnetic field through the optical tunneling gap. The complete theory determines the absolute phase change of electromagnetic radiation propagating through the entire FTIR system, independent of specification of the path through the gap. This is the first direct measurement of absolute optical phase change in optical tunneling covering both the thin and thick barrier limits in a single measurement due to the bandwidth available in the THz pulse.

### 3.3.1 Right angle Si prisms

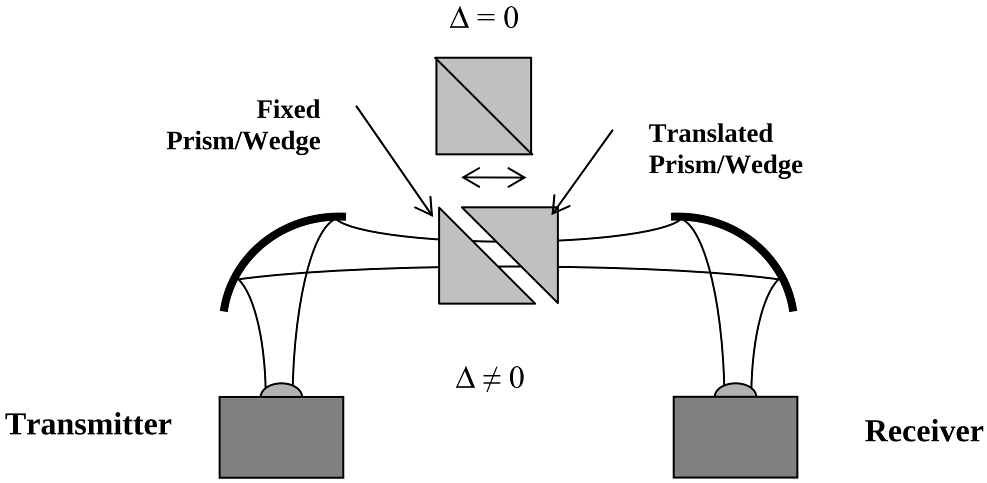

**Figure 3.1** Experimental schematic for FTIR experiments with both experimental systems. The prism/wedge nearest the receiver was translated to provide the optical tunneling barrier.

The THz-TDS system used to perform FTIR measurements is the same as the system in the introductory chapters with a matched prism pair or wedge optics in the position of the sample, as shown in Figure 2.1. The generated THz radiation forms a reasonably collimated beam which propagates through the silicon wedge optics to create an optical tunneling barrier. The receiver for these experiments was a 10-30-10 SOS dipole.

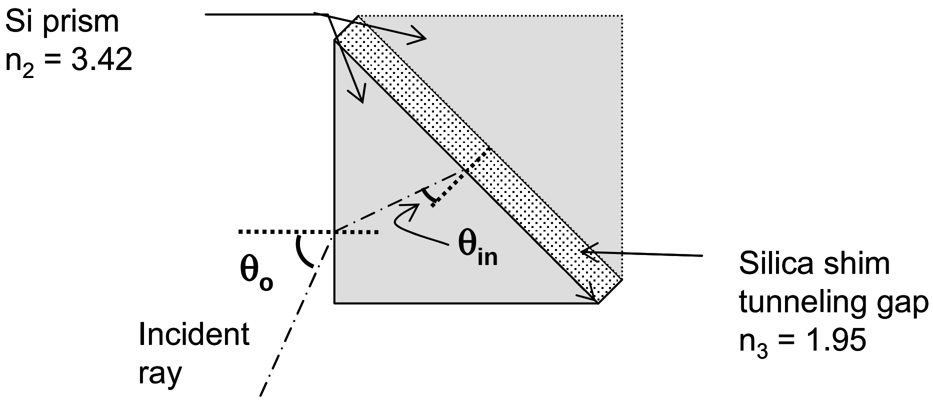

**Figure 3.2** Right angle prism pair with silica shim placed between the tunneling faces. Did not yield useful results.

Initial attempts to measure FTIR utilized a prefabricated pair of matched 45°-45°-90°silicon prisms. High resistivity silicon was used for prism materials since it has nearly negligible absorption across the THz frequency range with index variations less than 0.02%.[1] With the given geometry in Figure 3.2, the critical angle at the gap could not be achieved as described by Equation 3.4. At grazing incidence on the input face ($\theta_o = 90°$) the minimum angle at the long face of the prism would be $\theta_{in}$ = 28°, much larger than the $\theta_c$ = 17° for a Si-air interface. To counter this obstacle, the index of the gap from n = 1 of air was increased to n = 1.95 by inserting fused silica shims between the faces of the prism pair. This would require the proposed series of measurements for varying gap widths to be performed in a piecewise fashion, determined by the thickness of the fused silica shims. This technique is often used in FTIR interference filters.[16]

$$\theta_o = \sin^{-1}\left\{n_2 \sin\left[45° - \sin^{-1}(n_3 / n_2)\right]\right\} \qquad 3.4$$

With the shims, the $\theta_c$ = 34.8° required $\theta_o$ = 37.4°, which is a significant deviation from normal incidence on the prism faces. Further trials did not yield positive results and additional issues arising from the need to eliminate air gaps between the shim and prism faces.

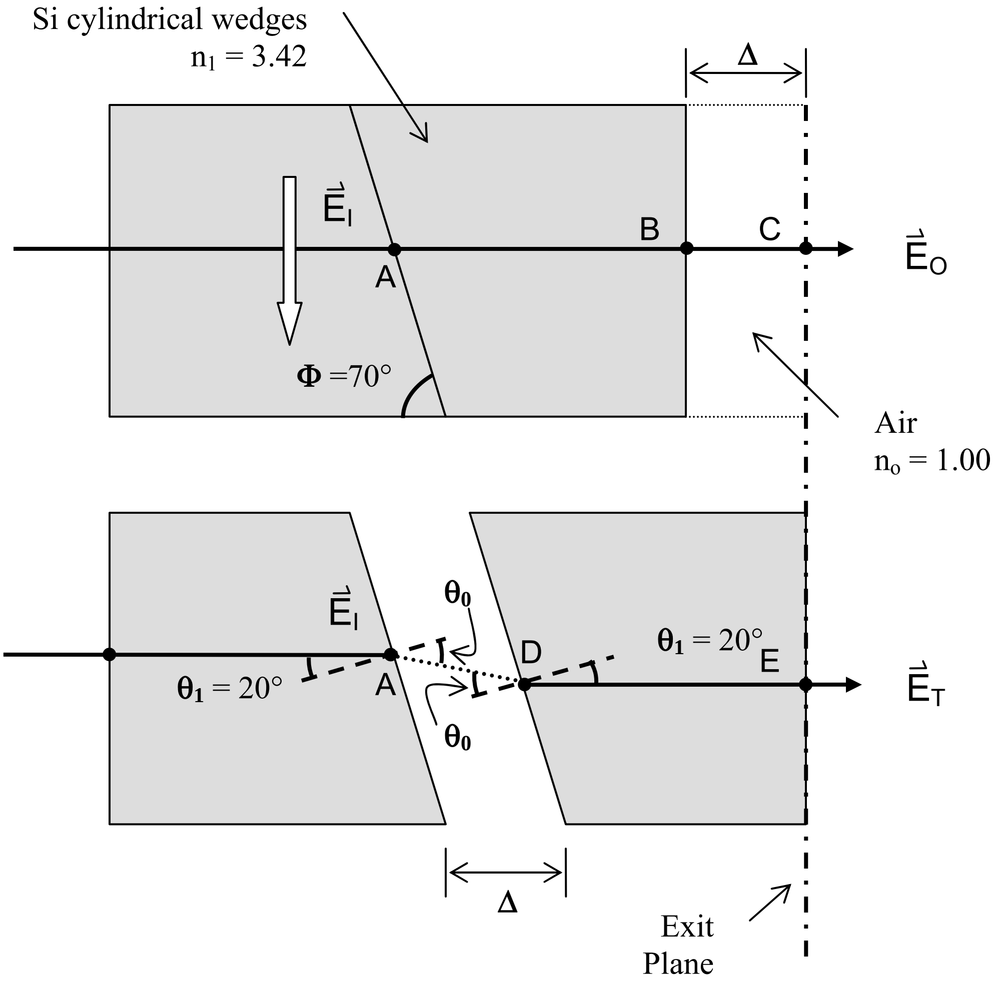

**Figure 3.3** Silicon wedges in contact and with air gap. The polarization of the incident pulse is in the plane of the page (P polarization.)

### 3.3.2 Silicon wedge prisms

In response to the difficulties that arose when attempting the experiment with the matched right angle prisms, a pair of cylindrical wedges was designed to create the optical tunneling barrier. The matched wedges, shown in Figure 3.3, are also of high resistivity silicon. They were fashioned from a boule section 75 mm in diameter and optically polished on input and output faces. The wedges have entrance and exit faces normal to the cylinder axis and inner faces with vertex angle, $\Phi = 70°$. When the wedges are in contact ($\Delta = 0$) they form a 68 mm long cylinder. Both the separation, $\Delta$, between the wedges along the cylinder axis and the angle of the THz system optical axis to the cylinder axis are adjustable with a resolutions of 1 μm and 0.1° respectively due to the mounting system shown in Figure 3.4.

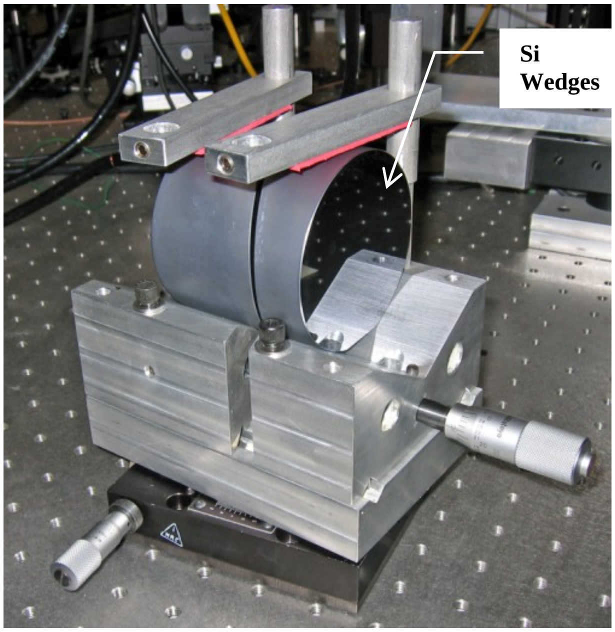

**Figure 3.4** Si wedges and custom translation system.

The THz beam entering normally to the input face is incident on the angled surface at 20°, 3° beyond the critical angle in silicon. At critical angle, $\theta_c = 17.01°$, the attenuation length of the evanescent wave in the gap has a singularity, and is extremely sensitive to the angle of incidence with 20× variation over a 0.01° range as demonstrated in Figure 3.5. Increasing the incidence angle beyond $\theta_c$, the attenuation length decreases becoming much less sensitive to the angle of incidence. The bounded THz beam utilized in this measurement has a 8.5 mm 1/e amplitude waist radius at 0.5 THz, corresponding to a range of incidence angles of the plane wave components which make up the bounded beam of less than ±0.5°[27]. At the gap, the optical system generates a beam waist with radius proportional to wavelength and a planar phase front. This minimizes the frequency dependence of the k vector uncertainty and angular effects on the attenuation distance, $\delta_z$ of the evanescent field in the gap as shown in Equation 3.5.[39]

$$\delta_z = \frac{\lambda}{2\pi \sinh b} = \frac{1}{ik_o\sqrt{n^2 \sin^2 \theta_i - 1}} \qquad 3.5$$

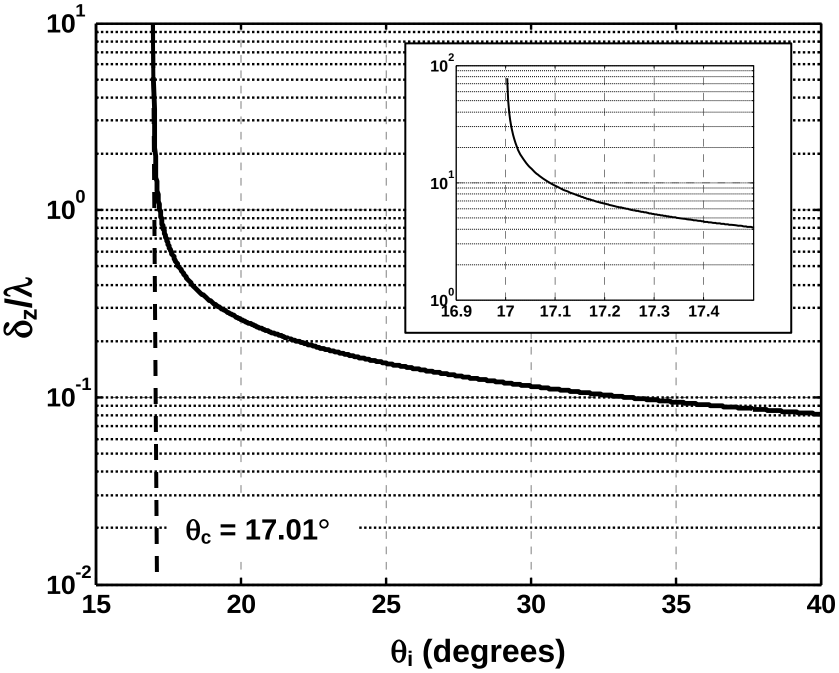

**Figure 3.5** Penetration depth of evanescent field normalized to free space wavelength with respect to incident angle beyond critical in Si for THz pulses.

The measurements detailed in this chapter were performed at $\theta_1 = 20°$ and with P polarization of the incident THz pulse unless otherwise specified.

The reference pulse, $E_O(t)$, was measured with the separation along the cylindrical wedge axes set to zero ($\Delta = 0$), shown in the upper most window of Figure 3.6. Measurements of the transmitted pulse, $E_T(t)$, which optically tunneled through the sample, were made for $\Delta = 100, 200, 500$, and 1000 μm; lower windows of Figure 3.6. The pulse measurements are shown as points in Figure 3.6 ($\theta_0 = \pi/2-\phi = 20°$). The THz pulses were polarized with detection extinction of over 1000:1 in power as determined with wire grid polarizers.

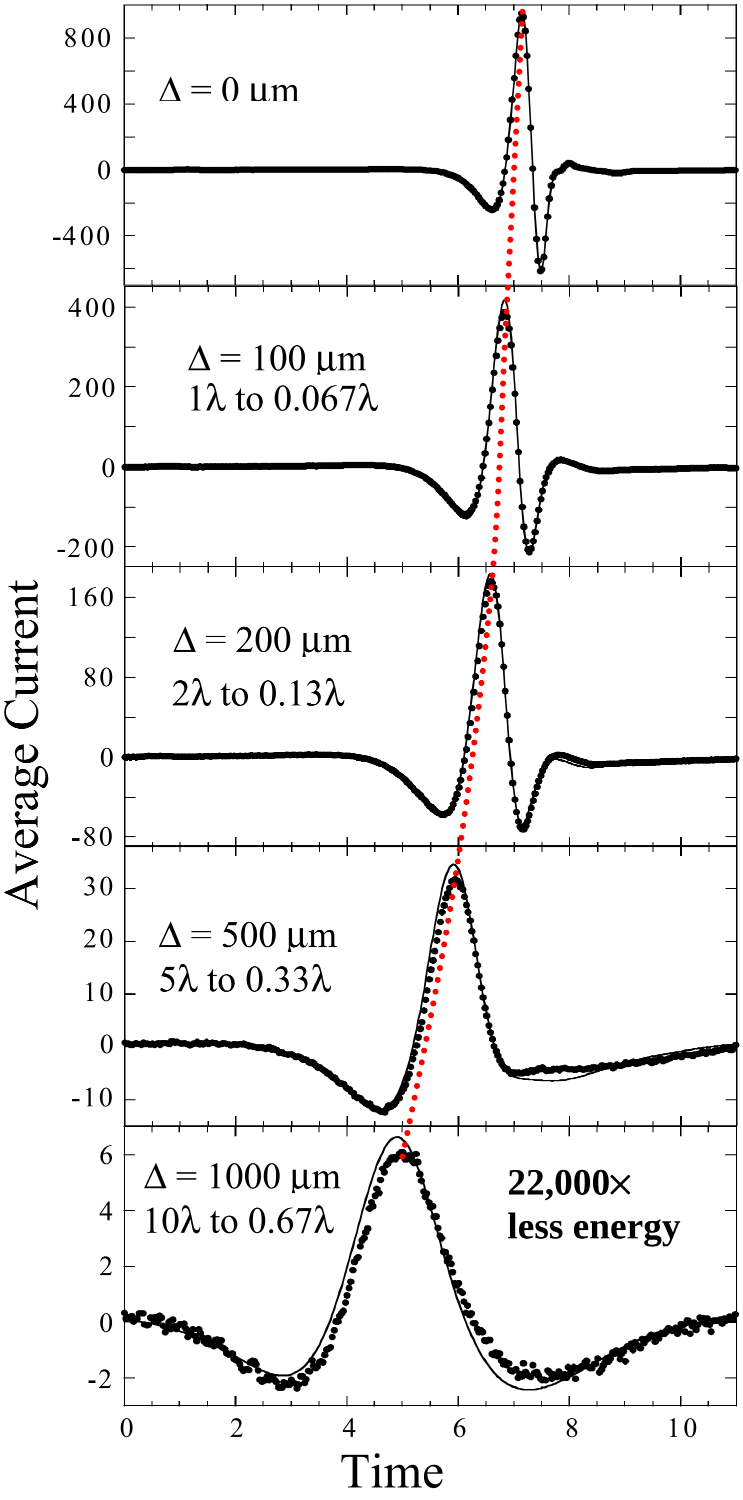

**Figure 3.6** Measured and calculated $E_O(t)$ (top window) and $E_T(t)$ for FTIR measurements as a function of Δ. The dotted line between successive measurements is included as a guide to the eye.

The peak of the transmitted THz pulse arrives earlier in time with increasing barrier width. The detected pulse peak for Δ = 1000 μm arrives 2.4 ps before the reference pulse (Δ = 0). A dotted line connects the peaks as a guide to the eye demonstrating the apparent time advance of the THz pulse.

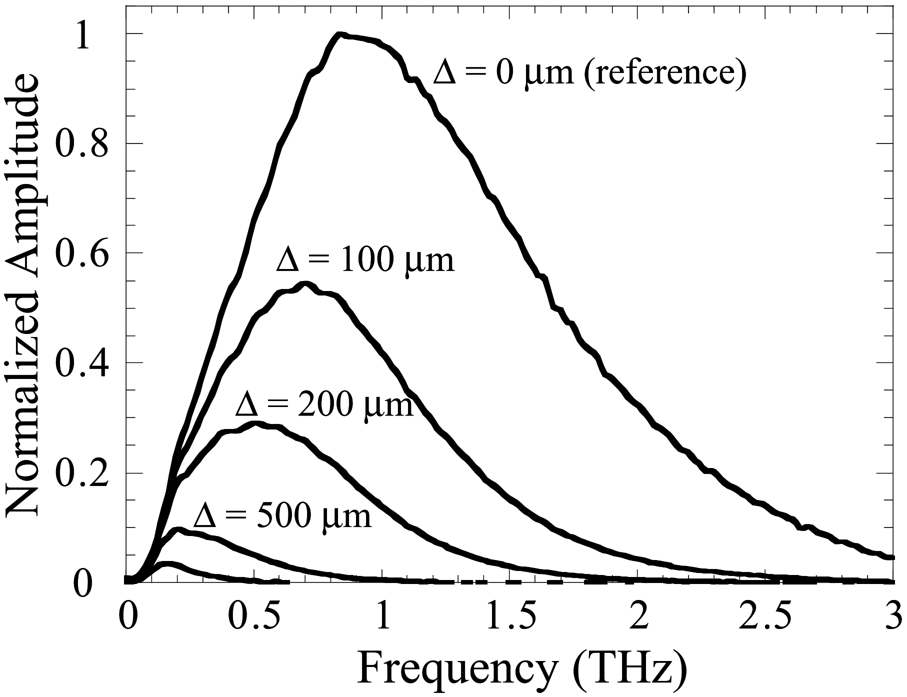

**Figure 3.7** Spectral magnitudes for the THz pulses shown in Figure 3.5 with the decreasing strength corresponding to an increasing Δ.

Strong attenuation of the high frequency components is observed as expected from the direct proportionality of the penetration into the gap, $\delta_z$, to wavelength. This frequency weighted change in spectrum results in pulse reshaping as Δ increases. The attenuation can be seen from the amplitude spectra, obtained from a numerical Fourier transform of the time-domain data and shown as points in Figure 3.7. The amplitude spectra have not been scaled. The area under each curve squared is proportional to the transmitted pulse energy. The energy of the transmitted pulse through the 1000 μm gap is approximately 22,000 times smaller than that of the reference pulse.

#### 3.3.2.1 Polarization dependence

Additional polarization dependent measurements were performed by rotating the wedges to have the electric field orientation of the THz pulse lie both in the plane of incidence (P polarization) and orthogonal to the plane of incidence (S polarization.) The resulting $E_O(t)$ and $E_T(t)$ values are shown in Figure 3.8. From visual examination of the results, P polarized pulses demonstrate less amplitude attenuation (as expected from the Fresnel coefficients in Appendix 9.2). However, P polarized pulses show a marked increase in arrival time, 0.7 ps earlier in peak arrival with $\Delta = 0.5$ mm. This indicates there is a different mechanism than propagating "*through the evanescent region with zero delay*"[15] as polarization orientation should only impact field amplitude.

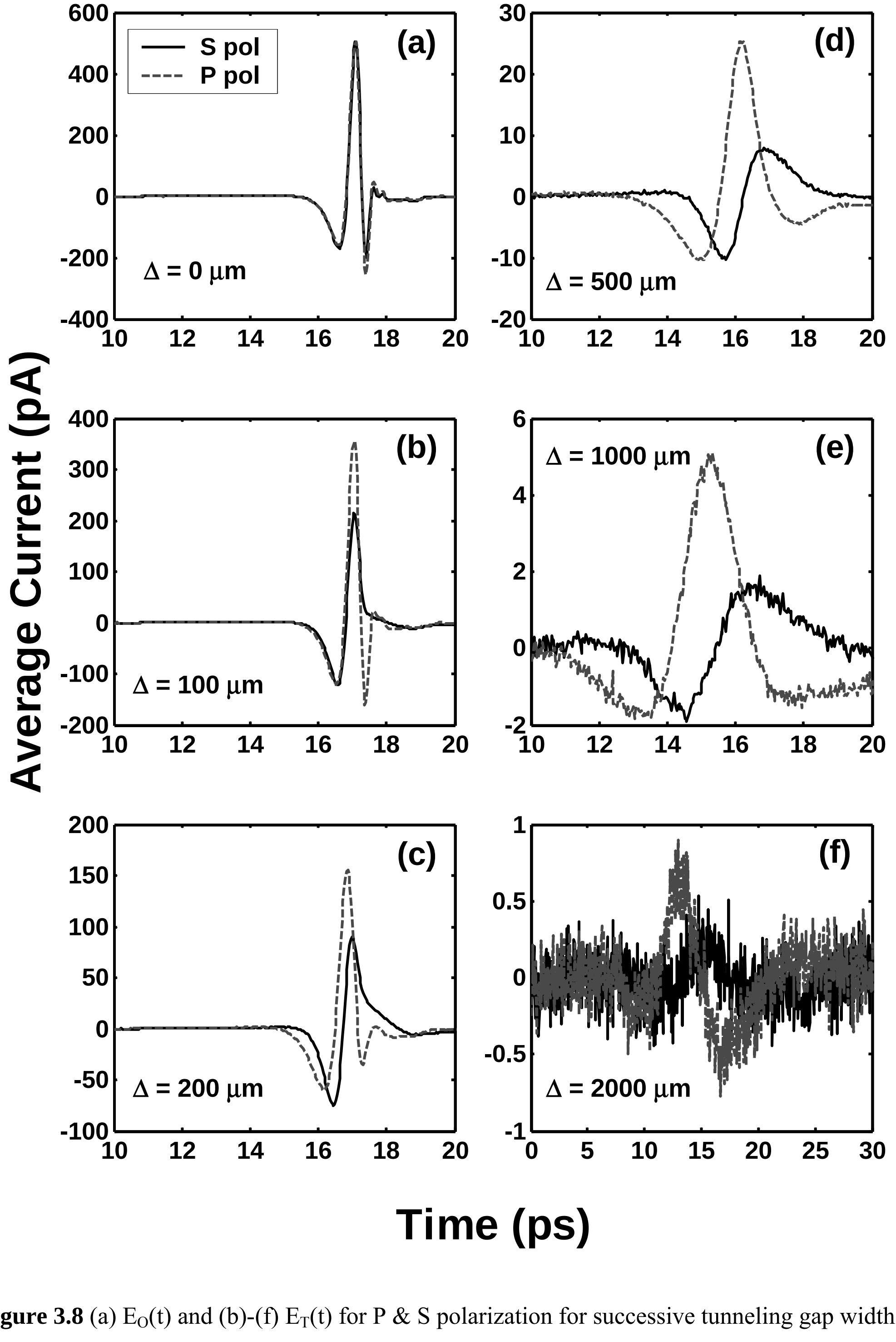

**Figure 3.8** (a) $E_O(t)$ and (b)-(f) $E_T(t)$ for P & S polarization for successive tunneling gap widths Δ.

## 3.4 **Analysis**

To address the optical tunneling, the THz pulse measurements are analyzed using linear dispersion theory. The Fourier transform of the time resolved electric field, E(t), gives the complex, frequency dependent amplitude, E(ω), of the plane wave components of the THz pulse. Each plane wave component propagates through the optical tunneling barrier, which can be treated as a dielectric slab. The analysis describes a slab with index $n_0$ surrounded by a medium with index $n_1$. It is assumed that $n_0 < n_1$ as is shown in Figure 3.9. (For the case when $n_0 > n_1$ see reference [17] though the end result is identical.) The field, $E_T(\omega)$, transmitted through a dielectric slab is obtained from the superposition of the directly transmitted field with the components which undergo multiple reflections from each interface (see reference[40], sections 1.6.4 and 7.6.1):

$$E_T(\omega) = \frac{t_{10} t_{01} e^{i\beta}}{\left(1 + r_{10} r_{01}\, e^{i2\beta}\right)} E_I(\omega) \qquad 3.6$$

The dielectric slab is of thickness, d, measured normal to the slab faces, and the radiation is incident at angle $\theta_0$. $E_I(\omega)$ is the incident field. The Fresnel coefficients are $t_{01}$, $t_{10}$, $r_{01}$, and $r_{10}$ for transmission and reflection at the $n_0$-$n_1$ and $n_1$-$n_0$ boundaries respectively, the subscripts correspond to the dielectric medium. $\beta = n_0 k_o d \cos\theta_1$ is the phase delay associated with multiple reflections inside the slab, with $k_o$ the wavevector in free space. $\theta_1$ is the angle of the transmitted radiation inside the slab determined from Snell's law, $n_0 \sin\theta_0 = n_1 \sin\theta_1$.

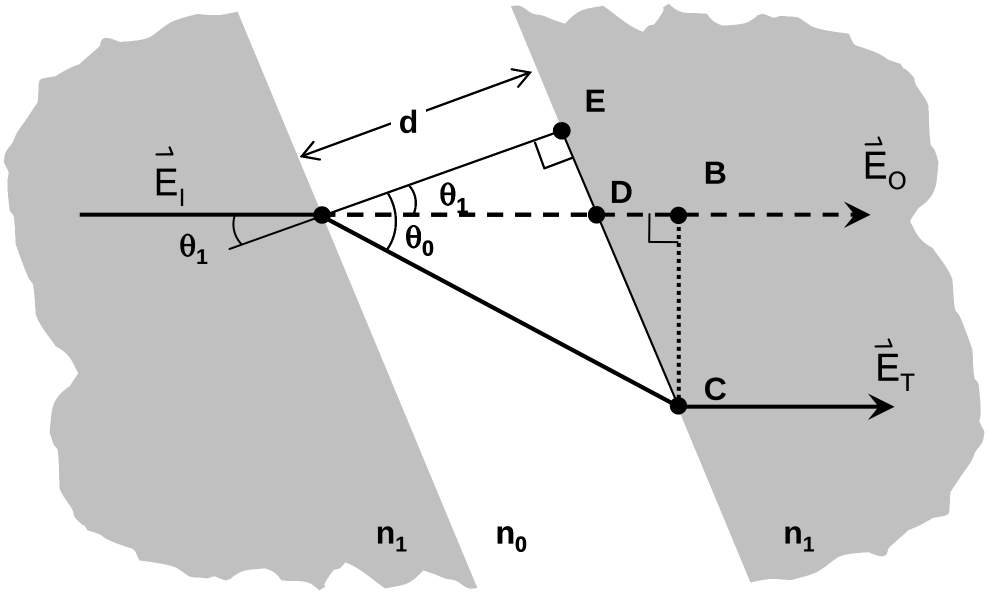

**Figure 3.9** Optical pathlength determination for the insertion of a slab of low index material into a region of high index material.

Adding a tilted dielectric slab to the THz beam path requires an additional phase term in Equation 3.6, which arises from replacing one medium ($n_1$) with another dielectric ($n_0 \neq n_1$). The THz-TDS experiment as described in this chapter is intended to measure the relative change in phase between the matched plane wave components of two pulses that have passed through the prism pair ($E_O$ and $E_T$.) This is subtly different from the treatment of a dielectric slab in Born and Wolf[40] where the phase change is between the incident field and the transmitted field ($E_I$ and $E_T$.) Plane waves have well defined phase fronts by their very nature, so any translation along the phase front perpendicular to the propagation direction has the same relative phase. Because there is a translation of the ray describing the plane waves that travel through the dielectric slab, the comparison must be made along coincidental phase fronts as shown in Figure 3.9 (CE line segment for exit plane) and in Figure 3.9 (BC line segment). The phase change is calculated from the optical path length difference between the phase of the beam with the slab removed (AB segment in Figure 3.9) and the phase of the beam transiting through the slab (AC segment.) The comparison between two paths must be made on the same plane. Any physically valid measurement must account for the displacement of one dielectric by the slab of different dielectric material. Ignoring the effect of the medium displaced by the slab is equivalent to measuring the phase at two different spatial points.

This additional phase term will now be evaluated for the dielectric slab illustrated in Figure 3.9. The input phase front is defined as point A, at the point where the beam would hit the interface between the two wedges using a ray treatment, and the output phase front is the line BC. This differs somewhat from the treatment presented in [17], but the results are entirely equivalent. The optical path length through the medium $n_1$ when there is no slab is AB = AD + DB. The optical lengths of the involved line segments can be determined from the geometry to be:

$$\begin{aligned} AD &= n_1 d / \cos\theta_1 \\ DB &= n_1 DC \sin\theta_1 \\ DC &= d\tan\theta_0 - d\tan\theta_1 \\ AD + DB &= n_1 d/\cos\theta_1 + n_1 d\tan\theta_0 \sin\theta_1 - n_1 d\tan\theta_1 \sin\theta_1 \end{aligned} \tag{3.7}$$

Defining $E_I(\omega)$ as the incident field at the input plane and $E_O(\omega)$ as the field which propagated through free space, $E_O(\omega) = E_I(\omega)\exp[ik_o(AD+DB)]$. Adding a dielectric slab (index $n_o$) to the beam path changes the optical path as described by the segment $AC = n_1 d/\cos\theta_0$. The field which propagates through the dielectric slab when $\Delta \neq 0$ is now $E_T(\omega) = E_I(\omega)\exp[ik_o(AC)]$.

For the dielectric slab, $E_O(\omega)$ and $E_T(\omega)$ are measured, but $E_I(\omega)$ can not be determined experimentally. Expressing the incident field in terms of the measured field transmitted through free space, $E_I(\omega) = E_O(\omega)\exp[-ik_o(AD+DB)]$, the measured phase delay of the initial pulse is determined from $E_T(\omega) = E_O(\omega)\exp[ik_o(AC-AD-DB)]$ where:

$$\begin{aligned} AC - AD - DB &= n_o d/\cos\theta_0 - n_1 d/\cos\theta_1 - n_1 d\tan\theta_0\sin\theta_1 + n_1 d\tan\theta_1\sin\theta_1 \\ &= (n_o d/\cos\theta_0 - n_1 d\tan\theta_0\sin\theta_1) - (n_1 d/\cos\theta_1 - n_1 d\tan\theta_1\sin\theta_1) \end{aligned} \qquad 3.8$$

Substituting $\sin\theta_1 = {}^{n_o}\!/_{n_1}\sin\theta_o$ from Snell's law into the first parenthetical term in Equation 3.8 and pulling out common factors, reduces the form for the phase delay between the transmitted reference pulse and the pulse that tunneled through the barrier to that shown in Equation 3.9.

$$\begin{aligned} AC - AD - DB &= n_o d/\cos\theta_0(1-\sin^2\theta_0) - n_1 d/\cos\theta_1(1-\sin^2\theta_1) \\ &= n_o d\cos\theta_0 - n_1 d\cos\theta_1 \end{aligned} \qquad 3.9$$

This phase delay applies to all terms, including the Fabry-Perot reflections represented by the denominator of Equation 3.6. In terms of measured quantities, the field transmitted through the dielectric slab is now given by:

$$E_T(\omega) = \frac{t_{10}t_{01}e^{i\beta}e^{-i\gamma}}{\left(1 + r_{10}r_{01}\,e^{i2\beta}\right)}E_O(\omega) \qquad 3.10$$

with $\beta = n_0k_o d\cos\theta_1$ and $\gamma = n_1k_o d\cos\theta_0$. The correction factor, $\gamma$, accounts for the displacement of a homogeneous medium with a dielectric material which occurs in any physical measurement. Neglecting the $\gamma$ term with $n_1 > n_0$ results in the non-physical situation of phase advance as the incident angle $\theta_0$ and optical path length increase.

To treat the cylindrical wedges shown in Figure 3.3, the wedges with no gap, $\Delta = 0$, are taken as a reference ($E_O$). The measured phase difference occurs between the phase front at the input, point A, and a phase plane corresponding to the output face after the wedges are separated, line CE. The measured amplitude and phase changes in the THz beam are due to two terms. The first arises from the gap (AD) created by translation of one wedge. The result is modeled as a dielectric slab of index $n_0$ surrounded by a medium with index $n_1$ with thickness $d = \Delta\sin\phi$, and tilted at angle $\theta_1 = \pi/2-\phi$ relative to the optical axis of the THz system. For incident angles below the critical angle ($\theta_{in} < \theta_c$), the path through the gap is well defined. The second term, $e^{i\Phi}$, arises from the fact that the gap was not achieved by removing silicon from the beam path, but by translation of the second wedge by an amount $\Delta$; the air space BC of index $n_0$ becomes filled with a medium of index $n_1$. This is clear in the upper portion of Figure 3.3. The transmitted field, $E_T(\omega)$, is then given by:

$$E_T(\omega) = \frac{t_{10}t_{01}e^{i\beta}e^{-i\gamma}}{\left(1 + r_{10}r_{01}\,e^{i2\beta}\right)} \times e^{i\Phi} \times E_O(\omega) = H(\omega)\,E_O(\omega) \qquad 3.11$$

The term $\exp[i\Phi]$ gives the phase change between the measured and reference pulses due to the translation of the exit face by $\Delta$ with $\Phi = n_1k_o\Delta - n_0k_o\Delta$, assuming normal incidence. Both $E_T(\omega)$ and $E_O(\omega)$ experience an identical decrease in strength due to reflection at the output face of the wedge, so only the components of the transfer function, $H(\omega)$, that are unique to the introduction of the tunneling gap (dielectric slab) are explicitly retained in the equation.

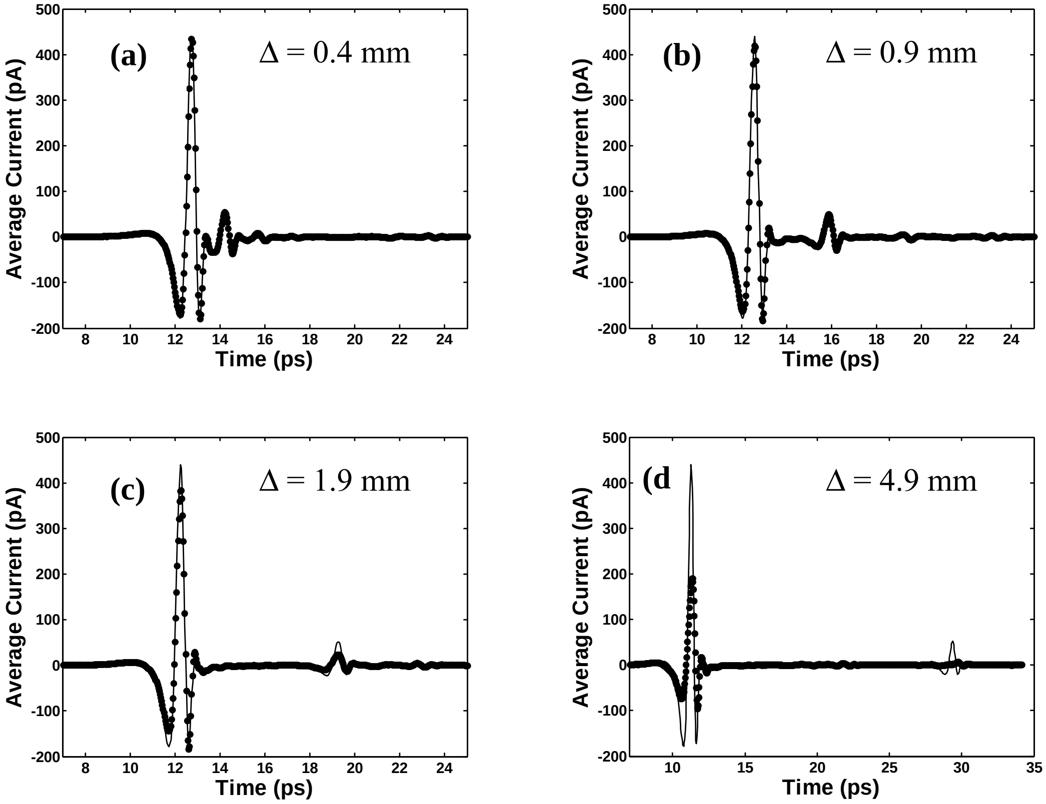

**Figure 3.10** Comparison of measured (dots) vs. values calculated with Equation 3.7 (solid) below critical angle. The incident angle was 13.7° on the gap ($<\theta_c$).

### 3.4.1 Validation of model

To validate this treatment, measurements were performed below critical angle ($\theta_1 < \theta_c$) using the same prism pair. Figure 3.10 shows the comparison of the results calculated from Equation 3.7 to measured THz pulses after propagating across the gap for Δ = 0.4 mm, 0.9 mm, 1.9 mm, and 4.9 mm. The prism pair was rotated to have the THz beam strike the input surface at 22° rather than at normal incidence. This had $\theta_1 = 13.7°$ at the gap (point A in Figure 3.9). The gap distances were 0.1 mm off from the intended values of $\Delta$ due to hysteresis in the translation stage that was discovered after the measurements were performed.

The THz pulse transmitted through the cylindrical wedges is calculated by taking the inverse Fourier transform of the complex amplitude $E_T(\omega)$ from Equation 3.11 generated from the measured $E_O(\omega)$ as outlined in Chapter 2. The calculations match the measurements well, validating Equation 3.11. Secondary pulses from multiple reflections in the gap are observable in all the subplots of Figure 3.10 and the calculations accurately predict the arrival times of the delayed pulses. The amplitudes of the predicted secondary pulses agree between theory and experiment for the small gap distances in Figure 3.10 (a) & (b), but the measurements are far less than that predicted for the larger prism spacings of Figure 3.10 (c) & (d). This is not a result of the transfer function breaking down; rather this is a consequence of the experimental limitations. As the wedges are translated, the transmitted pulse undergoes a lateral shifting. The beam exiting the wedges walks off of the optical axis of the THz system. For the $\Delta = 4.9$ mm case shown in Figure 3.10 (d) a significant walk off of 6.9 mm is expected for the multiply reflected trailing pulse, reducing the coupling efficiency into the THz receiver. A reduction in amplitude for the main transmitted pulse due to the lateral beam shift away from the optic axis of the THz system is also observed. This reduced coupling efficiency results in a lower detected pulse amplitude.

For an angle of incidence on the gap greater than critical angle, $\theta_1 > \theta_c$, the field within the gap becomes nonuniform, corresponding to creation of an evanescent field with exponentially decreasing amplitude in the gap to satisfy the boundary conditions[40] (section 1.5.4). The ray path AD in the gap is no longer well defined; the optical path does not directly correspond to a phase change. This uncertainty in the path of the pulses is one reason it has been so difficult to assign a characteristic time for optical tunneling[33]. However, mathematical specification of the path is not required for Equation 3.11 to remain valid. Following Born [40] (section 1.5.4), Equation 3.11 may still be applied for radiation incident past the critical angle, due to the plane wave expansion. The angle $\theta_0$ now becomes complex, $\theta_0 = a+ib$, with real part, $a = \pi/2$, and an imaginary part, $b = \pm\cosh^{-1}(n_1\sin\theta_1/n_0)$. The sign of b is chosen to avoid the non-physical situation of energy gain in the gap. The term $\beta$ in Equation 3.11 is now purely imaginary with $\cos\theta_0 = \pm i[(n_1/n_0)^2\sin^2(\theta_1) - 1]^{1/2}$, which rapidly increases from zero at $\theta_1 = \theta_c$ to approximately $(n_0/n_1)^{1/2}$ for $\theta_1 = 90°$. Since $\cos\theta_0$ enters into the Fresnel coefficients--$t_{10}$, $t_{01}$, and $r_{10}$-- an additional phase change can be equated to a temporal shift of the radiation propagating through the boundary.

Following the same procedure as outlined before for the validation process of Equation 3.11, the $E_T(t)$ was determined using the $E_O(\omega,\Delta = 0)$ and performing an inverse Fourier transformation. The calculated THz pulse is plotted as a solid line on top of the data for $\Delta = 100, 200, 500$, and $1000\ \mu m$ in Figure 3.6. The calculated amplitude spectra, again given as solid lines, are overlaid on the experimental measurements in Figure 3.6. Excellent agreement is obtained with no adjustable parameters, indicating the validity of Equation 3.11 beyond critical angle and into the regime where no well defined path exists.

The cylindrical wedges are a linear system, with $H(\omega)$ defined in Equation 3.11 as the complex frequency-domain system response function, $H(\omega) = H'(\omega) +$

$iH''(\omega) = E_T(\omega, \Delta)/E_O(\omega, \Delta=0)$. H(ω) is directly measured over the range from 100 GHz to over 3 THz. The real and imaginary parts of the system response are related by Kramers-Kronig relations (see Appendix 9.3), which are causal. The complex components of H(ω) were compared numerically over a wide frequency range and behave in an appropriately causal manner.[17]

## 3.5 Conclusion

Since the measured values of H(ω) give the complex phase change of the transmitted radiation through the prism system, the group velocity[41] (section 1.2), $v_g = \partial\omega/\partial k(\omega)$, can be obtained from the natural logarithm of H(ω). This however does not determine the velocity of energy propagation. The group velocity is strictly equivalent to the velocity of energy propagation only in lossless, dispersion free media and in the limit where the spectral bandwidth of the signal is narrow compared to the carrier frequency[41,42]. Additionally, to determine the velocity of energy propagation it is necessary to know the path the radiation takes through the prism. H(ω) is only measurable in this experimental configuration for the prism system as a whole. The theory developed treats the *entire* prism system and does not specify the path taken by the radiation. Previous reports of non-causal and superluminal propagation[15] made unfounded assumptions about this path.

# 4 Beam Profile Experiments

FTIR is not a one dimensional process, as pointed out in the previous chapter. The next step in examining the effects of THz pulses undergoing FTIR is to extend the previous series of measurements into two and three dimensions. The intent is to observe directly the Goos Hanchen (GH) shift and find a physical interpretation of the tunneling time across the optical barrier (FTIR).

A series of experimental techniques adapt the standard THz-TDS system into a beam profile imaging system suitable for FTIR investigation. This is accomplished by raster scanning the receiver to produce a three dimensional image in one or two spatial dimensions and in time.[10] The primary issues in raster scanning are maintaining precise optical focus on the dipole antenna, preserving the optical path length on the receiver delay arm between successive scans, and increasing the spatial resolution of the detector. The focus and delay issues are solved through fiber coupling the optical gating pulses to the receiver. The increased resolution is accomplished through reducing the aperture of the receiver. A secondary concern regarding the increase in scanning times by multiplying the individual scans to achieve raster scanning is addressed by using a rapid scanning delay line rather than lock-in detection.

## 4.1 Fiber Coupling

From Chapter 2, the location of the optical beam determines a standard FRU's position and the optical axis determines the FRU's alignment. (See Figure 2.2) The small gap between the dipole structures on the receiver (Figure 2.4b ) coupled with the small spot radius of the focused optical beam (~5 μm) requires precise control to keep small variations in beam pointing stability from introducing experimental errors into the measured THz induced current.

This sensitivity impacted THz ranging systems where a scattered field was sampled at a variety of angles with the requirement to maintain absolute timing and stable optical power on the receiver between each successive position. Complex arrangements of rotating periscopes and translating long optical paths inevitably introduce complications into spatially sensitive experiments.[34] To overcome these limitations, optical fiber was used to couple the femtosecond laser pulses to the THz antenna structures.[11]

### 4.1.1 Design Background

Commercial fiber coupled THz systems have been developed.[6] A number of considerations drove the decision to construct a more flexible and inexpensive system that included the most advantageous feature--fiber coupling of the optical beams.

The commercial fiber coupled THz system focused on a monolithic design. It had the optical fiber guiding the femtosecond laser pulses brought into physical contact with a bow tie structure THz antenna and then fixed into place with an optical adhesive. This requires precise positioning equipment and would tie the length of the fiber to the system. It also renders the entire transmitter or receiver inoperable if the fiber or fiber coupler was damaged.

The concept behind the fiber coupled receiver FRU was two-fold. First, image the small cores section of the fiber on the antenna with a pair of aspheric plano-convex lens in a unity conjugate ratio (1:1 imaging) configuration and take advantage of the already tightly confined optical beam. This optical coupling allows flexibility, i.e. switch the dipole for a 5-10-5 broadband or 10-50-10 antenna for sensitivity as required or change optical fibers in the case of damage or timing requirements. The second reason was to minimize the variation on the established FRU designs to maintain as much interchangeability as feasible, so expensive or limited resources such as silicon lenses or multiple antenna chips were not committed. Additionally, the optical imaging design accommodates future plans to use multiple fiber sources to pump the same antenna chip (see Chapter 7.) Figure 4.1 shows the schematic representation of the fiber coupled FRU.

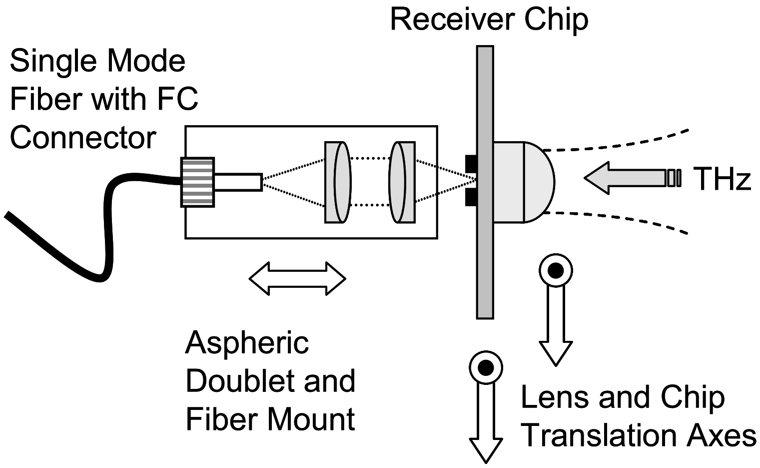

**Figure 4.1** Fiber mounting schematic for FRU. The asphere doublet and fiber connector are mounted in a fixed position relative to each other and are translated as a whole along the z axis.

### 4.1.2 Fiber Characteristics

Single mode fiber was chosen to prevent modal dispersion.[43] The inherently small mode field diameter was utilized in the 1:1 imaging scheme to provide a tightly focused beam waist on the probe beam. The fibers utilized in the spatial field measurements had the characteristics shown in Table 4.1. The fiber does **not** maintain polarization orientation.

| Operating Wavelength | Mode Field Diameter @ 850 nm | Cladding | Coating | Cut-off | Numerical Aperture |
|---|---|---|---|---|---|
| 780-970 nm | 5 μm ± 0.5 μm | 125 μm ± 1.5 μm | 245 μm ± 15 μm | 730 nm ± 15 nm | 0.12 |

**Table 4.1** Manufacturer's specifications for single mode fiber used in fiber coupled FRU.

Fiber systems were initially purchased with SMA type connectors, but this did not provide repeated positioning stability and that connector type has become less widely used in industry. FC connectors were chosen as the standard system, both for commercially acquired fibers and for the custom fabricated lengths.

Launching the Ti:Sapph beam into the optic fiber efficiently is accomplished through the use of a precision flexure stage (Thorlabs Model C260) and by matching the numerical aperture (NA) and mode field diameter of the fiber to that of the focusing lens.

$$N.A. = \frac{D_{beam}}{2 f_L} \qquad 4.1$$

$D_{beam}$ is the diameter of the beam, $f_L$ is the focal length for the lens, and the ratio of $D_{beam}/ f_L$ is the relative aperture. *N.A.* is the numeric aperture of the fiber determined by the index change between the fiber core and cladding ( $N.A. = (n_f^2 - n_c^2)^{1/2}$ ).[16] With a measured beam diameter of ~ 4 mm, a 15 mm focal length lens yields a value for Equation 4.1 of 0.13. Though this is slightly larger than the fiber *N.A.,* this lens provides a balance between available optics, focused beam waist (~ 4 μm), and relative aperture. The slightly smaller beam waist can be compensated for by moving the fiber face a short distance from the focal plane toward the lens in order to maximize the modal overlap determined by increased optical power coupling.

The coupling efficiency achieved is on the order of 35 % between free space input and output CW power. With CW power typically between 75-100 mW, this yields 26 to 35 mW prior to the imaging aspheric doublet. This optical power is more than sufficient to probe the receiver dipole antenna.

### 4.1.3 Dispersion Compensation

In the initial spatially resolved experiments, a 9 cm long single mode optical fiber was used to couple the probe beam to the receiver in order to provide a short range of motion while maintaining absolute timing. However, with the 50 fs pulses from the Ti:Sapph laser, even a short length of silica fiber would introduce chirp and increase the pulse width. In the 9 cm length, the gating pulse width would increase to 490 fs determined through numerical simulations. Subsequently, the measured current as a function of time would no longer be a valid approximation of the propagating THz field. This in turn would require the deconvolution of the broadened gating pulse with the distorted pulse to extract the THz waveform. In spectral measurements triggered with the broadened gating pulse, the precise THz waveform does not need to be preserved, though the high frequencies will be suppressed as a result. It was deemed preferable to precompensate the optical gating pulse by adding a negative chirp prior to launching into the fiber.

The principle behind precompensation is to introduce a relative phase shift between each of the frequency components that exactly cancels the frequency dependent phase shifts accumulated by propagating through the fiber. The fused silica fiber exhibits normal dispersion in the wavelengths of interest here, so the longer wavelengths incur less phase advance than the shorter wavelengths. This is counteracted by propagating the pulse through dispersive elements (prisms or gratings) to increase the optical path length experienced by the longer wavelengths with respect to the shorter wavelength components of the pulse spectrum. Thus the total optical path length (accumulated phase) through the dispersive precompensator and the normally dispersive fiber remains equal for all spectral components.

#### 4.1.3.1 Prism-pair compensator

A prism-pair compensator[44] introduced negative dispersion in the input pulse prior to launching into the fiber to correct the subsequent fiber-induced dispersion. The equilateral prisms (Edmund Optic—formerly Edmund Scientific) were a matched pair of SF-18 glass prisms, 35 mm x 35 mm faces and antireflection (AR) coated in the near infrared with 673 mm between the apexes of the prisms. The prism pair was utilized in a double pass configuration with a roof reflector introducing a vertical offset between the two optical beams for the return pass through the system.

The standard autocorrelation trace yielded a full-width-half-maximum (**FWHM**) of 135 fs which corresponds to a 90 fs FWHM optical pulse.[45]

Issues that arose from this configuration were losses in the prisms despite the AR coating and the large amount of physical space that would be introduced into the receiver optical beam if the fiber length was increased.

#### 4.1.3.2 Grating-pair compensator

A modified bistatic THz ranging system [11]was developed with a fiber coupled receiver to replace the free space configuration.[34] This system uses a 2 m length of optical fiber established as a standard length to the receiver FRU. To compensate for the group velocity dispersion in the fiber the optical beam is pre-compensated using a grating pair[46], because the prism pair compensator described in the previous section would introduce additional group delay in the glass, require too large of a footprint on the optical table, and was lossy despite the AR coatings.

A pair of gold gratings (Richardson Grating Laboratories) was chosen for high reflectivity in the infrared wavelengths with a blaze angle of 19.7° to maximize energy coupled into the first order diffraction mode. The ruled area is 26 × 26 mm with 830 grooves/mm and are placed 60 mm apart face-to-face. The grating compressor is a double pass system with a roof reflector introducing a vertical offset for the return pass through the system to recollimate the chirped optical beam.

The pulse, negatively chirped by the optical gating system, has a FWHM of 100 fs determined through standard autocorrelation procedures after propagating through a 2 m fiber cable.

### 4.1.4 Alignment Procedure

Alignment of a fiber coupled receiver can prove challenging. The standard operating procedures to achieve tight focusing on the dipole structure relies on imaging the back reflections on a screen. This is accomplished by passing the optical beam through a hole in a screen and then translating the optical lens in the z direction (see Figure 2.3) so the focus is no longer at the chip surface. The light that is reflected forms an image of the antenna structure on the screen. The antenna is centered within the image by proper adjustment of the incoming optical beam and translating the chip along the x-y axes. The optical lens is translated back to a tight focus. The induced photocurrent is measured as a gauge of beam alignment (maximized DC photocurrent coupled with increased position sensitivity.)

In a fiber coupled system, this back reflection process cannot be performed (see Figure 4.1) due to the fiber and associated mounting/coupling components. The alignment process for a fiber coupled receiver follows. In the case of a SOS receiver chip where optical alignment is most critical, the collimating Si lens is removed. The light that is transmitted through the substrate is directed onto a screen where a shadow image of the antenna structure is formed. The position of the beam is walked down onto the dipole, until a Fraunhofer diffraction pattern is observed on the screen. The x-y position of the chip and the lens translation is optimized when the single slit diffraction pattern is observed to be broadest. The Si lens is replaced and the photocurrent is peaked up normally.

The output end of the fiber tends to become damaged after several months of operation indicated by a sudden drop in peak signal. The damage to the core region of the fiber is obvious upon visual inspection with a microscope and distorts the mode of the beam increasing the focused beam spot and decreasing the optical power due to scattering. This damage may be due to the peak power of the recompressed pulse interacting with minor imperfections in the emitting surface. This damage is repaired by repolishing the fiber if seated in a ferrule or recleaving if the fiber is bare.

## 4.2 **Exposed Receiver**

To achieve high spatial resolution, a fiber coupled dipole antenna is used without a Si lens to focus the incident THz radiation on the active region. The metallic dipole structure is mounted on the side of the chip opposite the incident THz beam. Facing the antenna toward the optical gating pulse takes advantage of the field enhancement of a dipole on a dielectric surface. The small active area (50 μm × 20 μm for a 10-50-10) is intended to act as a point sampling device, trading signal strength and directivity for spatial resolution.

With a 10-50-10 dipole, the peak signal-to-noise ratio (PSNR) for the antenna with no lens is greatly reduced. Measurements indicate the spectral range is 0.1 to 1.0 THz with a PSNR of 28:1 at 0.5 THz. This is due to the small active area as well as the decreased directivity allowing unwanted signals to couple into the receiver.

Dipole antennas, unlike apertured antennas( i.e. lens coupled receivers), may have an effective size in excess of their physical size. Following the treatment of Balanis,[47] the effective maximum aperture is defined:

$$A_{em} = \frac{|V|^2}{8W_i}\frac{1}{R_A} = w_e l \qquad 4.2$$

$R_A$ ( $= R_r + R_L + R_s$ )is the total resistance of the antenna, including radiative resistance ($R_r$), loss ($R_L$), and scattering ($R_s$). $V$ is the induced voltage on the dipole and $W_i$ is the incident power. $l$ is the physical length of the dipole and the effective width is $w_e$. The effective length of a dipole is the physical length.

A very short lossless dipole imbedded in a dielectric medium (assuming bulk Si behavior) is taken as a maximum case model of the THz dipole receiver. Assuming no losses so the only antenna resistance is the radiative resistance ($R_A = R_r$) and assuming the dipole is short ($l < \lambda/50$) the antenna resistance $R_A$ is equal to the radiation resistance $R_r$ which is taken as shown in Equation 4.3.[47]

$$R_r = 80\left(\frac{\pi l}{\lambda}\right)^2 \qquad 4.3$$

This in turn will yield the maximum theoretical effective area for a very short dipole. The voltage induced across the dipole is taken as $V = El$. The power delivered by a uniform plane wave is $W_i = E^2/2\eta$ where $E$ is the field of the incident wave and $\eta$ is the impedance of the medium (~110 Ω for Si). Using these relations in Equation 4.3 results in a wavelength dependent effective area $A_{em}$ shown in Equation 4.4.

$$A_{em} = w_e l = \frac{\eta}{320\pi^2}\lambda^2 \qquad 4.4$$

The effective width of the dipole, $w_e$, is found from the effective area by dividing Equation 4.4 with $l$ = 50 μm and is plotted in Figure 4.2 as a function of frequency.

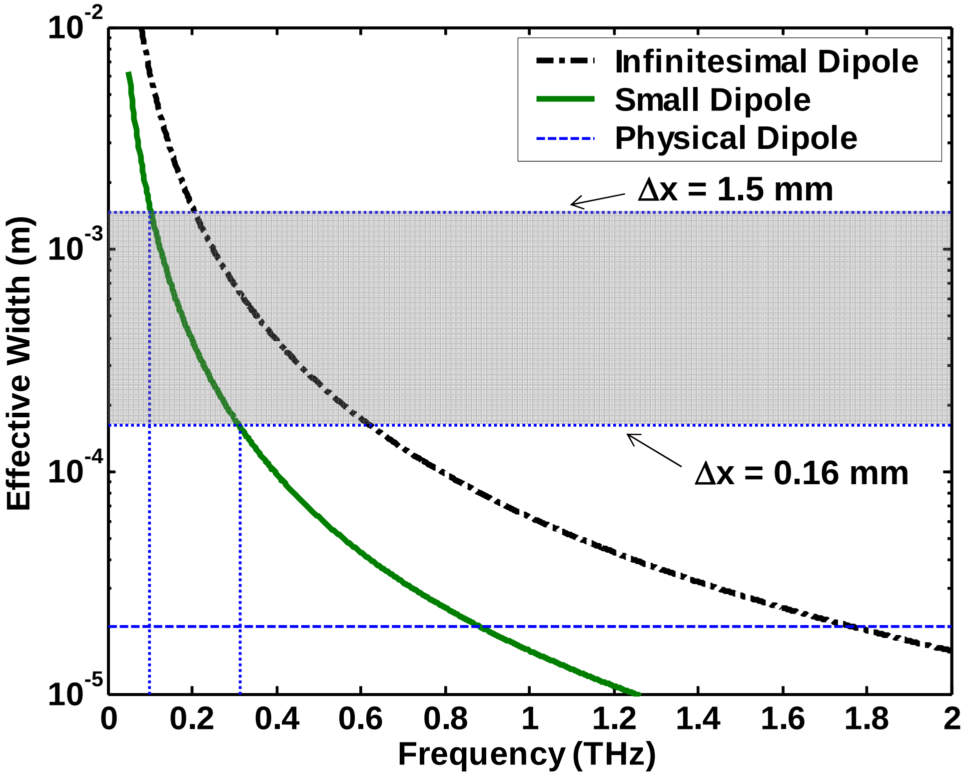

**Figure 4.2** Effective width for infinitesimal and short dipole antennas assuming no losses (maximum behavior). The shaded bar indicates the range of step sizes taken in spatial measurements. The effective width is greater than the step size for frequencies below 0.1 THz for Δx = 1.5 mm and 0.31 THz for Δx = 0.16 mm.

The assumption that the dipole is much smaller than a wavelength does not necessarily hold.[48] For a 50 μm dipole, $l = \lambda/12$ at 0.5 THz in free space and $l \approx \lambda/4$ in

Si, which is no longer in the $l << \lambda/50$ requirement for a very short dipole. Though the dipole cannot be treated as an infinitesimal dipole, the radiation resistance for a short dipole $R_r$ can be taken as ¼ $R_r$ for an infinitesimal dipole.[47] This serves to reduce the effective size of the dipole and is plotted in Figure 4.2

Figure 4.2 shows the plots of the effective width for the short lossless dipole and the very short lossless dipole compared to the physical width (20 μm) of the structure over the frequencies of interest. The shaded region in Figure 4.2 indicates the range of step sizes made with the x-y translation stage in the spatially resolved measurements. The step sizes were 1.5 mm, determined by the diameter of the reduced aperture lens, or 0.16 mm, limited by the minimum step size of the translation stage. The maximum effective size of the exposed receiver dipole is less than the step size above 0.1 THz for the $\Delta x = 1.5$ mm and 0.31 THz for $\Delta x = 0.16$ mm. The result for the infinitesimal dipole is for the ideal case, where the greatest disparity exists between physical size and electrical size. The short lossless dipole serves as a better approximation in the low frequency range where the effective size is on the order of the spatial step dimensions. Real losses were neglected in this upper limit calculation and the length of the dipole was assumed to be the physical length.

Any real antenna structure will have additional losses, from load mismatch, non-radiative coupling, scattering, etc., that will increase $R_A$ and further reduce the effective aperture of the small dipole. The current distribution in the dipole can also change the effective length.

A 10-30-10 dipole antenna on SOS substrate has a reported resistance of 22 MΩ when not illuminated and 550 Ω when the optical pulse is incident on the structure.[48] The resistance in the on state in turn could be taken as an approximation of the total resistance $R_A$ of the dipole neglecting any frequency dependence. This yields an effective area shown in Equation 4.5.

$$A_{em} = \frac{2\eta}{R_A} l^2 \tag{4.5}$$

Solving Equation 4.5 for the effective width produces $w_e = 12$ µm, much smaller than the physical 20 µm dipole width. The small effective width may be due to the transmission line losses included in the assumed resistance of the coplanar stripline dipole antenna structure and the impedance mismatch.

The ideal case of a short lossless dipole serves as the upper limit of effective dipole size for determining the spatial resolution of the exposed receiver. The physical size of the dipole acts as a lower boundary for spatial resolution. The effective dipole size is expected to be below the minimum step size of the translation system, though more detailed modeling or experimental measurements are needed to completely validate the use of an exposed receiver as a point sampling probe.

One experimental consequence of the exposed receiver was the multiple reflections within the sapphire substrate, both from the impinging THz pulse as well as the optical frequency probe pulse. In a receiver that has Si optics (n = 3.42) for collecting incident THz radiation, the high index material of the lens displaces the signals generated from reflections from the temporal window of interest. To take advantage of the time gating feature of time resolved THz measurements, a slab of polished 1 mm thick high resistivity Si was adhered to the front of the SOS receiver chip. Some reflections did occur between the modest index change between the sapphire and silicon, though reduced from a sapphire/air interface by a factor of 12.

The noise level tends toward ± 3 pA on the exposed receiver, which is comparable to the noise level on the standard lens receiver, however the dynamic range is reduced by a factor of 1000.[26]

## 4.3 Reduced Aperture Receiver

The exposed receiver provides a good method for sampling the THz electric field with high resolution, except that the sensitivity was decreased by the effective area of the dipole. The small effective area of the exposed dipole receiver requires measurements to be performed near the transmitter or subsequent beam waists where the field strength was highest.

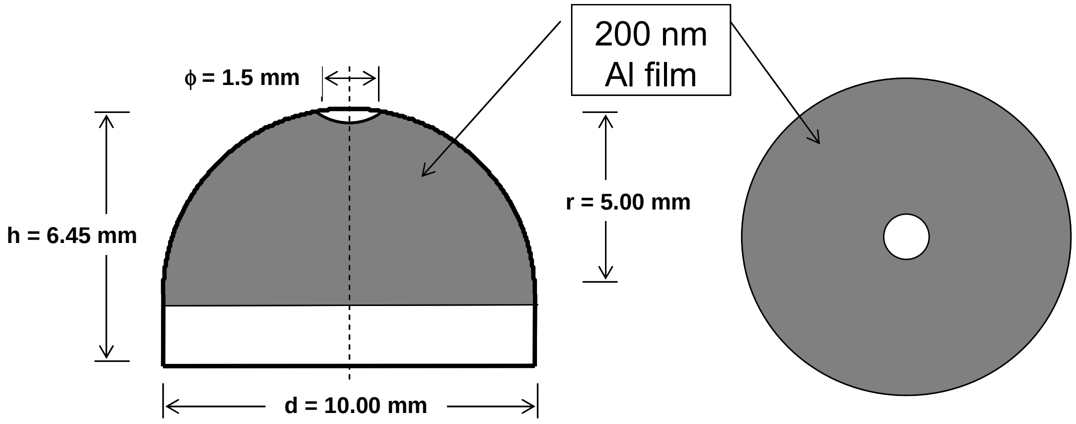

**Figure 4.3** Reduced aperture silicon lens. The shaded region indicates the metallized surface.

In order to increase the THz signal sensitivity above that of the exposed receiver while simultaneously increasing the spatial resolution above that of the full Si lens, a metalized aperture was formed directly on the Si lens as illustrated in Figure 4.3. A 200 nm thick coating of Al was evaporated onto a standard truncated hemispheric Si lens with a 1.5 mm diameter aperture on the apex.

The effect of this aperture is twofold. First it increases the spatial resolution of the measurement from a full 10 mm diameter lens to 1.5 mm diameter. Secondly, since the dipole receiver antenna is placed at the focal point of the lens, the antenna sees the Fourier transform of the field pattern over the lens aperture. By reducing the aperture, or spatial area over which the field is integrated, the Fourier plane pattern is broadened, reducing the sensitivity to the angle of incidence of the incoming radiation. Hence the reduced aperture lens has less directivity than an unmodified lens, which is important when mapping the time dependent spatial field distribution from all sources in space.

## 4.4 Rapid Scanning Delay Line

To reduce the time required to take multiple consecutive measurements while raster imaging the THz pulse, a rapid scanning delay line replaced the motorized stepper delay line. This changed the data acquisition device from a lock-in amplifier to an analog-to-digital card monitoring the real time output of the current pre-amplifier. The high dynamic reserve required for scanning at tens of Hertz dictated that the pre-amplifier be operated in the high response ($10^{-9}$ A/V gain) mode rather than the low noise setting ($10^{-7}$ A/V gain) mode.

The rapid scanning delay line is a Clark-MXR galvanometric oscillator driving a linear stage that translates the mounted retroreflector according to an input waveform. The typical operating parameters are a sine wave input at ~20 Hz. The range of the scanner can be adjusted up to 2 cm path length (corresponding to a 133 ps time range for a double delay line configuration.) Though the range of travel can be adjusted to this length, only the linear region about the zero crossing of the driving waveform is used for data collection. The typical scan length is 30 ps to 70 ps.

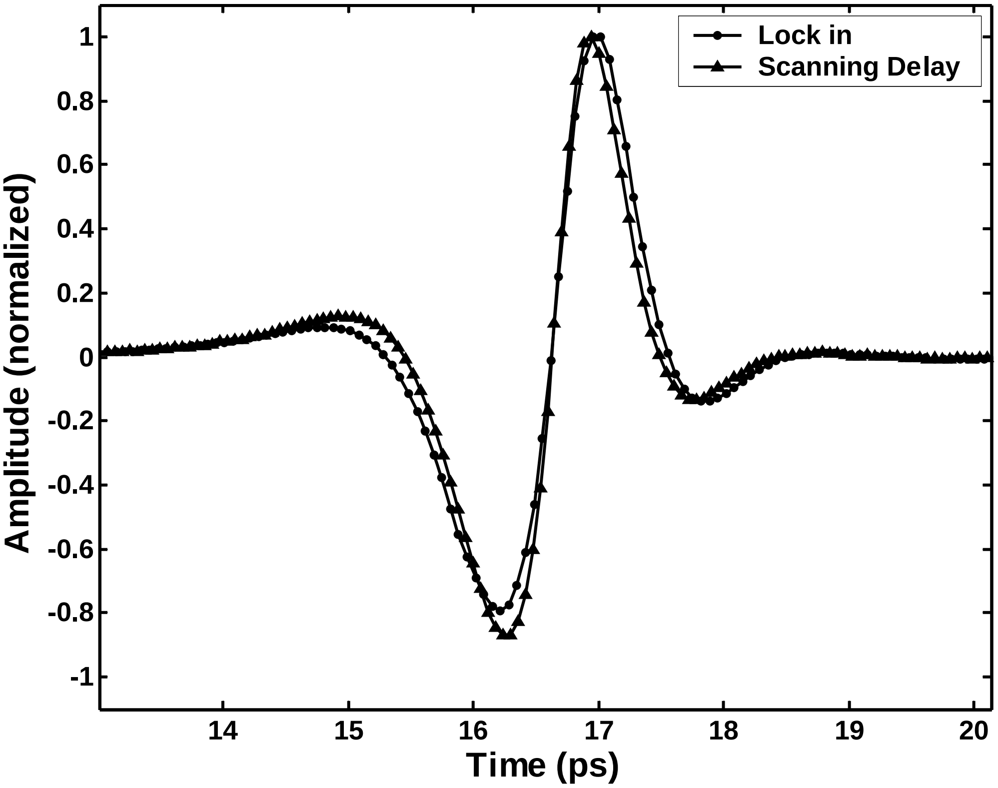

**Figure 4.4** Comparison between lock in and rapid scanning delay line measurements demonstrating comparable behavior for large THz fields.

Figure 4.4 shows a comparison between a measurement taken with a lock-in amplifier and the rapid scanning delay line. (The measurement is taken at the first frequency dependent beam waist as shown in Figure 4.11.) The lock-in measured the induced current from the THz receiver in 5 μm steps (33 ps) in the delay line over a range of 1024 steps modulating with an optical chopper at 273 Hz. Without the bandpass filtering of the lock in amplifier, rapid scanning delay line measurements are significantly noisier. Since the THz beam is not modulated, any response of the dipole antenna to incident radiation, from the transmitter or extraneous sources, is detected inducing additional noise and a non-zero background level. The scanning delay line measurement shown in Figure 4.4 was made with N = 64 averages and 59.5 fs/point. The analog-to-digital card sampled the output from the current amplifier at 30,000 points/sec.

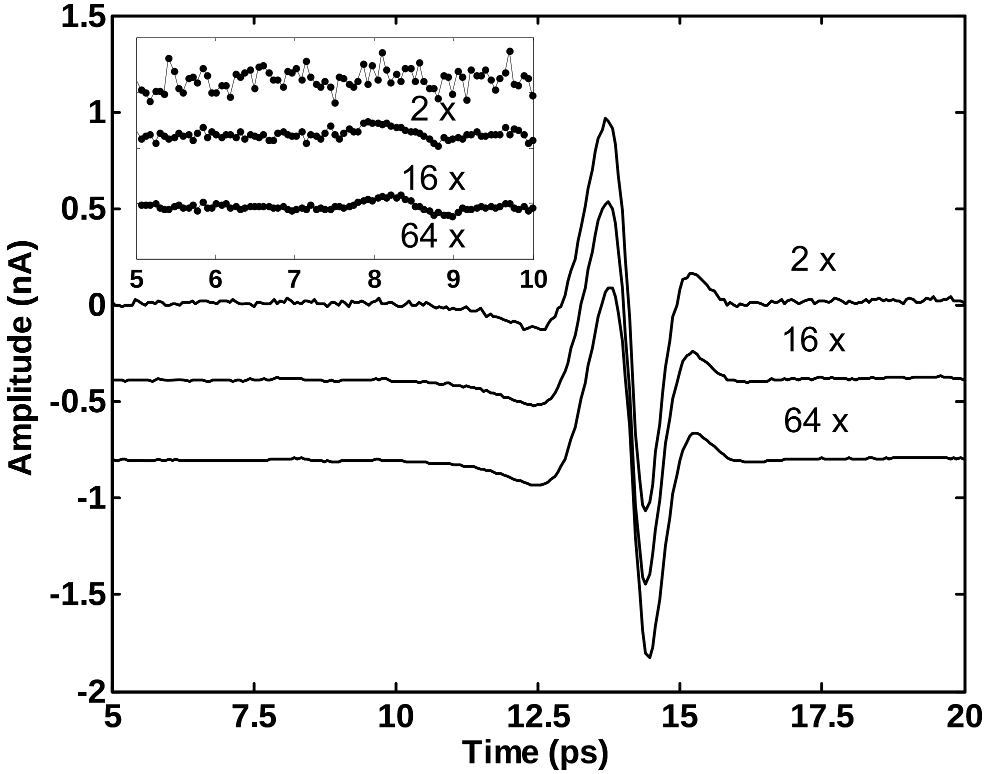

**Figure 4.5** Impact of signal averaging on measured pulse form using the rapid scanning delay line. The insert shows the noise prior to the pulse. Note the slight pulse due to optical reflections in the receiver clearly resolved at 8.5 ps for N = 64 averages.

In order too reduce the contribution of noise, the rapid delay signal was averaged. Figure 4.5 shows the effect of averaging for N = 2, 16, and 64 times on the same signal and offset for clarity. The inset shows a close up of the noise prior to the arrival of the THz pulse. A pulse form due to the reflection of the optical gating pulse on the receiver is resolved out of the noise level for the highest averaging rate.

Table 4.2 contains the comparison between the rapid scanning delay line and the lock-in amplifier measurements. The dynamic range is taken as the peak-to-peak amplitude of the measured THz pulse. The RMS noise is determined prior to the arrival of the signal, in the range prior to the inset of Figure 4.5. The ratio of the dynamic range to the RMS noise gives a figure of merit for the sensitivity of the system. The lock-in amplifier has the superior response by orders of magnitude. However, the acquisition time is the limiting factor. In a raster scan of $40 \times 40$ sample positions, a total of 1600 individual THz scans are made. Using a lock-in detector and automated translation stage, each 500 point trace takes about 1 minute to record, so a $40 \times 40$ measurement would require over 26 hours to take. The rapid scanning delay line, even at 64 × averaging, would require less than 2 hours at 4 seconds per individual time scan.

| Measurement | Dynamic Range (peak-peak) | RMS Noise | Approx. Ratio | Acquisition Time |
|---|---|---|---|---|
| Lock in | 6.7 nA | 1.28 pA | 5200:1 | 1 min. |
| 2 × averages | 20 nA | 105 pA | 192:1 | < 1 sec. |
| 16 × averages | 20 nA | 36 pA | 550:1 | 1 sec. |
| 64 × averages | 19 nA | 21 pA | 900:1 | 4 sec. |

**Table 4.2** Comparison o f dynamic range, noise, and acquisition time for the rapid scanning delay line data measurement vs. lock in amplifier.

The RMS noise does drop off as $\sqrt{N}$ between the 2 and 16 averages as expected. However the reduction in noise with increased averages began to level off at 64 averages.

## 4.5 **Beam behavior**

Both exposed and reduced aperture receivers have appropriate applications in measuring the beam behavior under propagation conditions. The reduced aperture receiver provides an increased peak signal to noise over the exposed receiver, but the beam must be significantly larger than 1.5 mm in order to resolve any spatial variations. The large beam conditions are readily achieved due to the highly diffractive nature of the THz beam. The exposed receiver provides a near point sampling capability at the sacrifice of signal strength, limiting high resolution measurements to regions of high field densities such as optical foci.

The two detection methods were used to image simple beam propagation. The THz beam was measured at three locations in the standard THz-TDS configuration: near the first paraboloidal mirror, at the frequency dependent beam waist, and at the second frequency independent beam waist.

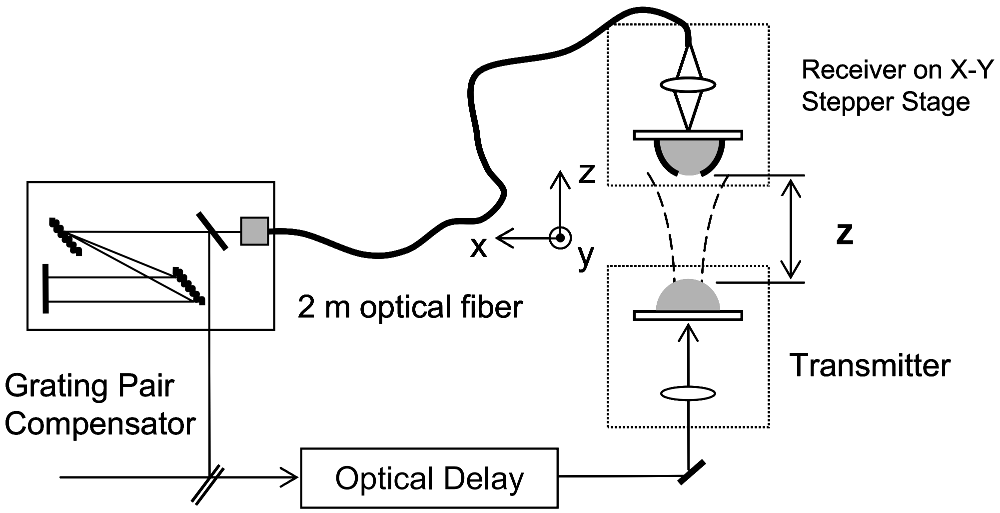

**Figure 4.6** Experimental set up for THz beam profile measurements after linear propagation of distance z.

### 4.5.1 Linear beam propagation

The experimental configuration shown in Figure 4.6 provided a direct measurement of the beam profile with the reduced aperture lens described previously. The THz receiver was a 10-50-10 dipole antenna. Using the reduced aperture lens, measurements were made in a 33 × 33 grid in the xy-plane with step sizes 1.46 mm × 1.44 mm respectively for a total area of 48.18 mm × 47.52 mm. A representative time resolved field measurement in the horizontal ( $\hat{x}\hat{z}$ ) plane taken at a propagation distance z = 116 mm is shown in Figure 4.7.[49]

The spatial resolution of the reduced aperture system is limited by the size of the aperture on the lens (1.5 mm dia.) compared to an unmodified Si lens with full aperture (10 mm dia.). The increased resolution is made at the expense of signal strength and continuous spectral coverage. The reduced aperture system attenuates signal strength below 0.3 THz limiting the useful bandwidth range from 0.35 to 1.5 THz with the given dipole.

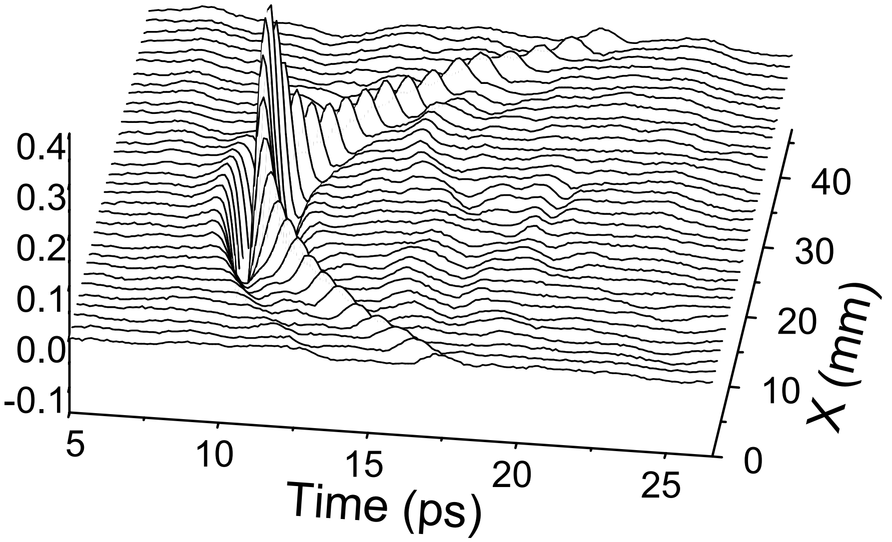

**Figure 4.7** THz pulses measured as a function of time and position on horizontal plane (x and y) through the optical axis.

By decreasing the angular sensitivity of the THz receiver the directivity of the receiver antenna can be neglected in these measurements as discussed in the following section. The current measurements are directly interpretable as proportional to the electric field at a given point in space. With the phase relationship between successive scans fixed by the fiber guided optical pulse coupled to the receiver, a reconstructed THz pulse can be measured at a plane in space.

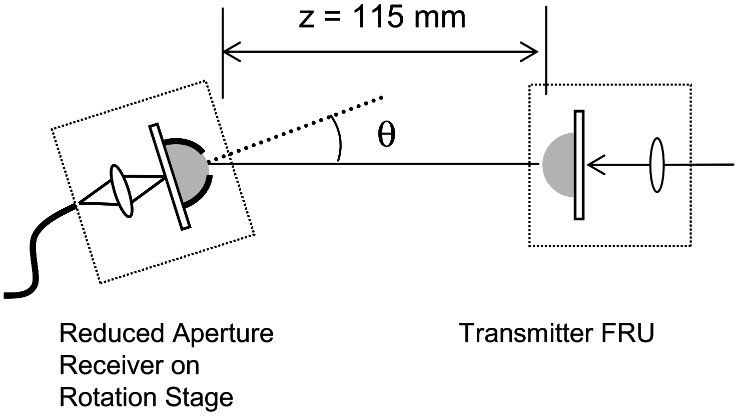

**Figure 4.8** Experimental schematic for the angular sensitivity comparison measurements. The reduced aperture lens was replaced with a Si lens of matching dimensions.

### 4.5.1.1 Directivity measurement of reduced aperture receiver

The directivity of the receiver was measured as a function of angle θ between THz source and receiver at z = 115 mm in steps of $\Delta\theta = 0.5°$ to a maximum angle of ±12°. Figure 4.8 shows the experimental configuration with the axis of rotation for the receiver through the front surface of the lens. The propagation distance is within the Rayleigh range of all the associated frequency components of the incident pulse assuming a 2.5 mm diameter initial beam waist at the transmitter. Thus the radial phase contribution of the propagating pulse can be neglected and individual frequency components will have a nearly planar phase front.

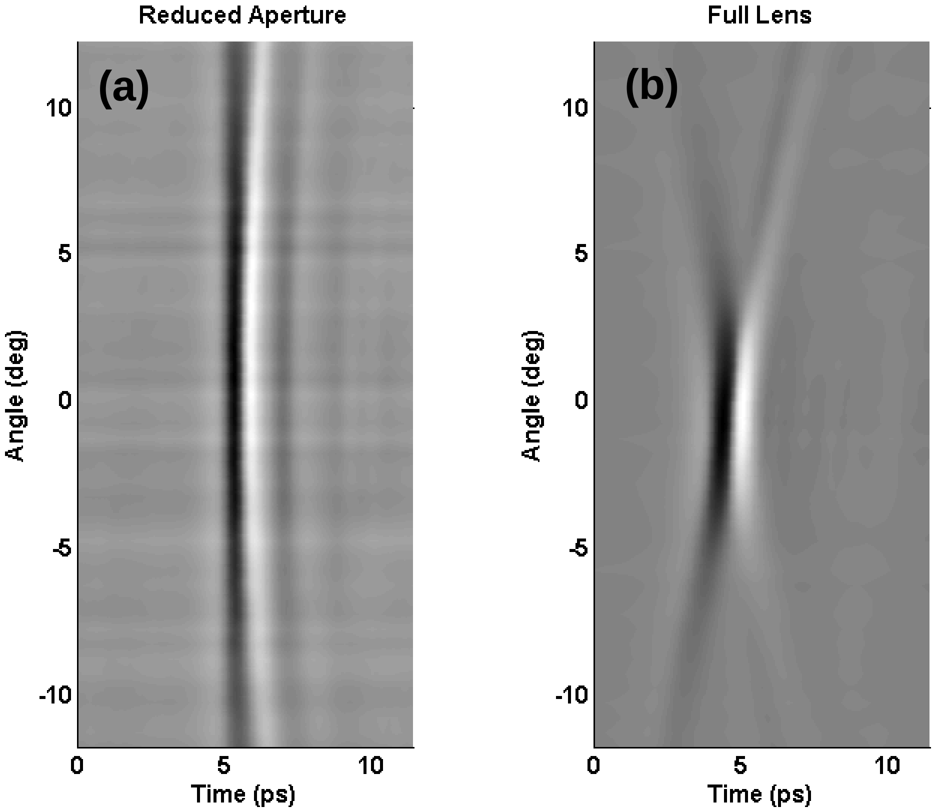

**Figure 4.9** Angular response in the time domain for the reduced aperture lens, (a), compared to a full lens, (b). The angle varied from $-12° < \theta < +12°$

Figure 4.9 shows time resolved field profiles measured through a 24° range for the reduced aperture and full lens receiver configuration. The reduced aperture pulse form, Figure 4.9 a), remains nearly constant across the range of measurements, though the detected field at more oblique angles does exhibit attenuation. The full lens pulse, Figure 4.9 b), is tightly localized within ± 4° of the center angle and demonstrates strong reshaping at larger angles.

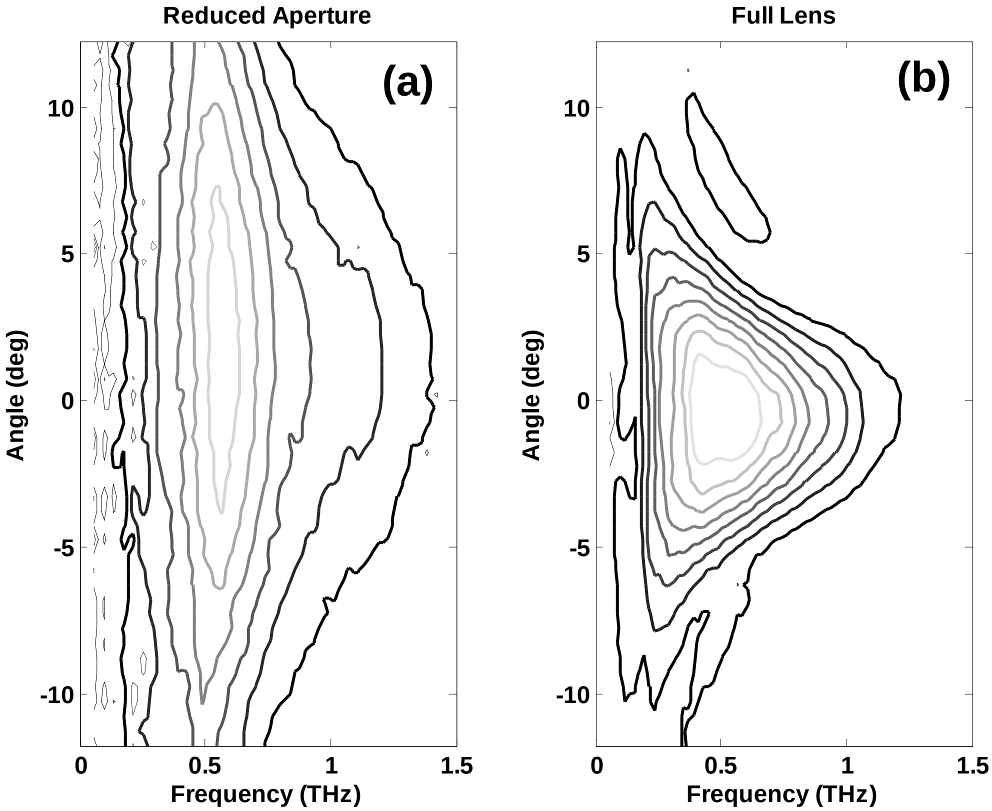

**Figure 4.10** Normalized pectral magnitudes of the reduced aperture, a), and full aperture lens, b).

Figure 4.10 shows the normalized spectral magnitudes for the pulses of Figure 4.9. The maximum angle between the transmitter and the measured beam is approximately 5°. The directivity contributes less than 3 % variation in field amplitude profile across the beam in the frequency range of interest. Directivity would be a significant concern if the receiver was equipped with a full aperture Si lens where the variation across the same range would be 5 to 20 times greater with strongly frequency dependent behavior.

### 4.5.2 Frequency dependent waist

The THz beam radius is shown in Figure 4.11 as a function of distance while propagating through a standard THz-TDS experiment. This is determined by applying standard Gaussian beam propagation techniques[28] for different frequencies assuming a starting beam waist of $w_{o1}$ = 2.5 mm for each frequency component and a planar phase front at the lens surface. (Measurements using the system in Figure 4.6 led to analysis that indicated this assumption does not strictly hold.[49]) This propagation calculation assumes perfectly aligned optics and treats the paraboloidal mirrors (see Figure 2.1) as thin lenses with focal length $f_L$ = 119 mm. The measurement of Section 4.5.1 corresponds to the beam profiles measured nearly at the paraboloidal mirror.

The frequency dependent beam waist, $w_{o2}$, is located at distance z = 238 mm, midway between the paraboloidal mirrors. The calculated beam waist varies from 22.7 mm at 0.2 THz to 2.3 mm at 2 THz.

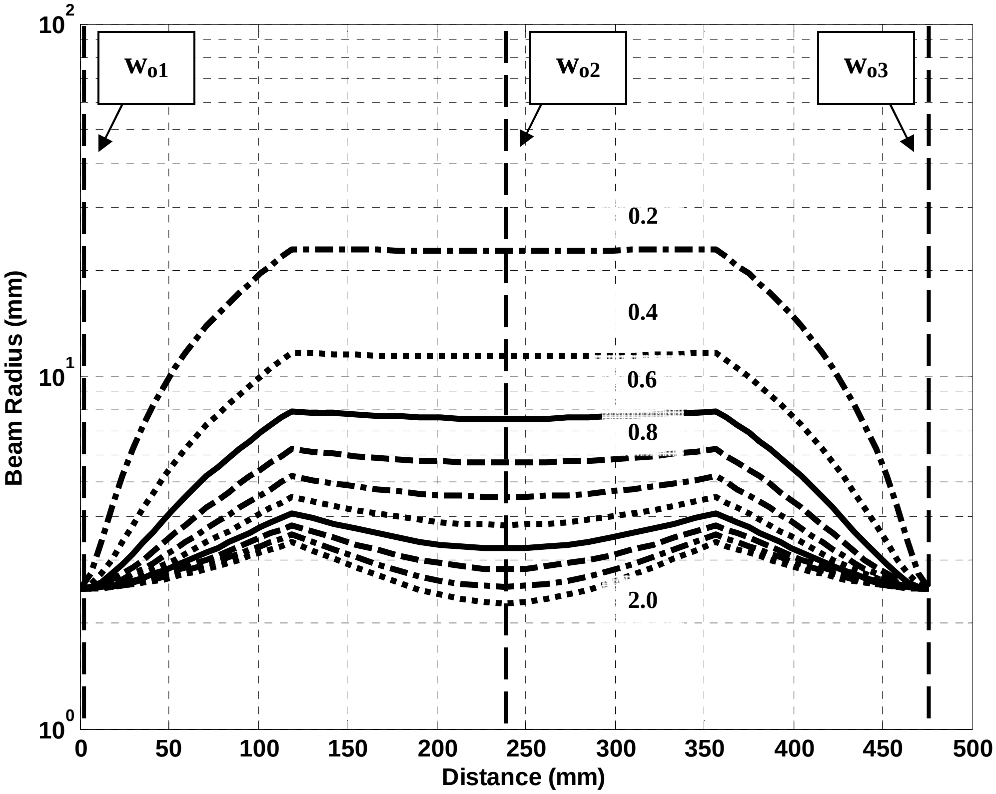

**Figure 4.11** Beam radius as a function of distance propagating through a standard confocal THz-TDS system starting from a beam waist of $w_{o1}$ = 2.5 mm at z = 0. A frequency dependent waist, $w_{o2}$, is located at z = 238 mm midway between the optics at z = 119 mm and 357 mm. The frequencies plotted start from 0.2 THz (top trace) in 0.2 THz steps to 2.0 THz.

In order to test the measurement systems, the effects of propagation on the THz beam the spatially resolved field was measured at the frequency dependent beam waist, $w_{o1}$ (z = 238 mm) Figure 4.12 shows the experimental set up for these measurements. A comparison is made between the reduced aperture receiver and the exposed chip receiver.

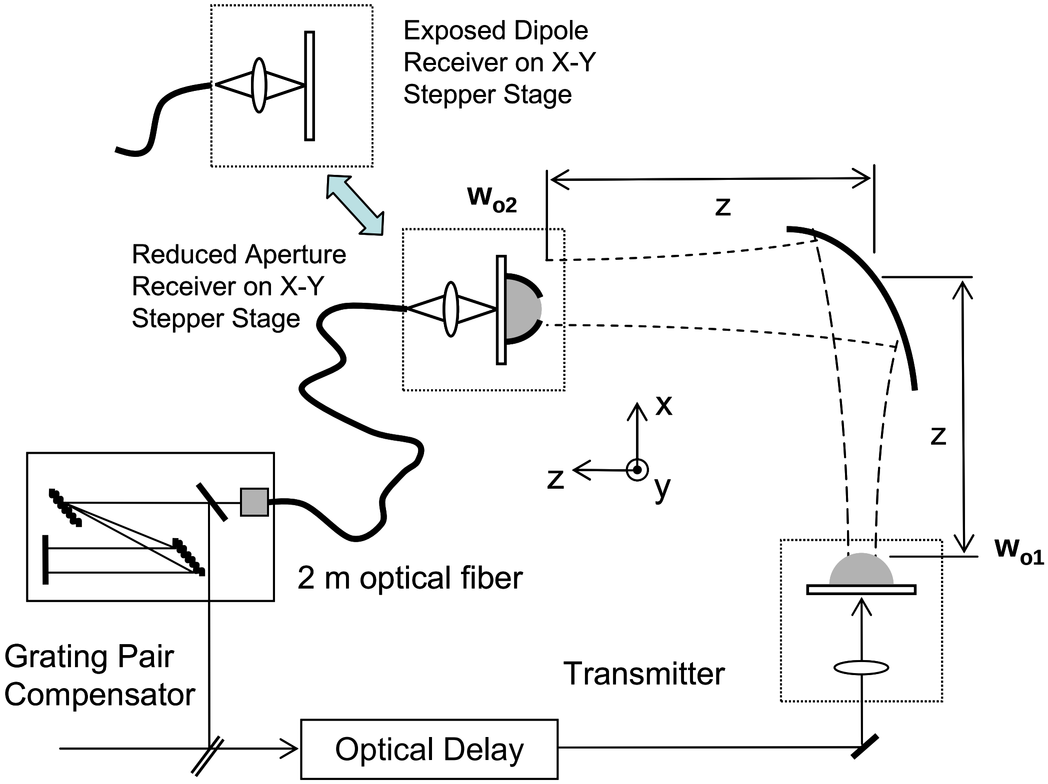

**Figure 4.12** Frequency independent beam waist measurement experiment comparing the exposed receiver response to the reduced aperture receiver.

These measurements would require significant post processing without the use of reduced aperture and exposed receiver capabilities. When the beam profile is on the order of the size of the aperture—such as at a beam waist—a complex deconvolution between the measured signal and the complex lens pattern would be required to extract an accurate representation of that beam profile. Spatial variations in the field would also be averaged out due to the windowing effect.

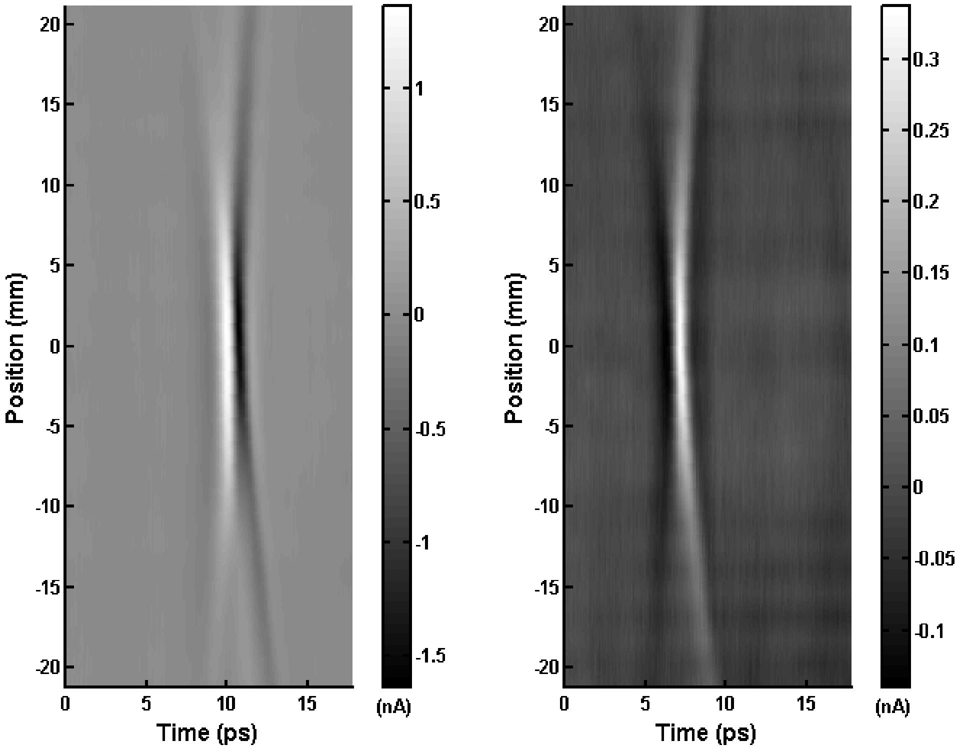

**Figure 4.13** Measurements taken at the frequency dependent waist $w_{o2}$ in the horizontal plane (E field oriented along the x plane.) (a) Reduced aperture receiver. (b) Exposed receiver (no lens).

Figure 4.13 shows representative two dimensional time resolved field measurement images in the vertical ( $\hat{y}\hat{z}$ ) plane taken at $w_{o2}$ extracted from the three dimensional scans. Both measurements for the reduced aperture and exposed receiver were taken under the same conditions. The scans were performed in a 30 × 30 grid in the xy-plane orthogonal to the direction of beam propagation with step sizes 1.46 mm × 1.45 mm respectively for a total area of 42.5 mm × 42.0 mm. The scans were averaged 64 times to reduce the noise level.

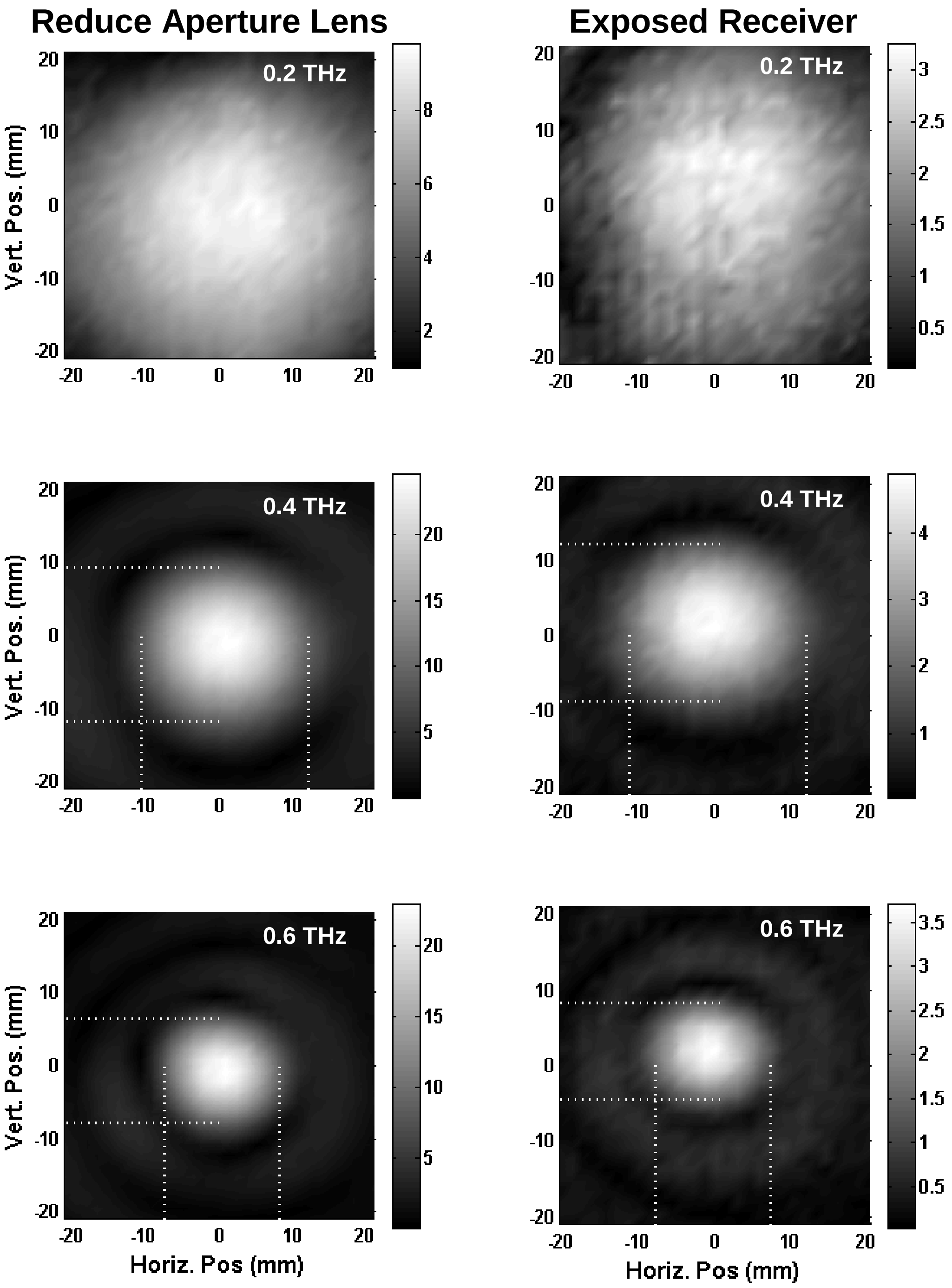

**Figure 4.14** Amplitude plots of frequency measurements at the frequency dependent waist, $w_{o2}$, for the reduced aperture and exposed receiver for 0.2, 0.4, and 0.6 THz. The dashed lines indicate the 1/e points and the numerical results are given in Table 4.3 the z axis is in arbitrary units. The beam profile for 0.2 THz was broader than the measurement range.

Each individual temporal scan was Fourier transformed numerically to yield the frequency dependent spatial distribution of the observed electric field. Figure 4.14 shows the spatial magnitudes for several frequencies compared between the reduced aperture and exposed receiver under identical measurement conditions. This demonstrates that the dipole receiver without a lens and receiver with a reduced aperture lens yield comparable beam profiles, providing that the spatial variation of the field amplitude is small compared to the aperture diameter. The reduced aperture lens and receiver system increases the signal-to-noise ratio by a factor of five over a receiver with no lens.

| | Reduced Aperture $\Delta x$ (mm) | Reduced Aperture $\Delta y$ (mm) | Exposed Receiver $\Delta x$ (mm) | Exposed Receiver $\Delta y$ (mm) | Gaussian Waist $w_{o2}$ (mm) |
|---|---:|---:|---:|---:|---:|
| 0.2 THz | NA | NA | NA | NA | 22.7 |
| 0.4 THz | 11.4 | 10.6 | 11.6 | 10.3 | 11.4 |
| 0.6 THz | 7.9 | 7.0 | 7.6 | 6.6 | 7.8 |

**Table 4.3** Measured beam radii at the frequency dependent waist ($w_{o2}$) from Figure 4.14. The Gaussian waist column is calculated with an initial beam waist of 2.5 mm as shown in Figure 2.1

The predicted frequency dependence is observed assuming lowest order Gaussian mode propagation. Figure 4.15 shows the frequency dependent beam profile as measured with the reduced aperture receiver along the horizontal plane ($\hat{x}\hat{z}$) compared with the Gaussian distributions ($= e^{-x^2/w_o^2}$) using the beam waists predicted (see Figure 4.11.) The peak amplitudes of the Gaussian predictions were matched to the measured frequency and the frequency traces were offset for clarity. The predicted waist sizes match well. (The observed structure in the wings of the frequency measurements are due to higher order modes.[49])

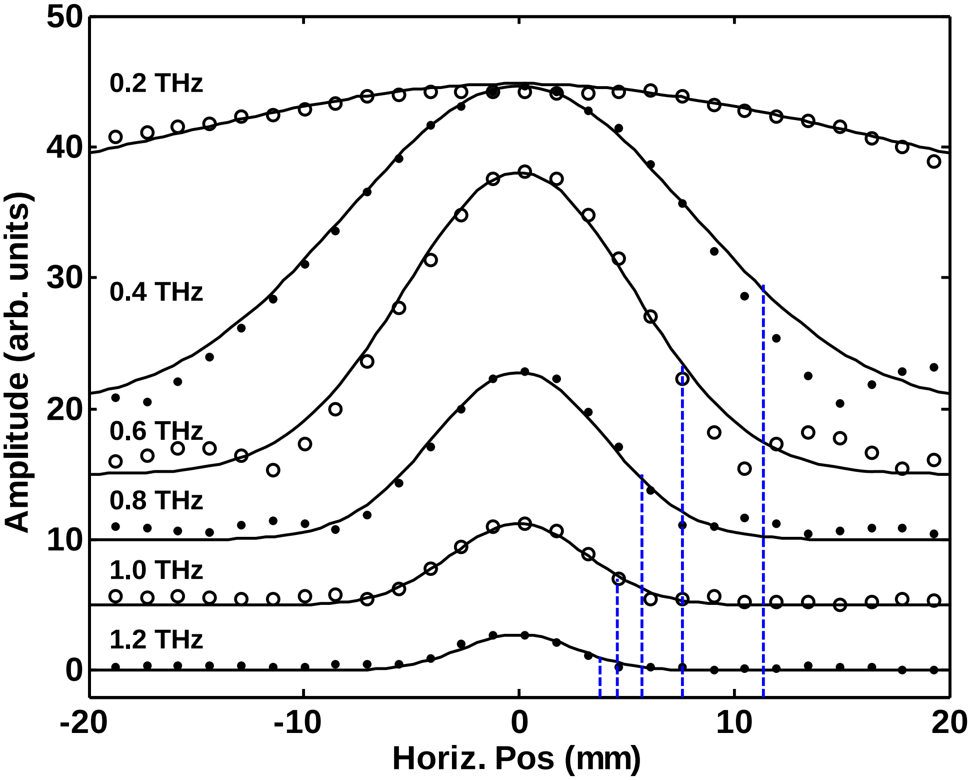

**Figure 4.15** Measured values (dots/circles) from reduced aperture receiver scans compared to simple Gaussian beam predictions (solid)—as shown in Figure 4.11—for the frequency dependent waist, $w_{o2}$. Only the horizontal position is shown. Frequency plots are offset vertically in steps of 5 for clarity (except 0.2 THz which was offset by 20.) The vertical dashed lines show the 1/e points for the calculated waist radii, 22.7 mm (outside range of graph), 11.3 mm, 7.6 mm, 5.7 mm, 4.5 mm, and 3.8 mm for 0.2 to 1.2 THz respectively.

The reduced aperture and exposed receiver demonstrate comparable spatial behavior for this application. The asymmetry observed in the beam profile is due to the radiation pattern interaction with the lens.[21,49]

### 4.5.3 Frequency independent beam waist

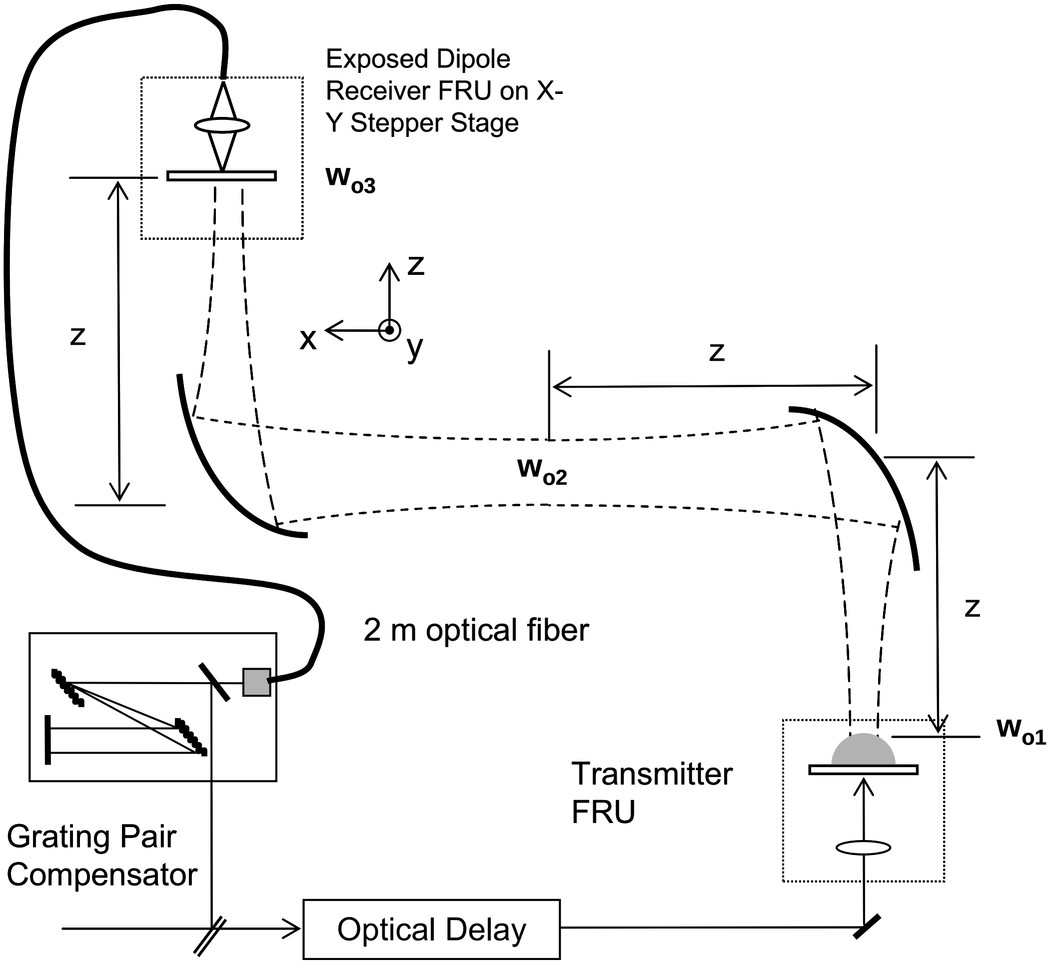

**Figure 4.16** Frequency independent beam waist measurement experiment using the exposed receiver fiber coupled FRU

The frequency independent beam waist, $w_{o3}$, of the standard THz-TDS system is located at the image plane of a pair of unity conjugate ratio optical systems. The third waist, $w_{o3}$, is a 1:1 image of $w_{o1}$ assuming matched foci for the optical system and proper system alignment. Although a perfect image is formed by ideal mirrors, the finite 50 mm diameter of the paraboloidal mirrors do aperture the optical system. This aperture will incur the loss of phase information and peripheral amplitude, so the complex field at the transmitter lens will not be perfectly imaged. The third waist, $w_{o3}$, is where the receiver is located in the standard THz-TDS system for highest signal strength. This allows direct imaging of the electric field near the Si lens on the transmitter FRU.[49]

As the spatial extent of the beam waist is on the order of 2.5 mm, the reduced aperture receiver does not provide the necessary resolution. This is an ideal application for the exposed receiver. Figure 4.16 shows the experimental configuration for the frequency independent beam waist measurement. The beam was raster scanned with an exposed receiver in a 60 x 80 grid of 0.24 mm x 0.16 mm step sizes for a total distance 14.64 mm x 18.66 mm. The current induced in the receiver antenna by the THz radiation was measured at a sensitivity of $10^9$ V/A and filtered to reduce noise before averaging 64 times to increase the signal-to-noise ratio.

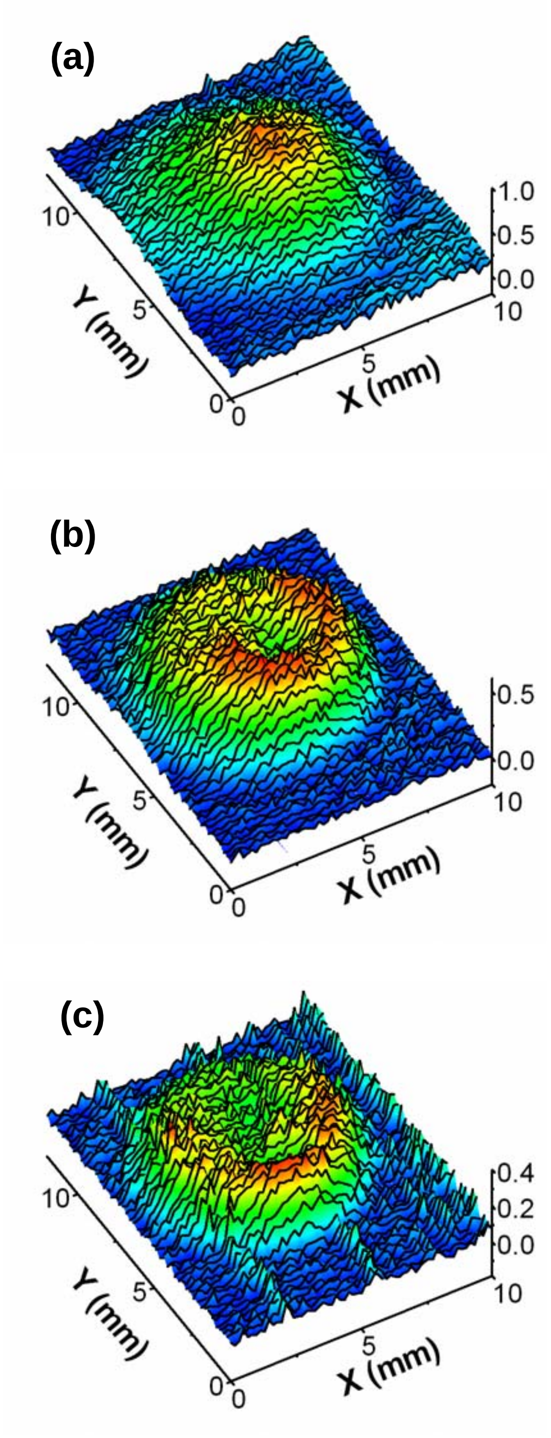

**Figure 4.17** Images of the frequency independent beam waist, wo3 for (a) 0.18, (b) 0.38, and (c) 0.58 THz. Note the annular intensity pattern evident in the less diffractive higher frequencies.

Figure 4.17 shows the results of the measured beam profile for frequencies of 0.18, 0.38 and 0.58 THz respectively at $w_{o3}$. As expected, the radius of the measured amplitude distribution demonstrates a near frequency independent radius. If the system is aligned properly to maximize the optical transfer function, the second focus should be an image of the intensity distribution at the surface of the transmitter silicon lens. A toroidal structure is seen in the intensity in good agreement with the theoretical results for a lens-coupled dipole radiator near a plane dielectric.[49] The low SNR of the exposed receiver precluded determination of the phase.

## 4.6 Conclusions

Discrepancies in the propagation predictions of lowest order $TEM_{00}$ Gaussian modes compared to measurements made using the reduced aperture and exposed receiver led to further investigation. As Reiten, et. al.[49] indicated, the complex behavior of the THz pulse form can be approximated by the $TEM_{00}$ Gaussian mode, however accurate modeling must include higher order modes to account for observed structure in the phase and amplitude and account for less beam divergence than predicted in propagation measurements. Likewise the imaging of the electric field near lens surface indicates that the assumption of a uniform frequency independent $TEM_{00}$ Gaussian distribution does not describe the radiation pattern.[49]

The capabilities to image THz propagation with fine spatial resolution can be applied to observing the three dimensional nature of FTIR.

# 5 FTIR—Part II

## 5.1 The questions of tunneling time

The question of energy propagation for quantum mechanical tunneling [50] and the FTIR analog[51] continues. In Chapter 3 the question of superluminal propagation was addressed through a one dimensional experiment and subsequent analysis. The experiment successfully demonstrated that a THz pulse propagating through an optical tunneling barrier (FTIR) follows the predictions of linear dispersion theory. The duration of the tunneling time remains unanswered as linear dispersion theory does not assume a path or explicitly assign propagation times. Though causality is inferred from the Kramers-Kronig relations between the measured real and imaginary components of the transfer function of Equation 3.11, [17,52] the question of tunneling time (barrier traversal time) continues to be a topic of interest.

As the width of the optical tunneling barrier $\Delta$ is increased, the required time to cross the barrier seemingly decreases (Chapter 3.3.2) which has led to conclusions of faster than light velocities under simplistic mathematical treatments. The debate is maintained by proponents supporting the interpretation of superluminal propagation under a wide variety of highly dispersive and/or lossy conditions, e.g. undersized waveguides, dielectric stacks, and FTIR.[51] In response to questions of causality, the superluminal adherents cite the propagation of Motzart's 40th symphony through an undersized waveguide to prove that information is transferred at a claimed 4.7 c velocity.[53] The FTIR experiments probed the opposite limit of those performed by

Wang, et. al.[54], who measured pulse propagation in the specific case of extremely narrow bandwidth pulses when the real part of the index is linear and gain is independent of frequency so that no pulse reshaping occurs.

The opponents of the superluminal interpretation have addressed the interpretations of the experimental observations on a situational basis.[17,18,52] This work focuses on the case of FTIR where the debate hinges on a primary misconception: the spatial beam profile measured at the output of the FTIR experiment is the same as the beam profile at the input. This is the spatial equivalent of following the peak of the THz time domain pulse. As discussed in Chapter 3, a one-to-one correspondence doesn't hold,[19] though tracking peaks was a method used previously as the observables were essentially time independent intensity rather than time resolved phase sensitive propagating fields. The desire to assign physical paths (single wave vectors) to beams as though the beam has an immutable nature gives rise to the claims of apparent superluminal transits of tunneling barrier.[15]

Other beam effects due to photon interaction with an optical barrier have been reported or proposed. Phenomena that could be investigated with the FTIR experiments in two or more resolvable dimensions include angular shifts,[20] beam reshaping, focal shifting, lateral shifting (GH shift),[19] negative lateral shifting (theoretical),[55] transverse shifting (optical Hall effect), [56], and resonant tunneling.[57]

The GH shift and the angular shift of the propagating beam play a role in the one dimensional FTIR experiment of Chapter 3. These effects impact the measurements for the standard THz-TDS system of Chapter 3 due to the strong frequency dependence of the optical transfer function. The ability to map the distribution of the electric field in space is required to directly observe these effects.

### 5.1.1 Tunneling times

The propagation of a short pulse through a tunneling barrier results in pulse reshaping due to attenuation and dispersion, a problem originally addressed by Brillouin and Sommerfeld[58]. As seen in the previous chapter, pulse reshaping makes it difficult to directly assign a tunneling time since simple center of mass or arrival time measurements do not suffice for strongly reshaped pulses.[59] Due to this pulse reshaping, two time scales have been proposed for tunneling[33]. A loss time is used to describe pulse attenuation, while a phase time describes temporal shifts or reshaping. Much of the current interest in optical tunneling is due, in large part, to an apparent saturation of some of these times measured for an optical wave packet to cross the tunneling gap in the thick barrier limit.[60] [20]

### 5.1.2 Goos-Hanchen Shift

The effect of the lateral shift of a beam was first reported by Goos and Hanchen[61] in total internal reflection experiments in the mid 1940's. The GH shift occurs during total internal reflection of a spatially bounded beam, and becomes large near the critical angle[41,62]. Figure 5.1 shows the concept of the GH shift and how this phenomena relates to FTIR.

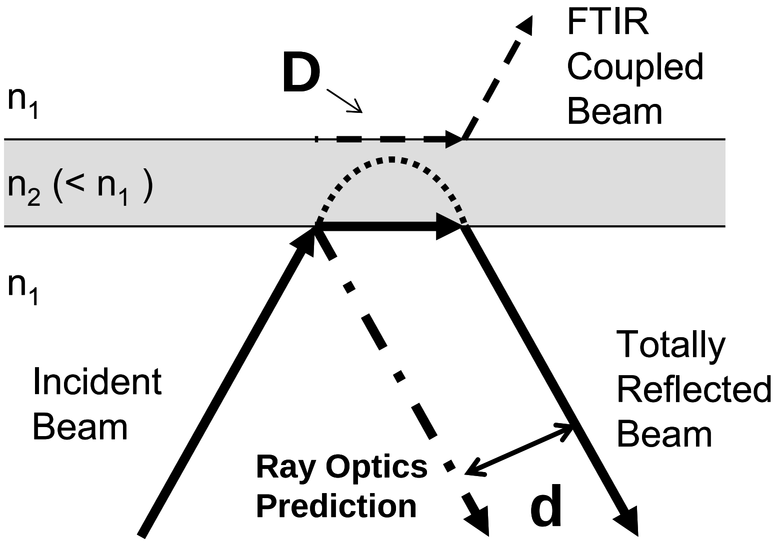

**Figure 5.1** Total reflection from a high index medium ($n_1$) from an interface with a lower index medium ($n_2<n_1$) beyond the critical angle, $\theta_c$. *D* is the distance the surface wave mode propagates. *d* is the Goos-Hanchen shift of the reflected beam. The dashed line denotes the component coupled through FTIR. The ray optics parth shown in the dash-dot line and the dotted line represents the penetration of the evanescent field into the less dense barrier medium.

Rather than experiencing a sharp boundary upon total internal reflection, the incident beam penetrates into the lower index medium with an evanescent field. The subsequent evanescent field is not a standing wave, but a surface wave that travels some distance along the interface between the two media.[19] This propagation distance is responsible for the observed GH shift and is why the effect is observable most readily with spatially bounded beams. The evanescent surface wave is the mechanism for coupling into the second high index region in the case of FTIR. This results in a shift of the transmitted beam that mirrors the GH shift in the reflected beam. Balcou et. al.[20] used the GH shift in the transmitted beam as a physical clock to determine the transit time of light through a FTIR barrier.

The lateral shift is not observable in the linear THz-TDS experiment, though the consequences of this lateral shift impacts the measurements. Two concerns were posed in Chapter 3 dealing with assumed optical path across the tunneling gap and reduced amplitude due to the transmitted beam walking off the optical axis of the THz system. When utilizing collection optics, the paraboloidal mirror and the Si lenses in front of the THz receiver—see Figure 3.1—essentially integrate the bounded beam along the x and y axis, erasing spatial information in exchange for an increased signal on the receiver. This could incur additional pulse reshaping due to the frequency dependence of the optical transfer function. To isolate the lateral shift, the experimental techniques and apparatuses of Chapter 4 are applied to detecting the THz pulse transmitted through an optical tunneling barrier (FTIR.)

## 5.2 **Experiment**

Measurements are performed to observe both the temporal and spatial reshaping of pulses after undergoing optical tunneling. As temporal pulse reshaping makes it impossible to assign a time to pulse tunneling[63], spatial pulse reshaping makes it impossible to assign a well defined path to spatially localized wave packets across a tunneling barrier. Through coherent measurement of the pulse's electric field, direct observation of the phase and amplitude shifts of the plane waves which form the THz pulse’s basis set are possible.

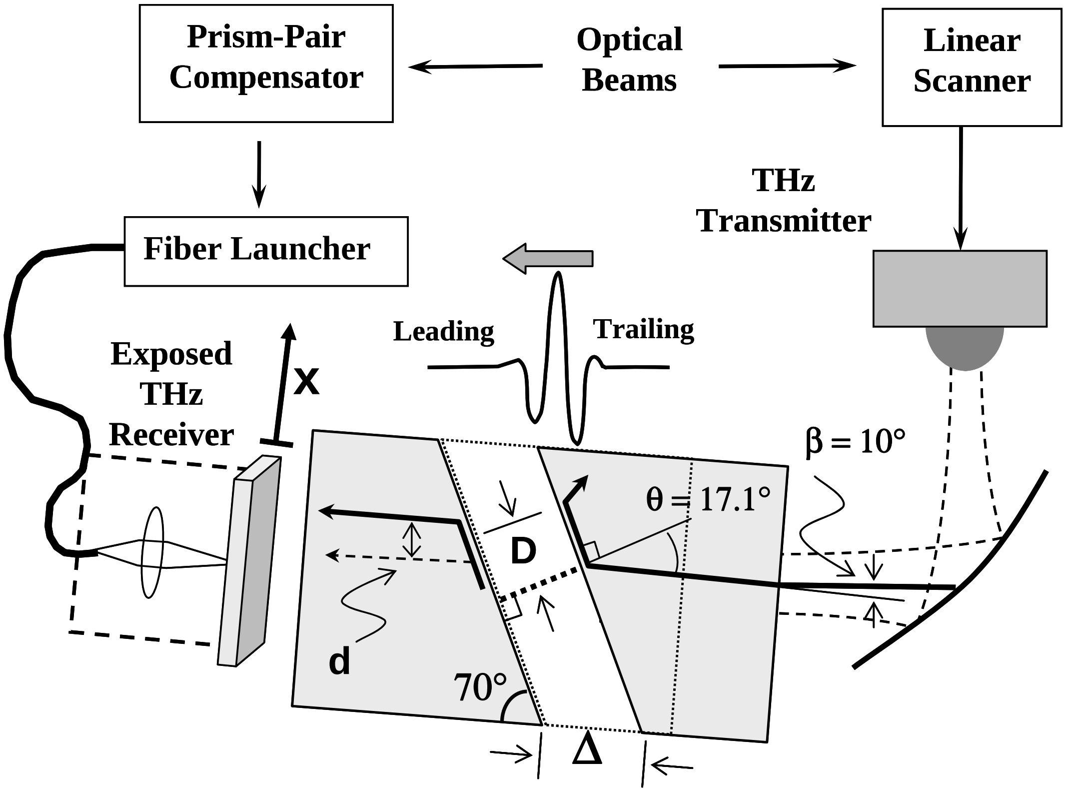

**Figure 5.2** Experimental set up for spatially resolved FTIR measurements. Δ is the gap distance between the Si wedges. *D* is the propagation distance of the surface wave in the gap and *d* is the GH shift for the transmitted beam when compared to the zero gap reference.

Figure 5.2 shows the experimental system used to observe the beam profile. Established THz generation and detection techniques are used. The first series of measurements were done in two dimensions, time (t) and horizontal position (x).

The THz pulse is detected after propagating through the wedges by an exposed 10-50-10 dipole antenna structure mounted on a linear translation stage. The position of wedges and fiber coupled THz detector were chosen to be at a waist of the THz beam to ensure near a planar phase front of the pulse entering the wedges. The receiver was placed at a distance of 150 mm from the paraboloidal mirror (f = 119 mm) due to the high index of the Si prisms extending the Rayleigh range. A 9 cm single mode fiber and prism-pair compensator (Chapter 4 Section 1.3.1) are used to couple the optical gating pulse and allow continuous spatial translation of the receiver chip while maintaining absolute timing. The THz field is polarized in the plane of incidence (P polarization).

The optical tunneling barrier of Figure 5.2 is compromised of the Si wedges used in the one dimensional FTIR experiment of Chapter 3. For the observations near critical angle, the angle between the system optical axis ($\hat{z}$ axis) and the cylinder axis, β, is set to 10° so the angle of incidence on the interior wedge face is $\theta_i = 17.1°$. This is required as the wedges were cut at an angle $\Phi = 70°$. Both the separation between the wedges along the cylinder axis, Δ, and the angle β of the system optical axis with respect to the cylinder axis are adjustable with a resolutions of less than 5 μm and 0.1° respectively. To preserve absolute timing, the fiber coupled receiver cannot move between measurements. For the spatially resolved measurements, the wedge closest to the paraboloidal mirror was moved in changing the tunneling gap thickness Δ. Due to the tilt of the cylinder axis relative to the THz beam propagation direction required to achieve $\theta_i = 17.1°$, a lateral shift of 152 μm is expected from the translation of the input wedge into the non-axially aligned THz beam. This is below the spatial resolution of this measurement.

The receiver was scanned horizontally in the x direction (normal to the THz beam axis) in 1 mm steps. The assumed cylindrically symmetric THz beam is thus measured along a line, yielding a two dimensional plot of electric field as a function of position along the x axis and time. The THz pulses recorded for each location were an average of 1024 scans with an 83 fs time resolution.

## 5.3 **Spatially Resolved Measurements**

Contour plots of the time resolved beam profiles are shown in Figure 5.3 for the reference pulse, $E_o(x,t)$ measured with $\Delta = 0$, and the pulse, $E_T(x,t)$, which has tunneled through an optical barrier of width $\Delta = 1000$ µm as in Figure 5.3. The peak value of the reference pulse was nearly 3 times that of the peak value of the transmitted pulse and the amplitude (z axis) is in units of nA.

The two measured profiles show dramatic differences if one considers the peak of the pulse. $E_T(x,t)$ shows an apparent shift of $\Delta t = -1.79$ ps relative to $E_O(x,t)$ and a lateral shift of $d = 2.8$ mm in the positive x direction, shown in Figure 5.3, determined from the centroid. The measured position of the pulse is observed to be in the opposite direction of that assumed in previous studies of a THz pulse undergoing optical tunneling with claims of noncausal behavior.[15] The observed shift $d$ shows that the transmitted pulse for non-zero gap, Δ, propagates through less high index material in the second prism than the reference pulse. This lateral displacement of the beam profile is due to the Goos-Hänchen phase shift.

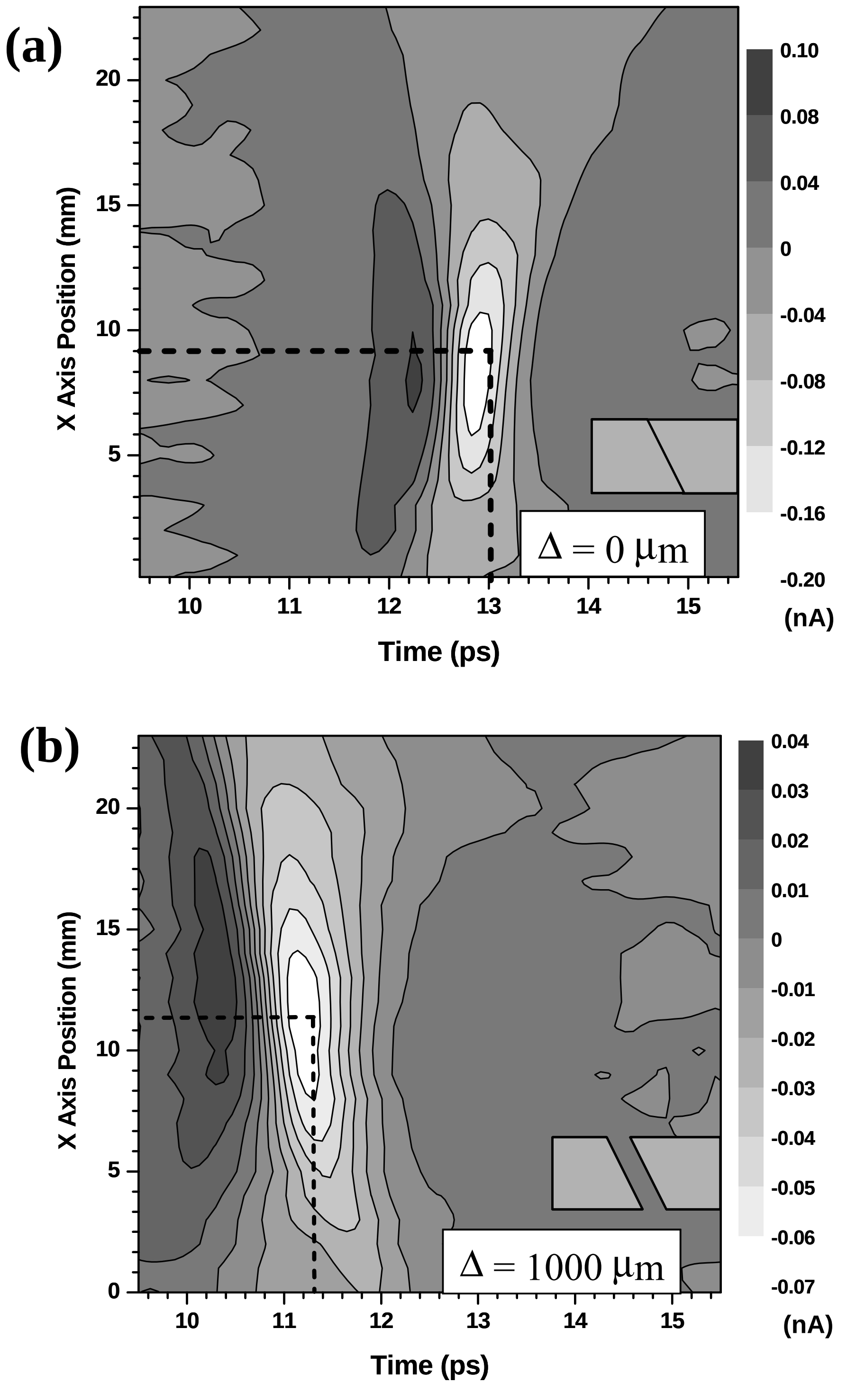

**Figure 5.3** Measured THz pulses after transmission through the Si wedges. (a) $E_O(x,t)$ and (b) $E_T(x,t)$. The inset shows the orientation of the tilted gap. The incident angle at the gap for the beams was 17.1°. The dotted lines show the relative shift in time of $\Delta t = -1.79$ ps and $d = +2.8$ mm between the peaks of the reference and tunneled pulses for a gap of $\Delta = 1000$ μm.

## 5.4 **Analysis**

Linear dispersion theory extended into two dimensions is applied to analyze the propagation of the time and spatially dependent pulses tunneling through an optical barrier. The pulse is expanded into a superposition of plane waves. The relative amplitude and phase of each sinusoidal component of a reference THz pulse $E(x_o,t)$ at a given spatial position, $x_o$, is obtained through a Fourier transform of the pulse propagated through the prisms with $\Delta = 0$ μm:

$$E\left(x_o,\omega\right)=\int_{-\infty}^{\infty}E\left(x_o,t\right)e^{-i\omega t}\partial t \qquad 5.1$$

For a given frequency, $\omega_o$, the spatial distribution of the electric field is measured by scanning the dipole antenna along the x axis and is given by $E(x,\omega_o)$. Any bounded electromagnetic beam is composed of a summation of plane waves corresponding to a distribution of incidence angles[42], each with a given amplitude and phase relationship. The total k vector (momentum) of each plane wave component is given by:

$$\vec{k} = k_x\hat{x}+k_z\hat{z} \qquad 5.2$$

with $|k|$ conserved. The overall k vector is given by $k = \omega n/c$ for a given frequency, where n is the refractive index of the medium, $\omega$ is the angular frequency, and c the speed of light.

The complex amplitude of each plane wave component, $E(k_x,\omega_o)$, for a given frequency and $\hat{x}$ component of the wave vector $k_x$, is obtained by a second Fourier transform:

$$E(k_x,\omega_o)=\int_{-\infty}^{\infty}E(r,\omega_o)e^{-ik_xx}\partial x \qquad 5.3$$

The effect of this two-dimensional Fourier transform is to convert the temporally and spatially localized THz pulse into a basis set of plane waves with propagation vectors in the $\hat{x}\hat{z}$ plane, with given amplitude and phase relationships.

The two dimensional Fourier transform of the measured reference electric field amplitude of Figure 5.3, $|E_O(k_x,\omega)|$, with $\Delta = 0$ μm is shown in Figure 5.4. There is a small experimental artifact in the measurement of $|E_O(k_x,\omega)|$ due to the requirement of the integration range in x to extend from negative to positive infinity while the experimental measurement is limited to 25 mm. The magnitude of the field after undergoing transmission through an optical barrier with $\Delta = 1000$ μm, $|E_T(k_x,\omega)|$ is shown in Figure 5.4.

The peak spectral component of $|E_T(k_x,\omega)|$ has shifted from 0.32 THz to 0.21 THz. This shift demonstrates pulse reshaping due to attenuation of the high frequencies as a result of the decay of the evanescent waves within the gap. Although the pulse advances in time, the pulse propagation is fully causal.

The spatially resolved pulses of Figure 5.3 are measured to have nearly planar phase fronts, expected from the experimental configuration which places the beam waist at the optical tunneling barrier. From Figure 5.5, the range of $k_x$ components tends to be in the range $\pm 50$ $m^{-1}$ compared to $|k| \approx 1\times10^4$ $m^{-1}$, so the $k_z$ component predominates.

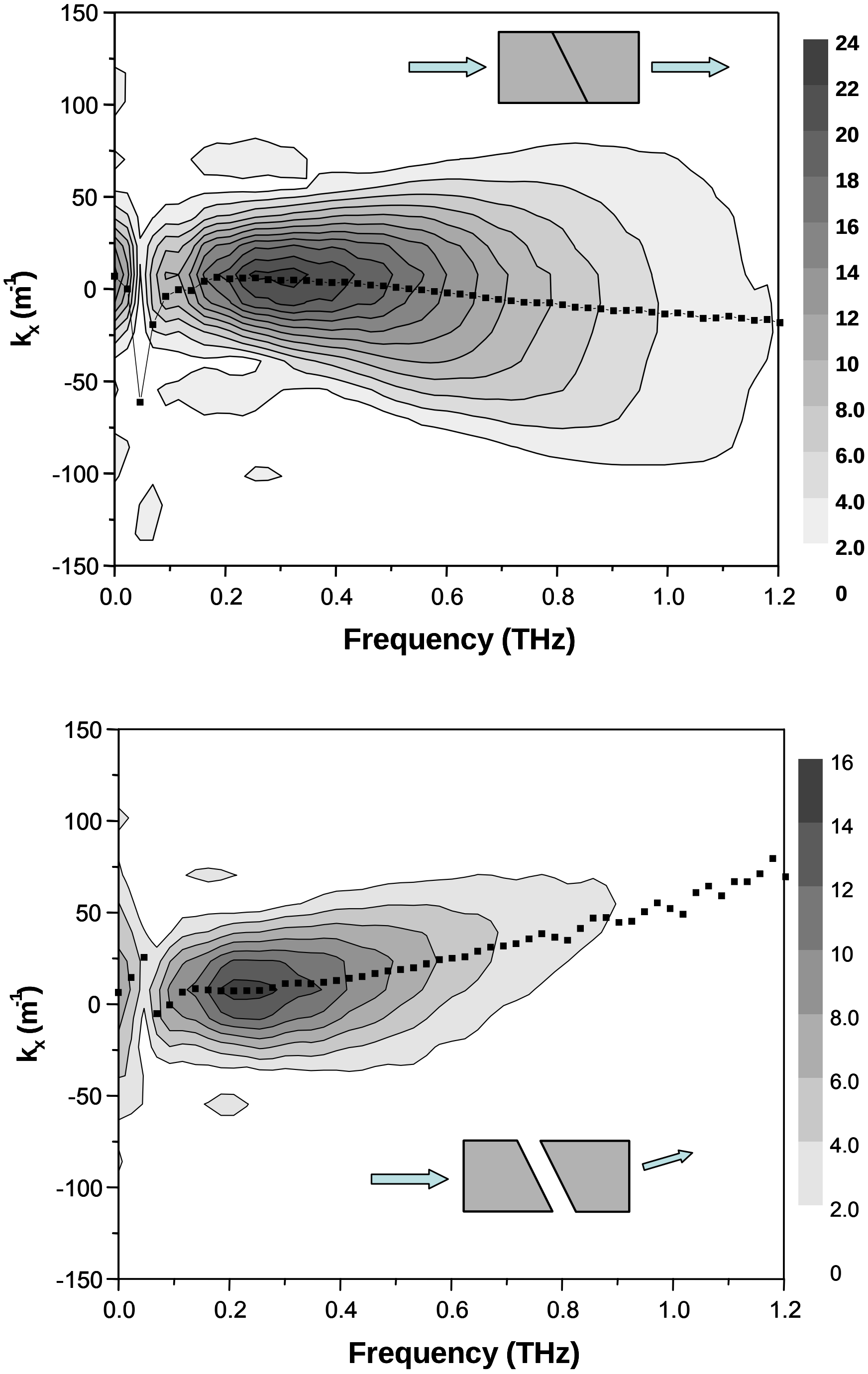

?

**Figure 5.4** The median k vector distribution a) $E_O(k_x,\omega)$ and b) $E_T(k_x,\omega)$ through $\Delta = 1000$ mm gap. The dots indicate expectation values for $<k_x>$ for each frequency and determine the mean propagation direction for each frequency component.

In addition to the previously measured filtering of spectral components of $|E_T(k_x,\omega)|$ along the $\omega$ axis in Figure 5.4, the amplitude spectrum also is reshaped, or filtered, along the $k_x$ axis. The expectation value for the $\langle k_x \rangle$ from Equation 5.4 components at a given frequency shift with the introduction of the FTIR tunneling barrier.

$$\langle k_x(\omega) \rangle = \frac{\int E(k_x,\omega) k_x E^*(k_x,\omega) dk_x}{\int E(k_x,\omega) E^*(k_x,\omega) dk_x} \qquad 5.4$$

This is shown in Figure 5.4 by the dots following the relative maximum for each sampled frequency. Physically this results from the rapid increase of the amplitude attenuation length ($\delta_z$ of Figure 3.5) as the incident plane waves approach the critical angle.

The shift in mean k vector does not provide a readily accessible physical picture of the filtering that results from traversing the FTIR barrier. Expressing $|E(k_x,\omega)|$ in terms of propagation angle $\theta \cong k_x nc/\omega$, yields $|E(\phi,\omega)|$ as shown in Figure 5.5. The relative angle of each plane wave component with respect to the z axis is[62]: $\theta = \arctan(k_x/k_z)$, where $k_z$ is determined by $k_z^2 = k^2 - k_x^2$. In this case $\theta << 1$, so $\theta \cong k_x/k_z \cong k_x/k$. For the data shown in Figure 5.5, negative values of $k_x$ correspond to an increase in the incidence angle on the barrier. This wave vector filtering results in a change in propagation direction for the overall pulse as observed previously at optical frequencies.[20] The filtering of the plane wave components of the incident pulse by the tunneling barrier, observed as wave vector and spectral narrowing, is the cause of the strong observed reshaping in both the temporal and spatial profiles.

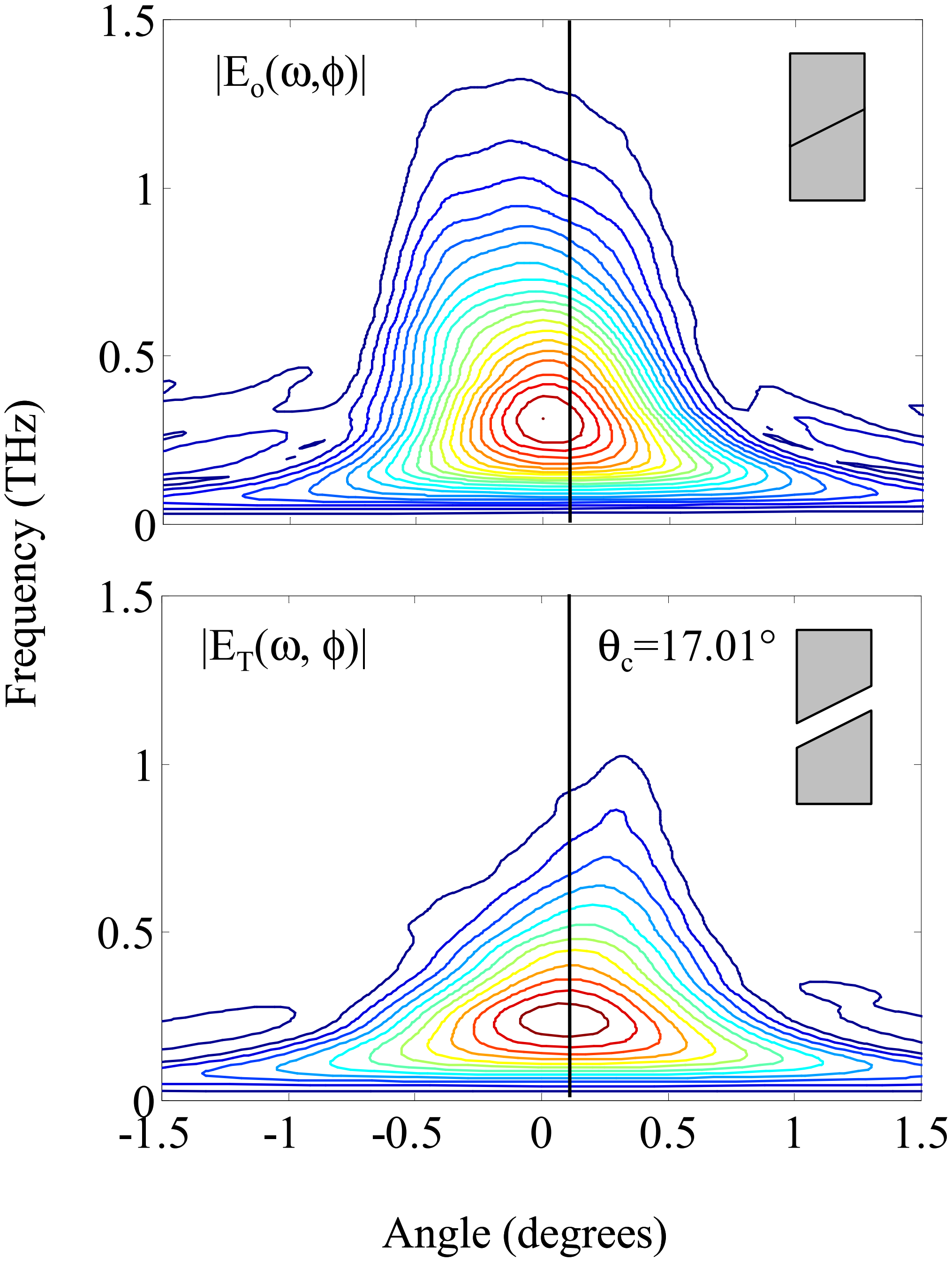

**Figure 5.5** Normalized field intensity distributions expressed in propagation angle and frequency. The vertical line indicates the critical angle, $\theta_c$, in Si for these frequencies. The insets indicates the orientation of the Si wedges.

The resulting angular dependent fields, $|E(\phi,\omega)|$, in Figure 5.5 are centered at the 17.1° incident angle. The positive angles interact with the tunneling barrier closer to normal incidence and the negative angles more obliquely. The reference spectrum $|E_O(\phi,\omega)|$ exhibits a nearly frequency independent angular spread confined to the ± 0.5° region and is a characteristic of the beam waist, $w_{o2}$ of Figure 4.11. The transmitted spectrum shows a strong reshaping for those components that strike the FTIR barrier at angles greater than the critical angle as expected.

Since the pulse entering the system is not identical to the pulse exiting, it is incorrect to directly determine the group velocity by measuring the difference in arrival times and locations of the reference and tunneling pulses.[63] Thus to describe the pulse propagation through the optical tunneling system the linear dispersion theory outlined in Chapter 3 is extended to include and define the system by a complex transfer function $H(k_x,\omega)$:

$$\frac{E_F(k_x,\omega)}{E_o(k_x,\omega)} = H(k_x,\omega) = \left|H(k_x,\omega)\right| e^{i\phi(k_x,\omega)} \qquad 5.5$$

with $E_o(k_x,\omega)$ and $E_F(k_x,\omega)$ the pulses measured with $\Delta = 0$ and $\Delta = 1000$ μm.

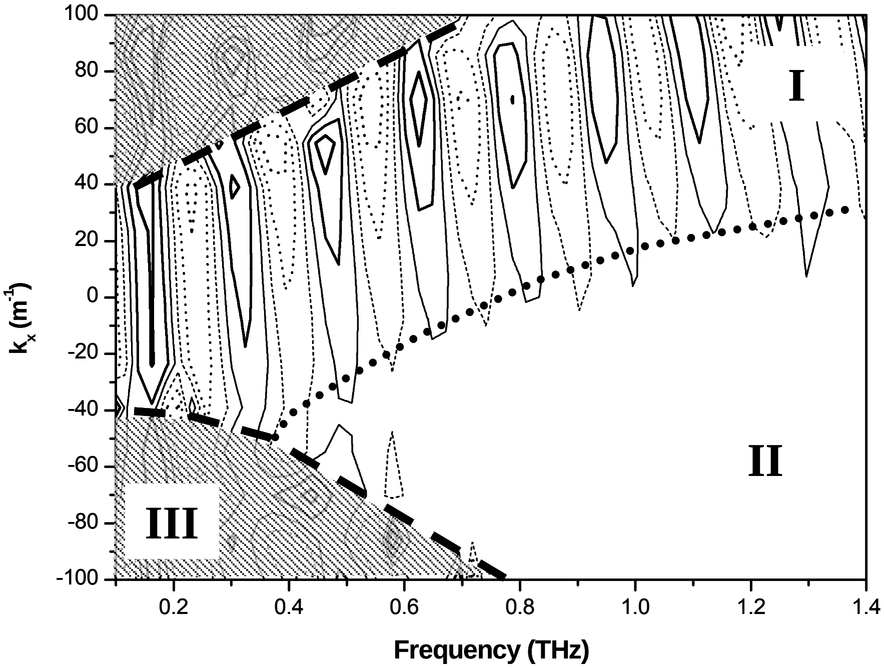

**Figure 5.6** The real components of the k vector transfer function. Note different regimes **I** Thin barrier/sub critical **II** Thick barrier limit. **III** Noise region due to low reference signal.

The real part of the complex transfer function, $H(k_x,\omega)$, is shown in Figure 5.6 and shows three distinct regimes: low signal limit, thick barrier limit and thin barrier limit. The area of least interest, shaded in Figure 5.6, is the region III where the denominator term in Equation 5.5, $E_O(k_x,\omega)$, has near zero amplitude making experimental determination of the transfer function impossible. The lower region II in Figure 5.6 is the thick barrier limit, where the transfer function has near zero value. In the thick barrier limit, $\Delta \gg \delta_z(k_x,\omega)$, the transmitted amplitude is strongly attenuated, and the transfer function is dominated by the exponentially decreasing amplitude, |H| << 1. The upper region I of Figure 5.6 is the thin barrier limit, where $\Delta \ll \delta_z(k_x,\omega)$, so the amplitude attenuation is small and $|H| \cong 1$. Thus the transfer function is dominated by the phase term, $e^{i\phi(\omega,kx)}$. The sinusoidal behavior in region I is expected for the real component for a phase dominated response. As a result of the strong amplitude attenuation in the thick barrier limit, the pulse measured on the far side of the optical barrier is filtered in both frequency and k vector such that the plane wave components in the thin barrier limit are preferentially transmitted. The dotted line in Figure 5.6 indicating boundary between the thick and thin barrier regions is a guide to the eye.

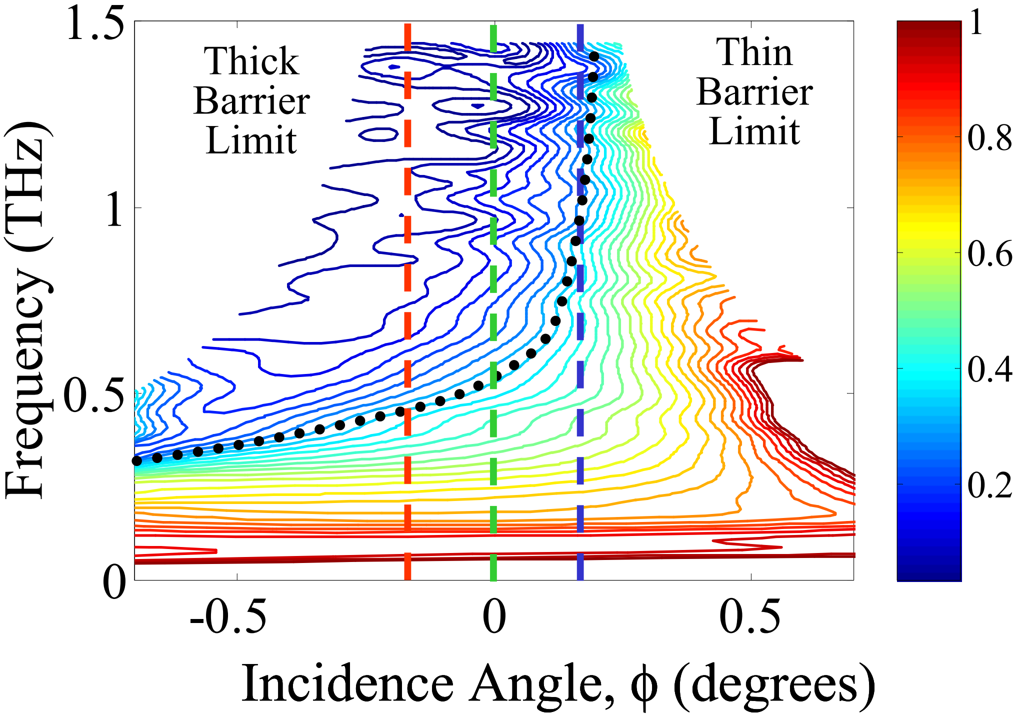

**Figure 5.7** Magnitude of the angular dependent transfer function, |H(ϕ,ω)|. The vertical lines are for ϕ = ± 0.15° and 0°.

Expressing the transfer function in terms of propagation direction yields Figure 5.7 from the ratio of the reference and transmitted angular field distributions of Figure 5.5. The two regions, thick and think barriers judging from the wavelength-gap proportionality, are visible. The dotted line between the regions in Figure 5.7 is a guide for the eye, but the actual demarcation from thick to thin regions is a gradual process.

### 5.4.1 Tunneling time analysis

For a single plane wave component in the x-z plane, A(x,z,t), a fixed frequency, $\omega_o$, and fixed propagation direction $\vec{k}$

$$A(x,z,t) = E_O e^{i(\omega t - k_z z - k_x x)} = E_O e^{i\Phi_O} \tag{5.6}$$

For the transfer function due to the tunneling gap

$$H(\omega,k) = \frac{E_T e^{i\Phi_T}}{E_O e^{i\Phi_O}} = \frac{E_T}{E_O} e^{i(\Phi_T - \Phi_O)} \tag{5.7}$$

where

$$\Phi = \Phi_T - \Phi_O = \omega \vartriangle t - k_z \vartriangle z - k_x \vartriangle x \tag{5.8}$$

A linear relationship (applying conservation of momentum) is assumed, so only amplitude and phase change, not in the direction of propagation of the given plane wave. Considering the phase change

$$\left.\frac{\partial\Phi}{\partial\omega}\right|_{k_x} = \vartriangle t\left(=\tau_\phi\right); \left.\frac{\partial\Phi}{\partial k_x}\right|_{\omega} = \vartriangle x\left(=D\right) \tag{5.9}$$

D is the distance in Figure 5.1 Since the transfer function contains a complete description of pulse propagation through the wedge-gap system as a whole, measurement of the complex transfer function permits a direct determination of the optical tunneling time for each plane wave component. Balcou and Dutriaux[20]indirectly determined the tunneling time by measuring the beam displacement due to the GH shift (*d* in Figure 5.2) and the angular deviation of the transmitted beam due to k vector filtering, or preferential transmission of those plane wave components near or below the critical angle.

The phase time calculated in [20] is shown in Equation 5.10. Note that the expression in the reference[20] as published is incorrect, requiring the exponent of the bracketed argument to be –1.

$$\tau_{\phi} = \left( \frac{c}{n \sin \theta_i} \right)^{-1} D \qquad 5.10$$

This yields a phase time $\tau_\phi = 9.4$ ps for D = 2.8 mm. If one accounts for the phase delay of the tunneling pulse due to the translation of the input face, an additional 8 ps for 1 mm of Si, the pulse time difference that was measured would be 9.6 ps just by following the peaks. However, this result must be taken lightly as it assumes the gap is large with respect to the wavelength and the beam consists of a single frequency. Neither case is true for THz propagation through a 1 mm FTIR barrier.

A complex traversal time, $\tau_c = \tau_\phi + i\tau_L$ is defined for propagation of the THz pulse through the wedge/gap system.[20] The complex traversal time is given by the phase time $\tau_\phi$ (also called the net group delay) and a loss time, $\tau_L$. The phase time corresponds to the group velocity, while the interpretation of the loss time is the time shift due to the pulse reshaping.

$$\tau_\phi = \frac{\partial \phi}{\partial \omega}; \quad \tau_L = -\frac{\partial \ln \left| H(k_x, \omega) \right|}{\partial \omega} \qquad 5.11$$

The amplitudes and phase relationships of $H(\phi,\omega)$ as a function of frequency for three values of $\phi$, corresponding to the dashed lines in Figure 5.7, are shown in Figure 5.8. The magnitude of the measured transfer function falls exponentially with increasing frequency and depends strongly on $\phi$. The slopes directly yield loss times of $\tau_L$ = 3.4 ps, 2.4 ps, and 1.4 ps for $\phi = -0.15°$, 0°, and + 0.15° respectively. $H(\omega)$ shows a linear phase shift between the signal and reference pulses, Figure 5.8, with negative slope corresponding to a shift forward in time, as observed in Figure 5.3. The slopes give the phase times of the system, $\tau_\Phi$ = -1.25, -1.18, -1.06 ± 0.15 ps for $\phi$ = -0.15°, 0°, and +0.15°. The phase times are on the same order as the measured peak shift of -1.79 ps. These loss and phase times are analogous to those measured previously by measuring beam angle divergence with CW optical frequencies,[20] but are determined directly from phase coherent data over a broad spectral range. For the value of $\Delta$ = 1000 μm and frequency spectrum measured here, we do not observe saturation of the phase times.[20]

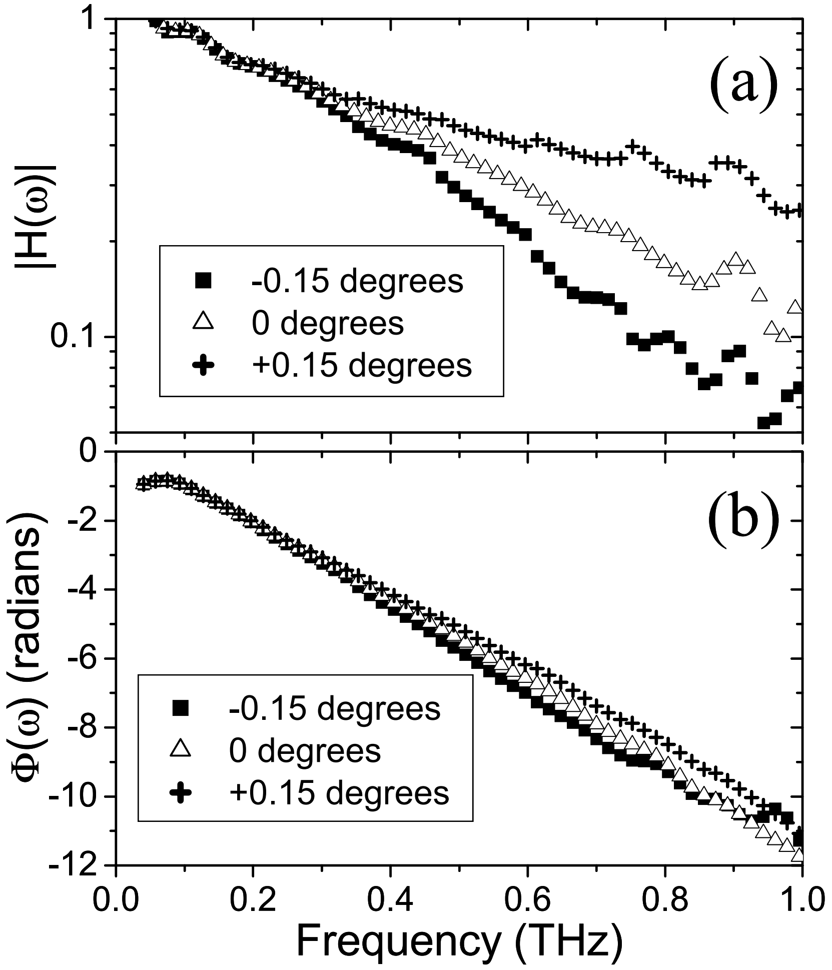

**Figure 5.8** (a) Semilog plot of |H(ϕ,ω)|, (b) phase, Φ(ϕ,ω) for ϕ = –0.15°, 0°, +0.15°.

Treatment of pulse propagation in optical tunneling must include the entire system of silicon wedges (n = 3.42) plus optical gap (n = 1) since the effects of the gap cannot be isolated without assuming a specific path as shown in Chapter 3. When considering the *Δt* = –1.79 ps time shift between the reference (Δ = 0 μm) and tunneling (Δ = 1000 μm) THz pulse peaks in figure 1(c) and the measured phase times, it is vital to recognize that the paths are not the same for the reference and tunneling pulses shown in Figure 5.3. The –1.79 ps time delay between pulse centers does not consider the x translation of the beam. A simple time domain measurement is misleading since pulses are spatially localized, unlike plane waves. The phase shift is determined by the sum of the path length through the entrance wedge (independent of Δ), the time spent in the gap (dwell time), and the path through the exit wedge, z(x); the latter two of which are dependent upon the x spatial shift of each plane wave component. The observed spatial shift of the THz pulse in the +x direction thus is responsible for the observed discrepancy between phase time and time measured with peaks or centroids. This lateral shift of the beam explains why the pulse seemingly travels superluminally: *it travels through less high index material.* The nearly constant phase times measured can qualitatively be explained since the x shift in the gap and resulting path length change in the exit wedge result from the observed Goos-Hänchen shift. The GH shift, *d*, is proportional to wavelength[41], hence each plane wave component will accrue a constant phase shift along the gap, as k is inversely proportional to wavelength.

### 5.4.2 Numerical Treatment

Direct experimental observation of the pulse undergoing FTIR has not been performed as any probe of the evanescent field would perturb the process of transiting a gap. A finite difference time domain (**FDTD**) analysis of a short pulse bounded in space undergoing FTIR can provide deeper physical insight into the tunneling process. FDTD applied to electromagnetic propagation essentially solves Maxwell's equations at a series of finely spaced (sub-wavelength) points where the interaction of the electric and magnetic fields in adjoining cells determine the subsequent temporal behavior of the fields over the computational region.[64] To this end, numerical simulations approximating the experimental conditions were performed. As of this writing, FDTD analysis has not been performed to address pulse propagation through a simple FTIR process, though results for evanescent wave investigations on photonic bandgap structures[65] and for a cursory CW demonstration[66] have been published.

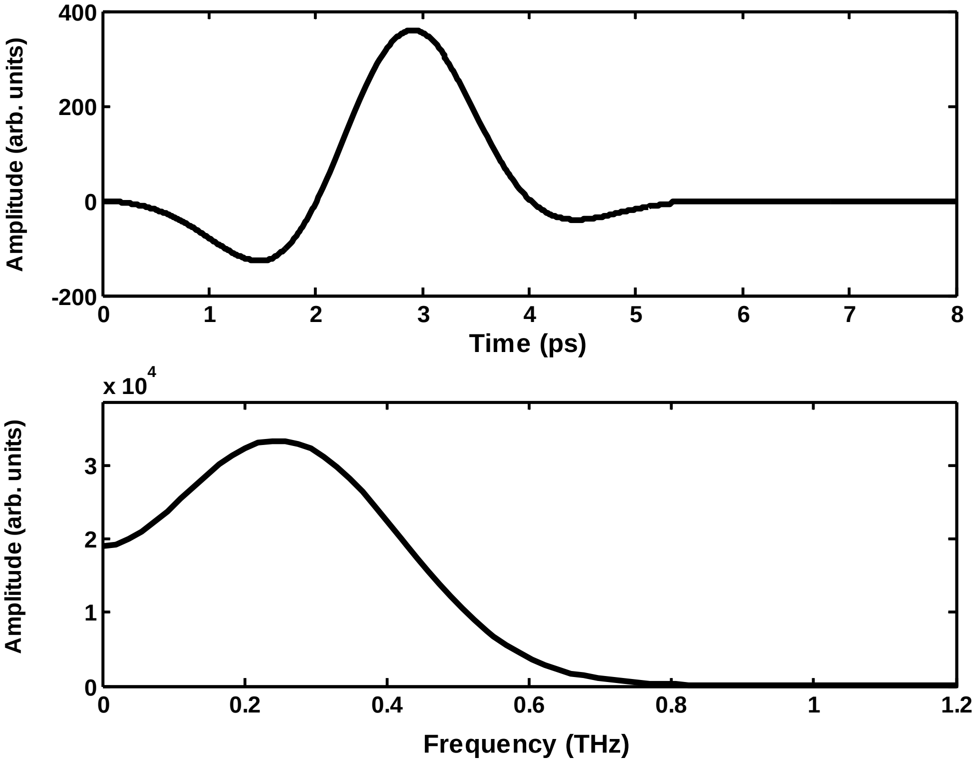

**Figure 5.9** Simulated pulse temporal waveform and spectral response for FDTD.

The FDTD treatment utilized simple second order Yee's algorithm in two dimensions with Berenger PML regions at the boundary of the space.[67] The center frequency of the pulse was taken as $f_o = 0.25$ THz, which is the peak frequency response of the experimental system using the exposed 10-50-10 receiver. This yields a free space center wavelength $\lambda_o = 1.2$ mm. The source determines the actual spatial grid size ($\delta x$), because a near single cycle THz pulse has an associated broad bandwidth and the spatial steps $\delta x$ must be significantly smaller than the wavelength of the propagating field. If the source is modeled as shown in Figure 5.9, as a sine function operating at $f_o$ under a sub wavelength Gaussian envelope, the maximum frequency will be approximately $f_{max} = 0.8$ THz. This arbitrary choice of maximum frequency includes the high frequency tail. The reference pulse from the laboratory experiment as seen in Figure 5.4 had frequency components out to 1.2 THz, so the simulated pulsewidth is somewhat broadened to reduce computational overhead. The corresponding free space wavelength for $f_{max} = 0.8$ THz would be $\lambda_{max} = 0.375$ mm. However wavelength scales inversely with the index and the pulse will be generated in high index Si, so the actual $\lambda'_{max} = \lambda_{max}/n = 0.110$ mm with n = 3.42, which in turn would require $dx = \lambda'_{max}/10 = 10$ μm. The calculations presented here chose $\delta x = \lambda_o/150 = 8$ μm to prevent numerically induced dispersion in the propagating pulse form. The large zero frequency component visible in the spectrum of the pulse in Figure 5.9 is due to the approximation of the THz waveform. The resulting time step to ensure stability of the solutions is then required to be $\delta t = \delta x/2c = 13.3$ fs where c is the speed of light in free space.[64]

The incident pulse was bounded by a Gaussian envelope along the x dimension with a radius of 2.4 mm and a planar phase front, in approximation to the reference pulse characteristics measured in Figure 5.3. The MATLAB code for the numerical simulations is relegated to Appendix 9.4.

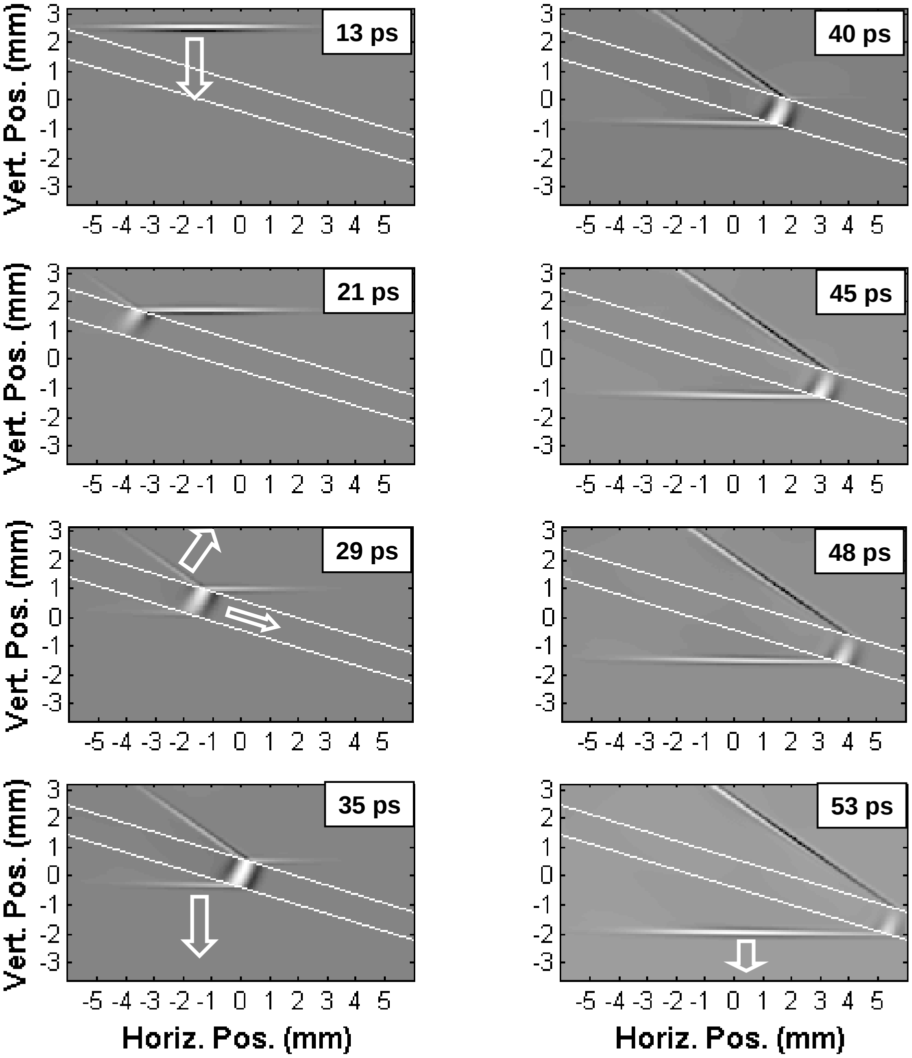

**Figure 5.10** Sequence of images for gap interaction beyond critical angle (17.1°). The white lines represent the edges of the gap $\Delta = 1000\ \mu$m. The white arrows indicate direction of propagation.

### 5.4.3 Time domain observations of FTIR

Figure 5.10 displays a sequence of images for the spatial distribution of the electric field of a THz pulse interacting with an optical tunneling barrier. The fields are the x-component in the plane of incidence, which matches the polarization (P) of the laboratory experiment. Though not shown, the numeric simulation returned similar pulse propagation behavior for S polarization fields. The pulses shown in Figure 5.10 were generated in a 900 × 1500 grid with an 8000 step time loop for the full simulation.

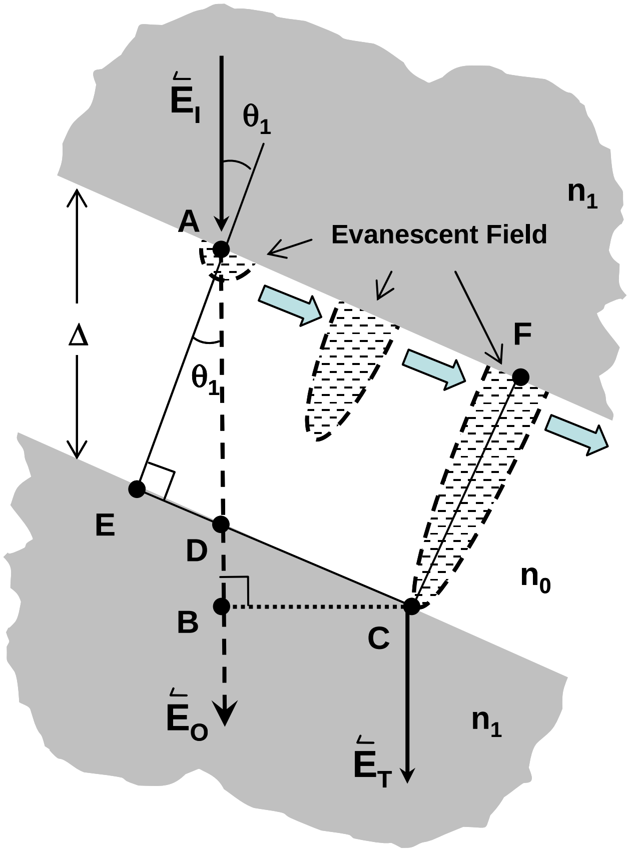

**Figure 5.11** Schematic of evanescent interaction with gap oriented to reflect the simulation geometry. The hashed areas represent the evanescent surface wave as it propagates in the direction of the block arrows along the interface. The field undergoes a lateral shift from the propagation direction of the incident field (segment AF). No path is assumed, but a "dwell time" is measured in the FDTD simulation.

As long as the pulse is incident on the barrier, the evanescent field remains in the gap, propagating as a surface wave as expected.[19] The surface wave couples into the second medium in the case of FTIR. A time is required for the field to build up in the gap, typically referred to as a dwell time.[38,68] The dwell time coupled with the shift in horizontal position results in a lateral shift of the beam after the optical tunneling barrier. An angular shift is evident in the transmitted pulse when looking at the pulse front and is the result of the preferential k-space filtering process of the previous sections. The surface wave continues to propagate after the incident pulse has reflected away, coupling through to the exit face of the optical barrier (48 and 53 ps windows of Figure 5.10) into the transmitted pulse. The k vectors contributing to this apparent effect are those that are closer to normal incidence on the boundary and primarily propagate in the thin barrier region observed in Figure 5.6 and Figure 5.7.

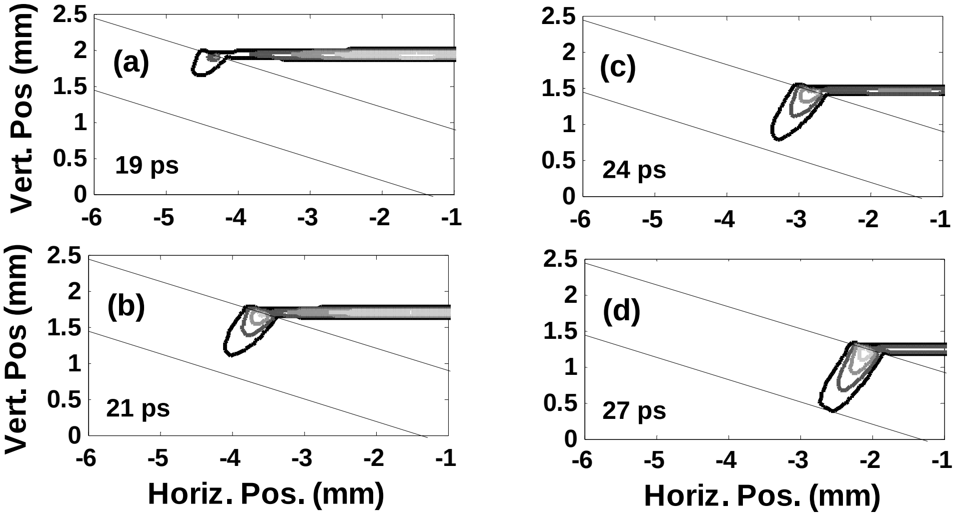

**Figure 5.12** Close up of simulated evanescent field in gap for sequential times to illustrate dwell time estimate. Only the positive field values are shown. In (a) at 19 ps the incident pulse has just created a evanescent field of a specified amplitude across the top gap face. The incident pulse propagates and the driving point also shifts as seen in (b) and (c) while the evanescent field extends further into the gap. In (d) the evanescent field has reached the bottom gap face. The amplitudes are determined by the spatial distribution E(x,y,t) of the incident pulse.

By observing the time steps required for the evanescent field to couple across the gap as illustrated in Figure 5.12, the dwell time can be estimated for those conditions. This is not an instantaneous transit normal to the interface. With an incident pulse of 5 mm width, 0.09° beyond critical angle, center frequency at 0.25 THz and a gap $\Delta = 1000$ μm, the dwell time is 10.9 ps. The dwell time is taken as the difference in arrival times for the $e^{-1}$ level of the evanescent field from the top gap face to the bottom gap face and is shown in Figure 5.13 for the left edge of the propagating pulse as a function of time and horizontal position. The top gap face is line segment AF and the bottom gap face is line segment DC in Figure 5.11.

During this dwell time the surface wave advances 2.6 mm along the Si-air interface, which leads to a change in propagation path. If $\Delta = 0$ μm as for the reference pulse, the phase accumulated from a simple geometrical optics view point would be 20.5 ps due to the gap distance (line segment AD with index $n_1$) plus the additional high index due to path changes (line segment DB with index $n_1$.) This gives rise to a measured difference time in the simulation for transiting the gap between the reference and tunneled pulse of $\Delta t = -9.6$ ps ($\Delta t = -1.55$ ps if the additional phase shift due to the $\gamma$ term resulting from the shift of the entrance wedge of Equation 3.10 is included.)

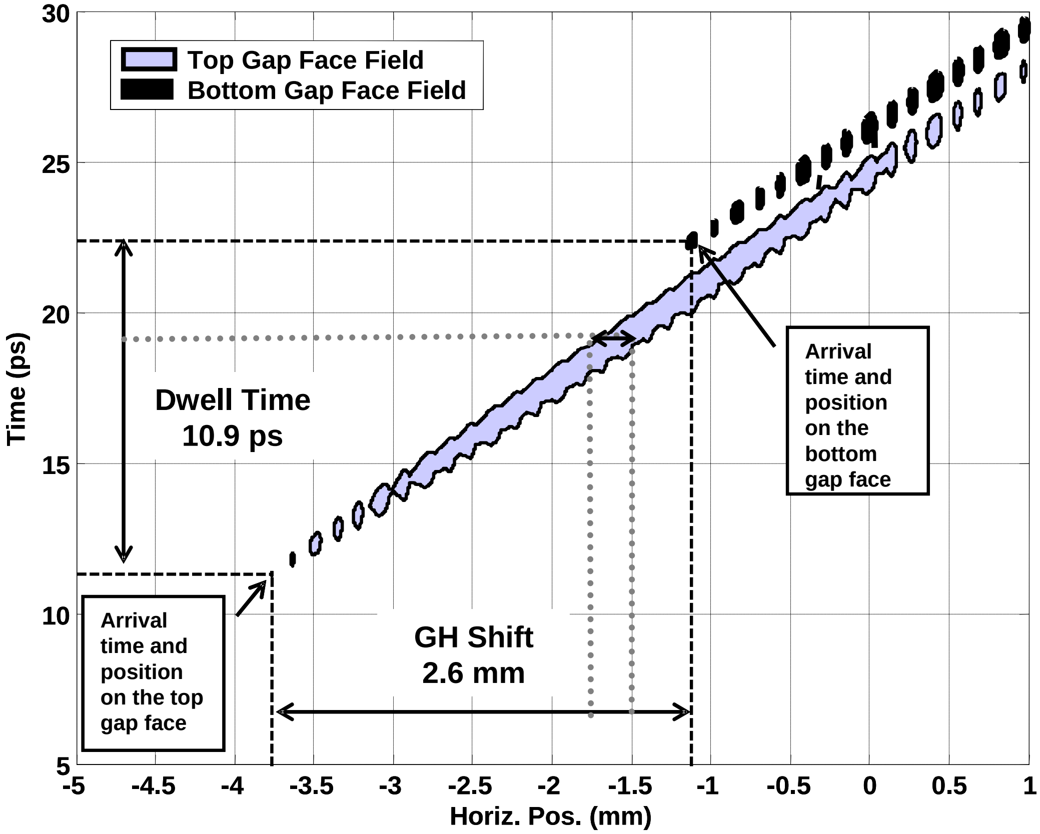

**Figure 5.13** Arrival time and position of 1/e level of evanescent field in the optical tunneling gap determined from the FDTD simulation for Δ = 1000 μm. The areas are for the top gap face (white) and the bottom gap face (black) and represent the extent of the 1/e level of the evanescent field at the surface for a given time. For example, in Figure 5.12(a) at 19 ps shown as dots, the evanescent field extends Δx = 0.2 mm along the top gap face, but does not appear on the bottom gap face. The gap position is shown along the x axis of Figure 5.11 following the surface wave propagation. The dwell time is the difference in arrival times for the 1/e level from the top gap face to the bottom gap face. The GH shift is the difference in arrival positions for the 1/e level from the top gap face to the bottom gap face.

Despite claims to the contrary, [51] Maxwell's equations do reproduce the features observed in experiment.

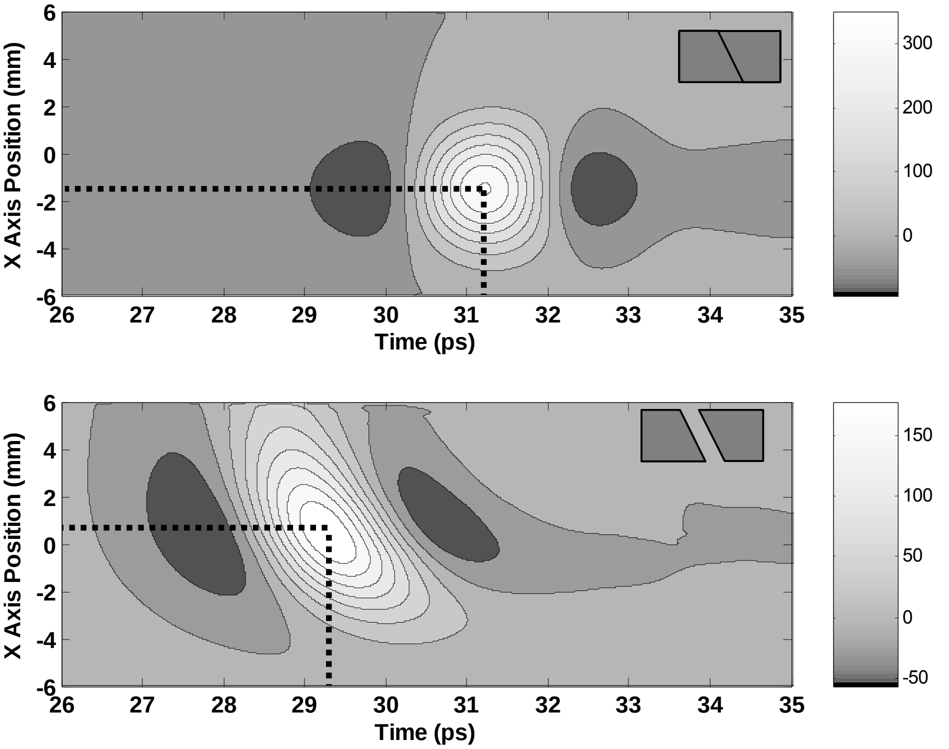

**Figure 5.14** Contour plots showing results from the simulation of experiment measured at a plane after the FTIR gap with $E_{Osim}(x_x,t)$ with $\Delta = 0$ μm (top) and $E_{Tsim}(x_x,t)$ $\Delta = 1000$ μm (bottom). The measured distance for the GH shift would be $d = 1.9$ mm and the subsequent time shift $\Delta t = -1.95$ ps

### 5.4.4 Analysis of simulated experiment

The propagating field was measured at a plane a short distance from the FTIR barrier gap as a function of time to simulate the scanning exposed receiver. These temporal measurements of the propagating pulse are shown in Figure 5.14. The pulse transmitted through the gap arrived earlier in time than the reference pulse and had a positive GH shift with respect to the peak of the reference pulse. Both simulations had identical input pulse distributions. The slight distortion near the top edge of the $\Delta = 1000$ μm pulse simulation ($x \approx 6$ mm in Figure 5.14) is due to interaction with the perfectly matched layer at the edge of the computational space.

The simulated peak-to-peak arrival time difference $\Delta t = -1.92$ ps is slightly larger than the measured –1.79 ps from Figure 5.3. The additional phase shift incurred from the movement of the input Si wedge was taken into account (see Chapter 3 Section 3.4) to properly compare the relative arrival times between the reference and tunneled pulses. If this additional phase shift, $\gamma$ of Equation 3.10, due to the conditions of the experiment had not been factored into the comparison, the time difference between the pulses would have been –10 ps, as expected from the dwell time observation and the predicted phase time of Equation 5.10.

The simulated GH shift yielded $d = 1.84$ mm, smaller than the 2.8 mm shift measured in Figure 5.3, though the difference is within the 1 mm step size of the laboratory experiment. The simulated pulse of Figure 5.9 has a frequency independent profile, unlike the laboratory experiment, which detects a frequency dependent beam waist. Likewise the beam is significantly stretched along the + x direction, which may result in overstating the lateral beam shift in the laboratory experiment.

The results of the simulated experiment agree quite well with the laboratory experiment.

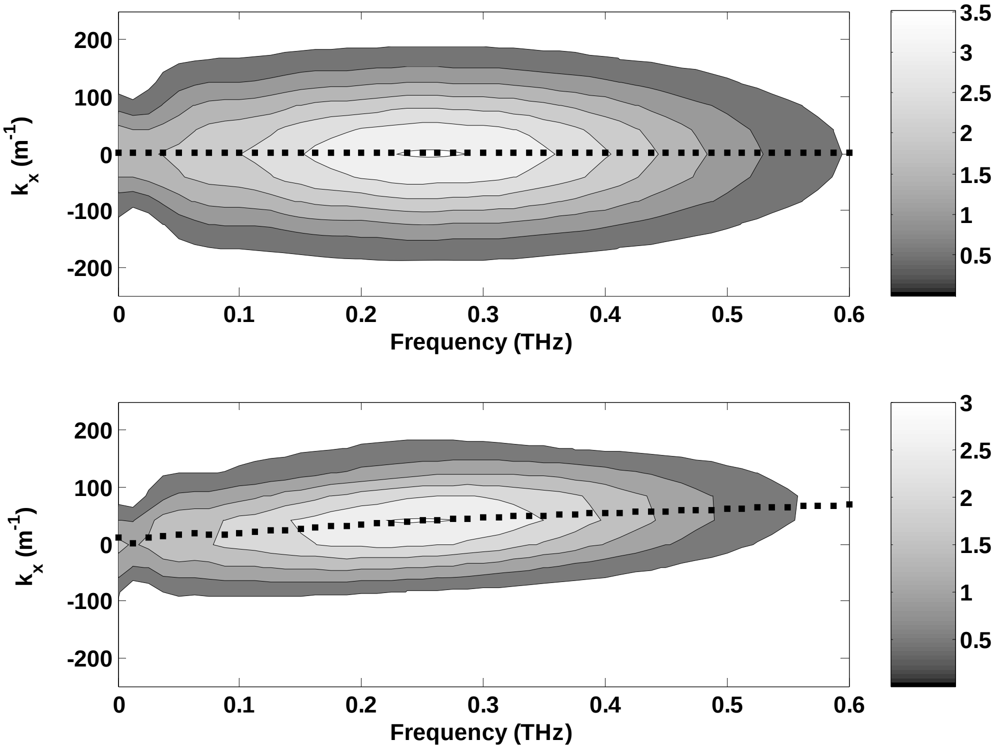

**Figure 5.15** $|E(k_x,\omega)|$ distribution from FDTD simulated pulses for $|E_{Osim}(k_x,\omega)|$ reference (top) and $|E_{Tsim}(k_x,\omega)|$ transmitted through $\Delta = 1000$ mm gap (bottom). $\langle k_x(\omega)\rangle$ is shown in squares. See Figure 5.4 for comparison to laboratory experiment.

Figure 5.15 contains the transformed field magnitudes after undergoing a two dimensional Fourier transform, $E(x,t) \rightarrow E(k_x,\omega)$. This reproduces the behavior of Figure 5.4 for the laboratory experiment. A shift of the $\langle k_x \rangle$ is observed due to the spatial filtering of the FTIR barrier. The spread of $k_x$ is also reduced, expected from the broadening of the pulse along the x-axis in Figure 5.14. The spectral filtering is less evident in the simulation due to the reduced bandwidth of the driving pulse.

The transfer function between the reference $E_{Osim}(k_x,\omega)$ ($\Delta = 0$ μm) and the transmitted $E_{Tsim}(k_x,\omega)$ ($\Delta = 1000$ μm) displays the same behavior as the transfer function generated by the laboratory experiment. Thick and thin barrier regions are visible in Figure 5.16 and qualitatively reproduce the behavior observed in Figure 5.6.

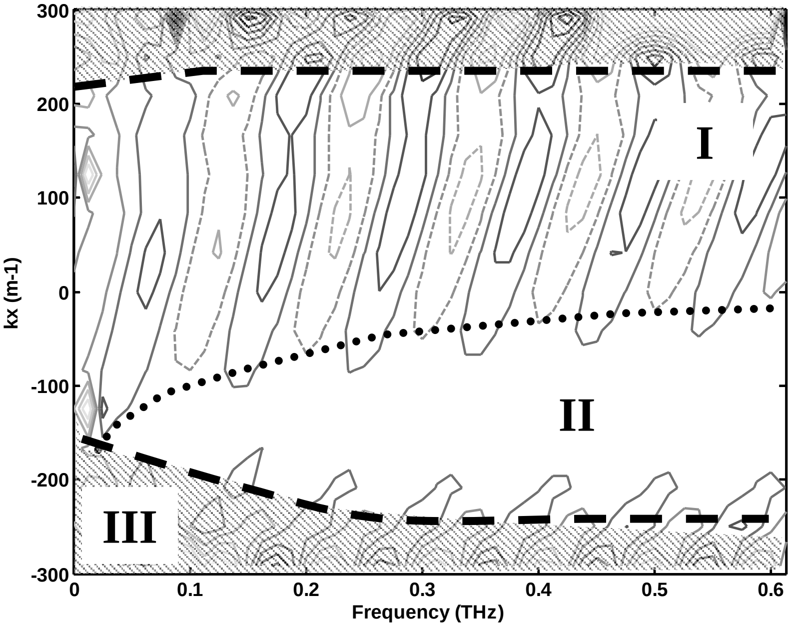

**Figure 5.16** The real components of the k vector transfer function generated from the results of the numeric simulation. Note different regimes I Thin barrier/sub critical II Thick barrier limit. III Noise region due to low reference signal.

The transfer function plotted against angle of propagation for a given plane wave component for the simulated transfer function as shown in Figure 5.17. Again the behavior follows that of the laboratory experiment. In the transformational mapping from $E(k_x,\omega) \rightarrow E(\phi,\omega)$, an interpolation function was performed on the data that introduced some numerical noise into the distribution.

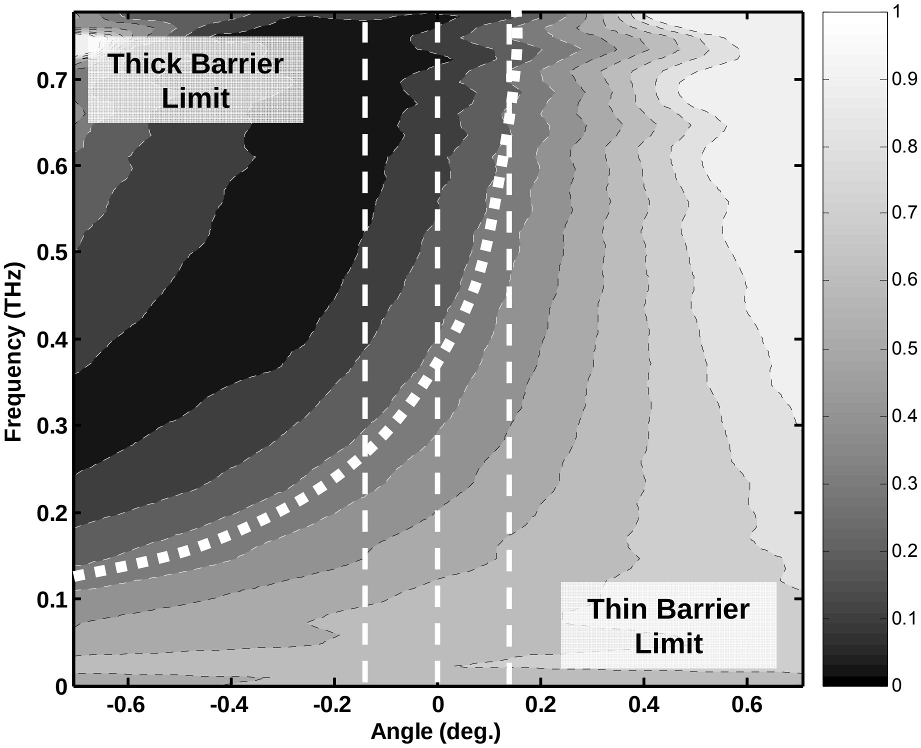

**Figure 5.17** Magnitude of the angular dependent transfer function for the simulated experiment. The dashed vertical lines are for $\phi = \pm 0.15°$ and 0°. The dotted line separates the thick and thin barrier regions.

The amplitudes and phase relationships of $H(\phi,\omega)$ as a function of frequency for three values of $\phi$ are shown in Figure 5.18 and a direct equivalence to those in Figure 5.5,. The magnitude of the simulated transfer function behaves as seen in the laboratory experiment. The slopes directly yield loss times of $\tau_{Lsim}$ = 3.7 ps, 2.6 ps, and 1.4 ps for $\phi$ = -0.15°, 0°, and +0.15° respectively. The slopes of the phase plot of Figure 5.18b) give the phase times of the system, $\tau_{\Phi sim} = -1.6 \pm 0.15$ ps for all three values of $\phi$. The lack of jitter in the phase relationships from cell to cell in the simulation results in the single value for the three sample angles, whereas the laboratory experiment demonstrated a slight difference between each. The phase times are on the same order as the measured peak shift of -1.92 ps.

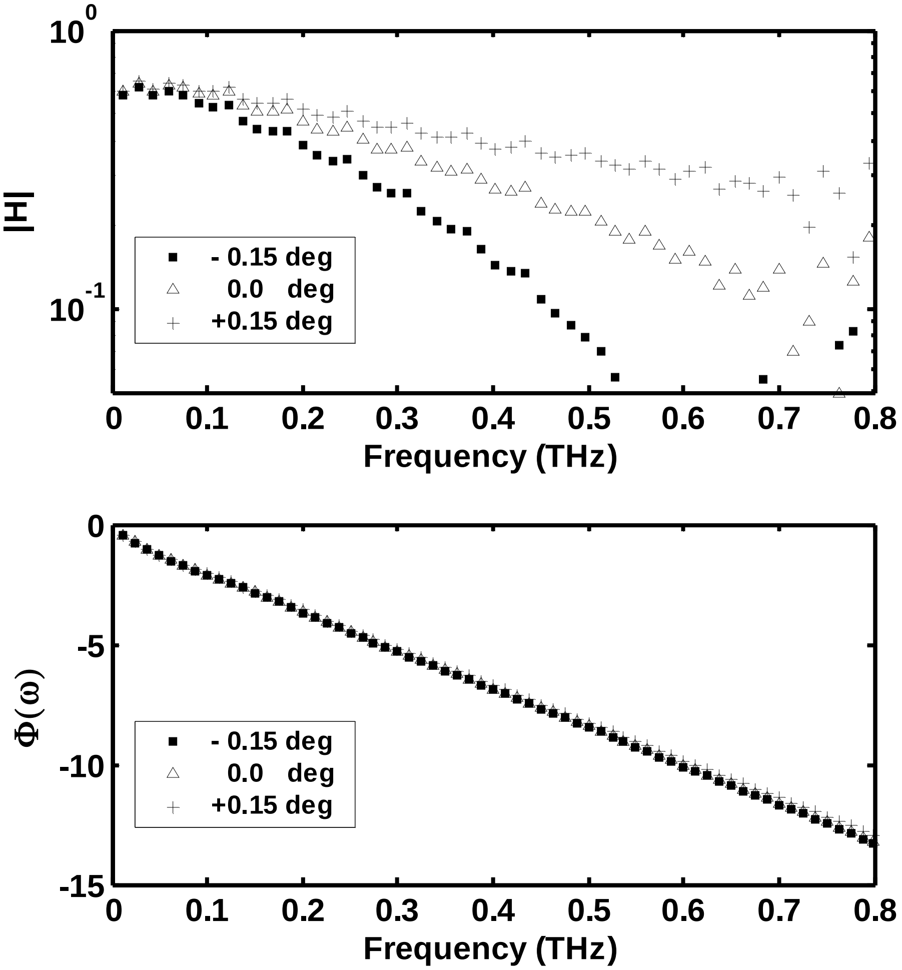

**Figure 5.18** (a) Semilog plot of $|H(\phi,\omega)|$, (b) phase, $\Phi(\phi,\omega)$ for $\phi = -0.15°, 0°, +0.15°$ generated from the simulation results.

The results of the simulations provide results similar to the laboratory experiment observations. This increases the confidence in the observations made within the simulation regarding the evolution of the pulse through the optical barrier. The FDTD treatment can help improve the understanding of the FTIR processes.

| | Laboratory Experiment | | | Simulated Experiment | | |
|---|---|---|---|---|---|---|
| $\Delta t$ (peak-to-peak) | −1.79 ps | | | −1.92 ps | | |
| $d$ (peak-to-peak) | 2.8 mm | | | 1.84 mm | | |
| $\tau_\phi$ (−0.15°, 0.0°, +0.15°) | 1.25 ps | 1.18 ps | 1.06 ps | 1.6 ps | 1.6 ps | 1.6 ps |
| $-\tau_L$ (−0.15°, 0.0°, +0.15°) | 3.4 ps | 2.4 ps | 1.4 ps | 3.7 ps | 2.6 ps | 1.4 ps |

**Table 5.1** Comparison of results for simulation and laboratory experiment for two dimensional tunneling times.

### 5.4.5 Effect of initial waist size on resulting beam profile

A bounded beam is required to observe the GH shift.[41] The bounded beam has an associated k vector spread that is inversely proportional to the radius of the beam ($\Delta k \Delta x \geq 1/2$.)[28] This k vector spread was shown previously to be filtered by the presence of the FTIR barrier with the resulting plane wave components with k vectors closer to the normal of the barrier surface being preferentially transmitted. However, the evanescent field is only present in the gap when the driving field of the pulse is incident on the gap. As reflection is a spatial effect, the interaction time for the incident pulse with the gap is determined by the beam width. A broad beam will have a longer interaction time with the FTIR barrier and allow the evanescent field to interact beyond the dwell time increasing coupling across the gap. The wide beam will consequently have a narrow range of associated k vectors, which in turn will limit the coupling across the gap.

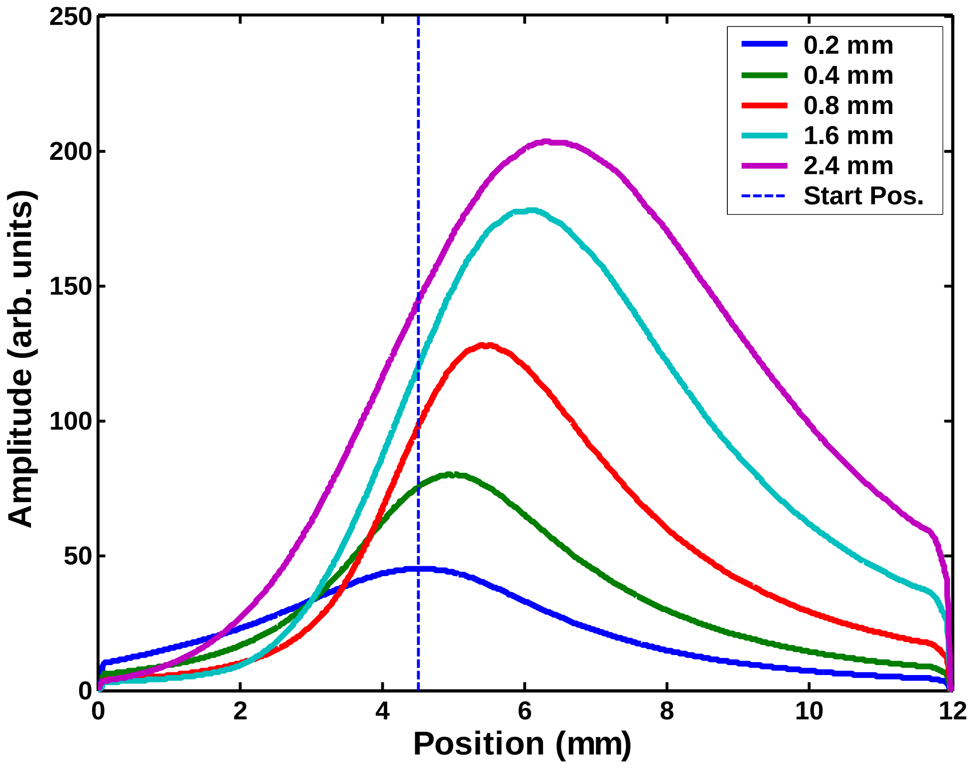

**Figure 5.19** Exit beam profile traces for varying incident beam waists, wo = 0.2, 0.4, 0.8, 1.6, and 2.4 mm. The vertical dashed line corresponds to the incident beam location (x = 4.5 mm). $w_o$ = 2.4 mm corresponds to the measurement and simulation beam widths. The discontinuities in the beam profiles at 0 mm and 12 mm are due to the absorbing boundaries of the simulation. The peak amplitude of each incident pulse is 376.

A range of incident beam widths were modeled in the FDTD simulation of gap interaction to investigate the impact of incident beam waist size on FTIR barrier transversal. The gap width was kept at $\Delta$ = 1000 μm and the temporal duration of the incident test pulse was the same as used in the previous simulations (shown in Figure 5.9.) The initial beam waists were chosen smaller than the 2.4 mm waist due to the confinement of the computational space.

Figure 5.19 shows the resulting beam profile traces. Traces were made of the peak field as the small initial waist pulses (divergent) were distorted in time and profile by the FTIR barrier. The center of mass for the resulting pulses, as a figure of distortion when compared with the peak, was not calculable due to the truncation of the pulse shapes at the wings.

| Initial Beam Waist | Lateral Shift d |
|---|---|
| 0.2 mm | 0.035 mm |
| 0.4 mm | 0.5 mm |
| 0.8 mm | 1.0 mm |
| 1.6 mm | 1.5 mm |
| 2.4 mm | 1.8 mm |

**Table 5.2** Laterals shift of the peak amplitudes for various incident beam waists.

The pulse with $w_o$ = 0.2 mm corresponds to a very tightly focused beam with a correspondingly large range of propagation directions, so it interacts with the tunneling barrier close to normal incidence. The tightest focused beams demonstrated pulse distortion in time as well as position. A strong effect in amplitude transmission and GH shift appears to be due to the width of the pulse and corresponding gap interaction time.

## 5.5 Full beam profile measurements

The assumed cylindrically symmetric THz beam had been measured along the x-t plane through the peak of the field. All effects due to FTIR were assumed to occur in the plane of incidence.

A predicted transverse shift—the Imbert-Fedorov shift[69]—would not likely be observed with linear polarization as it is strongly polarization dependent. The transverse shift $\delta_y$ is expected near critical angle upon total internal reflection as shown in Equation 5.12.[70]

$$\delta_y = \mp \frac{\lambda_o}{\pi n \sin\theta_1 \cos\theta_1} \tag{5.12}$$

Here, $\lambda_o$ is the free space wavelength, $n$ is the index of the medium and the low index medium is assumed to be air, and $\theta_1$ is the incident angle. The transverse shift is zero for linearly polarized fields and is maximized for circular polarization.[56,70] The maximum transverse shift expected for 0.25 THz would be $\delta_y$ = 400 μm with circularly polarized light. With the slight elliptical polarization (28:1 in field measured with wire grid polarizers), a shift may occur for the fraction of the field that is circularly polarized. It must be noted that the magnitude of the shift is below the measurement capability of the system as presented and would likely be obscured by the dominant linearly polarized component of the field even if spatially resolvable. As of this writing, the transverse shift has yet to be directly measured in transmission in part due to a lack of ¼ wave plates for broad band THz pulses to generate circular polarization.

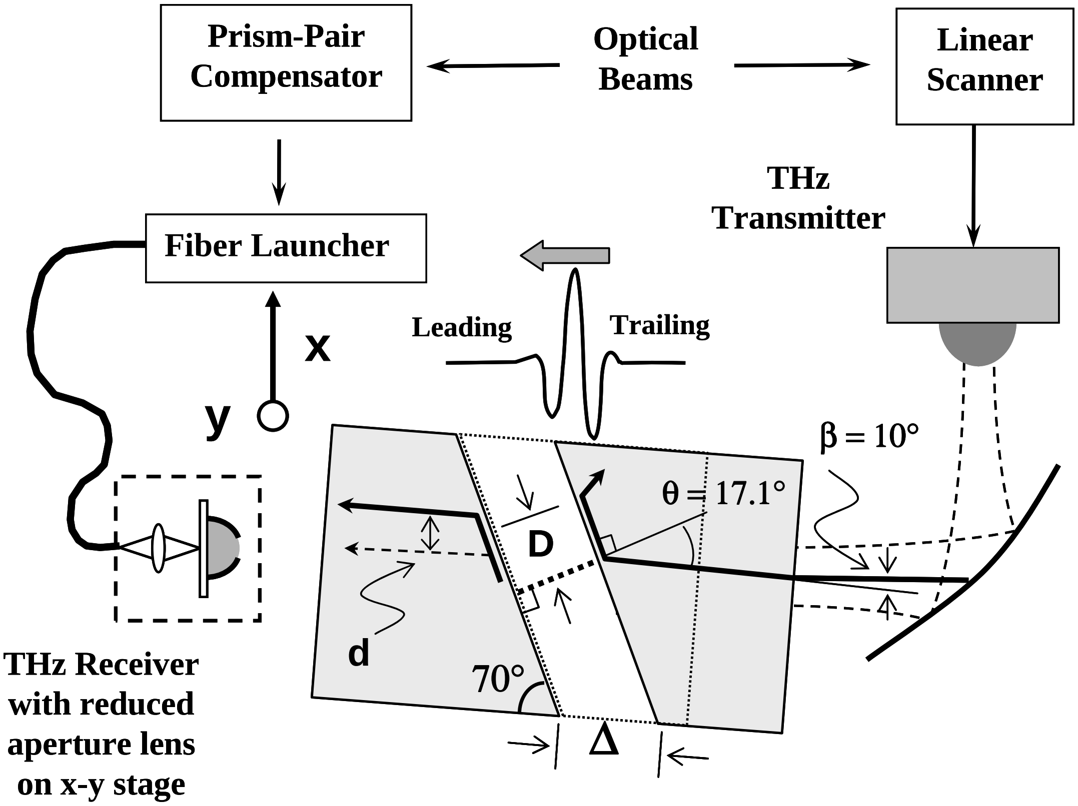

**Figure 5.20** Experimental set up for the full beam profile measurement for FTIR. A reduced aperture lens receiver and x-y raster scanning stage replace the exposed receiver and linear stage of Figure 5.2.

### 5.5.1 Three dimensional profile measurement of FTIR

Measurements were taken with the 1.5 mm reduced aperture receiver as described in Chapter 4 mounted an x-y stepper stage replacing the exposed receiver as shown in Figure 5.20. The reduced aperture receiver was chosen over the exposed receiver in order to increase the signal-to-noise and because time limitations on the data acquisition process precluded dipole-effective-area limited step sizes. The experimental conditions were reproduced with the Si wedge angle and position with respect to the transmitter. The field was sampled in a 25 × 17 grid with a 1.46 × 1.45

mm step for a total area of 38 × 24 mm. Each position measurement was taken at a 28 Hz scanning rate and averaged 64 times.

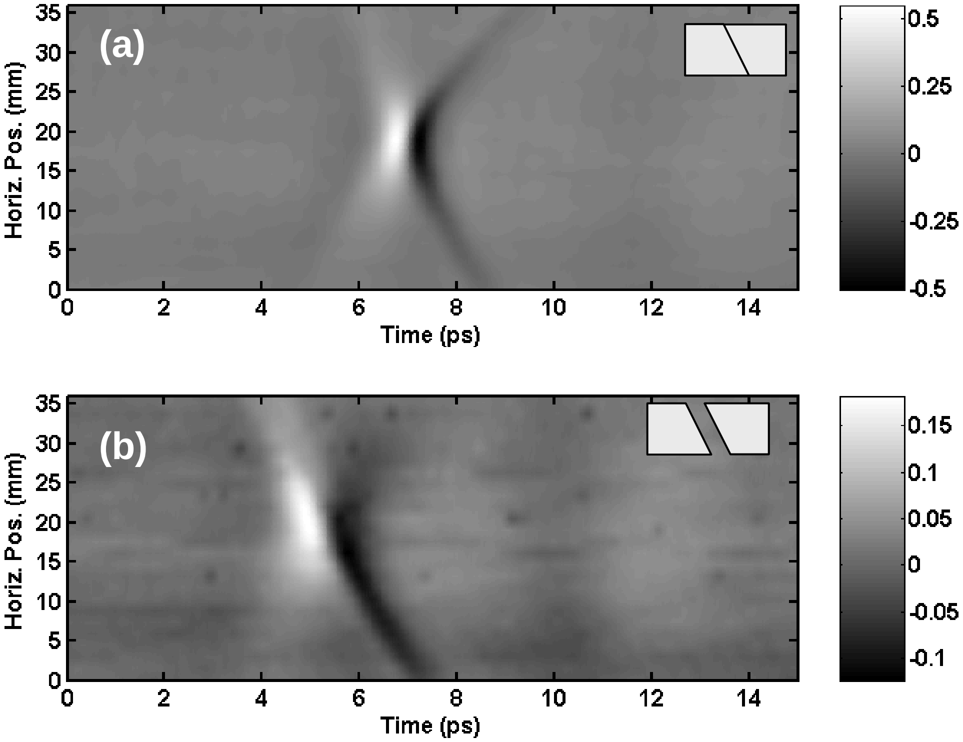

**Figure 5.21** Pulse profile taken from 3 dimensional measurements through peak of the pulse in the x-t plane for (a) $E_O(x,t)$ Δ = 0 μm and (b) $E_T(x,t)$ Δ = 1000 μm. Note the strong angular shift in (b) due to the k-vector filtering of the gap. Inset shows orientation of the Si wedges.

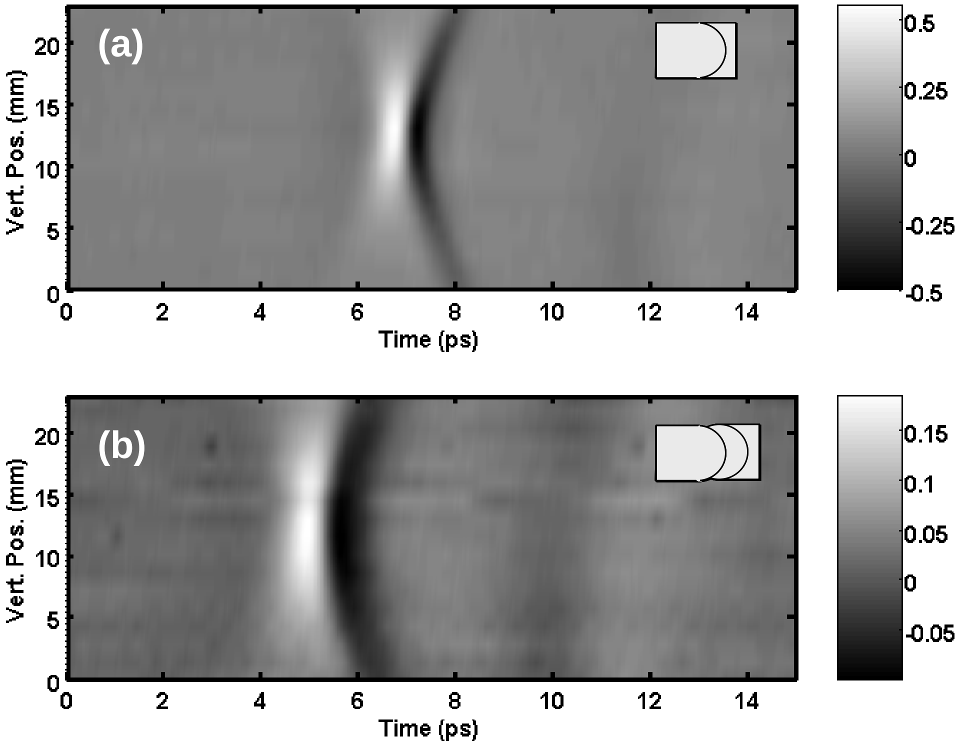

**Figure 5.22** Pulse profile taken from 3 dimensional measurement through peak of the pulse in the y-t plane for (a) $E_O(y,t)$ $\Delta = 0$ μm and (b) $E_T(y,t)$ $\Delta = 1000$ μm. Note that minimal angular shift is observed in (b) due to introduction of the gap. The vertical range is different than the horizontal range of Figure 5.21. The inset shows the orientation of the Si wedges with respect to the beam measurement (rotated 90° about the optical axis with respect to Figure 5.21.)

Figure 5.21 and Figure 5.22 show the field E(x,y,t) as measured in the x-t horizontal plane (in the plane of incidence with the gap) and the y-t vertical plane (orthogonal to the plane of incidence with the gap.)

The horizontal peak-to-peak shift was between 1.5 mm and 3.0 mm, consistent with previous 2-D observations. The beam profile does not have a well defined local maximum identifiable as the peak introducing uncertainty in the horizontal position in the raw data. A higher resolution is needed to make a more accurate comparison. The temporal peak-to-peak shift for both vertical and horizontal axes was comparable $\Delta t_x = -1.83$ ps and $\Delta t_y = -1.79$ ps. A strong angular shift in the pulse front is evident in the plane of incidence in Figure 5.21(b) when compared to Figure 5.22(b).

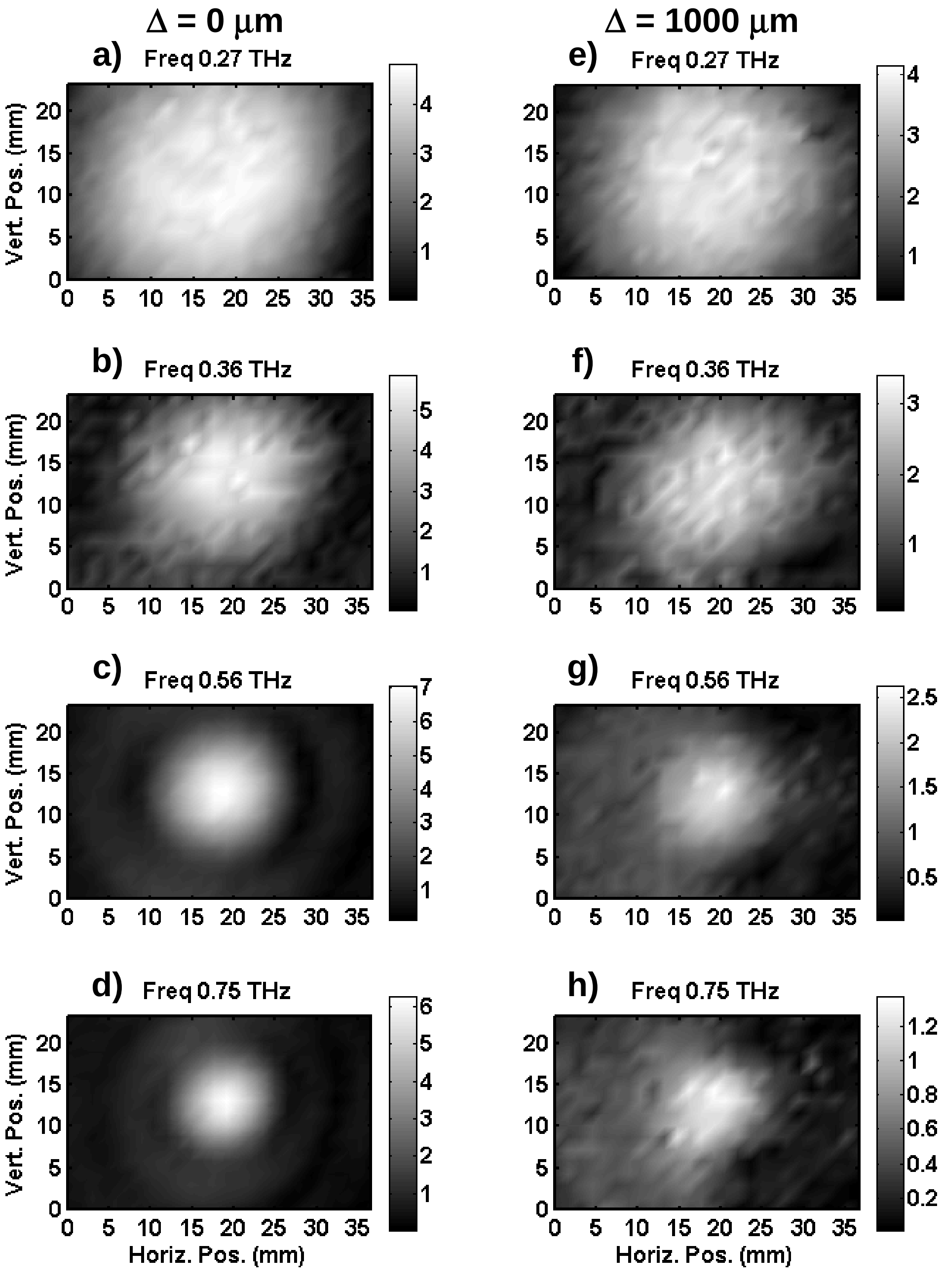

**Figure 5.23** Interpolated beam profiles as a function of frequency for reference and FTIR pulses, $|E_O(x,y,\omega)|$ and $|E_T(x,y,\omega)|$.

The Fourier transformed pulses yielded a spectral distribution over the face of the beam. The frequency dependent behavior on beam radius as seen in Chapter 4 is observed. The introduction of the gap reduces the detected field amplitude linearly with wavelength. The low dynamic range due to discrete sampling results in an averaged signal-to-noise ratio of 15:1 for the reference spectrum and 8:1 for the transmitted spectrum over the range of 0.27 to 0.75 THz.

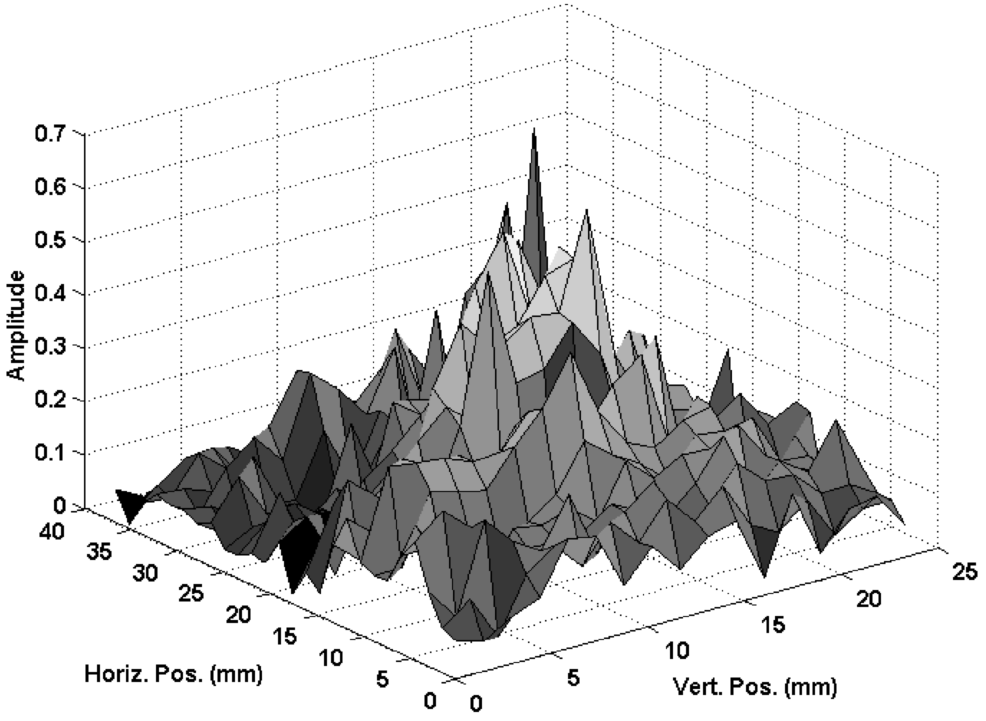

**Figure 5.24** Representative beam profile for 0.75 THz with $\Delta = 1000$ μm without linear interpolation. This is the same profile as shown in Figure 5.23h).

Tracing the peaks of the frequency profiles to compare relative shifts of the beam is complicated by the increased noise of the reduced signal. Figure 5.24 shows a higher frequency profile as generated from the full pulse profile. By fitting a

Gaussian profile $Z_{fit}$ as in Equation 5.13 to the measured profile, the beam position ($x_o$ and $y_o$) and beam radius ($w_x$ and $w_y$) can be extracted as a function of frequency.

$$Z_{fit} = Ae^{-(x-x_o)^2/w_x^2}e^{-(y-y_o)^2/w_y^2} + B \qquad 5.13$$

Here, A is the amplitude and B is the adjusted floor value due to noise. Figure 5.25 shows a representative fitting for 0.56 THz (corresponding to Figure 5.23c) for the reference with Δ = 0 μm.)

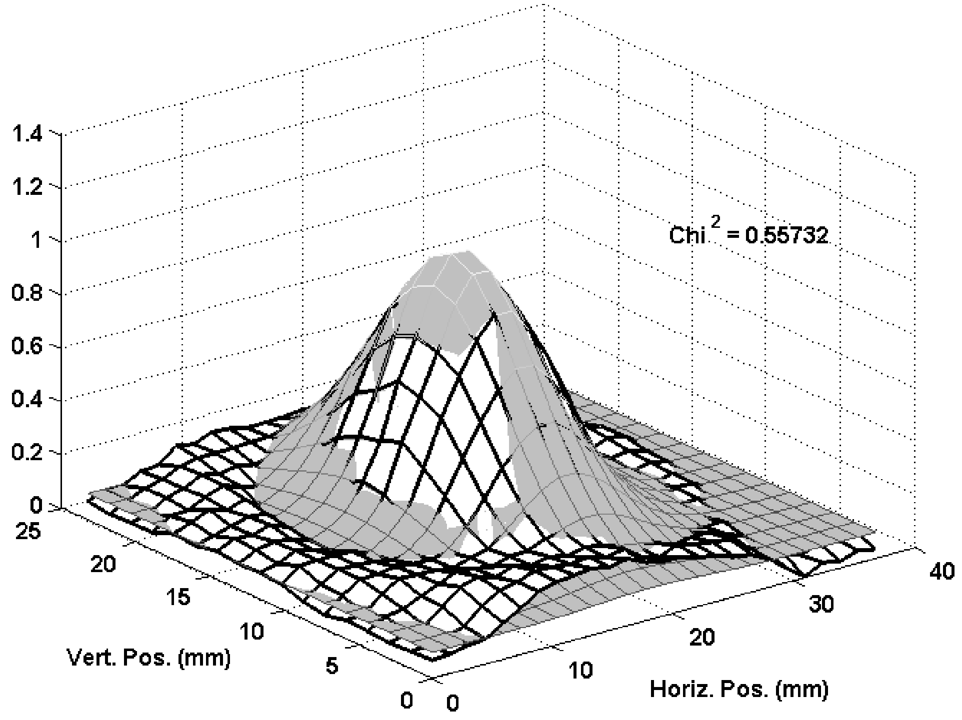

**Figure 5.25** Plot showing a measured beam profile (black and white mesh) with best fit Gaussian (gray mesh) for Δ = 0 μm. The peak position ($x_o$,$y_o$) and beam radius ($w_x$, $w_y$) are allowed to vary in the fitting process. The frequency was fixed at the measured 0.56 THz. Note the additional structure near the baseline of the measured beam profile.

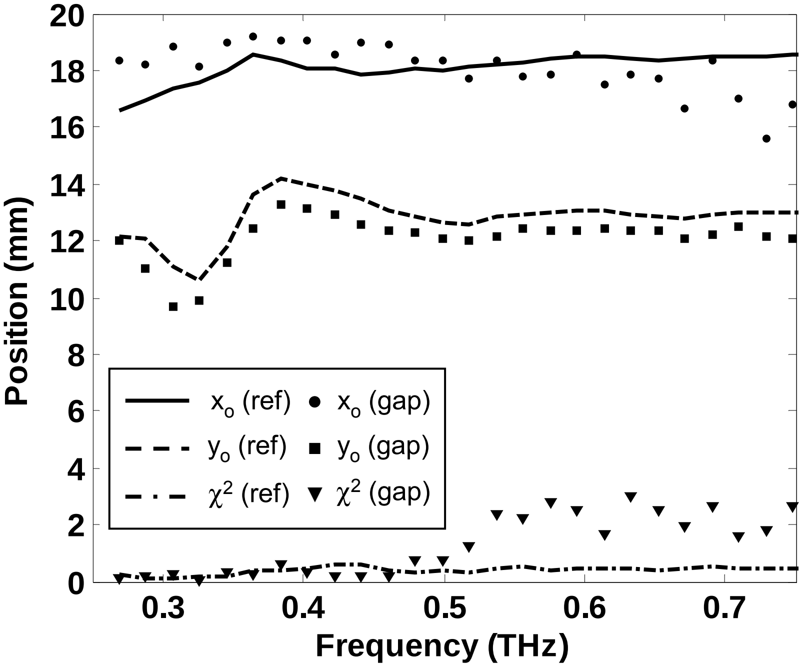

**Figure 5.26** Fitted beam position, horizontal $x_o$ and vertical $y_o$, and $\chi^2$ confidence as a function of frequency. The point markers correspond to $\Delta = 1000$ μm. The lines correspond to $\Delta = 0$ μm. Noise greatly increases the $\chi^2$ after 0.5 THz. The GH shift is observed in $x_o$ to 0.5 THz from the fitting results.

The fitting procedure yielded spatial positions as shown in Figure 5.26 for the best fit two dimensional Gaussian distributions. The lateral GH shift is visible in the $x_o$ data up to 0.5 THz. The crossing of the reference position coincides with a sudden increase in the $\chi^2$ term which indicates a decrease in the goodness of the fit. This is due to decreased signals, reduced beam waist radii for the higher frequencies, and the k-vector distortion of the beam profile. The $y_o$ fitting results show a consistently displaced vertical position averaging 800 μm below the fit for the reference beam profile. This is most likely an artifact of the fitting routines as it does not show the same sensitivity to the goodness of fit as the horizontal position.

The structure around the base of the assumed Gaussian profile increases with frequency (see Figure 5.25 and (d) and (g) of Figure 5.23) and causes subsequent difficulties in fitting profiles for propagating beams. This observation led to investigations that showed the emitted THz beam has a more complicated structure than typically supposed due to the interaction of the dipole antenna pattern and the Si lens.[49]

## 5.6 Conclusion

Bounded electromagnetic beams are comprised of plane wave components. Detecting the phase and amplitude of a THz pulse with high spatial resolution in the time domain provides the means to perform previously impossible experiments directly investigating FTIR.

Optical tunneling near critical angle has demonstrated that FTIR filters the energy spectrum as well as the wave vector spread, which reshapes the pulse in time and space. Thus, near critical angle, the transmission can become extremely sensitive to the spatial profile of the beam. Measurements of the beam profile confirm displacement from the Goos-Hänchen phase shift of a pulse after undergoing optical tunneling. This spatial shift highlights the pitfalls of assuming the path of propagation through a highly dispersive system. Both the thin and thick barrier regimes of optical tunneling have been observed in the same experiment by use of a broadband pulse. The propagation time through the entire optical tunneling system is determined.

Numerical simulations have reproduced the same tunneling behavior for FTIR as measured in the laboratory, providing additional insight to the physical process of optical tunneling. By solving the time dependent Maxwell's equations (FDTD) a "dwell time" within the gap is estimated, clearly demonstrating the transmission through the gap itself is not instantaneous.

The main point of this chapter warrants repeating for emphasis. The lateral GH shift of the beam explains why the pulse seemingly travels superluminally: *it travels through less high index material*.

# 6 Lens profile—Near field

This chapter focuses on applying beam profile capabilities to observing the behavior due to interaction with specific lens structures. Evanescent propagation in the form of surface waves is observed on the lenses. Pulse propagation through a collimating lens is simulated numerically.

Evanescent propagation exists on the boundary between the high and low index mediums for the period of time that the incident pulse is reflecting from the interface beyond the critical angle. The evanescent field propagates as a surface wave along the boundary, eventually reradiating back into the high index medium in the case of total internal reflection or coupling across the gap to another high index medium in the case of FTIR.

Surface waves radiate when propagating along a curved surface.[71] In the case of metallic objects, this is due to an induced surface current.[71] In the case of dielectric objects, fields at tangential incidence couple into propagating surface modes.[34,35]

For a high resistivity collimating Si lens, such as those used for THz emitters or receivers (see Chapter 2), the emitting face is a spherical dielectric surface. The curvature introduces a relative phase shift across the pulse front originating at the Hertzian dipole at the focus of the lens and shapes the propagation behavior of the emitted pulse. Investigations identified that THz beam profiles do not have a simple Gaussian distribution, though Gaussian based beam behavior could be used for modeling, either by considering only the central lobe[26] or by applying superpositions of higher order modes.[49]

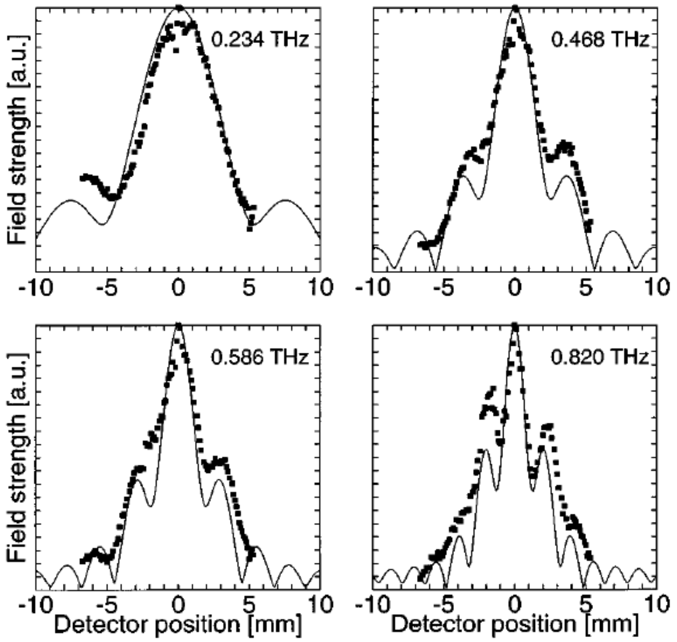

**Figure 6.1** From "Generation and detection of terahertz pulses from biased semiconductor antennas" by Jepsen, et.al.[26] Two dimensional beam profile measurements taken at 35 mm from a THz emitter are shown for representative frequencies with an exposed receiver corresponding to the profile measurements shown in Chapter 4. The authors state that the ripples in the calculated antenna pattern (lines) is due to diffraction from the aperture caused by the critical angle in the THz lens.

Figure 6.1 shows the beam profile measurements for the radiation emitted from a THz transmitter as well as the calculated antenna pattern at 35 mm by Jepsen, et. al.[26] The authors attribute the additional structure in the field after propagation to the effective aperture induced by total internal reflection at critical angle inside the collimating Si lens. Figure 6.2 shows the collimating lens with the frequency independent radiation pattern of the THz dipole antenna on a dielectric boundary(Figure 2.2) superimposed on the left side for both S and P polarizations. The critical angle for the air-silicon interface in a lens with the given geometry is the angle $\theta_c$, which intersects the antenna pattern. THz radiation is incident on the curved interface beyond critical angle and can couple into propagating surface waves.

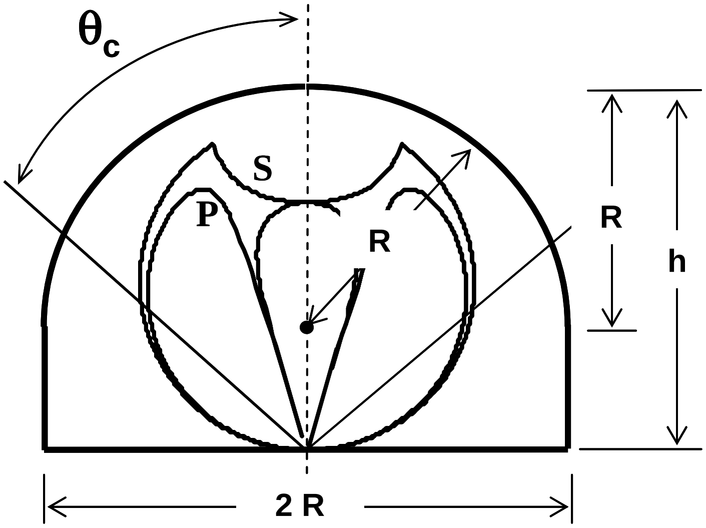

**Figure 6.2** Collimating silicon lens schematic. The radius of the spherical portion is R with an overall height of h. The S and P polarization antenna patterns are displayed on the left half and are symmetric about the optical axis.

With a pulsed experiment the end point of the rays can be observed directly. Spatially resolved measurements of the propagating THz pulse reveal interesting structure in the time domain that gives rise to the observed spectral features and that surface wave radiation contributes to the pulse form.

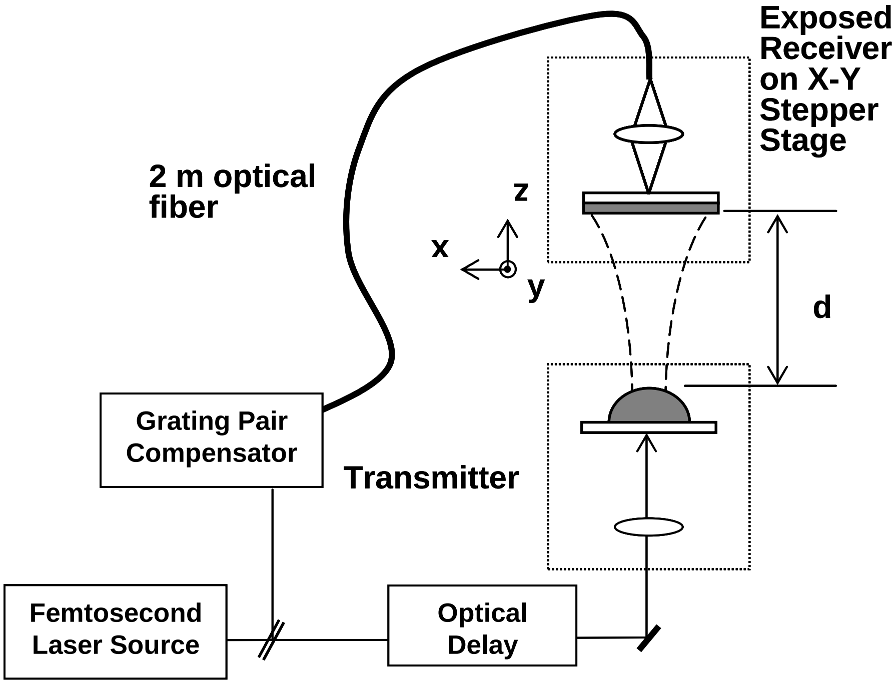

**Figure 6.3** Beam profile experiment similar to that of Figure 4.6.

## 6.1 Experiment

The experiment used to measure time resolved phase fronts has been discussed in Chapter 4, and is shown schematically in Figure 6.3. The optically generated THz pulse is polarized along $\hat{x}$ and propagates along $\hat{z}$. The silicon collimating lens, Figure 6.2, has a 5 mm radius of curvature and 6.45 mm total height. The Si lens was affixed directly to the GaAs substrate with UV curing epoxy at four points along the edge of the lens in order to remove aperture-pulse interaction caused by mechanical mounting. No additional apertures were introduced into the system by optical components, unlike previous profile measurements[49] where the lens holder on the transmitter could modify the pulse emitted. Eliminating apertures prevented effects due to polarization dependent phase shifts arising from reflections and spatial filtering of low frequencies. The substrate for the photoconductive switch lends an additional 0.5 mm of GaAs for the overall lens-dipole system. The index difference between the Si lens and GaAs substrate was ignored for the subsequent analysis.

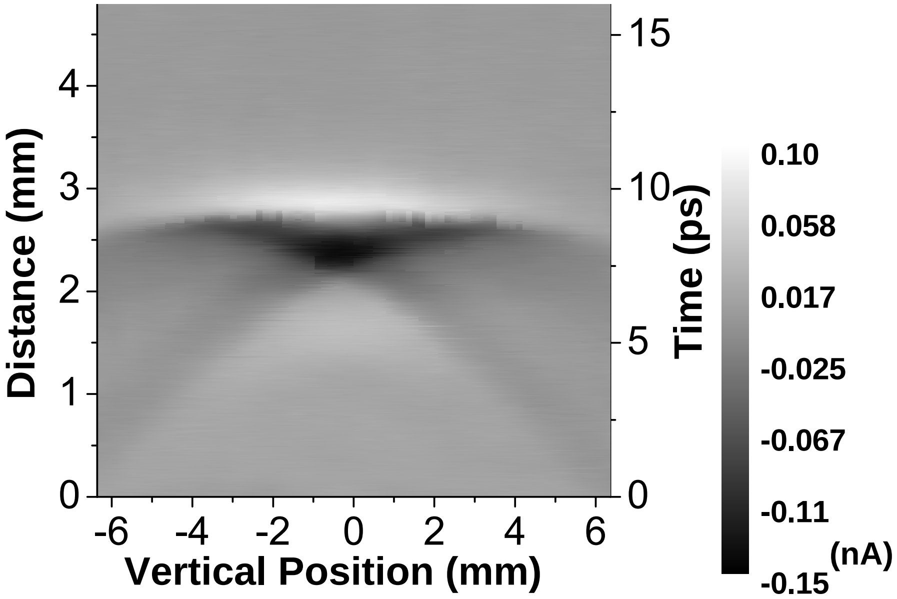

**Figure 6.4** Beam profile (S polarization) measured at a distance d = 16 mm from the THz emitter with a fiber coupled exposed receiver. The distance axis on the left shows the spatial extent of the pulse by rescaling the time axis shown on the right. The amplitude is measured in units of nA.

Raster scans of 80 points with 160 μm spacing with a fiber coupled exposed receiver (10-50-10) mapped the THz field along the y axis (S polarization) at distances of 16 mm and 3.2 mm from the surface of the silicon lens. S and P polarization (x axis) measurements are qualitatively similar and only S polarization measurements are included in this chapter.

The measured pulse at 16 mm, Figure 6.4, is a near planar pulse front followed by trailing edges or "wings"; classified in catastrophe theory as a swallowtail cusp.[72] Catastrophe theory[73] classifies the behavior of families of polynomial equations, i.e. spherical aberration, according to the number of solutions at each point in a parameter space, here the number of stationary phase points at each location in space-time. Catastrophe theory maps regions of real solutions and allows prediction of the temporal pulse shape from the spatial behavior of the families of solutions. The swallowtail shape has been directly observed in acoustics[73] and THz pulses[21] and will refer to the trailing edges of the pulse structures presented here.

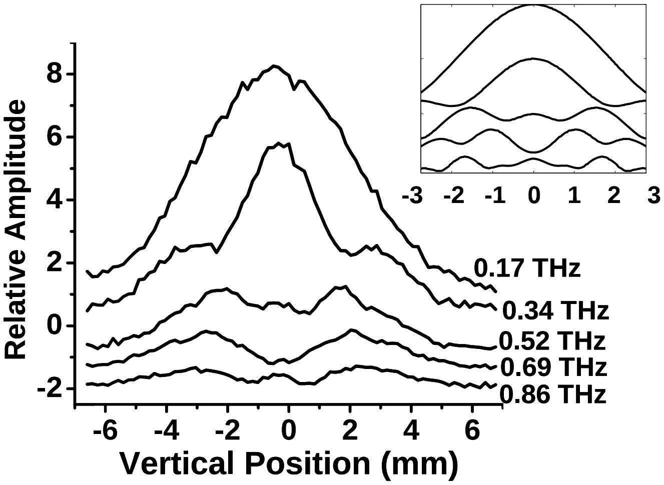

**Figure 6.5** Amplitude profiles for selected frequencies for the pulse form of Figure 6.4. The inset shows the spectral amplitude profiles calculated from the results of a stationary phase (time-of-flight) approximation.

The distinctive swallowtail shape results from the inherent spherical aberration in the collimating lens.[21] The spatial amplitude distributions obtained from a numerical Fourier transform for five discrete frequencies are shown in Figure 6.5. The frequency dependent spatial amplitude distribution results from interference between the time delayed “wings” of the swallowtail and the leading edge.

Figure 6.6 shows the pulse form measured at d = 3.2 mm from the source lens. Spatial inhomogeneities of the source field arise both from the field pattern of a dipole on a surface[22], Figure 6.2, and because the critical angle in silicon is near Brewster's angle, leading to more efficient coupling around the annulus of the lens.[49] The broad trailing edge of the pulse in Figure 6.6 is due to efficient coupling of low frequency components to free space due to surface waves.

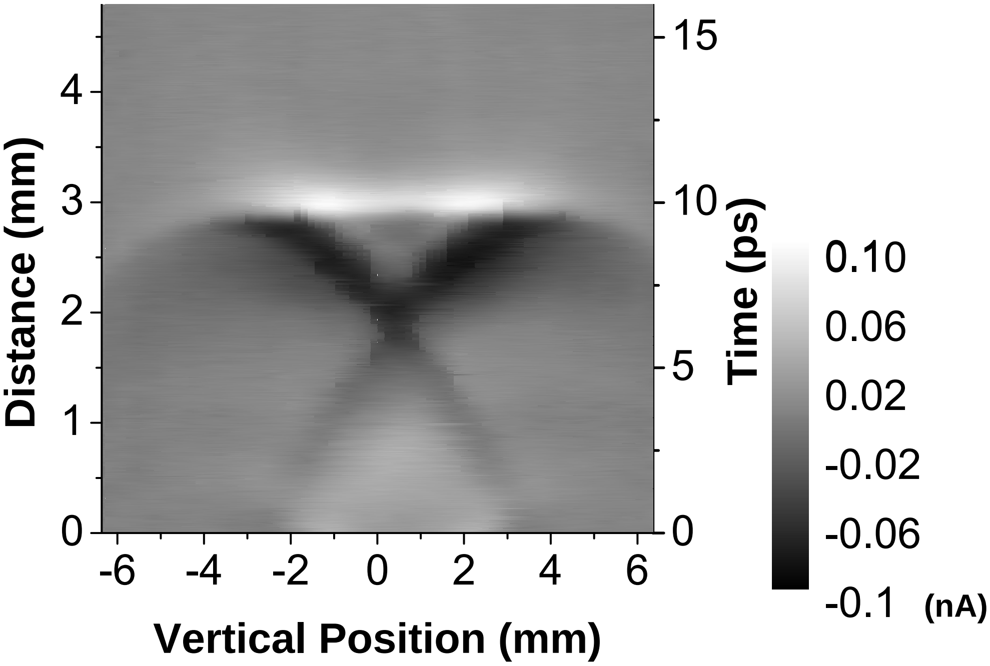

**Figure 6.6** Beam profile (S pol.) measured at d = 3.2 mm. Note the swallowtail features trailing the main pulse front. The field amplitude is measured in units of nA.

The increased field amplitude in an annular region close to the lens is more visible in the surface plot Figure 6.7. The increased field is also observed in the spectral profile of the imaged lens surface shown in Chapter 4 (Figure 4.17). The temporal waveform has the same annular amplitude distribution as that calculated in the frequency domain[49] as expected from Parseval's theorem, which states that energy distributions are equal in both temporal and frequency domain representations.

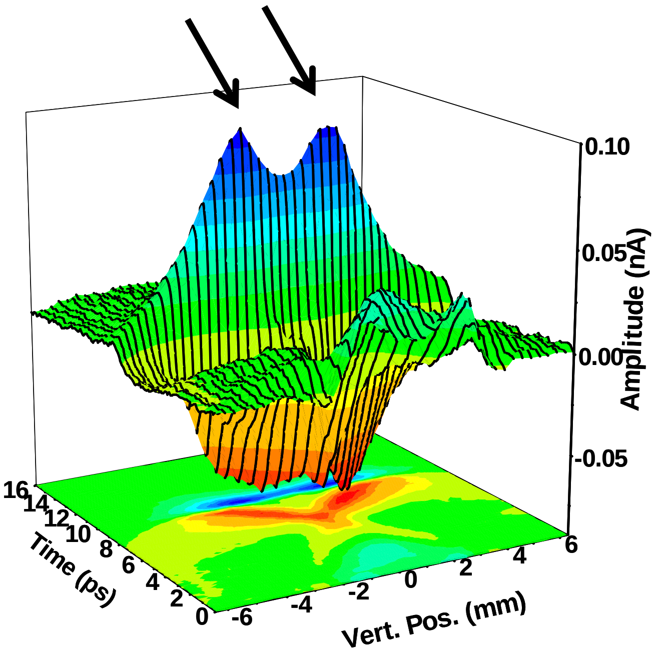

**Figure 6.7** Surface plot of the measurement shown in Figure 6.6. Note the peaks in the field around the optic axis as indicated by the arrows.

## 6.2 Stationary phase analysis

To describe the swallowtail pulse shape in the near field region of the lens, three regions—direct (*i*), marginal (*ii*), and surface waves (*iii*)—are defined in Figure 6.8. These regions are determined by the angles, θ, γ, and ϕ as shown in Figure 6.8 and explicitly stated in Equation 6.1.

$$\begin{aligned}\gamma &= \phi - \sin^{-1}\{n\sin(\phi-\theta)\} \\ \phi &= \sin^{-1}\left\{\left((h-R)\cos\theta + \sqrt{R^2+(h-R)^2\sin^2\theta}\right)\cdot\sin\theta/R\right\}\end{aligned} \tag{6.1}$$

γ is the angle of the ray outside the lens with respect to the propagation axis with negative angles to the left and positive to the right. θ is the angle with respect to the optic axis at the source dipole, and ϕ is the angle of the interior ray with respect to the lens surface normal. The total height of the lens plus substrate is given by *h*, and *R* is the radius of curvature for the lens.

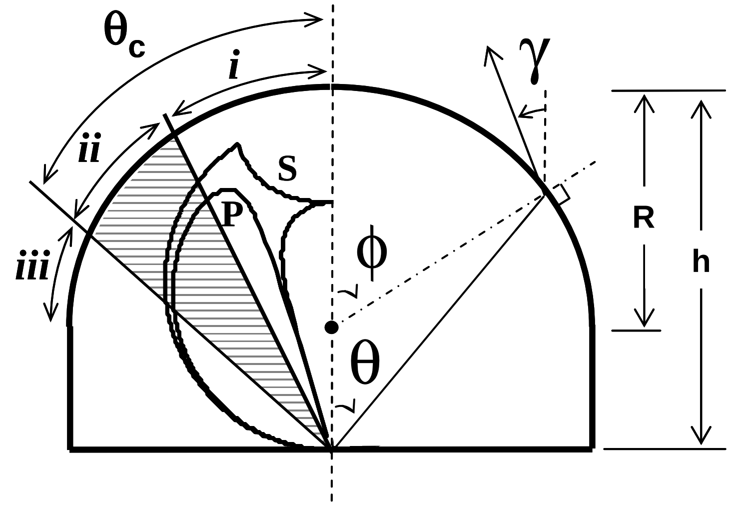

**Figure 6.8** Three regions are shown *(i)* direct, *(ii)* marginal, and *(iii)* surface wave. The boundary between regions *(i)* and *(ii)* is the point where the exterior propagation angle $\gamma$ changes sign with respect to the optic axis. The boundary between regions *(ii)* and *(iii)* is at critical angle $\theta_c = \phi - \theta$ between Si and air for a ray originating from the focus. For the standard collimating lens with R = 5 mm and total h = 6.96 mm with substrate, region (iii) is bounded at $\theta = 48.2°$ and the marginal/direct boundary is at $\theta = 25.4°$.

In the direct region (*i*), $\gamma \leq 0$ in the left hand plane of the lens as shown in Figure 6.8 (with opposite signs on the mirror symmetric right hand side), so rays never cross the optical axis. The direct rays originate from a 6.00 mm diameter aperture centered on the optic axis of the lens. The marginal region (*ii*) corresponds to rays that cross the axis of propagation ($\gamma > 0$) but are incident on the lens below critical angle. The marginal region is an annular surface bounded between the direct ray region and a 9.15 mm diameter aperture. The marginal region makes a large contribution to the propagating pulse due to the dipole field pattern and large values of the Fresnel transmission coefficients.[49] The surface ray region (*iii*) is where the angle of incidence of the ray on the internal surface of the lens, $\phi - \theta$, is beyond critical angle. The field external to the lens is typically evanescent in region (*iii*), but energy may be coupled to free space through surface waves due to the curved interface.[74]

While most rigorous in the high frequency limit, time-of-flight models can be valid for near single cycle pulses.[75] As a result of the broad bandwidth of the THz pulses, phase differences rapidly accumulate to suppress propagation components that are non-ray like in behavior.

The stationary-phase approximation, $\delta\Phi/\delta\Psi = 0$, determines the time-of-flight of the pulse front to a given observation point.[40] The stationary point on a ray corresponds to the pulse. $\Phi$ is the accumulated phase for a given frequency component, $\Phi = k_o\Psi$, to any spatial point (y,z), determined from the angle-dependent optical path length, $\Psi$:

$$\Psi = n_L\sqrt{R^2 + w^2 + 2Rw\cos\beta} + \sqrt{(R\sin\beta - z)^2 + (y + R - R\cos\beta)^2} \qquad 6.2$$

where $\beta = \phi - \theta + \gamma$, $w = h - R$ and $n_L = 3.42$ is the index of the silicon lens. For a swallowtail pulse, the phase function contains three stationary points (pulses) near the optic axis. For the extreme marginal ray contributions, rays with large $\gamma$, only one stationary point exists. The transition surface between the spatial regions where the number of real solutions to Equation 6.2 change is a caustic surface (or focal surface.)[40] The relationship between families of caustic surfaces and the temporal pulses that pass through caustic surfaces is described by catastrophe theory.[73]

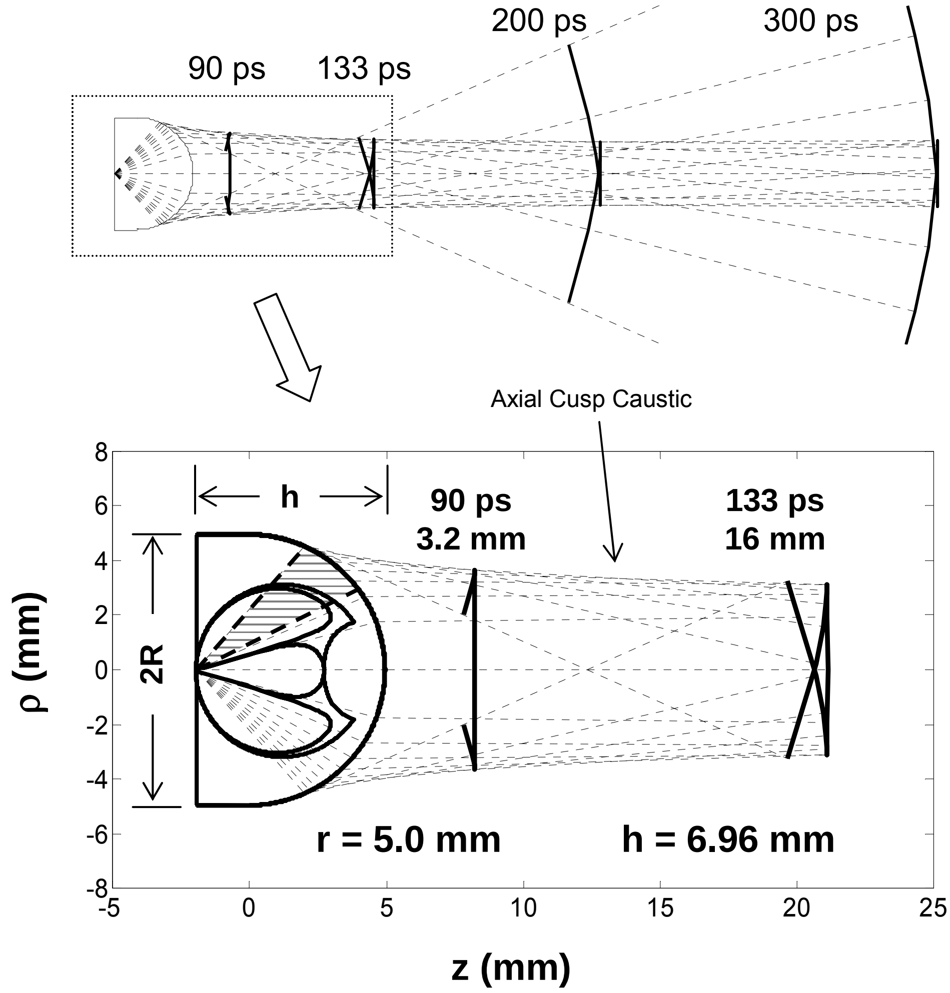

**Figure 6.9** Stationary phase calculations for the pulse profile for different propagation times. 90 ps corresponds to propagation from the dipole source to 3.2 mm from the lens surface. 133 ps corresponds to propagation from the dipole source to 16 mm from lens surface. The envelope formed at the edge of the rays is an axial cusp caustic.

The evolution of the pulse front calculated from the time-of-flight model is shown as a heavy solid line in Figure 6.9 at 90, 133, 200, and 300 ps following optical excitation, the lighter dashed lines represent normals to the phase front (rays).[72] In the far field limit the stationary points of the leading and trailing edges of the swallowtail pulse approach a spherical phase front.

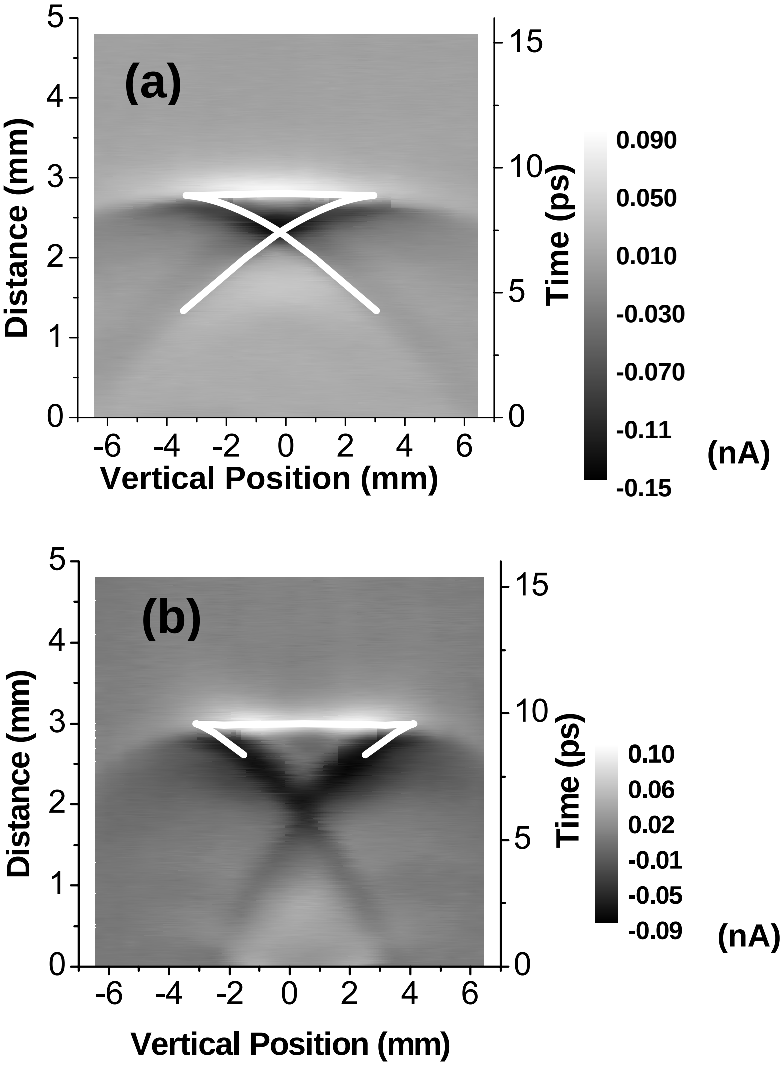

**Figure 6.10** Stationary phase traces overlaid on measurements for (a) 16 mm (133ps) and (b) 3.2 mm (90 ps). The times-of-flight account for propagation through the high index lens in addition to the free space distance.

Figure 6.10 shows a comparison of the time-of-flight analysis (white line) with the measured pulses. The flat leading edge of the swallowtail pulse corresponds to the contribution by direct rays (*i*), while trailing edges of the swallowtail pulse are from marginal and surface rays (*ii*, *iii*).

The inset to Figure 6.5 shows the spatially resolved amplitude distribution calculated from the time-of-flight model with the trailing edge pulse amplitude 40%

of the leading edge and a near π Gouy phase shift due to propagation through a caustic surface.[40] The calculated interference is multiplied by a Gaussian distribution with a 4.5 mm waist. The simple model qualitatively reproduces the amplitude distribution observed, with the exception that the calculated distributions have smaller spatial extent, possibly due to diffraction.

The time-of-flight model does not explicitly account for surface waves generated in region (*iii)* of the lens as seen by disagreement of the time-of-flight model, Figure 6.10(b), with the observed pulse shapes at d = 3.2 mm. The time of flight model (white line) predicts the trailing wings of the pulse front coupled out of region (*ii)* will be obscured by the geometric shadow of the lens surface. The trailing wings of the swallowtail pulse arise from radiation of surface waves[76] generated by the pulse front incident on the lens surface in region (*iii)*. Critical angle is strictly defined in the limit of r/λ approaching infinity, i.e. for flat surfaces. For frequencies such as the peak 0.5 THz, λ = 600 μm and the lens curvature R = 5 mm, the ratio is only around 8 wavelengths, substantially less than infinite. The transition between transmission and total internal reflection becomes wavelength dependent and results in coupling into surface waves,[76] creating a caustic tangent to the lens surface.[74]

## 6.3 FDTD Analysis

FDTD techniques are well suited to this problem, just as in the investigation of FTIR tunneling times and pulse deformation. By use of short pulses, the lens-dipole system behavior can be determined over the frequencies of interest. FDTD provides a visualization tool in following the time advance for propagation of short pulses. Surface waves, reflection, refraction and diffraction of a propagating beam are inherent in properly set up FDTD simulations.

### 6.3.1 FDTD Parameters

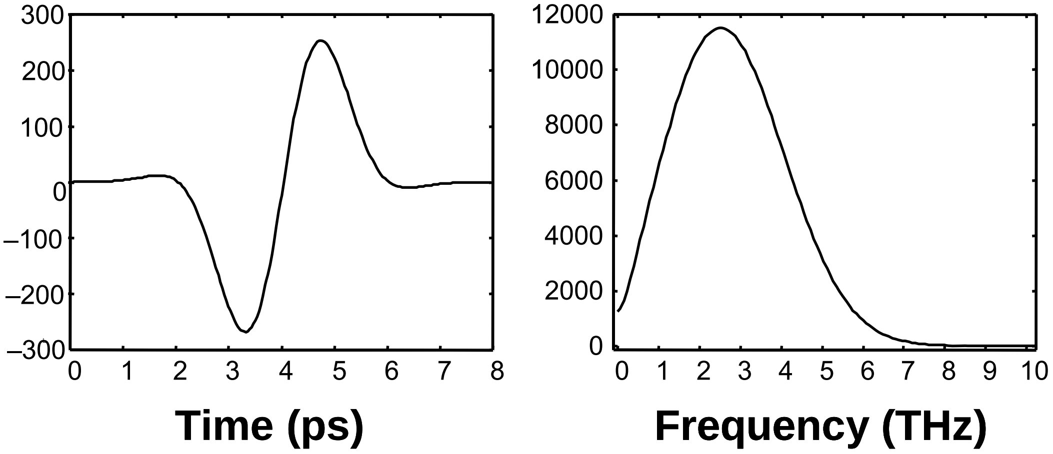

**Figure 6.11** FDTD source behavior for the Hertzian dipole emission.

The silicon lens is modeled by a region of high index material (n = 3.42 ) located within the center of a two dimensional space. The Si is treated as a lossless dielectric as was done in the previous chapter for FTIR investigations. The size of the FDTD lens region is the same as the physical dimensions of the collimating lens used. The edges of the FDTD region have a perfectly matched layer that is a total of 8 cells deep.

The center frequency of the pulse was taken as $f_o = 0.25$ THz, which is half of the peak frequency of the experimental system. This yielded a free space center wavelength $\lambda_o = 1.2$ mm. If the source is modeled as shown in Figure 6.11, as the superposition of a sine function operating at $f_o$ superimposed with a Gaussian distribution, the maximum frequency of interest will be approximately $f_{max} = 0.6$ THz.

As Figure 6.11 shows, this choice of maximum frequency neglects the highest frequency components in the interest of computational feasibility. The corresponding free space wavelength for the maximum frequency would be $\lambda_{max}$ = 0.5 mm. This would lead to a spatial grid dimension of $dx = \lambda_{max}/10$ = 50 µm. This would not be sufficient as the propagation within the high index material is of primary interest, just as in the case of FTIR. The wavelengths scale inversely with the index so the actual $\lambda'_{max} = \lambda_{max}/n$ = 0.14 mm, which in turn would require $dx = \lambda'_{max}/10$ = 14 µm. This treatment only went to $dx = \lambda_o/50$ = 24 µm in the interest of computation time.

The driving term was limited to a single cell on the boundary in approximation of the Hertzian dipole. The current induced by optical excitation is assumed to be linear and directly perpendicular to the transmission line orientation. As the region of photo excitation is limited to the spot illuminated by the short pulse laser which is on the order of 5 µm. The limited area for the induced current allows the driving field to be taken as well polarized at least to first approximation. This assumption may not be strictly valid if one considers the field within the GaAs substrate between two transmission lines separated by 100 µm and held at a 70 V or higher potential difference.

From the limitations placed on the modeled source field, the problem can be divided into TE ($E_x$, $E_y$, $H_z$) and TM ($H_x$, $H_y$, $E_z$) treatments. The TE and TM solutions are the P and S polarizations respectively and can be experimentally measured by along the horizontal or vertical axes of the silicon lens. For TM case the $E_z$ would be the initial source. It is vital to assign appropriate starting values to the H fields about the source cell as well, or else non physical behavior erupts.

### 6.3.2 FDTD Results:

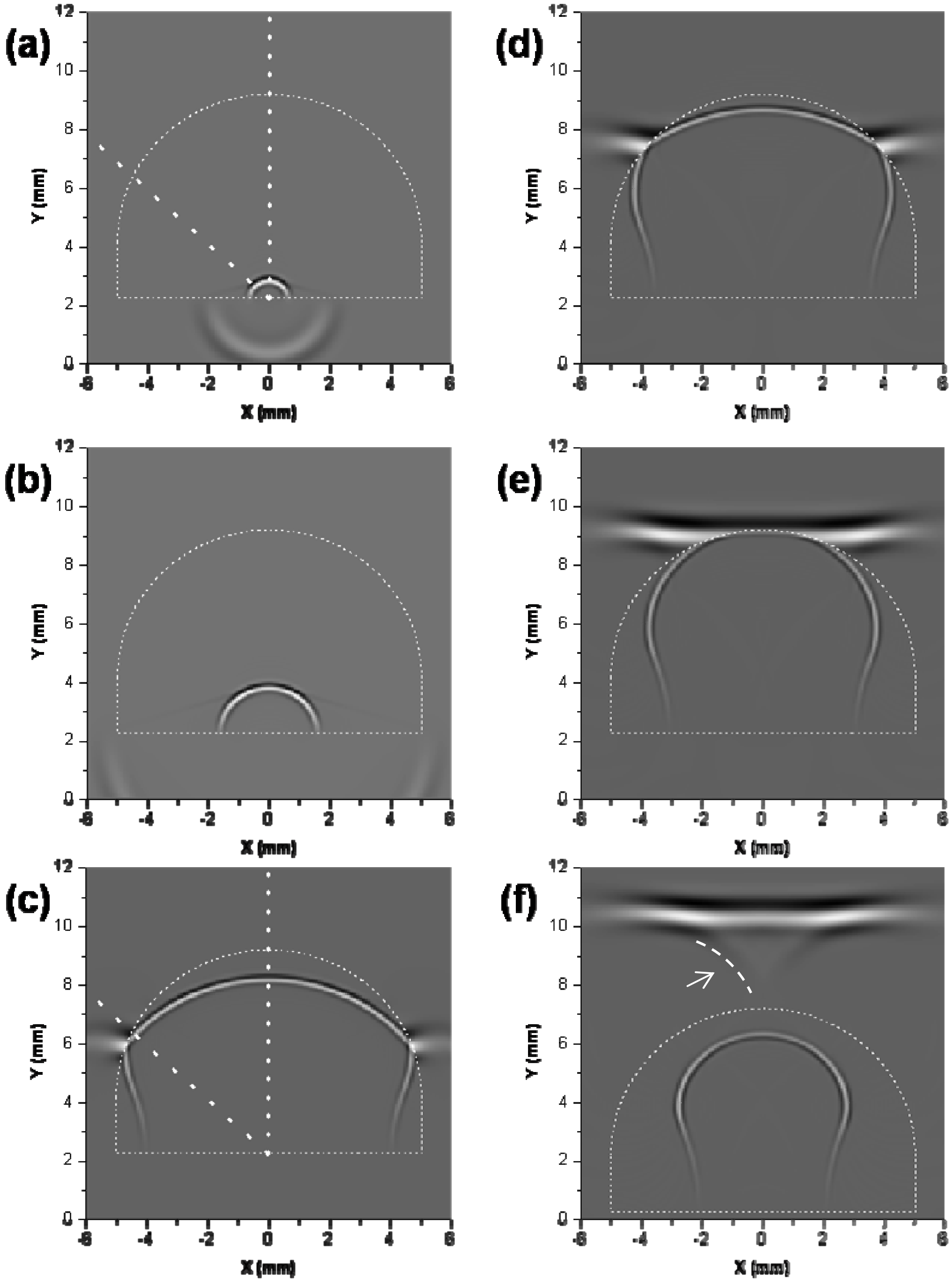

**Figure 6.12** Sequence of FDTD simulations of pulse propagation from a Hertzian dipole for (a) 11 ps, (b) 22 ps, (c) 61.5 ps (d) 66 ps (e) 77 ps (f) 88 ps with the lens profile. The dotted lines in (a) and (c) indicate the optic axis and the critical angle for the radially propagating pulse. The arrow in (f) is a guide to the eye for the surface wave radiation (dashed line).

Figure 6.12 (a) through (f) shows a sequence of FDTD generated THz pulse distributions. In Figure 6.12,

(a) Note the radiated pulse out of the reverse side of the lens propagating in free space as well as the associated shockwave(von Schmidt's lateral wave[41]) with the field external to the lens reradiating into the silicon.

(b) The shockwave has reached the edge of the lens structure. The main pulse continues to propagate outwards.

(c) The simulated pulse interacts with the lens in region *(iii)* and an evanescent field is evident. Even though the evanescent field location moves along the surface, it simply keeps pace with the internal driving field of the incident pulse until nearing the critical angle at the boundary to region *(ii)*.

(d) The pulse is emitted from the marginal region of the lens.

(e) The pulse is emitted from the direct region of the lens.

(f) Shows the pulse near the propagation distance (time) for the measured THz pulse taken at z = 3.2 mm of Figure 6.6. Trailing edge pulses are visible (indicated by the arrow in Figure 6.12(f) as a guide to the eye.)

The trailing edge pulses contribute to the swallowtail pulse structure. If the pulses were simply due to diffraction effects at a sharp aperture formed by the critical angle, the radiation pattern would be uniform and centered on the boundary between regions (iii) and (ii). The trailing edge pulses in Figure 6.12(f) are due to radiating surface waves as they are preferentially guided along the gradient of the lens face.

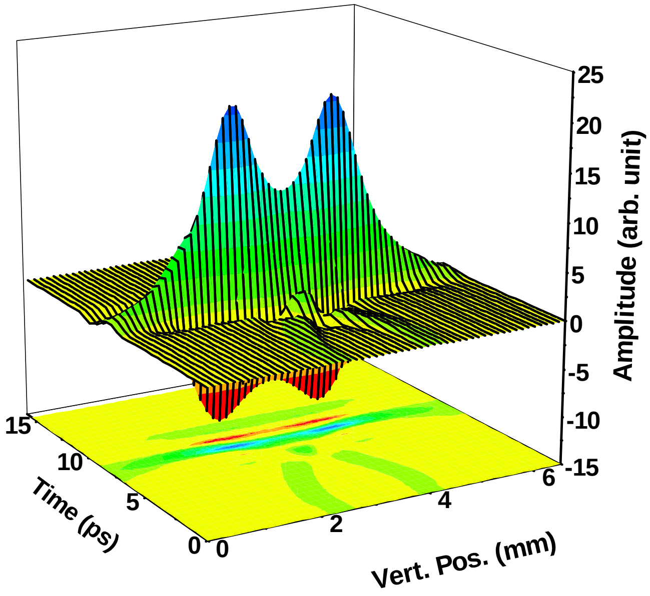

**Figure 6.13** Comparison to the measured THz pulse profile of Figure 6.7.

The pulse shape shown in Figure 6.13 conforms to that of the measured pulse shape shown in Figure 6.6. The results of the FDTD support the observation that the lens dipole systems act as annular emitters (consequently annular receivers as well.) The annular emission in turn reduces the aperture efficiency of a THz transmitter or receiver.[47] Aperture efficiency is defined as the maximum effective area divided by the physical aperture. The effective area is the proportion of power delivered to the antenna from a uniform plane wave incident on the physical aperture. The reduced aperture efficiency will not impact the standard THz-TDS system because it has a unity optical transfer function, generally replicating the field distribution of the emitter at the surface of the receiving lens (as in Figure 4.17.) In the case of incident planar pulse fronts, as in scattering, or when tightly focusing, such as waveguide coupling, the reduced aperture efficiency may play a role in a decreased signal strength.

Figure 6.14 displays the simulated pulse allowed to propagate to z = 16 mm as in Figure 6.4. The salient features of the pulse are reproduced. The "swallowtail" pulses are not as evident in the FDTD simulated results as with the laboratory experiment. The reduction may be due to limitations in the simulation.

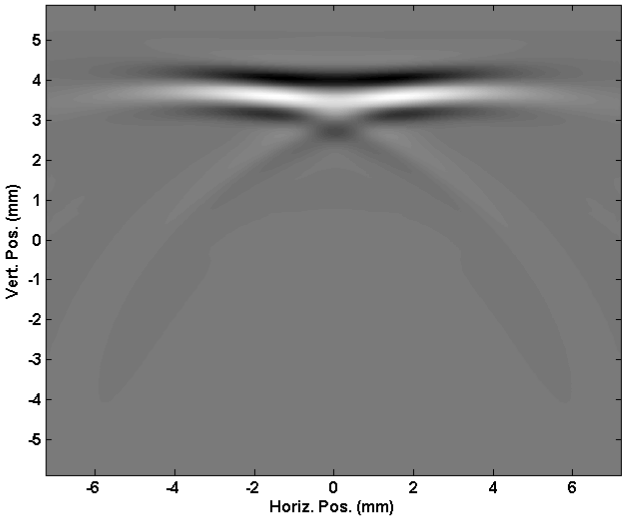

**Figure 6.14** FDTD simulated pulse propagating z =16 mm. The vertical position does not represent the distance propagated.

### 6.3.3 Considerations for FDTD results regarding the lens surface

Surface wave propagation is highly sensitive to the surface geometry. Irregular surfaces and sharp features tend to suppress surface wave propagation, causing radiation. The inevitable roughness that is introduced into the model of the smoothly varying curved lens face by the finite grid pattern of FDTD will modify the surface wave behavior in the simulation. The solution utilized in the modeling process presented in this chapter is to ensure the grid is fine enough to appear continuous to the highest frequency of interest. Other methods could be used to minimize the impact of the discretization of a smoothly curved surface.

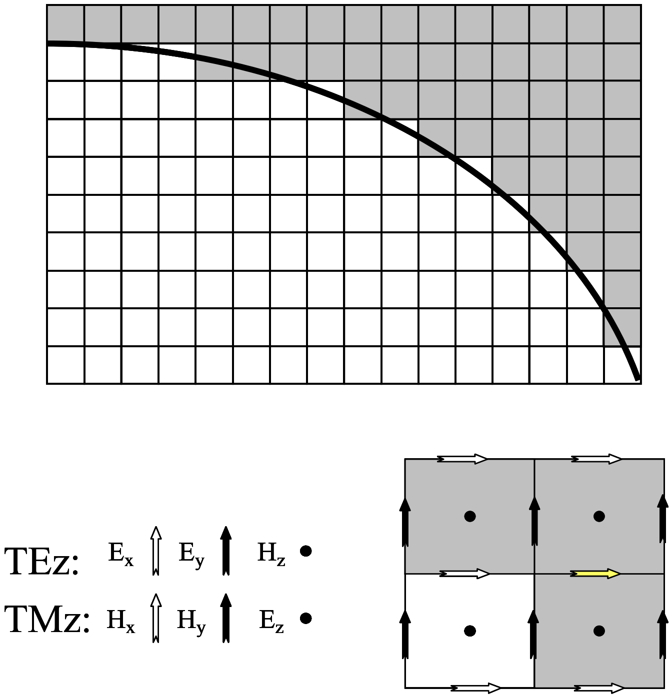

**Figure 6.15** Schematic of discretization roughness for a grid approximating a smoothly varying and continuous interface. The smaller grid shows the relationship between the different fields for TE and TM case.

Figure 6.15 shows a schematic representation of a smooth surface approximated by a finite grid. For a two dimensional analysis, fields will be directed along the grid lattice. No discretization problems arise as long as the interface runs parallel with the direction of the surface wave propagation. However, rather than undergoing a continuously slowly varying change in energy propagation, the surface wave interacts with a change in medium, transfers energy to adjoining electric or magnetic fields which then must reradiate along the boundary interface again. This abrupt change is a departure from the normal case assumed for surface wave propagation.

Nadobny, et. al., proposed imposing explicit boundary conditions during post-processing.[77] The correction enforces the true geometry by interpolating between the fields generated by FDTD and replaces the averaged value of ε that results on a grid boundary with the true material permittivity. This is however a purely frequency domain technique that would prevent the identification of the physical radiation processes.

Another treatment analyzed the accumulated error that arises from the discrete interface.[78] Waves reflected from a PEC and guided waves within a parallel plate structure were reflected. Results for reflection and guided waves when the PEC interface was aligned with the grid and when the PEC interface was at 45° with respect to the grid were compared. In all cases the phase velocity decreased with increasing frequency when the grid size was too large with respect to the associated wavelength. The resulting dispersion reshapes the propagating pulses and renders quantitative predictions useless (such as precise phase shifts from reflection or surface wave propagation velocities) though the overall qualitative behavior would remain the same. The effect of an averaged dielectric constant along an interface may enhance surface guided modes.

## 6.4 **THz Lenses**

The origin of the swallowtail pulse front is due to spherical aberration with surface wave contributions. The overlap of multiple pulses along with phase shifts associated with caustic surfaces may limit the time resolution of the propagated THz beam.

The temporal shape of the THz pulse coupling to free space and power coupling between source and detector is dependent upon the lens geometry.[23] Lenses with a large *h* focus the THz pulse, and beyond the focus the pulse front becomes nearly spherical as shown in Figure 6.16(a). Figure 6.16(b) illustrates the phase front for small *h*, the aplanatic hyperhemispheric lens[79] which exhibits no real caustics; only single solutions to the ray propagation exist everywhere outside the lens. Although the collimating lens, Figure 6.9, has a focus at infinity with three real solutions for all z near the optic axis , the three solutions approach the same limiting value at large distances and a spherical phase front is experimentally observed.

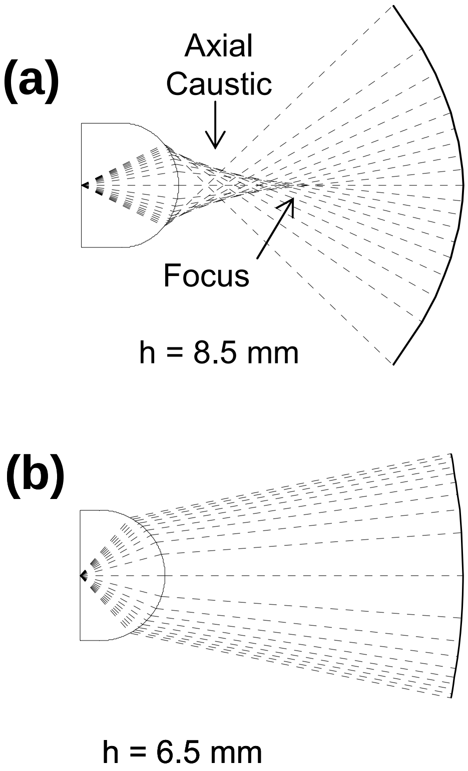

**Figure 6.16** (a) Focusing lens and (b) hyperhemisphere lens. Both lens designs show curved phase fronts for a propagation time of

Both lens designs of Figure 6.16 remove the multiple solutions to the stationary phase. Figure 6.16(a) has a short focal length, which does produce an axial cusp caustic. Within the envelope of this caustic (between the lens surface and the focus) three solutions exist, just as in the case of the collimating lens. However, once the pulse propagates through the caustic surface, only one solution exists and all the pulses accumulate the same π Gouy phase shift[40] ( π/2 phase shift in the case of a two dimensional caustic. [80])

### 6.4.1 Aspheric Lens

The findings of this chapter are applied to producing an aspheric lens[81] in order to minimize spatial inhomogeneities due to the interference effects of pulses while maintaining the near planar phase front produced by the collimating lens. A silicon aspheric lens was fabricated (International Scientific Products, Irvington NY) to the following specifications in order to minimize spherical aberration.

$$x = \frac{Cy^2}{1+\sqrt{1-C^2y^2}} + A_4 y^4 + A_6 y^6 + A_8 y^8 + A_{10} y^{10} \qquad 6.3$$

C: 0.20

A4: $+1.1399 \times 10^{-3}$

A6: $-1.7242 \times 10^{-4}$

A8: $+1.0858 \times 10^{-5}$

A10: $-2.4653 \times 10^{-7}$

The spatial coordinates of the aspheric surface are *x* and *y* (ρ and z in Figure 6.17) with the first term on the right hand side in Equation 6.3 corresponding to a spherical lens. The appropriate coefficients are listed. Only even terms in the polynomial are included due to axial symmetry.

The stationary phase model applied to the aspheric lens yields a nearly flat phase front for the pulse. Figure 6.17 shows the results for propagation times of 137 ps (z = 17.8 mm measurement distance) and 300 ps. Only a 50 fs variation in pulse front arrival is expected across a 9 mm diameter aperture of the aspheric lens after propagating 137 ps.

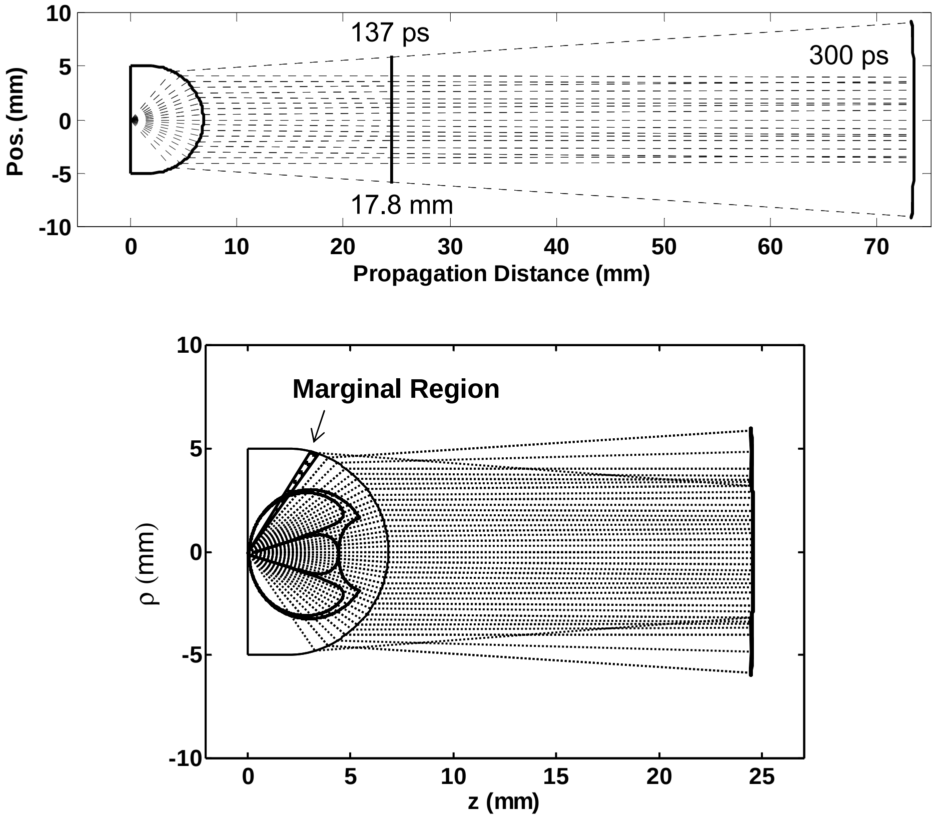

**Figure 6.17** Stationary phase time of flight results for the aspheric silicon lens. Note the minimal marginal region and nearly planar phase front associated with the emitted pulse. 17.8 mm (137 ps propagation time) corresponds to the measurement distance from the maximum height of the aspheric lens. (Compare to Figure 6.9 with the collimating lens.)

Though some spherical aberration is evident, it is only in the most marginal of rays. The initial propagating angle θ as defined in Figure 6.8 reaches 54° before changing sign on propagation direction. The corresponding propagation angle for a collimating lens is θ = 25.4°, nearly half the angle. Likewise, in the aspheric lens, θ = 56° before reaching critical angle. These angles produce an aperture of 9.6 mm for the direct ray region and 9.68 mm for marginal ray contributions, which leads to a nearly negligible spatial region to contribute to spherical aberration as indicated in Figure 6.17.

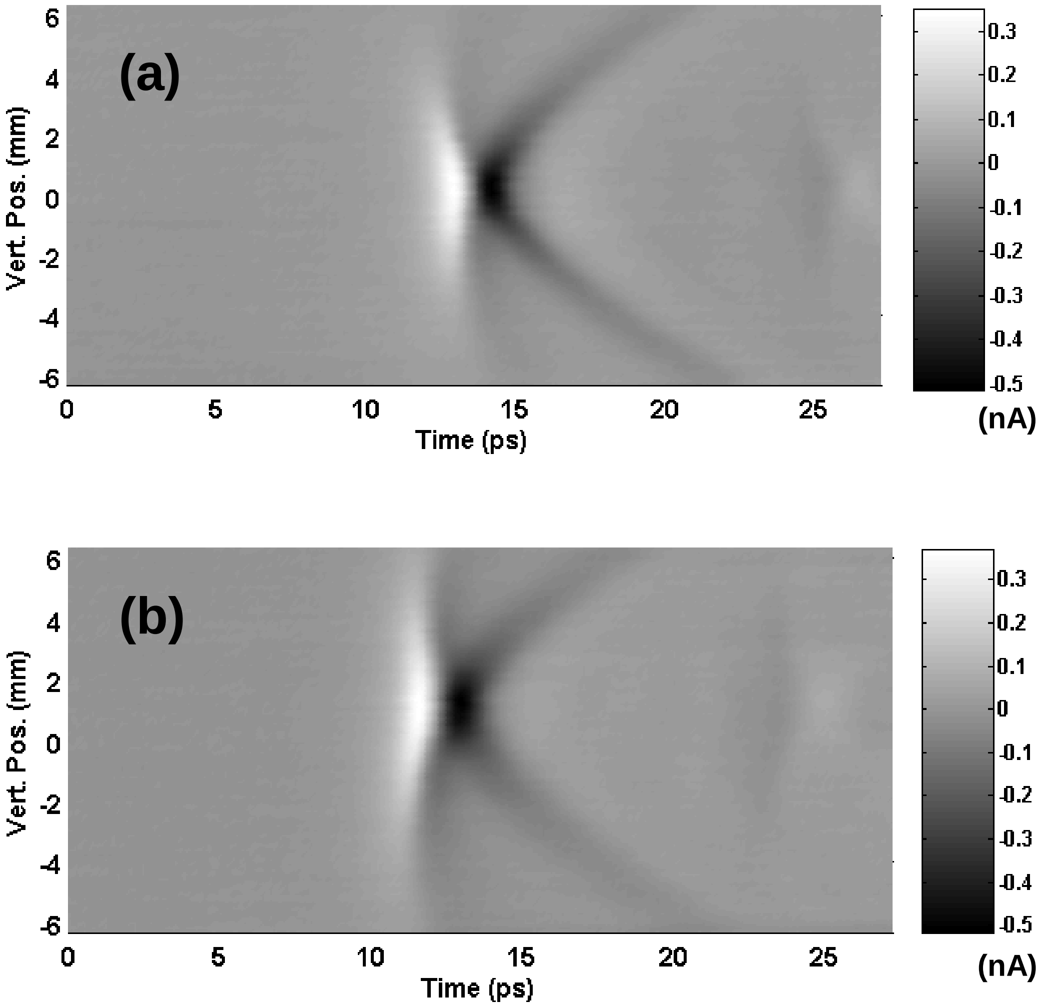

**Figure 6.18** (a) Collimating lens beam profile and (b) aspheric lens beam profile measured at z = 17.8 mm in the vertical direction (S polarization: electric field is out of the image.) The z axis is measured current in nanoamperes. Vertical step size Δy = 160 μm. Time step Δt = 136 fs.

Figure 6.18 and Figure 6.19 show comparisons between beam profile measurements for a standard collimating silicon lens and the aspheric for S and P polarization respectively. The measurements were taken with the experimental configuration shown in Figure 6.3 with z = 17.8 mm.

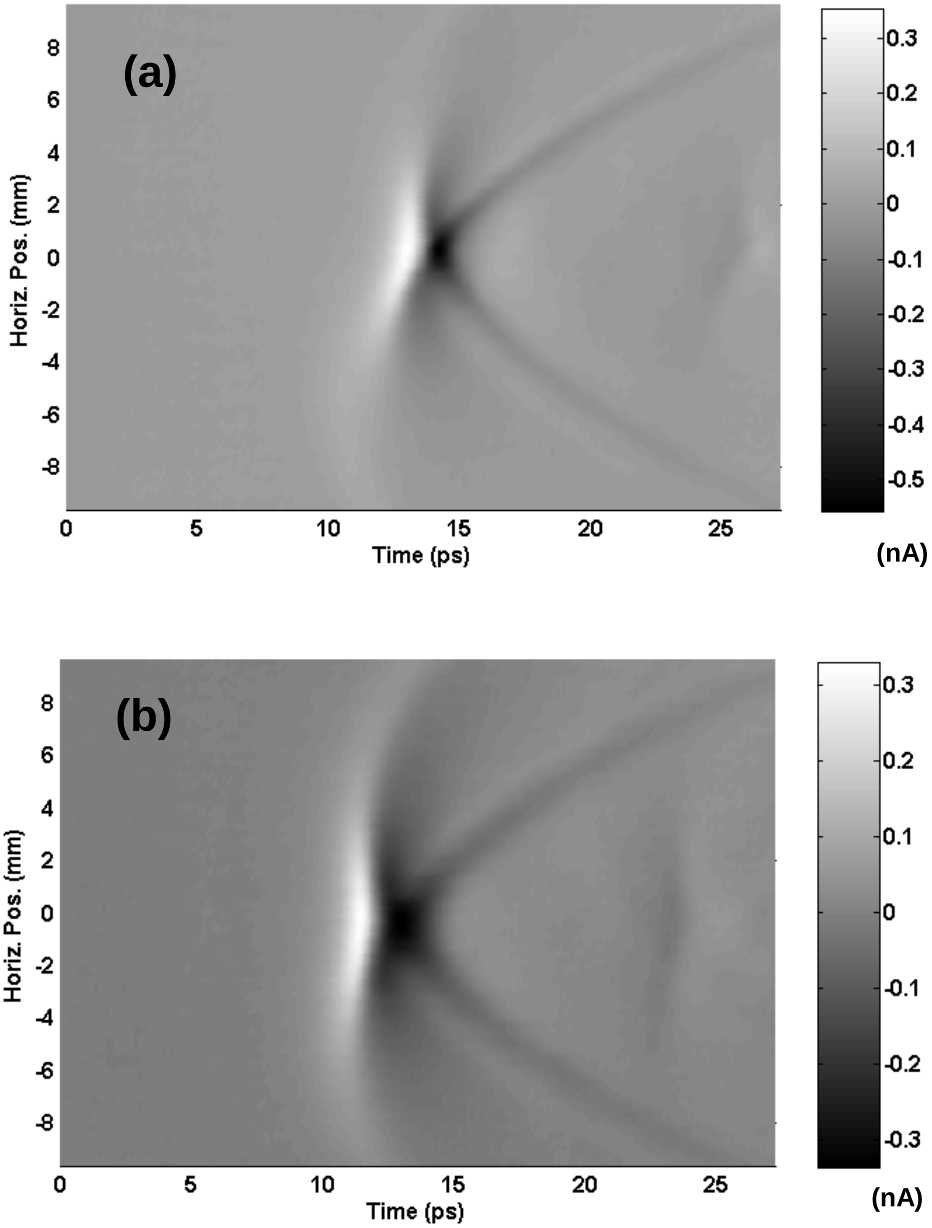

**Figure 6.19** (a) Collimating lens beam profile and (b) aspheric lens beam profile at z = 17.8 mm in the horizontal direction (P polarization: electric field in the plane of the image) measured from the apex of the lenses. The z axis is measured current in nanoamps. Horizontal step size Δx = 240 μm. Time step Δt = 136 fs.

Both measurements were taken on the same transmission line, same optical power (12 mW), and same bias voltage (78 $V_{dc}$). Both lenses were affixed to the

GaAs transmission line chip; no apertures were introduced into the beam line due to lens holding apparatus.

The trailing swallowtail wings are evident for both lens designs, though reduced in amplitude with respect to the lead pulse for the asphere. A slight misalignment of the collimating lens is evident in the angled pulse front of the collimating lens (Figure 6.18(a) and Figure 6.19(a)) and occurred during the removal of the transmitter FRU for lens replacement.

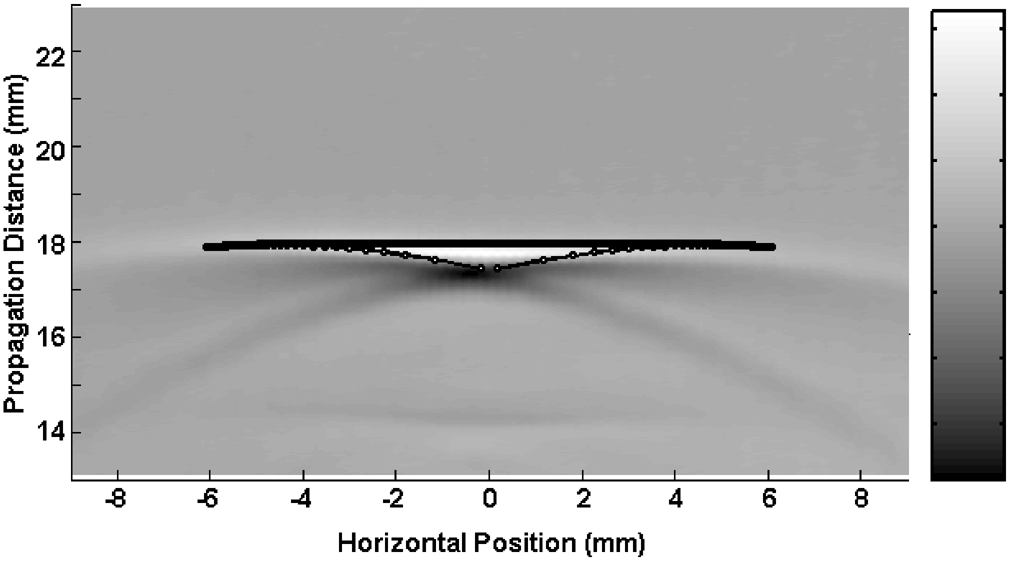

**Figure 6.20** Stationary phase predictions for the time of flight for 137 ps (z = 17.8 mm) overlaid with the measured THz pulse from Figure 6.19(b).

The stationary phase prediction for the time of flight for the aspheric lens is shown in Figure 6.20 for the P polarization case measured in Figure 6.19(b). The distance for the measured pulse has been shifted according to the measured propagation distance. The propagation distance for the stationary phase treatment of Figure 6.17 was modified by the thickness of the lens used in the ray tracing program (h= 6.85 mm). The predictions for the pulse shape conform well to measurements. The swallowtail structure to the pulse is still evident even with the drastically decreased contributions due to spherical aberration indicating surface wave contribution to the pulse structure near the emitting lens.

The decrease in the swallowtail contribution in the time data as presented in the images of Figure 6.18 and Figure 6.19 can be difficult to observe. However, as previously noted and demonstrated, the swallowtail components to the pulse modify the spatial distribution of the spectra for the pulses.

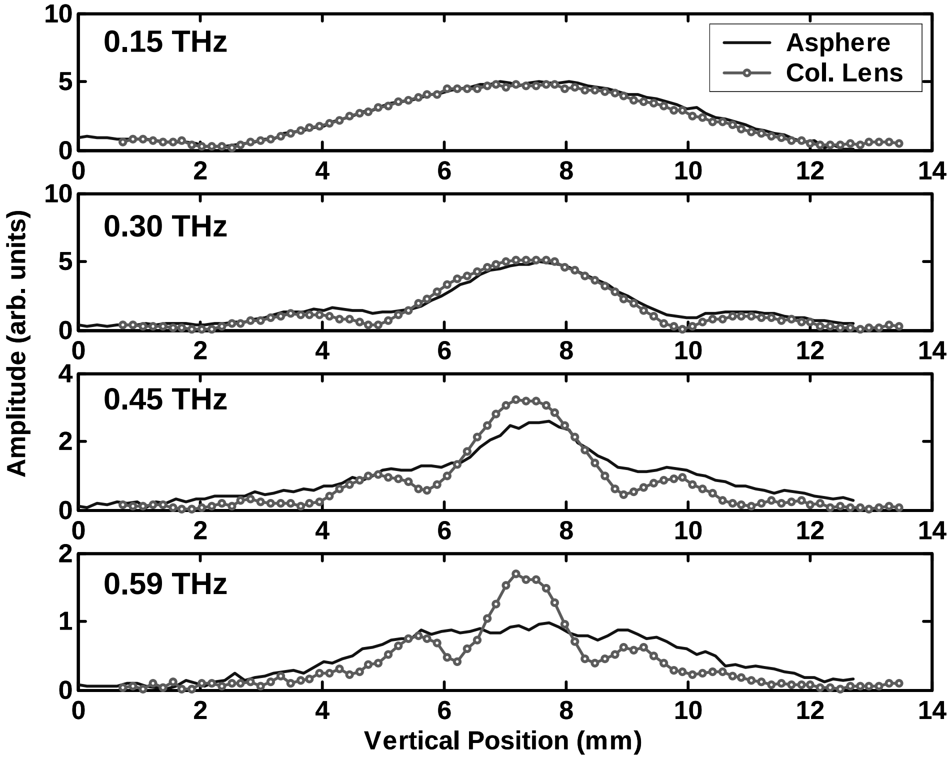

**Figure 6.21** Spatial distribution for 0.15, 0.30, 0.45 and 0.59 THz calculated from the measured pulse forms of Figure 6.18 in the vertical plane (S polarization).

Figure 6.22 shows the results of the Fourier transform of the pulse forms of Figure 6.18 plotted for fixed frequencies as a function of vertical position. The field is S polarized with respect to the plane of incidence. The collimating lens spectral profiles demonstrate the previously observed structure.[26] The aspheric lens gives a more uniform amplitude distribution.

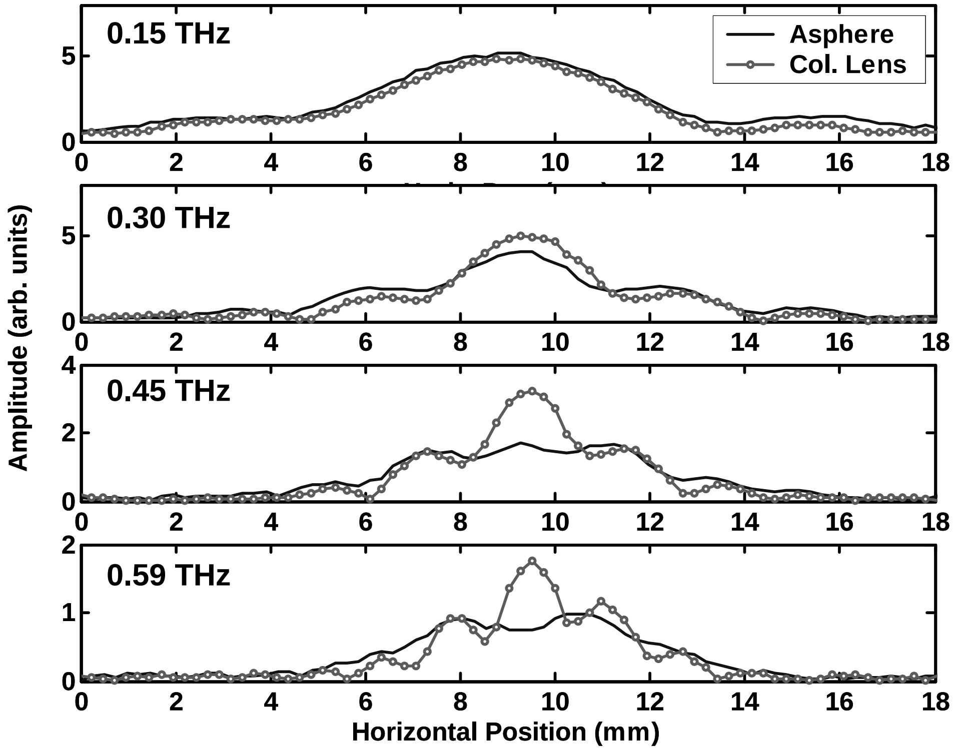

**Figure 6.22** Spatial distribution for 0.15, 0.30, 0.45 and 0.59 THz calculated from the measured pulse forms of Figure 6.19 in the horizontal plane (P polarization).

Figure 6.22shows the results of the Fourier transform of the pulse forms of Figure 6.19. The slight misalignment of the collimating lens is evident in the asymmetry of the spectral distributions.

The relative contribution of the field in the swallowtail pulse has decreased as evident in the unmodulated beam profile measured for the asphere. For the higher frequencies, the measured field for the asphere more directly represents the radiation pattern associated with the small dipole at a dielectric surface. The lower frequencies have a similar spatial distribution for both the collimating lens and the aspheric lens, due to the preferential out coupling of surface waves for long wavelengths as well as possible diffraction effects.

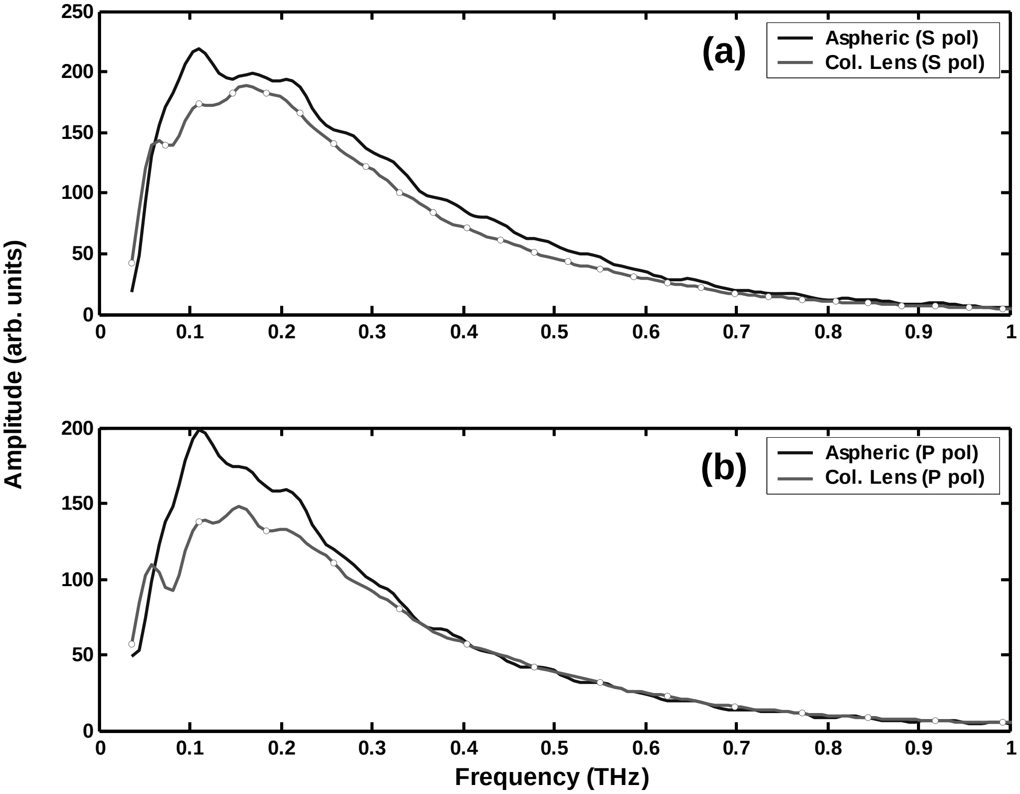

**Figure 6.23** Comparison of the total spectral response for the pulses of Figure 6.21 and Figure 6.22.

A numeric integral taken over the spatial extent of the field amplitude for each Fourier transformed pulse was used to reconstruct the pulse spectra. The spectral overlays, shown in Figure 6.23, demonstrate that even though the peak field is higher for the on axis component for the collimating lens with respect to the aspheric lens for the higher frequencies, the total field amplitude is the same or less.

The peak response is shifted to lower frequencies than expected if one compares Figure 6.23 with the spectral response of a standard TDS system even accounting for the limited bandwidth of the exposed receiver. The spectral lowering may be attributed to the effects of the surface wave contributions. The swallowtail pulse shape does smooth out into a spherical wave for a sufficient propagation distance. Subsequently, the peak of the spectra will tend to shift to higher frequencies due to the highly divergent surface wave radiation due to the propagation distance and apertures due to optical components in a standard TDS system.

## 6.5 **Conclusion**

By applying the tools developed to observe with the evanescent behavior of FTIR coupled with the increased understanding of surface waves resulting from modeling, the effect of lenses has been demonstrated on the propagating THz pulse form.

Aspheric lenses do minimize the effects of spherical aberration and is evident in the spectral profile of the THz beam. Surface wave contributions to the THz pulse continue, but could be readily blocked by the introduction of an aperture without incurring major diffraction features without discarding a majority of the energy.

# 7 Future Directions and Conclusions

## 7.1 FTIR

The spatial measurements of the beam propagation through the FTIR gap presented in Chapter 5 can be continued into various other aspects of evanescent coupling and propagation. Using the exposed receiver chip as a probe to measure the coupling times directly may prove to be a method to look at the build up of the evanescent field or map out the field as a function of time and distance. Further measurements into the coupling of the surface wave modes at the gap interface should be detectable at the edge of the gap a significant distance from the location of the incident beam.

### 7.1.1 Silicon wedge translation improvement

The most basic improvement would be to change the translation orientation of the silicon wedges. The original design for the custom translation system (Figure 3.4) was meant to replicate a standard FTIR experiment where the overall phase is not resolved. A phase correction factor had to be included ($\gamma$ in Equation 3.10) for the linear dispersion theory treatment and the added propagation time had to be accounted for in the spatial FTIR experimental results due to the translation of either an entrance or exit silicon wedge.

A lateral translation rather than a linear translation could be performed as shown in Figure 7.1. The relatively large input face (78 mm dia.) of the silicon wedges would readily accommodate the beam profiles and spatial shifts so far observed. The entrance and exit planes of the system would be the entrance and exit faces of the silicon wedge pair. The introduced gap would go as $\delta\mathbf{X} = \Delta \tan\Phi$, which would require a 2.7 mm lateral displacement to achieve a 1.0 mm gap for the given wedge angle $\Phi = 70°$.

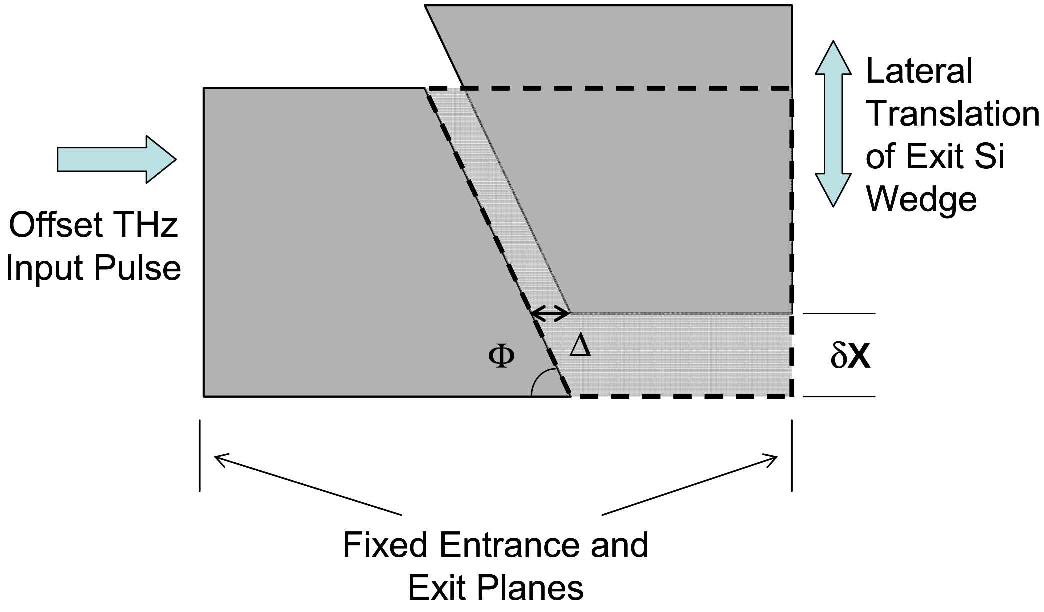

**Figure 7.1** Schematic of improved THz FTIR gap control. The measurement planes would align with the entrance and exit faces of the wedges. A $\delta\mathbf{X} = 2.7$ mm horizontal shift would yield a $\Delta = 1.0$ mm gap.

A redesign of the wedge translation system is required to accomplish the new translation scheme. The observed time shift of the pulse transiting the FTIR barrier would increase with respect to that solely due to the addition of the gap. The exposed receiver chip could be placed directly in contact with the exit face for raster scanning purposes, which would ensure alignment positioning and minimize reflections. The ability to eliminate the stand-off space between the exposed receiver and the exit face of the silicon wedge for both reference and signal pulses would eliminate errors introduced by measurements taken in a plane that is not normal to the optical axis.

### 7.1.2 Beam profile dependence on FTIR

The Goos-Hanchen shift is a consequence of a spatially bounded beam. The spatial shifts observed were under similar circumstances. However the numerical experiment where the incoming beam radii were varied, generated strongly varying transmitted pulse responses (see Chapter 5). A full series of measurements could be designed investigating the k vector filtering processes and dwell time as a function of gap distance ($\Delta$) and starting beam radius ($w_o$) to confirm the predictions of the FDTD model. This may lead to a more clear physical picture of the processes involved, comparing the lateral pulse width with the observed tunneling saturation time associated with the opaque barrier limit.[20]

### 7.1.3 Longitudinal beam shift observation in transmission

The development of a l/4 plate to create circular polarization for the THz beam would facilitate the observation of a predicted longitudinal beam shift also called the optical Hall effect. A shift in the orthogonal direction for circularly polarized beams is expected. This was discussed in the three dimensional profile measurements of Chapter 5. As of this writing, the longitudinal shift has not been experimentally observed in transmission to the author's knowledge.

An x-y translation stage with finer step sizes and greater stability would also be required to resolve the shift.

### 7.1.4 Direct observation of evanescent fields (almost)

The evanescent field cannot be directly measured, requiring the introduction of the frustrating medium or necessitating measurements involving multiple reflections.[37] Once the evanescent field interacts with a higher index medium it is no longer evanescent. However the elusive non-propagating evanescent field could be probed with a specially designed receiver antenna.

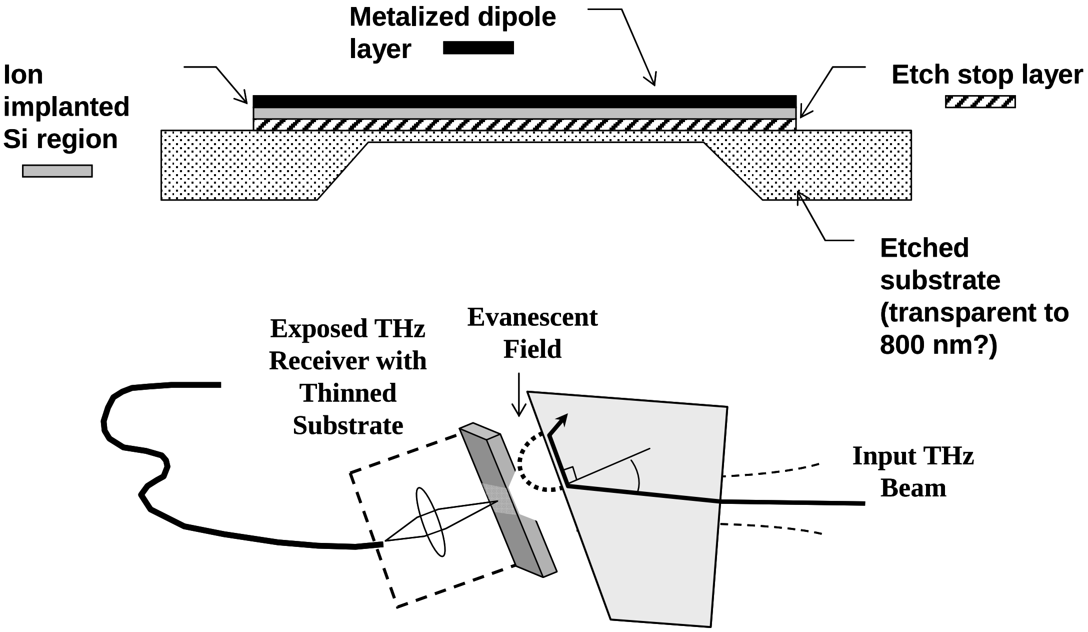

**Figure 7.2** Proposed evanescent probe with thinned substrate exposed receiver dipole and application. The dipole is pictured with the antenna structure oriented toward the optical beam.

Work has been performed with transmission lines on substrates thinned down to micron thicknesses.[82] The sub-wavelength scale of the resulting substrate (~ 10 microns or less) may reduce the perturbation of the antenna structure sufficiently to map the surface wave behavior without the use of the exit wedge for FTIR.

Figure 7.2 shows an illustration of an application of the thinned substrate receiver to investigating the evanescent field in the case of total internal reflection near critical angle. The physical area of the thinned substrate might impact the spatial resolution. The cross section shows the thinned substrate dipole antenna layers. If the etch stop layer is silicon dioxide and sufficiently thin, the supporting substrate could be etched completely down to the mostly transparent etch stop layer. If the etch stop layer was exposed, the receiver could be turned around to direct the dipole antenna toward the exit face of the wedge. If a substrate that provided a favorable chemical etching profile was available that was also relatively transparent to the 800 nm optical gating beam, this reversed orientation could also be implemented, though the orientation would sacrifice the field enhancement due to the high index of the material.[22]

## 7.2 **Imaging**

A fiber coupled variable angle system was constructed utilizing the capabilities developed during the FTIR investigation. Fiber coupling the receiver allows for independent repositioning and orientation of the detection plane while maintaining a fixed time relationship between successive measurements.

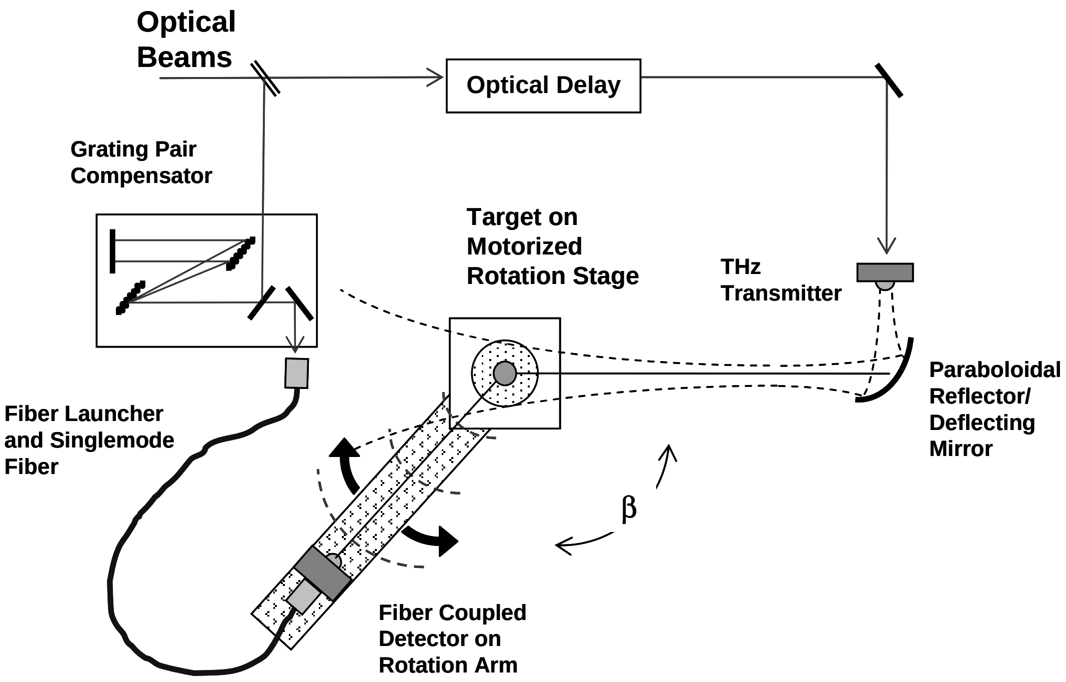

**Figure 7.3** Variable angle THz ranging system with fiber coupled receiver.

### 7.2.1 Synthetic Aperture and Time Based Imaging

Synthetic aperture imaging has been demonstrated using the variable angle THz ranging system.[11] The phase coherence between successive angular measurements, whether from repositioning of the receiver or the target, allows reconstruction of the target information.

For a large ranges of angles, imaging techniques common to medical tomography may have more specific applications. The inverse radon transform is a specific mathematical back projection method, which can be used to develop images of complex surfaces.[83]

The inverse radon back-projection method essentially is a mapping of a cylindrical coordinate system into a Cartesian coordinate system. This simplistic approach works best with opaque scatterers such as metal targets and can be extended to transparent objects as well. Figure 7.4 shows the sinogram (angle vs. scattering time) measurement using the variable angle THz ranging system for a pair of brass cylinders. The dotted lines in Figure 7.4(a) follow the specular reflections from the surface of the cylinders. Signals arriving later in time occur with multiple scattering events, reflections between the cylinders or surface waves. Figure 7.4(b) shows the reconstructed images of the cylinders.

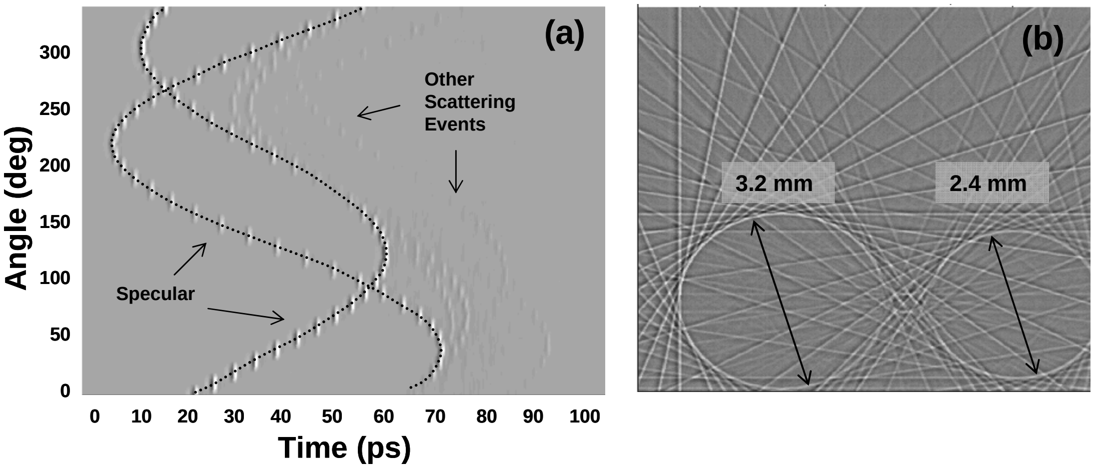

**Figure 7.4** (a) Sinogram (angle vs. scattering time) measurement from two brass cylinders rotated from 0° to 340° in 10° increments. The dotted line provides a guide to the eye for the primary specular reflections from the cylinders. Other scattering events are visible later in time. (b) Back projection image reconstructed from the sinogram in (a).

Fully time based imaging may be performed using sinogram back-projection techniques. However, this method assumes specular type reflections. Identification of non-specular responses such as critical angle events, GH shifts or radiative surface wave propagation, may provide further insight into imaging non-conductive and transparent targets.

## 7.3 Non-destructive testing

One application that has provided encouraging initial results is in the use of THz techniques developed for the investigation of FTIR to nondestructive testing and evaluation of ceramic and composite materials.

A fully fiber-coupled THz transmitter/detector may become feasible for military ordnance personnel for rapid testing of the current and next generation of armor. Ceramic and Kevlar composites have become responsible for protecting soldiers in hostile environments, from personal body armor to hardening otherwise soft-skinned vehicles with removable plates.

**Figure 7.5** Soldier in the Salong Pass of the Hindu Kush mountain range in central Afghanistan during the winter of 2003. He is wearing Interceptor™ Body Armor comprised of a ballistic nylon vest, layers of Kevlar, and ceramic composite strike plates, front and back.

With the advances in fiber lasers and periodically poled lithium niobate doubling structures, a robust ultrafast laser system may find its way out of the optics laboratory and into a field environment. Coupling the short optical pulses to THz transmitters and receivers with fiber would remove the vibration sensitivity of the pointing stability for free space optical coupling. A fiber based delay scheme, such as piezo stretching or "lock-to-clock" pulse sweeping (Spectra Physics) with a pair of fiber lasers, would complete the fully portable system. Merging these technologies could allow THz systems to serve as structural health sensors applied to non-metallic composite or ceramic materials.

### 7.3.1 Fracture detection

Many common industrial ceramics are transparent to THz frequencies and opaque or highly diffusive at optical frequencies. This transparency leads to a potential method to nondestructively detect structural defects in a wide range of previously characterized dielectric materials by exploiting the time domain response.

THz impulse ranging [84] may prove a valuable addition to non-destructive testing (NDT) throughout the manufacturing process of ceramic objects. Powdered ceramic is molded and compacted using binding materials, typically long chain polymers, into green body ceramics. Flaw population in the green body influences the strength of the final structure.[85] When the green body ceramics enter the sintering phase (heating in an oxygen atmosphere), voids and microcracks may originate. Gas desorption can lead to bloating, where trapped gasses expand after sintering, likely due to adsorbed monolayers of water at grain boundaries. THz imaging would work well during the sintering process as it is insensitive to ambient temperatures and is highly sensitive to water vapor.[7] Other flaws in ceramic objects can originate from surface machining and lapping during the final stages.

Ceramic forms such as turbine blades, bearings, ballistic armor, and grinding media find widespread use due to their high temperature tolerance, wear resistance, and surface hardness. Failure modes of ceramic parts tend to be catastrophic due to low plastic deformability resulting from the high activation energy required for lattice deformation. This in turn drives the requirement to detect surface and sub-surface flaws that can initiate failure. Fracture behavior is of special interest for energy dissipation in ceramic armor. [86]

Initial experiments have been performed on ceramic spheres as a demonstration of concept using the variable angle fiber coupled ranging system of Figure 7.3.[87] Alumina bearings, 6.25 mm diameter (Salem Specialty Ball Company) were used as targets in a late time target response (**LTTR**)[31] measurement. One bearing served as a reference target while the other had fractures induced by thermal shock. The surface fractures were on the order of 5 to 25 μm gauged by optical microscopy. The internal fractures have not yet been characterized.

Figure 7.6 shows the results of the LTTR measurements for scattering from the undamaged and damaged bearing. Measurements were taken with $\beta = 45°$ between the THz transmitter and receiver.

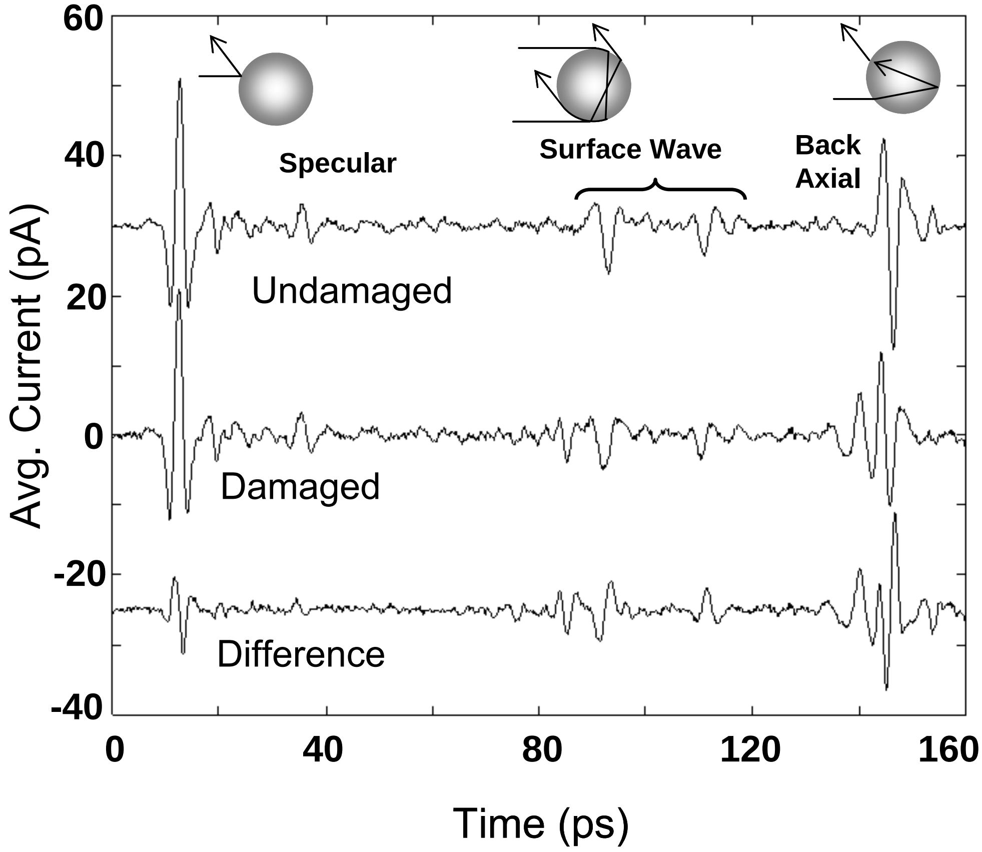

**Figure 7.6** Late time target response (LTTR) for an alumina bearing showing results for a thermally damaged bearing to an undamaged bearing. The primary scattering mechanisms affected are the back axial and the surface wave contributions.

Scattering mechanisms that contribute the LTTR have been identified previously in spheres and cylinders.[34,80] These scattering mechanisms are specular, back axial, and surface wave scattering as indicated in Figure 7.6. The surface wave contribution is due to tangential coupling of the incident beam into the sphere, in essence a time-reversed critical angle event. The damaged bearing exhibits a significant change in scattering response. Understanding the surface wave coupling and propagation of the THz pulses may lead to an improved ability to characterize sub-wavelength inhomogeneities.

Application of the time resolution available to THz TDS and scattering techniques may also allow measurement of fracture propagation in ceramic objects. The mechanisms for detecting sub-wavelength scale fractures within the damaged sample are not currently understood. It may be due to incidence angle and increased reflectivity or interference with other non-specular effects such as the GH shift prompting further investigation.

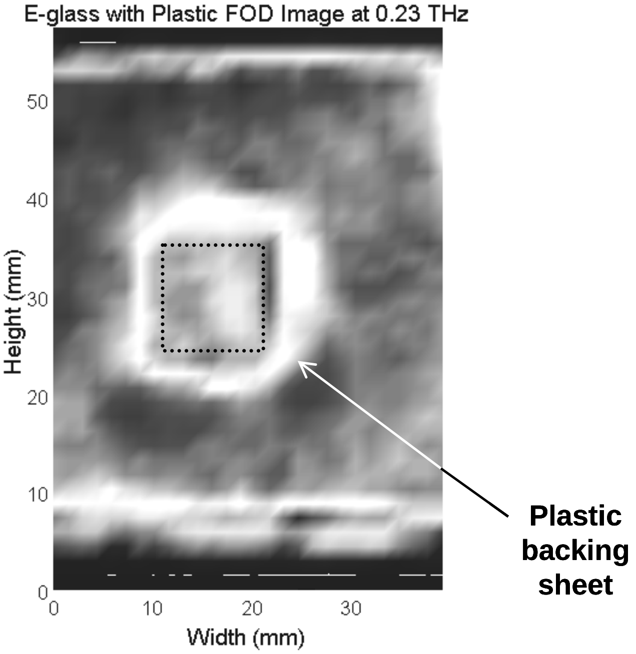

**Figure 7.7** Plastic foreign object damage (FOD) debris, 10 mm × 10 mm, sandwiched between layers of epoxy-glass weave imaged in reflection.

### 7.3.2 Foreign Object Damage Detection

The imaging capabilities with raster scanning a fiber coupled receiver is currently being evaluated for foreign object damage (FOD) detection for use in the manufacturing process of composite structures. Figure 7.7 shows the results of a small plastic sheet, typical of the protective backing for prepared laminate materials, being sandwiched between two non-conductive epoxy-glass weave sheets. The FOD weakens the resulting composite structure. This sheeting may be covered with obscuring paint, preventing direct optical inspection. The presence of the FOD is clearly visible in the measurements due to the index change of the air gap surrounding the debris.

Current ceramic armors are typically protected by layers of Kevlar or other high tensile strength fabrics for protection prior to employment and to control the fracture response.

## 7.4 Improvements

The low power per THz pulse in the systems described in this work can be an asset, for example when probing a material that is thermally sensitive. However it can also be a limiting factor when conducting intrinsically lossy scattering or FTIR measurements. Similarly, maximizing the coupling from THz transmitters to receivers by understanding the propagation of the short pulses and interactions with lens structures may provide directions for further improvements.

### 7.4.1 Fiber coupled transmitters *

Considering the limitations on the THz transmitter in regard to incident optical power and bias voltage, one method of increasing the generated power would be to simultaneously excite multiple transmission line structures. Different methods have already been attempted, including interlaced comb structures with large area optical excitation[88] or linear focusing of the optical beam on a single transmission line structure. Fiber coupling provides the capability to have several different optical beams focused coherently on transmission line structures and individually control the arrival time of the fs pulses. This in turn could lead to phased array type THz transmitters (or matched receivers for multiple simultaneous observation angles.)

### *Fiber arrays*

A fiber array was designed to image multiple optical gating pulses onto a transmitter. The concept of the design was to have commercially available 1 × 2 fiber couplers (50/50 split) take a precompensated optical pulse beam and direct it into matched optical path length single mode fibers. These fibers were kept unjacketed and wrapped around heating elements to synchronize the arrival times of the gating pulses to the transmitter by fine tuning the temperature dependent index of refraction. The fiber array (custom made by Fiber Guide Industries) consisted of a 4 × 4 array of single mode fibers arranged to the pitch of a standard F chip THz transmitter. Figure 7.8 shows the diagram of the fiber array configuration and the fiber array head. Fiber-to-fiber coupling between the splitters, unjacketed matched fibers, and the pigtails to the fiber array is made through bulkhead FC connectors which are inexpensive, but lossy. The output image of the fiber array is imaged using a large aperture achromat is formed on the transmission line structures of the THz transmitter chip.

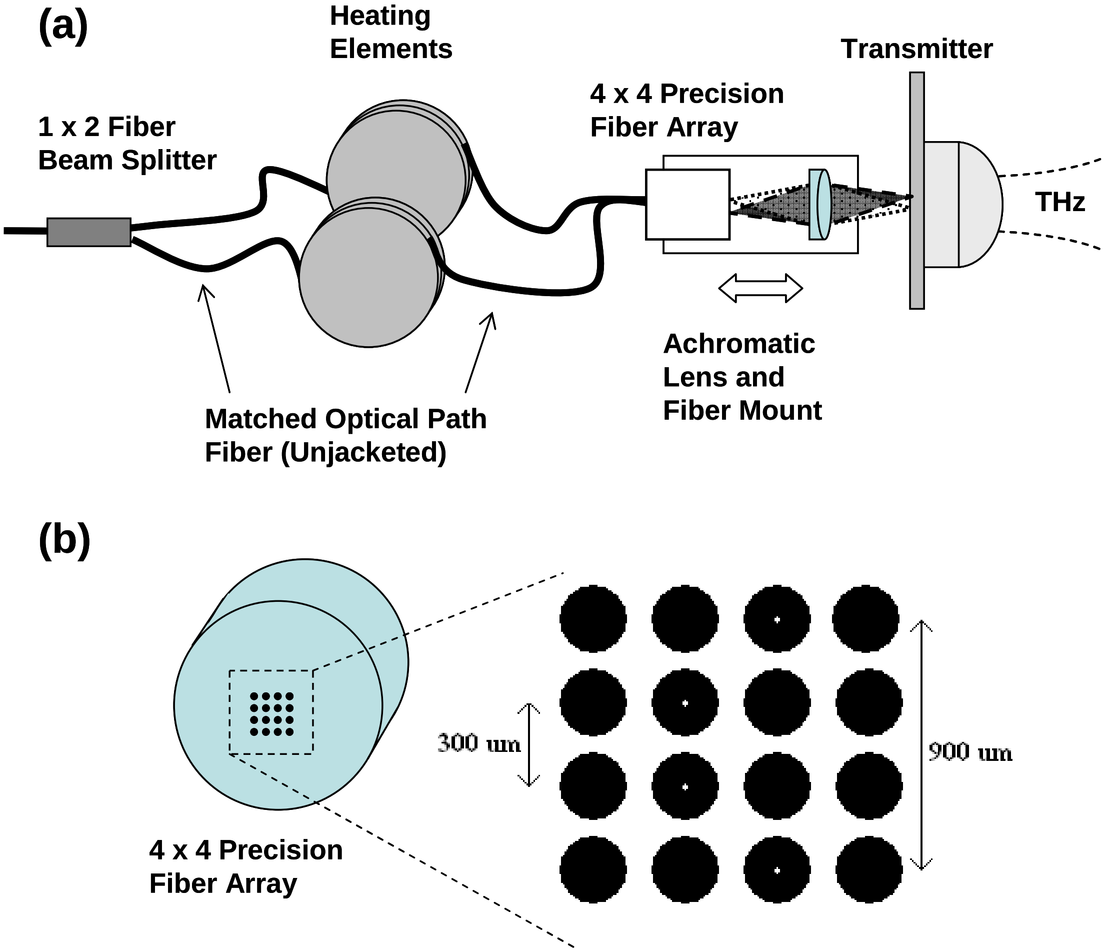

**Figure 7.8** (a) Concept of controlled multiple transmission line excitation on a single chip including major components. Only two fibers are shown, though system could be scaled up to 16 fibers, limited by losses in the optical beam and accumulated path length differences between each arm. (b) 4 × 4 fiber array head schematic where the white dots show the core locations.

The initial results of the multiple line excitation on a single transmitter chip are promising for both a single transmission line and adjacent transmission lines. Figure 7.9 shows the overlay of the THz pulses generated from adjacent transmission lines on a single GaAs chip. Both transmission lines were biased at 73 Vdc, but balancing optical power to the transmission lines was problematic due to coupling losses. Additional phase time loss was introduced by the fiber beam splitter that required the temperature tuning for the pulse arrival time to exceed the rated operating parameters for the single mode fiber.

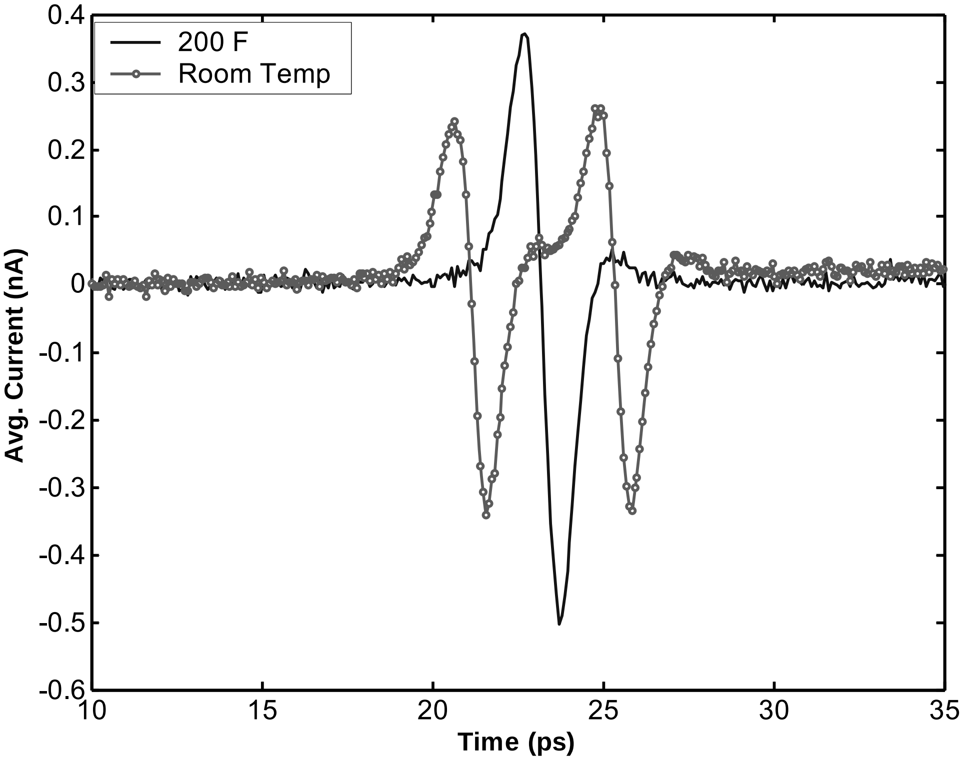

**Figure 7.9** Overlay of THz pulses generated from matched fibers at room temp with both pulses overlapping in time with one fiber heated to 200 F. Complete overlap was not achieved due to additional optical path length differences between the arms of the fiber beam splitter.

With the advent of commercially available hollow core photonic crystal fibers (Thorlabs , a fundamental change in the fiber coupled FRU is underway. The hollow core fibers have been tuned to have a low nonlinear optical coefficient (propagating in air rather than silica) that suppresses supercontinuum generation that plagued earlier efforts while minimizing dispersion. The dispersion compensated hollow core fiber will remove the need for pulse precompensation with associated optical intensity losses and expenses and allow a more robust fiber coupled system to be produced.

## 7.5 **Conclusions**

Superluminal propagation does not occur in frustrated total internal reflection in a matched prism pair system. Linear dispersion theory adequately describes the propagation through an optical barrier without invoking instantaneous transit times for evanescent fields. By examining the spatial profile of a THz pulse after undergoing FTIR, the effects of the barrier are observed in the k-vector filtering of a finite beam. The Goos-Hanchen shift is directly observed in transmission. FDTD modeling provides physical insight into the FTIR tunneling time and is in concurrence with observations.

Evanescent fields and surface wave propagation contribute to THz beam profiles in collimating silicon lenses. Aspheric lenses may prove a method to reduce pulse deformation for short path propagation.

The spatially resolved measurements were only possible through the combined application of fiber-coupling, fast scanning delay lines, and reduced aperture receivers.

# 8 Bibliography

[1] D. Grischkowsky, S. Keiding, M. van Exter et al., "Far-infrared time-domain spectroscopy with terahertz beams of dielectrics and semiconductors", J. Opt. Soc. Am. B **7** (10), 2006 (1990).

[2] R. A. Cheville, M. T. Reiten, R. W. McGowan et al., in *Sensing with Terahertz Radiation*, edited by D. M. Mittleman (Springer, Berlin, 2003), pp. 237.

[3] D. L. Woolard, E. R. Brown, M. Pepper et al., "Terahertz Frequency Sensing and Imaging: A Time of Reckoning Future Applications?" Proceedings of the IEEE **93** (10), 1722 (2005).

[4] W. Robertson, *Optoelectronic Techniques for Microwave and Millimeter-Wave Engineering*. (Artech House, Massachusetts, 1995).

[5] D. Grischkowsky, "An ultrafast optoelectronic THz beam system: applications to time-domain spectroscopy", Optics & Photonics News **3** (5), 21 (1992).

[6] Picometrix.

[7] R. A. Cheville and D. Grischkowsky, "Far-infrared terahertz time-domain spectroscopy of flames", Optics Letters **20** (15), 1646 (1995).

[8] H. Harde and D. Grischkowsky, "Time-domain spectroscopy of molecular vapors with subpicosecond pulses of THz radiation", (1992).

[9] R D. Averitt, A. I. Lobad, C. Kwon et al., in *Ultrafast Phenomena XII*, edited by T. Elsaesser, S. Mukamel, M. M. Murnane et al. (Springer-Verlag, Berlin, 2001), Vol. 12, pp. 434.

[10] D. M. Mittleman, R. H. Jacobsen, and M. C. Nuss, "T-Ray Imaging", IEEE J. Sel. Top. Quan. Elec. **2** (3), 679 (1996).

[11] K. McClatchey, M. T. Reiten, and R. A. Cheville, "Time resolved synthetic aperture terahertz impulse imaging", Appl. Phys. Lett. **79** (27), 4485 (2001).

[12] M. M. Awad and R. A. Cheville, "Transmission terahertz waveguide-based imaging below the diffraction limit", Appl. Phys. Lett. **86**, 221107 (2005).

[13] A. B. Ruffin, J. V. Rudd, J. Decker et al., "Time Reversal Terahertz Imaging", IEEE J. Quant. Elec. **38** (8), 0018 (2002).

[14] J. O'Hara and D. Grischkowsky, "Synthetic phased-array terahertz imaging", Optics Letters **27** (12), 1070 (2002).

[15] John J. Carey, Justyna Zawadzka, Dino A. Jaroszynski et al., "Noncausal Time Response in Frustrated Total Internal Reflection?" Phys. Rev. Lett. **84** (7), 1431 (2000).

[16] E. Hecht, *Optics*. (Addison Wesley, San Francisco, 2002).

[17] M. T. Reiten, D. Grischkowsky, and R. A. Cheville, "Optical Tunneling of Single Cycle, THz Bandwidth Pulses", Phys. Rev. E **64**, 036604 (2001).

[18] M. T. Reiten, K. McClatchey, D. Grischkowsky et al., "Incidence-angle selection and spatial reshaping of terahertz pulses in optical tunneling", Optics Letters **26** (23), 1900 (2001).

[19] R. H. Renard, "Total Reflection - New Evaluation Of Goos-Hanchen Shift", Journal Of The Optical Society Of America **54** (10), 1190 (1964).

[20] Ph Balcou and L. Dutriaux, "Dual optical tunneling times is frustrated total internal reflection", Phys. Rev. Lett. **78** (5), 851 (1997).

[21] M.T. Reiten and R. A. Cheville, "Effect of spherical aberration and surface waves on propagation of lens-coupled terahertz pulses", Optics Letters **30** (6), 673 (2005).

[22] W. Lukosz and Zurich Switz Eth, "Light emission by magnetic and electric dipoles close to a plane dielectric interface. III. Radiation patterns of dipoles with arbitrary orientation", J. Opt. Soc. Am. **69** (11), 1495 (1979).

[23] J. C. G. LeSurf, *Millimetre-wave Optics, Devices, and Systems*. (Adam Hilger, Bristol, 1990).

[24] F. E. Doany, D. Grischkowsky, and C. C. Chi, "Carrier Lifetime Versus Ion-Implantation Dose In Silicon On Sapphire", Applied Physics Letters **50** (8), 460 (1987).

[25] M. C. Nuss, D. H. Auston, and F. Capasso, "Direct Subpicosecond Meaurement of Carrier Mobility of Photoexcited Electrons in Gallium Arsenide", Phys. Rev. Lett. **58** (22), 2355 (1987).

[26] P. U. Jepsen, R. H. Jacobsen, and S. R. Keiding, "Generation and detection of terahertz pulses from biased semiconductor antennas", J. Opt. Soc. Am. B **13** (11), 2424 (1996).

[27] P. Uhd Jepsen and S. R. Keiding, "Radiation patterns from lens-coupled terahertz antennas", Opt. Lett. **20** (8), 807 (1995).

[28] J. T. Verdeyen, *Laser Electronics*. (Prentice Hall, Englewood Cliffs, 1995).

[29] R. Gonzalez and P. Wintz, *Digital Image Processing*, Second ed. (Addison Wesley, 1987).

[30] M. van Exter, Ch Fattinger, and D. Grischkowsky, "Terahertz time-domain spectroscopy of water vapor", Optics Letters **14** (20), 1128 (1989).

[31] R. A. Cheville, R. W. McGowan, and D. Grischkowsky, " Late Time Target Response Measured with THz Impulse Ranging", IEEE Trans. Ant. Prop. **AP-45**, 1518 (1997).

[32] P. U. Jepsen and B. M. Fischer, "Dynamic range in terahertz time-domain transmission and reflection spectroscopy", Optics Letters **30** (1), 29 (2005).

[33] R. Y. Chiao and A. M. Steinberg, in *Progress in Optics*, edited by E. Wolf (Elsevier, Amsterdam, 1997), Vol. 37, pp. 345.

[34] M.T. Reiten, D. Grischkowski, and R. A. Cheville, "Properties of surface waves determined via bistatic terahertz impulse ranging", Applied Physics Letters **78** (8), 1146 (2001).

[35] R. W. McGowan, R. A. Cheville, and D. Grischkowski, "Experimental Study of the Surface Waves on a Dielectric Cylinder via THz Impulse Radar Ranging", IEEE Trans. on Microwave Theory and Techniques **48**, 417 (2000).

[36] B. E. A. Saleh and M. C. Teich, *Fundamentals of Photonics*. (J. Wiley and Sons, New York, 1991).

[37] S. Zhu, A. W. Yu, D. Hawley et al., "Frustrated total internal reflection: A demonstration and review", Am. J. Phys. **54** (7), 601 (1986).

[38] A. M. Steinberg and R. Y. Chiao, "Tunneling delay times in one and two dimensions", Phys. Rev. A **49** (5), 3283 (1994).

[39] P. Lorrain, D. R. Corson, and F. Lorrain, *Electromagnetic Fields and Waves*, 3rd ed. (Freeman, 1988).

[40] M. Born and E. Wolf, *Principles of Optics*, 7 ed. (Cambridge University Press, New York, 1999).

[41] Helmut K.V. Lotsch, "Reflection and Refraction of a beam of light at a plane interface", J. Opt. Soc. Am. **58** (4), 551 (1968).

[42] B. R. Horowitz and T. Tamir, "Lateral displacement of a light beam at a dielectric interface", J. Opt. Soc. Am. **61** (5), 586 (1971).

[43] G. P. Agrawal, *Fiber-Optic Communication Systems*, Second ed. (Wiley-Interscience, 1997).

[44] O.E. Martinez, "Grating and prism compressors in the case of finite beam size", J. Opt. Soc. Am. B **3** (7), 929 (1986).

[45] M. T. Reiten, Rice University, 1994.

[46] Edmond B. Treacy, "Optical Pulse Compression With Diffraction Gratings", IEEE Journal of Quantum Electronics **QE-5** (9), 454 (1969).

[47] C. A. Balanis, *Antenna Theory*, Second ed. (Wiley, 1997).

[48] M. van Exter and D. R. Grischkowsky, "Characterization of an optoelectronic terahertz beam system", IEEE Trans. Microwave Theory Tech. **38** (11), 1684 (1990).

[49] M. T. Reiten, S. A. Harmon, and R. A. Cheville, "Terahertz beam propagation measured through three-dimensional amplitude profile determination", J. Opt. Soc. Am. B **20** (10) (2003).

[50] P. Davies, "Quantum tunneling times", Am. J. Phys. **73** (1), 23 (2005).

[51] G. Nimtz, "Superluminal Signal Velocity and Causality", Found. Phys. **34** (12), 1889 (2004).

[52] V. Gasparian, G. Schon, J. Ruiz et al., "Kramers-Kronig relations and the barrier interaction time problem", Eur. Phys. J. B **9**, 283 (1999).

[53] G. Nimtz, "On superluminal tunneling", Prog. in Quant. Opt. **27**, 417 (2003).

[54] L. J. Wang, A. Kuzmich, and A. Dogariu, "Gain-assisted superluminal light propagation", Nature **406** (20 July), 277 (2000).

[55] C. F. Li and Q. Wang, "Prediction of simultaneously large and opposite generalized Goos-Hanchen shifts for TE and TM light beams in an asymmetric double-prism configuration", Phys. Rev. E **69**, 055601 (2004).

[56] M. Onoda, S. Murakami, and N. Nagaosa, "Hall Effect of Light", Phys. Rev. Lett. **93** (8), 083901 (2004).

[57] S. Longhi, "Resonant tunneling in frustrated total internal reflection", Opt. Lett. **30** (20), 2781 (2005).

[58] L. Brillouin, *Wave Propagation and Group Velocity*. (Academic Press, New York, 1960).

[59] Rolf Landauer, "Light faster than light?" Nature **365** (21), 692 (1993).

[60] Ajoy Ghatak, Swagata Banerjee, and Indian Inst Technol New Delhi India Phys. Dep, "Temporal delay of a pulse undergoing frustrated total internal reflection", Appl. Opt. **28** (11), 1960 (1989).

[61] F. Goos and H. Hanchen, Ann. Physik **1** (333) (1947).

[62] A. K. Ghatak, M. R. Shenoy, I.C. Goyal et al., "Beam propagation under frustrated total internal reflection", Opt. Comm. **56** (5) (1986).

[63] R. Landauer and Th. Martin, "Barrier interaction time in tunneling", Rev. Mod. Phys. **66** (1), 217 (1994).

[64] M. Saiduku, *Numerical Techniques in Electromagnetics*, 2nd ed. (CRC Press, 2001).

[65] J. Jiang, J. Cai, G. P. Nordin et al., "Parallel microgenetic algortihm design for photonic crystal and waveguide structures", Opt. Let. **28** (23), 2381 (2003).

[66] W. Harshawardhan, Q. Su, and R. Grobe, "Numerical solution of the time-dependent Maxwell's equations for random dielectric media", Phys. Rev. E **62** (6), 8705 (2000).

[67] A. Taflove and K. Umashankar, "Review of FD-TD Numerical Modeling of Electromagnetic Wave Scattering and Radar Cross Section", Proc. IEEE **77** (5), 682 (1989).

[68] A. Stahlhofen, "Photonic tunneling time in frustrated total internal reflection", Phys. Rev. A **62**, 012112 (2000).

[69] F. Pillon, H. Gilles, and S. Girard, "Experimental observation of the Imbert-Fedorov transverse displacement after a single total reflection", Appl. Opt. **43** (9), 1863 (2004).

[70] C. Imbert, "Calculation and Experimental Proof of the Transverse Shift Induced by Total Internal Reflection of a Circularly Polarized Light Beam", Phys. Rev. D **5** (4), 787 (1972).

[71] J. D. Murphy, P. J. Moser, A. Nagl et al., "A Surface Wave Interpretation for the Resonances of a Dielectric Sphere", IEEE Trans. Ant. Prop. **28** (6), 924 (1980).

[72] P L Marston, *Geometrical and Catastrophe Optics Methods in Scattering*. (Academic Press, 1992).

[73] T. Poston and I. N. Stewart, *Catastrophe Theory and Its Applications*. (Pitman, London, 1978).

[74] L. Felsen, "Evanescent Waves", J. Opt. Soc. Am. **66** (8), 751 (1976).

[75] D. M. Mittleman, in *Optical Sciences* (Springer, Berlin, 2003).

[76] J. A. Lock, "Semiclassical scattering of an electric dipole source inside a spherical particle", J. Opt. Soc. Am. A **18** (12), 3085 (2001).

[77] J. Nadobny, D. Sullivan, P. Wust et al., "A High-Resolution Interpolation at Arbitrary Interfaces for the FDTD Method", IEEE Trans. MTT **46** (11), 1759 (1998).

[78] A. C. Cangellaris and D. B. Wright, "Analysis of the Numerical Error Caused by the Stair-Stepped Approximation of a Conducting Boundary in FDTD Simulations of Electromagnetic Phenomena", IEEE Trans. Ant. Prop. **39** (10), 1518 (1991).

[79] J. V. Rudd and D. M. Mittleman, "Influence of substrate-lens design in terahertz time-domain spectroscopy", J. Opt. Soc. Am. B **19** (2), 319 (2002).

[80] R. W. McGowan, R. A. Cheville, and D. Grischkowsky, "Direct observation of the Gouy phase shift in THz impulse ranging", Applied Physics Letters **76** (6), 670 (2000).

[81] R. Kingslake, *Lens Design Fundamentals*. (Academic Press, New York, 1978).

[82] W. H. Knox, J. E. Henry, K. W. Goossen et al., "Femtosecond Excitonic Optoelectroncs", IEEE J. Quant. Elec. **25** (12), 2586 (1989); H. J. Cheung, J. F. Whitacker, T. M. Weller et al., "Terahertz-Bandwidth Characteristics of Coplanar Transmission Lines on Low Permittivity Substrates", IEEE Trans. MTT **42** (12), 2399 (1994).

[83] Y. Dai, E. J. Rothwell, K. M. Chen et al., "Time-Domain Imaging of Radar Targets Using Sinogram Restoration for Limited-View Reconstruction", IEEE Trans. Ant. Prop. **47** (8), 1323 (1999).

[84] R. A. Cheville, D. Grischkowsky, and Oklahoma State Univ Stillwater O. K. U. S. A. Sch. Electr. Computer Eng, "Time domain terahertz impulse ranging studies", Appl. Phys. Lett. **67** (14), 1960 (1995).

[85] A.G. King, *Ceramic Technology and Processing*. (William Andrew Publishing/Noyes, 2002).

[86] J. Jovicic, A. Zavaliangos, and F. Ko, "Modeling of the ballistic behavior of gradient design composite armors", Composites A **31**, 773 (2000).

[87] M.T. Reiten, L. Hess, and R. A. Cheville, "Nondestructive evaluation of ceramic materials using terahertz impulse ranging", Proc. SPIE **TBP** (2006).

[88] A. Dreyhaupt, S. Winnerl, T. Dekorsy et al., "High-intensity terahertz radiation from a microstructured large-area photoconductor", Applied Physics Letters **86** (12) (2005).

[89] J. D. Jackson, *Classical Electrodynamics*, 2nd ed. (1975).

# 9 Appendices

## 9.1 **Complex angles**

Following the treatment of Corson and Lorrain[39] the magnitude of an angle θ (in radians)

$$|\theta| = \frac{a}{r} \quad 9.1$$

and Euler's formula

$$e^{i\theta} = \cos\theta + i\sin\theta \quad \text{A.2}$$

Total reflection gives rise to complex propagation angles. From Snell's law, with the subscript 1 referring to the incident medium and angle and subscript 2 referring to the transmitted medium and angle

$$n_1 \sin\theta_1 = n_2 \sin\theta_2 \quad \text{A.3}$$

or solving with the transmitted angle $\theta_2 = \pi/2$ yields (resulting ray emitted tangential to the interface)

$$\theta_c = \sin^{-1}\left(\frac{n_2}{n_1}\right) \quad \text{A.4}$$

Critical angle is then $\theta_c = 17.01°$ for $n_1 = 3.42$ and $n_2 = 1.0$ for the transition from high resistivity silicon into air. This solves exactly for critical angle where a single real solution exists. For incident angles greater than $\theta_c$ and applying EquationA.2, a complex angle is assumed for $\theta_2 = a + ib$

$$\sin\theta_2 = \frac{e^{i(a+ib)} - e^{-i(a+ib)}}{2i} = \frac{e^{ia}e^{-b} - e^{-ia}e^{b}}{2i} \quad \text{A.5}$$

However, Equation A.3 places the constraint that the values must be real in Equation A.5. This only occurs when $a = \pi/2$ so:

$$\sin\theta_2 = \frac{e^{-b} + e^{b}}{2} = \cosh b \qquad \text{A.6}$$

## 9.2 **Fresnel Reflection and Transmission Coefficients**

The transmission and reflection coefficients for field are given in Equations 9.7, 9.8, 9.9, and 9.10 for parallel (P) and perpendicular (S) polarizations.[16] The subscripts of 1 and 0 correspond to the incident medium and the transmitted medium respectively. The subscripts of *i* and *t* correspond to incident angle and transmitted angle with respect to the surface normal.

$$r_{10P} = \left(\frac{E_{rP}}{E_{iP}}\right) = \frac{n_1\cos\theta_i - n_0\cos\theta_t}{n_1\cos\theta_i + n_0\cos\theta_t} \qquad 9.7$$

$$t_{10P} = \left(\frac{E_{tP}}{E_{iP}}\right) = \frac{2n_1\cos\theta_i}{n_1\cos\theta_i + n_0\cos\theta_t} \qquad 9.8$$

$$r_{10S} = \left(\frac{E_{rS}}{E_{iS}}\right) = \frac{n_0\cos\theta_i - n_1\cos\theta_t}{n_0\cos\theta_i + n_1\cos\theta_t} \qquad 9.9$$

$$t_{10S} = \left(\frac{E_{tS}}{E_{iS}}\right) = \frac{2n_1\cos\theta_i}{n_1\cos\theta_t + n_0\cos\theta_i} \qquad 9.10$$

The reflection and transmission coefficients are valid with complex angles.[40]

## 9.3 **Kramers Kronig Relations**

Following the treatment in Jackson [89], the Kramers-Kronig relations are derived from the primary assumption of causality. Causality as defined is that only electric field values from earlier times [$E(t < t_o)$] effect the instantaneous electric field

[$E(t_o)$] and that future values of the electric field [$E(t > t_o)$] play no role. Three other conditions also apply: linearity, stability, and the values over all the range of interest must be finite. Starting with the relationship between displacement and electric field, $\vec{D}(\vec{r},\omega)=\varepsilon(\omega)\vec{E}(\vec{r},\omega)$, the resulting dispersion relations for complex permittivity [ε(ω)] are:

$$\operatorname{Re}\{\varepsilon(\omega)\}=1+\frac{2}{\pi}P\int_0^\infty \frac{\omega'\operatorname{Im}\{\varepsilon(\omega')\}}{\omega'^2-\omega^2}d\omega' \qquad \text{A.11}$$

$$\operatorname{Im}\{\varepsilon(\omega)\}=-\frac{2\omega}{\pi}P\int_0^\infty \frac{[\operatorname{Re}\{\varepsilon(\omega')\}-1]}{\omega'^2-\omega^2}d\omega' \qquad \text{A.12}$$

In this case, P indicates a principle value integral.

The results of numerically calculating the Kramers-Kronig relations for the complex transfer function $H(\omega)=H'(\omega)+iH''(\omega)$ expressed in Equation 3.11 over a range of frequencies from 0 to 20 THz is shown in Figure C.1.

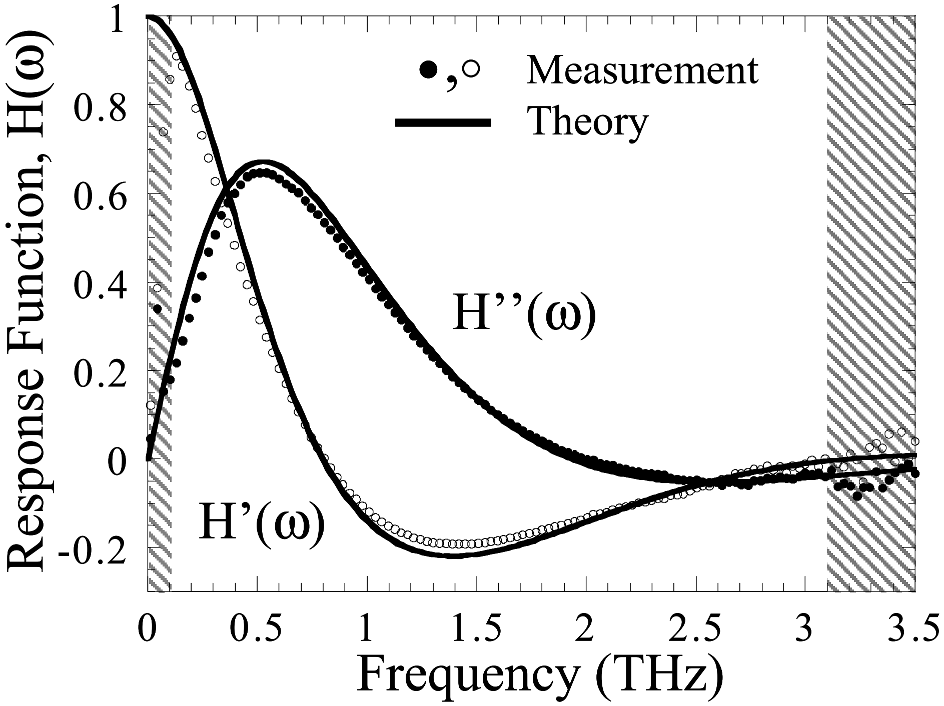

**Figure C.1** Real and imaginary components of the complex transfer function given in Equation 3.11and extrapolated from the measured results.[17]

The expressions for the Kramers-Kronig relations is shown in Equations A.13 and A.14 and are equivalent to Equations A.11 and A.12 for the given transfer function.

$$H'(\upsilon) = \frac{2}{\pi}\int_0^\infty \frac{sH''(\upsilon)}{\upsilon^2 - s^2}\partial s \qquad \text{A.13}$$

$$H''(\upsilon) = \frac{2}{\pi}\int_0^\infty \frac{\upsilon H'(\upsilon)}{\upsilon^2 - s^2}\partial s \qquad \text{A.14}$$

The range for the calculations was limited by the bandwidth of the system, but the results fit over the measured region.

The real and imaginary components of the complex traversal time, $\tau_\phi$ and $\tau_L$ of Equation 5.11 are also related by the Kramers-Kronig relationship.[52] Equations A.15 and A.16 express the causal relationship between the two times.

$$\tau_\phi = \tau_o + \frac{2}{\pi} P \int_0^\infty \frac{\omega' \tau_L(\omega')}{\omega'^2 - \omega^2} d\omega' \qquad \text{A.15}$$

$$\tau_L = -\frac{2\omega}{\pi} P \int_0^\infty \frac{\tau_\phi(\omega') - \tau_o}{\omega'^2 - \omega^2} d\omega' \qquad \text{A.16}$$

$\tau_o$ = Zn/c is the traversal time for the entire system (total propagation distance Z of index n) without introduction of a FTIR barrier. As of this writing, the measured values for the complex traversal time have not been tested against Equations A.15 and A.16.

## 9.4 **Matlab Code**

The finite difference time domain scripts used in this investigation were significantly modified from "te_horn.m" by William V. Andrew and distributed with Balanis's *Antenna Theory* textbook.[47] The modified code follows.

### FTIR Gap Code

```
%********************************************************************************************
%
%     Modified te_horn.m file to have a propagating gaussian-like pulse
%     interact with a FTIR barrier.  Assumes no
%     absorption inside the material.  Generates proper pattern.
%
clear

%********************************************************************************************
%     Initialize some constants
%********************************************************************************************

npmls=12;                % Depth of PML region in # of cells

nmax=8000;               % Number of time steps

ie=901;                % Number of elements in y
ib=ie+1;
ic=round(ie/2-50);             % Center for source in y
ip=ie-npmls;

je=1501;                 % Number of elements in x
jb=je+1;
jc=je/2;               % Source center in x
jp=je-npmls;

muo=4.0*pi*1.0e-7;      % Permeability of free space
epso=8.854e-12;         % Permittivity of free space

epsr=11.7*epso;         % Permittivity in Si for THz freqs
co=1.0/sqrt(muo*epso);   % Speed of light in free space

c = 1/sqrt(muo*epsr);
aimp=sqrt(muo/epso);     % Wave impedance in free space

eta = sqrt(muo/epsr);    % Wave impedance in Si for THz
freq=2.5e+11;             % Frequency of excitation
lambda=co/freq;          % Wavelength of excitation
dx=lambda/150.0;          % FDTD cell size (in meters)
dt=dx/co/2.0;           % Time step size
```

```
%************************************************************************
%     .... Set up the Berenger PML ABC material constants ....
%          no number = free space; 2 indicates silicon
%************************************************************************

sigmax=-3.0*epso*co*log(1e-5)/(2.0*dx*npmls);

sigmax2=-3.0*epsr*co*log(1e-5)/(2.0*dx*npmls);

rhomax=sigmax*(aimp^2);

rhomax2 = sigmax2*(eta^2);

for m=1:npmls;
sig(m)=sigmax*((m-0.5)/(npmls+0.5))^2;

sig2(m)=sigmax2*((m-0.5)/(npmls+0.5))^2;

rho(m)=rhomax*(m/(npmls+0.5))^2;

rho2(m)=rhomax2*(m/(npmls+0.5))^2;
end;

%************************************************************************
%     .... Set up constants needed in the FDTD equations for the ....
%     .... Berenger PML ABCs (exponential difference expressions)....
%************************************************************************

for m=1:npmls;
re=sig(m)*dt/epso;

re2 = sig2(m)*dt/epsr;
rm=rho(m)*dt/muo;

rm2=rho2(m)*dt/muo;
ca(m)=exp(-re);
cb(m)=-(exp(-re)-1.0)/sig(m)/dx;

ca2(m)=exp(-re2);

cb2(m)=-(exp(-re2)-1.0)/sig2(m)/dx;
da(m)=exp(-rm);
db(m)=-(exp(-rm)-1.0)/rho(m)/dx;

da2(m)=exp(-rm2);

db2(m)=-(exp(-rm2)-1.0)/rho2(m)/dx;
end;

%************************************************************************
%   Initialize all of the matrices for the field components HZ, HZX,
%   HZY, EX, EY, CAEX, CAEY, DAHZX, DAHZY, CBEX, CBEY, DBHZX, and DBHZY.
%************************************************************************

% Spatial coordinates xx and yy
xx =dx*[-je/2:je/2];
```

```
yy = dx*[-ie/2:ie/2];

H = 0e-3 % optical tunneling barrier thickness

trunx = 0;  % truncated length x of space for viewing

truny = 50;   % truncated length y of space for viewing

for i=1:ie;           % Sets up zeros for ex
for j=1:jb;
ex(i,j)=0.0;
caex(i,j)=1.0;          % Si
cbex(i,j)=dt/epsr/dx;    % Si
end;
end;

for i=1:ib;           % Set up zeros for ey
for j=1:je;
ey(i,j)=0.0;
caey(i,j)=1.0;         % Si
cbey(i,j)=dt/epsr/dx;   % Si
end;
end;

theta = 17.1*pi/180;                % Angle of incidence on slab
tilt = round((jb-jc)*tan(theta));  %# of cells offset on the boundary
slope = tilt/(jb-jc);              % Slope of gap

% Generate list of y axis indices to be free space
for n = 1:jb;
gap(n,1:round(H/dx))=ic + tilt - round(slope*n) + [1:round(H/dx)];
end;

ilensb = ic+round(H/dx); % top index part of rect section yy (ic - 1 is bottom portion)

for i=1:1:round(H/dx);      % Sets gap
for j=1:jb;
cbex(gap(j,i),j)=dt/epso/dx;    % free space
cbey(gap(j,i),j)=dt/epso/dx;     % free space
end;
end;


for i=1:ie;
for j=1:je;
hz(i,j)=0.0;
hzx(i,j)=0.0;
dahzx(i,j)=1.0;          % Free space
dbhzx(i,j)=dt/muo/dx;     % Free space
hzy(i,j)=0.0;
dahzy(i,j)=1.0;          % Free space
dbhzy(i,j)=dt/muo/dx;     % Free space
end;
end;
disp('Ready')
```

```
%pause
%*******************************************************************
%     Initialize all of the matrices for the Berenger PML absorbing
%     boundaries.
%*******************************************************************

%<<<<<<<<<<<<<<<<<<<<<<<<< Ex Fields >>>>>>>>>>>>>>>>>>>>>>>>>>>>>>>

%        ..... Left and Right PML Regions .....

for i=2:ie;
for j=2:npmls+1;
m=npmls+2-j;
caex(i,j)=ca2(m);
cbex(i,j)=cb2(m);
end;
for j=jp+1:je;
m=j-jp;
caex(i,j)=ca2(m);
cbex(i,j)=cb2(m);
end;
end;

%<<<<<<<<<<<<<<<<<<<<<<<<< Ey Fields >>>>>>>>>>>>>>>>>>>>>>>>>>>>>>>

%        ..... Back and Front PML Regions .....

for j=2:je;
for i=2:npmls+1;
m=npmls+2-i;
caey(i,j)=ca2(m);
cbey(i,j)=cb2(m);
end;
for i=ip+1:ie;
m=i-ip;
caey(i,j)=ca2(m);
cbey(i,j)=cb2(m);
end;
end;

for j = 2:npmls+1;
m=npmls+2-j;
caey(gap(j,[1:round(H/dx)]),j)=ca(m);
cbey(gap(j,[1:round(H/dx)]),j)=cb(m);

caex(gap(j,[1:round(H/dx)]),j)=ca(m);
cbex(gap(j,[1:round(H/dx)]),j)=cb(m);

end;
for j=jp+1:je;
m=j-jp;
caey(gap(j,[1:round(H/dx)]),j)=ca(m);
cbey(gap(j,[1:round(H/dx)]),j)=cb(m);

caex(gap(j,[1:round(H/dx)]),j)=ca(m);
cbex(gap(j,[1:round(H/dx)]),j)=cb(m);
```

```
end;


%<<<<<<<<<<<<<<<<<<<<<<<<<<< Hz Fields >>>>>>>>>>>>>>>>>>>>>>>>>>>>>>>>

%       ..... Left and Right PML Regions .....

for i=2:ie;
for j=1:npmls;
m=npmls+1-j;
dahzy(i,j)=da2(m);
dbhzy(i,j)=db2(m);
end;
for j=jp+1:je;
m=j-jp;
dahzy(i,j)=da2(m);
dbhzy(i,j)=db2(m);
end;
end;

%       ..... Front and Back PML Regions .....

for j=2:je;
for i=1:npmls;
m=npmls+1-i;
dahzx(i,j)=da2(m);
dbhzx(i,j)=db2(m);
end;
for i=ip+1:ie;
m=i-ip;
dahzx(i,j)=da2(m);
dbhzx(i,j)=db2(m);
end;
end;

%       ..... Along the edge of the gap .....

for j = 2:npmls+1;
m=npmls+2-j;
dahzy(gap(j,[1:round(H/dx)]),j)=da(m);
dbhzy(gap(j,[1:round(H/dx)]),j)=db(m);

end;
for j=jp+1:je;
m=j-jp;
dahzy(gap(j,[1:round(H/dx)]),j)=da(m);
dbhzy(gap(j,[1:round(H/dx)]),j)=db(m);

end;

%*********************************************************************
%        .....TIME-STEPPING LOOP.....
%*********************************************************************

for n=1:nmax;
```

```
%**********************************************************************
%         .....EX FIELD UPDATE.....
%**********************************************************************

ex(1:ie,2:je)=caex(1:ie,2:je).*ex(1:ie,2:je)+...
cbex(1:ie,2:je).*(hz(1:ie,2:je)-hz(1:ie,1:je-1));

%**********************************************************************
%         .....EY FIELD UPDATE.....
%**********************************************************************

ey(2:ie,1:je)=caey(2:ie,1:je).*ey(2:ie,1:je)+...
cbey(2:ie,1:je).*(hz(1:ie-1,1:je)-hz(2:ie,1:je));

%**********************************************************************
%    ..... Generate incoming pulse excitation and read pulse.....
%**********************************************************************

if n<400;
rng = [2:jb];
ey(ie-20,rng)=-aimp*(exp(-(n-200)^2/1e4))*sin(2*pi*freq*(n-1)*dt).*...
exp(-((rng-jc*3/4)./300).^2);
end;

if n>3000;
ant_field(n-3000,:)=ey(round(ic-tilt),5:5:je);

end;


%**********************************************************************
%         .....HZ FIELD UPDATE.....
%**********************************************************************

hzx(1:ie,1:je)=dahzx(1:ie,1:je).*hzx(1:ie,1:je)+...
dbhzx(1:ie,1:je).*(ey(1:ie,1:je)-ey(2:ib,1:je));

hzy(1:ie,1:je)=dahzy(1:ie,1:je).*hzy(1:ie,1:je)+...
dbhzy(1:ie,1:je).*(ex(1:ie,2:jb)-ex(1:ie,1:je));

hz(1:ie,1:je)=hzx(1:ie,1:je)+hzy(1:ie,1:je);

%**********************************************************************
%    .....Create the movie frame by frame.....
%    .....Take a frame every 5th time step.....
%**********************************************************************
maxz = max(max(ey))+1;
minz = min(min(ey))-1;

if rem(n,100)==0;
s=num2str(n*dt);
n2=n/100;
clf;

surf(xx(1:5:je-trunx),yy(1:5:ie-truny),(ey(1:5:ie-truny,1:5:je-trunx)));
```

```
axis([min(xx(1:je)) max(xx(1:je-trunx)) min(yy(1:ie)) max(yy(1:ie-truny)) -maxz maxz]);

lighting phong;
view(0,90);

colorbar

caxis([-maxz maxz]);
shading interp;

% Fill in guide to the eye for gap > 0
%       z = line([xx(1);xx(jb-trunx)],[yy(ic-1+tilt);yy(gap(jb-trunx,1))],[maxz,maxz]);
%       set(z,'Color','k')
%       z = line([xx(1);xx(jb-trunx)],[yy(ilensb+tilt);yy(gap(jb-trunx,round(H/dx)))],[maxz,maxz]);
%       set(z,'Color','k')
if n==3;
M=moviein(70);
end;
t2=['THz  Model. Time ',s];
title(t2);
hold;
M(:,n2)=getframe;
end;

%**********************************************************************
%     End time step loop
%**********************************************************************

end;
```

## Lens Propagation Code

```
%**********************************************************************
%
%     Modified te_horn.m file to handle a small dipole near a
%     dielectric interface (ie THz transmitter) radiates in the s
%     plane.  Assumes no absorption inside the material.  Generates
%     proper pattern.  E field along z direction.

clear

%**********************************************************************
%     Initialize some constants
%*********************************************************************

npmls=8;                 % Depth of PML region in # of cells

nmax=20;                 % Number of time steps

ie=600;                % Number of elements in y
ib=ie+1;
ic=ie/2-160;             % Center for source in y
ip=ie-npmls;

je=600;                % Number of elements in x
jb=je+1;
```

```
jc=je/2;                % Source center in x
jp=je-npmls;

muo=4.0*pi*1.0e-7;      % Permeability of free space
epso=8.854e-12;         % Permittivity of free space
epsr=11.7*epso;         % Permittivity in Si for THz freqs
co=1.0/sqrt(muo*epso);  % Speed of light in free space
c = 1/sqrt(muo*epsr);
aimp=sqrt(muo/epso);    % Wave impedance in free space
eta = sqrt(muo/epsr);   % Wave impedance in Si for THz
freq=2.5e+11;           % Frequency of excitation
lambda=co/freq;         % Wavelength of excitation
dx=lambda/150.0;        % FDTD cell size (in meters)
dt=dx/co/2.0;           % Time step size

%***********************************************************************
%     .... Set up the Berenger PML ABC material constants ....
%***********************************************************************

sigmax=-3.0*epso*co*log(1e-5)/(2.0*dx*npmls);
rhomax=sigmax*(aimp^2);

for m=1:npmls;
sig(m)=sigmax*((m-0.5)/(npmls+0.5))^2;
rho(m)=rhomax*(m/(npmls+0.5))^2;
end;

%***********************************************************************
%     .... Set up constants needed in the FDTD equations for the ....
%     .... Berenger PML ABCs (exponential difference expressions)....
%***********************************************************************

for m=1:npmls;
re=sig(m)*dt/epso;
re2 = sig(m)*dt/epsr;
rm=rho(m)*dt/muo;
ca(m)=exp(-re);
cb(m)=-(exp(-re)-1.0)/sig(m)/dx;
ca2(m)=exp(-re2);
cb2(m)=-(exp(-re2)-1.0)/sig(m)/dx;
da(m)=exp(-rm);
db(m)=-(exp(-rm)-1.0)/rho(m)/dx;
end;

%***********************************************************************
%   Initialize all of the matrices for the field components HZ, HZX,
%   HZY, EX, EY, CAEX, CAEY, DAHZX, DAHZY, CBEX, CBEY, DBHZX, and DBHZY.
%***********************************************************************

% Spatial coordinates xx and yy
xx =dx*[-je/2:je/2];
yy = dx*[-ie/2:ie/2];
R = 5e-3;               % Lens radius
H = 4.96e-3 - R + .5e-3 % Lens height

for i=1:ib;             % Sets up zeros for ex
```

```
for j=1:jb;
ez(i,j)=0.0;
ezx(i,j)=0.0;
caezx(i,j)=1.0;          % Free space
cbezx(i,j)=dt/epso/dx;   % Free space
ezy(i,j)=0.0;
caezy(i,j)=1.0;          % Free space
cbezy(i,j)=dt/epso/dx;     % Free space
end;
end;

jlensl = jc-round(R/dx);  % left index limit of lens
jlensr = jc+round(R/dx);  % right index limit of lens
ilensb = ic+round(H/dx); % top index part of rect section yy (ic - 1 is bottom portion)
ilenst = ilensb+round(R/dx);   % top index of lens in yy

for i=ic-1:ilensb;      % Sets lens parameters for bottom section
for j=jlensl:jlensr;  % of lens... below hemisphere
cbezx(i,j)=dt/epsr/dx;    % not free space
cbezy(i,j)=dt/epsr/dx;     % not free space
end;
end;

for j = jlensl:jlensr;
yr(j-jlensl+1)=yy(ilensb);
for i = ilensb:ilenst;
if (sqrt((yy(i)-yy(ilensb)).^2+(xx(j)-xx(jc))^2)<=5e-3);
cbezx(i,j)=dt/epsr/dx;
cbezy(i,j)=dt/epsr/dx;
if (yy(i)>=yr(j-jlensl+1));
yr(j-jlensl+1)=yy(i);
end;
end;
end; end;

for i=1:ib;
for j=1:je;
hx(i,j)=0.0;
dahx(i,j)=1.0;          % Free space
dbhx(i,j)=dt/muo/dx;     % Free space
end; end;

for i = 1:ie;
for j = 1:jb;
hy(i,j)=0.0;
dahy(i,j)=1.0;          % Free space
dbhy(i,j)=dt/muo/dx;     % Free space
end;
end;
disp('Ready')

%*****************************************************************
%    Initialize all of the matrices for the Berenger PML absorbing
%    boundaries.
%*****************************************************************
```

```
%<<<<<<<<<<<<<<<<<<<<<<<<<< Ez Fields >>>>>>>>>>>>>>>>>>>>>>>>>>>>>>>>

%       ..... Left and Right PML Regions .....

for i=2:ie;
for j=2:npmls+1;
m=npmls+2-j;
caezy(i,j)=ca(m);
cbezy(i,j)=cb(m);
end;
for j=jp+1:je;
m=j-jp;
caezy(i,j)=ca(m);
cbezy(i,j)=cb(m);
end;
end;

%       ..... Back and Front PML Regions .....

for j=2:je;
for i=2:npmls+1;
m=npmls+2-i;
caezx(i,j)=ca(m);
cbezx(i,j)=cb(m);
end;
for i=ip+1:ie;
m=i-ip;
caezx(i,j)=ca(m);
cbezx(i,j)=cb(m);
end;
end;

%<<<<<<<<<<<<<<<<<<<<<<<<<< Hx Fields >>>>>>>>>>>>>>>>>>>>>>>>>>>>>>>>

%       ..... Left and Right PML Regions .....

for i=2:ie;
for j=1:npmls;
m=npmls+1-j;
dahx(i,j)=da(m);
dbhx(i,j)=db(m);
end;
for j=jp+1:je;
m=j-jp;
dahx(i,j)=da(m);
dbhx(i,j)=db(m);
end;
end;

%<<<<<<<<<<<<<<<<<<<<<<<<<< Hy Fields >>>>>>>>>>>>>>>>>>>>>>>>>>>>>>>>
%       ..... Front and Back PML Regions .....

for j=2:je;
for i=1:npmls;
m=npmls+1-i;
dahy(i,j)=da(m);
```

```
dbhy(i,j)=db(m);
end;
for i=ip+1:ie;
m=i-ip;
dahy(i,j)=da(m);
dbhy(i,j)=db(m);
end;
end;

%***********************************************************************
%          .....TIME-STEPPING LOOP.....
%**********************************************************************
tic
for n=1:nmax;

%***********************************************************************
%          .....EZ FIELD UPDATE.....
%**********************************************************************

ezx(2:ie,2:je)=caezx(2:ie,2:je).*ezx(2:ie,2:je)+...
cbezx(2:ie,2:je).*(hy(2:ie,2:je)-hy(1:ie-1,2:je));

ezy(2:ie,2:je)=caezy(2:ie,2:je).*ezy(2:ie,2:je)+...
cbezy(2:ie,2:je).*(hx(2:ie,1:je-1)-hx(2:ie,2:je));

ez(2:ie,2:je)=ezx(2:ie,2:je)+ezy(2:ie,2:je);

%***********************************************************************
%     ..... Hard Source ramped sinusoidal excitation .....
%***********************************************************************

for n = 1:200;
ezx(ic,jc)=aimp*(exp(-(n-100)^2/1200))*sin(2*pi*freq*(n-1)*dt);
ezy(ic,jc)=ezx(ic,jc);
hy(ic,jc)=ezy(ic,jc)/aimp;
hx(ic,jc)=ezx(ic,jc)/aimp;
end;

%***********************************************************************
%          .....HX FIELD UPDATE.....
%**********************************************************************

hx(1:ib,1:je)=dahx(1:ib,1:je).*hx(1:ib,1:je)+...
dbhx(1:ib,1:je).*(ez(1:ib,1:je)-ez(1:ib,2:jb));

%***********************************************************************
%          .....HY FIELD UPDATE.....
%**********************************************************************

hy(1:ie,1:jb)=dahy(1:ie,1:jb).*hy(1:ie,1:jb)+...
dbhy(1:ie,1:jb).*(ez(2:ib,1:jb)-ez(1:ie,1:jb));

%***********************************************************************
%    .....Create the movie frame by frame.....
%    .....Take a frame every 5th time step.....
%**********************************************************************
```

```
maxz = max(max(ez))+1;
minz = min(min(ez))-1;
if rem(n,20)==0;
s=num2str(n*dt);
n2=n/20;
clf;

surf(xx(1:je),yy(1:ie),ez(1:ie,1:je));
axis([min(xx(1:je)) max(xx(1:je)) min(yy(1:ie)) max(yy(1:ie)) minz maxz]);
view(0,90);
colorbar
caxis([-maxz maxz]);
shading interp;

% Fill in guide to the eye for lens structure
z = line([xx(jlensl);xx(jlensr)],[yy(ic-1);yy(ic-1)],[maxz-1,maxz-1]);
set(z,'Color','k')
z = line([xx(jlensl);xx(jlensl)],[yy(ic-1);yy(ilensb+1)],[maxz-1,maxz-1]);
set(z,'Color','k')
z = line([xx(jlensr);xx(jlensr)],[yy(ic-1);yy(ilensb+1)],[maxz-1,maxz-1]);
set(z,'Color','k')
hold on
z = plot3([xx(jlensl):dx:xx(jlensr)],yr,maxz-1+yr*0,'k');
hold off
if n==3;
M=moviein(70);
end;
t2=['THz 2D Lens Model P Pol. Time ',s];
title(t2);
hold;
M(:,n2)=getframe;
end;

%**********************************************************************
%     End time step loop
%*********************************************************************
end;

%**********************************************************************
%     Save the movie to file ``te_pulse_p.mat''
%*********************************************************************
toc
%  save te_pulse_s M;
```

[1] D. Grischkowsky, S. Keiding, M. van Exter et al., "Far-infrared time-domain spectroscopy with terahertz beams of dielectrics and semiconductors", J. Opt. Soc. Am. B **7** (10), 2006 (1990).

[2] R. A. Cheville, M. T. Reiten, R. W. McGowan et al., in *Sensing with Terahertz Radiation*, edited by D. M. Mittleman (Springer, Berlin, 2003), pp. 237.

[3] D. L. Woolard, E. R. Brown, M. Pepper et al., "Terahertz Frequency Sensing and Imaging: A Time of Reckoning Future Applications?" Proceedings of the IEEE **93** (10), 1722 (2005).

[4] W. Robertson, *Optoelectronic Techniques for Microwave and Millimeter-Wave Engineering*. (Artech House, Massachusetts, 1995).

[5] D. Grischkowsky, "An ultrafast optoelectronic THz beam system: applications to time-domain spectroscopy", Optics & Photonics News **3** (5), 21 (1992).

[6] Picometrix.

[7] R. A. Cheville and D. Grischkowsky, "Far-infrared terahertz time-domain spectroscopy of flames", Optics Letters **20** (15), 1646 (1995).

[8] H. Harde and D. Grischkowsky, "Time-domain spectroscopy of molecular vapors with subpicosecond pulses of THz radiation", (1992).

[9] R D. Averitt, A. I. Lobad, C. Kwon et al., in *Ultrafast Phenomena XII*, edited by T. Elsaesser, S. Mukamel, M. M. Murnane et al. (Springer-Verlag, Berlin, 2001), Vol. 12, pp. 434.

[10] D. M. Mittleman, R. H. Jacobsen, and M. C. Nuss, "T-Ray Imaging", IEEE J. Sel. Top. Quan. Elec. **2** (3), 679 (1996).

[11] K. McClatchey, M. T. Reiten, and R. A. Cheville, "Time resolved synthetic aperture terahertz impulse imaging", Appl. Phys. Lett. **79** (27), 4485 (2001).

[12] M. M. Awad and R. A. Cheville, "Transmission terahertz waveguide-based imaging below the diffraction limit", Appl. Phys. Lett. **86**, 221107 (2005).

[13] A. B. Ruffin, J. V. Rudd, J. Decker et al., "Time Reversal Terahertz Imaging", IEEE J. Quant. Elec. **38** (8), 0018 (2002).

[14] J. O'Hara and D. Grischkowsky, "Synthetic phased-array terahertz imaging", Optics Letters **27** (12), 1070 (2002).

[15] John J. Carey, Justyna Zawadzka, Dino A. Jaroszynski et al., "Noncausal Time Response in Frustrated Total Internal Reflection?" Phys. Rev. Lett. **84** (7), 1431 (2000).

[16] E. Hecht, *Optics*. (Addison Wesley, San Francisco, 2002).

[17] M. T. Reiten, D. Grischkowsky, and R. A. Cheville, "Optical Tunneling of Single Cycle, THz Bandwidth Pulses", Phys. Rev. E **64**, 036604 (2001).

[18] M. T. Reiten, K. McClatchey, D. Grischkowsky et al., "Incidence-angle selection and spatial reshaping of terahertz pulses in optical tunneling", Optics Letters **26** (23), 1900 (2001).

[19] R. H. Renard, "Total Reflection - New Evaluation Of Goos-Hanchen Shift", Journal Of The Optical Society Of America **54** (10), 1190 (1964).

[20] Ph Balcou and L. Dutriaux, "Dual optical tunneling times is frustrated total internal reflection", Phys. Rev. Lett. **78** (5), 851 (1997).

[21] M.T. Reiten and R. A. Cheville, "Effect of spherical aberration and surface waves on propagation of lens-coupled terahertz pulses", Optics Letters **30** (6), 673 (2005).

[22] W. Lukosz and Zurich Switz Eth, "Light emission by magnetic and electric dipoles close to a plane dielectric interface. III. Radiation patterns of dipoles with arbitrary orientation", J. Opt. Soc. Am. **69** (11), 1495 (1979).

[23] J. C. G. LeSurf, *Millimetre-wave Optics, Devices, and Systems*. (Adam Hilger, Bristol, 1990).

[24] M. C. Nuss, D. H. Auston, and F. Capasso, "Direct Subpicosecond Meaurement of Carrier Mobility of Photoexcited Electrons in Gallium Arsenide", Phys. Rev. Lett. **58** (22), 2355 (1987).

[25] P. U. Jepsen, R. H. Jacobsen, and S. R. Keiding, "Generation and detection of terahertz pulses from biased semiconductor antennas", J. Opt. Soc. Am. B **13** (11), 2424 (1996).

[26] P. Uhd Jepsen and S. R. Keiding, "Radiation patterns from lens-coupled terahertz antennas", Opt. Lett. **20** (8), 807 (1995).

[27] J. T. Verdeyen, *Laser Electronics*. (Prentice Hall, Englewood Cliffs, 1995).

[28] R. Gonzalez and P. Wintz, *Digital Image Processing*, Second ed. (Addison Wesley, 1987).

[29] M. van Exter, Ch Fattinger, and D. Grischkowsky, "Terahertz time-domain spectroscopy of water vapor", Optics Letters **14** (20), 1128 (1989).

[30] R. A. Cheville, R. W. McGowan, and D. Grischkowsky, " Late Time Target Response Measured with THz Impulse Ranging", IEEE Trans. Ant. Prop. **AP-45**, 1518 (1997).

[31] P. U. Jepsen and B. M. Fischer, "Dynamic range in terahertz time-domain transmission and reflection spectroscopy", Optics Letters **30** (1), 29 (2005).

[32] R. Y. Chiao and A. M. Steinberg, in *Progress in Optics*, edited by E. Wolf (Elsevier, Amsterdam, 1997), Vol. 37, pp. 345.

[33] M.T. Reiten, D. Grischkowski, and R. A. Cheville, "Properties of surface waves determined via bistatic terahertz impulse ranging", Applied Physics Letters **78** (8), 1146 (2001).

[34] R. W. McGowan, R. A. Cheville, and D. Grischkowski, "Experimental Study of the Surface Waves on a Dielectric Cylinder via THz Impulse Radar Ranging", IEEE Trans. on Microwave Theory and Techniques **48**, 417 (2000).

[35] B. E. A. Saleh and M. C. Teich, *Fundamentals of Photonics*. (J. Wiley and Sons, New York, 1991).

[36] S. Zhu, A. W. Yu, D. Hawley et al., "Frustrated total internal reflection: A demonstration and review", Am. J. Phys. **54** (7), 601 (1986).

[37] A. M. Steinberg and R. Y. Chiao, "Tunneling delay times in one and two dimensions", Phys. Rev. A **49** (5), 3283 (1994).

[38] M. Born and E. Wolf, *Principles of Optics*, 7 ed. (Cambridge University Press, New York, 1999).

[39] Helmut K.V. Lotsch, "Reflection and Refraction of a beam of light at a plane interface", J. Opt. Soc. Am. **58** (4), 551 (1968).

[40] B. R. Horowitz and T. Tamir, "Lateral displacement of a light beam at a dielectric interface", J. Opt. Soc. Am. **61** (5), 586 (1971).

[41] G. P. Agrawal, (Wiley-Interscience, 1997).

[42] O.E. Martinez, "Grating and prism compressors in the case of finite beam size", J. Opt. Soc. Am. B **3** (7), 929 (1986).

[43] M. T. Reiten, Rice University, 1994.

[44] Edmond B. Treacy, "Optical Pulse Compression With Diffraction Gratings", IEEE Journal of Quantum Electronics **QE-5** (9), 454 (1969).

[45] C. A. Balanis, *Antenna Theory*, Second ed. (Wiley, 1997).

[46] P. Bhartia, K. V. S. Rao, and R. S. Tomar, *Millimeter-wave microstrip and printed circuit antennas*. (Artech House, 1991).

[47] M. T. Reiten, S. A. Harmon, and R. A. Cheville, "Terahertz beam propagation measured through three-dimensional amplitude profile determination", J. Opt. Soc. Am. B **20** (10) (2003).

[48] P. Davies, "Quantum tunneling times", Am. J. Phys. **73** (1), 23 (2005).

[49] G. Nimtz, "Superluminal Signal Velocity and Causality", Found. Phys. **34** (12), 1889 (2004).

[50] V. Gasparian, G. Schon, J. Ruiz et al., "Kramers-Kronig relations and the barrier interaction time problem", Eur. Phys. J. B **9**, 283 (1999).

[51] G. Nimtz, "On superluminal tunneling", Prog. in Quant. Opt. **27**, 417 (2003).

[52] L. J. Wang, A. Kuzmich, and A. Dogariu, "Gain-assisted superluminal light propagation", Nature **406** (20 July), 277 (2000).

[53] C. F. Li and Q. Wang, "Prediction of simultaneously large and opposite generalized Goos-Hanchen shifts for TE and TM light beams in an asymmetric double-prism configuration", Phys. Rev. E **69**, 055601 (2004).

[54] M. Onoda, S. Murakami, and N. Nagaosa, "Hall Effect of Light", Phys. Rev. Lett. **93** (8), 083901 (2004).

[55] S. Longhi, "Resonant tunneling in frustrated total internal reflection", Opt. Lett. **30** (20), 2781 (2005).

[56] L. Brillouin, *Wave Propagation and Group Velocity*. (Academic Press, New York, 1960).

[57] Rolf Landauer, "Light faster than light?" Nature **365** (21), 692 (1993).

[58] Ajoy Ghatak, Swagata Banerjee, and Indian Inst Technol New Delhi India Phys. Dep, "Temporal delay of a pulse undergoing frustrated total internal reflection", Appl. Opt. **28** (11), 1960 (1989).

[59] F. Goos and H. Hanchen, Ann. Physik **1** (333) (1947).

[60] A. K. Ghatak, M. R. Shenoy, I.C. Goyal et al., "Beam propagation under frustrated total internal reflection", Opt. Comm. **56** (5) (1986).

[61] R. Landauer and Th. Martin, "Barrier interaction time in tunneling", Rev. Mod. Phys. **66** (1), 217 (1994).

[62] M. Saiduku, *Numerical Techniques in Electromagnetics*, 2nd ed. (CRC Press, 2001).

[63] J. Jiang, J. Cai, G. P. Nordin et al., "Parallel microgenetic algortihm design for photonic crystal and waveguide structures", Opt. Let. **28** (23), 2381 (2003).

[64] W. Harshawardhan, Q. Su, and R. Grobe, "Numerical solution of the time-dependent Maxwell's equations for random dielectric media", Phys. Rev. E **62** (6), 8705 (2000).

[65] A. Taflove and K. Umashankar, "Review of FD-TD Numerical Modeling of Electromagnetic Wave Scattering and Radar Cross Section", Proc. IEEE **77** (5), 682 (1989).

[66] A. Stahlhofen, "Photonic tunneling time in frustrated total internal reflection", Phys. Rev. A **62**, 012112 (2000).

[67] F. Pillon, H. Gilles, and S. Girard, "Experimental observation of the Imbert-Fedorov transverse displacement after a single total reflection", Appl. Opt. **43** (9), 1863 (2004).

[68] C. Imbert, "Calculation and Experimental Proof of the Transverse Shift Induced by Total Internal Reflection of a Circularly Polarized Light Beam", Phys. Rev. D **5** (4), 787 (1972).

[69] J. D. Murphy, P. J. Moser, A. Nagl et al., "A Surface Wave Interpretation for the Resonances of a Dielectric Sphere", IEEE Trans. Ant. Prop. **28** (6), 924 (1980).

[70] P L Marston, *Geometrical and Catastrophe Optics Methods in Scattering*. (Academic Press, 1992).

[71] L. Felsen, "Evanescent Waves", J. Opt. Soc. Am. **66** (8), 751 (1976).

[72] D. M. Mittleman, in *Optical Sciences* (Springer, Berlin, 2003).

[73] J. A. Lock, "Semiclassical scattering of an electric dipole source inside a spherical particle", J. Opt. Soc. Am. A **18** (12), 3085 (2001).

[74] C. A. Balanis, "Antenna Theory: A Review", Proc. IEEE **80** (1992).

[75] J. Nadobny, D. Sullivan, P. Wust et al., "A High-Resolution Interpolation at Arbitrary Interfaces for the FDTD Method", IEEE Trans. MTT **46** (11), 1759 (1998).

[76] A. C. Cangellaris and D. B. Wright, "Analysis of the Numerical Error Caused by the Stair-Stepped Approximation of a Conducting Boundary in FDTD Simulations of Electromagnetic Phenomena", IEEE Trans. Ant. Prop. **39** (10), 1518 (1991).

[77] J. V. Rudd and D. M. Mittleman, "Influence of substrate-lens design in terahertz time-domain spectroscopy", J. Opt. Soc. Am. B **19** (2), 319 (2002).

[78] R. W. McGowan, R. A. Cheville, and D. Grischkowsky, "Direct observation of the Gouy phase shift in THz impulse ranging", Applied Physics Letters **76** (6), 670 (2000).

[79] R. A. Cheville and D. Grischkowsky, "Time domain terahertz impulse ranging studies", Appl. Phys. Lett. **67** (14), 1960 (1995).

[80] A.G. King, *Ceramic Technology and Processing*. (William Andrew Publishing/Noyes, 2002).

[81] MIL-HDBK-793(AR), (U.S. Department of Defense, 1989).

[82] M.T. Reiten, L. Hess, and R. A. Cheville, "Nondestructive evaluation of ceramic materials using terahertz impulse ranging", Proc. SPIE **TBP** (2006).

# VITA

Matthew Thomas Reiten

Candidate for the Degree of

Doctor of Philosophy

Thesis: SPATIALLY RESOLVED TERAHERTZ PROPAGATION

Major Field: Electrical Engineering

Biographical:

Personal Data: Born in Grand Forks, North Dakota.

Education: B.S. Physics, B.S. Engineering Physics, and B.S. Electrical Engineering 1991, University of North Dakota, Grand Forks, North Dakota. M.S. Applied Physics, 1994, Rice University, Houston, Texas. Completed the Requirements for the Doctor of Philosophy degree at Oklahoma State University in May 2006.

Experience: Simulated density of state behavior due to dislocations in two dimensional lattices in the Research Experience for Undergraduates at the Cornell Supercomputing Facility; grew high temperature superconductors during a Science and Engineering Research Semester at Argonne National Laboratory; conducted research in non-linear optics under Dr. Naomi Halas at Rice University; served in the US Army as a signal officer in Bosnia and Germany; investigated terahertz beam propagation under Dr. Alan Cheville at Oklahoma State University in the Electrical and Computer Engineering Department; trained the Afghan National Army in communication procedures during Operation Enduring Freedom

Name: Matthew T. Reiten Degree: May, 2006

Institution: Oklahoma State University Location: Stillwater, Oklahoma

Title of Study: SPATIALLY RESOLVED TERAHERTZ PROPAGATION

Pages in Study: 208 Candidate for the Degree of Doctor of Philosophy

Major Field: Electrical Engineering

Scope and Method of Study: The focus of the research was to investigate the spatial behavior of near single cycle freely propagating terahertz radiation. The terahertz pulses were generated through optoelectronic means and the experimental systems based on established terahertz time domain spectroscopy techniques. By raster scanning the terahertz beam orthogonally to the optic axis with a fiber-coupled reduced aperture receiver, the electric field of the beam could be directly measured. This system was used to investigate the propagation of a broad bandwidth pulse through an optical tunneling barrier comprised of a matched pair of high resistivity silicon prisms cut at an incident angle above critical angle. Spectral analysis through numeric Fourier transforms was used to interpret the behavior and test claims of superluminal (faster than the speed of light) propagation through an optical tunneling barrier.

Findings and Conclusions: Superluminal propagation does not occur in the case of frustrated total internal reflection. Linear dispersion theory, experimental evidence of a lateral beam shift (the Goos-Hanchen effect), and numeric simulation support the conclusion that propagation across an optical tunneling barrier is causal. Exposed receiver dipole antennas provide sufficient resolution to observe fine features in the propagating beam profile. The starting beam waist of the incident terahertz beam strongly influences the pulse profile after transiting an optical tunneling barrier. Standard silicon collimating lenses give rise to frequency dependent beam profiles due to interference caused by a complex temporal pulse structure. The complex pulse structure results from lens aberrations, antenna radiation patterns, and surface wave contributions. Aspheric lenses minimize the observed pulse structure due to spherical aberration and are a better choice of lens for measuring incident plane wave terahertz radiation.

ADVISER’S APPROVAL: ______________________________